LA-UR- 01-2199

Approved for public release; distribution is unlimited.

Title: A Regional Flow and Transport Model for Groundwater at Los Alamos National Laboratory

Author(s): Elizabeth H. Keating
Edward M. Kwicklis
Velimir V. Vesselinov
April M. Idar
Zhiming Lu
George A. Zyvoloski
Marc S. Witkowski

Submitted to: Hydrogeologic Characterization Program Progress Report

Los Alamos
NATIONAL LABORATORY

Form 836 (10/96)

A Regional Flow and Transport Model for Groundwater at Los Alamos National Laboratory

Hydrogeologic Characterization Program

A progress report
October 31, 2000

Elizabeth Keating
Ed Kwicklis
Velimir Vesselinov
April Idar
Zhiming Lu
George Zyvoloski
Marc Witkowski

EES-5
Earth and Environmental Sciences Division
Los Alamos National Laboratory

PRELIMINARY DRAFT

Acknowledgements

This work was funded by DP Programs, as part of the Hydrogeologic Characterization Program. A portion of this work, developing stochastic approaches to modeling heterogeneity in sedimentary rocks, was jointly funded by the ALDSSR Office. We have benefited by conversations with many members of the GIT, including Bill Stone, Steve McLin, and David Rogers. We would like to thank Bill Carey and Greg Cole, in particular, for their work on the hydrostratigraphic model, which provides an important foundation for this work.

TABLE OF CONTENTS

1. Executive Summary and Recommendations

This report describes activities that were conducted in FY00 as part of the regional aquifer-modeling project. Initial model development and related data interpretation has been described in previous reports (Keating et al. 1998; Keating et al. 1999; Keating and Warren 1999; Keating et al. 1999). The broad goals of regional modeling are 1) to synthesize hydrologic, geochemical, and geologic data relevant to the regional aquifer, 2) to provide a quantitative tool for refining our conceptual model, to 3) through uncertainty analyses, set priorities for data collection and 4) predict flow directions and velocities, along with technically defensible estimates of uncertainty for these predictions.

The specific goals for FY00 were to provide modeling support to well siting decisions, to integrate any new geologic or hydrologic data collected into the regional model, to formally integrate geochemical tracers (^{3}H, 14C, $\delta^{18}O$, Cl) into the process of model development and validation, and to begin development of a facies-based approach to modeling heterogeneity within the Puye Formation. This last element was funded jointly by the ALDSSR Office; implications of this work to transport of HE in the regional aquifer are described in Robinson, Keating and others (2000).

To provide modeling support to siting of R-5 as a monitoring well for hydraulic testing purposes, we simulated a pump test at O-1 and predicted levels of drawdown under a variety of scenarios (Chapter 2). The primary goal of this work was to provide estimates of between-well distances that would be favorable for data collection. We estimated that the maximum between-well distance for adequate response in the monitoring well was approximately 400m; closer distances would be preferable. An important ancillary benefit of this work was the development of general methodologies for using FEHM to study hydraulics during a pump test, assuming a non-uniform hydraulic conductivity field. This capability allows us to map heterogeneous aquifer properties, distributed according to hydrostratigraphic zonations, onto a numerical mesh appropriate for pump test analysis. The methods developed for this particular application (pumping at O-1) can be easily applied to pump test design and/or interpretation at other sites in the future.

The process of integrating new geologic and hydrologic data into the flow model was dominated by issues raised by changes in the site-wide geologic model (Carey et al. 1999)

(Chapter 3). In addition, we incorporated new water level data and pump test results from R-wells into the model parameterization and calibration process. We focused much of our attention on estimating permeability variations within the regional aquifer, using a combination of data summary and analysis (Chapter 4) and inverse modeling techniques (Chapter 5). The inverse modeling methods, including model calibration and sensitivity analysis, provided us with detailed information about the sensitivity of model results to parameter uncertainty. This information can be used to prioritize data collection efforts and to focus future model development.

Progress in our development of facies-based model for the Puye Formation was difficult due to the Cerro Grande Fire, since access to Puye outcrops in canyons was very limited and staff members with field expertise regarding the Puye were redirected to fire-related efforts. Nevertheless, we were able to compile and comprehensive literature review, conduct reconnaissance field trips, and provide initial, bounding estimates for facies geometries (Chapter 7). Due to the limited nature of our initial dataset, we used a Gaussian approach (Gomez-Hernandez 1991) (rather than a facies-based approach) to simulate stochastic hydraulic conductivity fields. As the dataset improves, we expect to move to a facies-based method. The simulated stochastic hydraulic conductivity fields allowed us to provide ranges of travel times from TA16 to the PM wellfield that were much better constrained (Robinson et al. 2000) than those provided by our initial simulations, which were based on a deterministic model of the Puye (Keating et al. 1999).

To resolve small-scale features in the Puye Formation, we were forced to increase the resolution of our numerical mesh beyond practical limits, given the scale of the basin model. Therefore, we developed a sub-model of the basin model, focused on the Pajarito Plateau, which allowed us to improve the vertical resolution in the mesh. The disadvantage of this approach is that lateral model boundaries can no longer be assumed to be no-flow, and transport calculations may be sensitive to these lateral fluxes. Therefore, we used the basin model to calculate "best estimate" fluxes to the submodel boundaries, and also calculated uncertainty limits for these estimates. These results are preliminary; we expect uncertainty in these estimates to decrease as new data from R-wells is collected.

Finally, we present transport calculations for groundwater tracers (^{3}H, ^{14}C, _ ^{18}O, Cl) (Chapter 6). All of these simulations were designed to estimate steady-state concentrations of

tracers in groundwaters, and so should reflect "background" concentrations in the aquifer if it were completely unaffected by human activities. For each of these tracers, we compare simulated and measured concentrations in wells. Favorable comparisons serve as a measure of independent model validation, since no parameters were adjusted or calibrated during the transport simulation process. Poor comparisons indicate model insufficiency and/or anthropogenic influences on the system. As reported in Chapter 6, the results of each of these transport simulations provided some measure of model validation; predicted concentrations were qualitatively consistent with measurements, particularly in those wells in the vicinity of LANL. Nevertheless, the simulations did highlight aspects of the model that could be improved. For example, the model underestimated ^{14}C ages in waters near the Rio Grande, indicating that improvements are necessary in the region beneath the river. Also, the model did not capture small-scale variations in $\_^{18}O$ within the LANL site; to do so would probably require a more detailed recharge model.

All data and model results presented in this report are preliminary and subject to change in the future. This is a work in-progress

Recommendations

Based on the results described in this report, we would like to make the following recommendations:

1) Field-scale hydraulic conductivity data should continue to be collected for the regional aquifer, ideally in cross-hole tests. To compliment data collection, inverse flow modeling should be used as a method for identifying large-scale permeability features in the aquifer.

2) Additional outcrop data should be collected on both the Santa Fe Group and the Puye formation, to estimate facies geometries. We also need to develop methodologies for relating outcrop information to borehole data, such pump tests and geophysical logs.

3) We need to continue to re-evaluate our conceptual model regarding facies within the Santa Fe group. Through flow modeling, we conclude that the current hydrostratigraphic model delineation of the "Los Alamos aquifer", as a relatively large-scale, high-permeability facies, cannot be reconciled with hydrologic data such as water level measurements and baseflow discharge estimates. Alternative models of this unit should be developed.

4) Since data concerning hydrostratigraphy in the regional aquifer is likely to continue to be sparse (many R wells have not penetrated the Santa Fe Group, for example) the hydrostratigraphic model will continue to be associated with significant uncertainty. We recommend that formal approaches be developed to handle this uncertainty in our models.

5) Porosity of aquifer rocks is a key unknown that will become increasingly important in transport calculations. Cross-hole tracer tests and modeling studies of naturally-occurring tracers (such as those included in this report) are the best approaches to determination of effective (field-scale) porosity.

2 Simulation of Pump Test at Otowi-1

2.1 Background

The primary goal of the Hydrogeologic Work Plan is to characterize the regional aquifer; a key element of aquifer characterization is spatial distribution of hydraulic conductivity and storativity. Unfortunately, there is a strong scale-dependency to these parameters. Extrapolation of small-scale measurements (from core and slug tests) to large-scale models of flow and transport is problematic. The best measures of field-scale aquifer characteristics are those drawn from field scale testing, including pump tests with one or more monitoring wells.

One strategy for collecting pump test data is to locate a new R-well sufficiently close to an existing supply well so that it can be using as a monitoring well. This report is intended to provide technical support to the decision concerning possible siting of R-5 such that it could be used as a monitoring well during a pump test at O-1. In order to place R-5 in an optimal position for pump test monitoring purposes, the size and character of the expected drawdown cone must be estimated a priori. Groundwater flow models are well suited for this purpose; this report describes a suite of simulations that have been conducted to predict the range of behaviors that might be expected during a pump test at O-1.

2.2 Pump test design and aquifer characteristics

Otowi 1 is a municipal supply well located near the confluence of Pueblo and Los Alamos Canyons, drilled in 1990 to a total depth of 2609 feet. Well construction and lithologic details are shown in Figure **2-1**, modified from Purtymun (1995). Most of the well is screened within the Tesuque Formation, although basalts and Puye Formation rocks occur above the top of the screen. Of these post-Santa Fe group units, only one is present below the water table: a thin layer of Totavi Lentil.

A short pump test (14 hour) was conducted at O-1 in 1990 ((Purtymun et al. 1990). Pumping rates were increased in stepwise fashion from 676 to 1375 gpm over the course of the test. Preliminary estimates of aquifer characteristics were derived from this test: transmissivity (T) = 8,803 gpd/ft and storativity (S) = 0.088. However, authors of the pump test report

emphasized the uncertainty of these estimates due to 1) the very short duration of the test, and 2) the lack of a monitoring well. It was also noted that water levels in TW1, located approximately 250 m from O-1, did not respond to the test. It is unclear whether the lack of response is due to the horizontal distance of TW1 from O-1, the vertical separation (total depth of TW1 = 635 ft), the very short duration of the pump test, or a combination of these factors.

Figure 2-1 Geologic log of Otowi 1 (Purtymun, 1995) Depth to top of screen: 1017 ft, depth to bottom of screen:

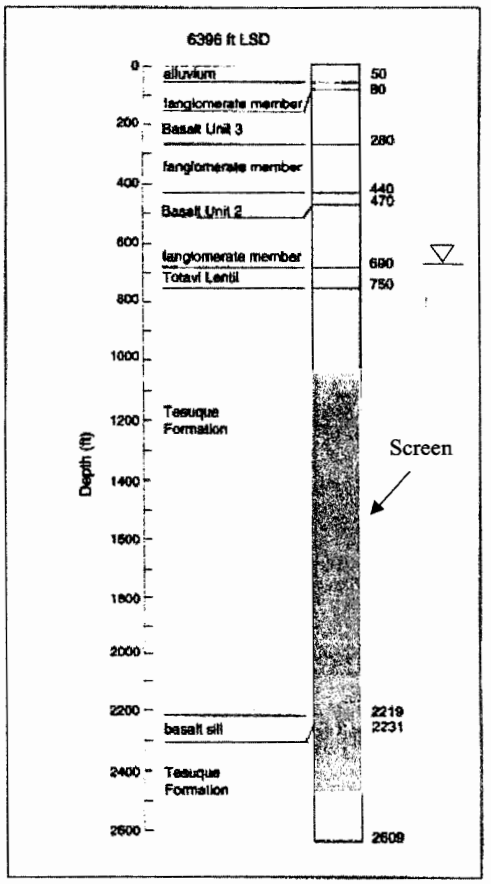

2477 ft. Depth to water (1995): 673 ft.

For the proposed pump test at O-1, using R-5 as a monitoring well, we assume that O-1 will be pumped at a rate of 800 gpm for 30 days (McLin, pers. comm., 2000). For the pump test simulations described below, we define a "base case" using aquifer characteristics according to

the 1990 report. Since these estimates are uncertain, however, we vary these parameters within reasonable ranges and report the resulting range of expected drawdown.

2.3 Numerical Simulations

2.3.1 Model Validation

The numerical code used for these simulations is FEHM (Zyvoloski et al. 1997). To measure the performance of FEHM in correctly simulating pressure changes due to pumping, comparisons of FEHM to Theis analytical solutions for simple aquifer geometries were made. The grid used for these simulations is a 2-D radial geometry grid, with a fully-penetrating well at x=0.

Figure **2-2** illustrates comparisons of numerical and analytical methods for predicted drawdowns. Three cases were simulated, using various combinations of hydraulic conductivity and storativity (see Table **2-1**). A fourth case was tested using a more refined grid to examine the effect of grid resolution on solution accuracy. These figures demonstrate that FEHM performs very well for this class of problems. These cases also illustrate that drawdowns are much more sensitive to hydraulic conductivity than to storativity.

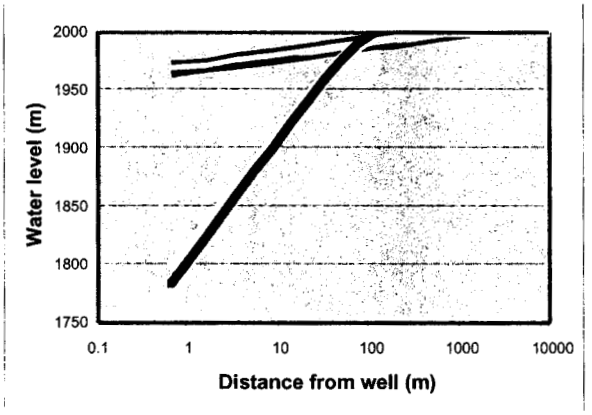

Figure **2-2**. Comparison of FEHM to Theis solution for three cases, as described in Table 2-1

Table 2-1. Description of model validation cases and Theis solution.
Theis solution: T=kb; $S=S_s b$; b=1000m, Q= 50 kg/s

$$u = \frac{x^2 S}{4Tt}$$

Case	k(m^2)	S_s (m^{-1})	Maximum drawdown (m)	Error (m) at x=10m from well	Error (m) at x=100m from well
1	2.0E-13	1.8E-6	35	1	0.6
2	2.0E-13	1.8E-4	27	1	0.2
3	2.0E-14	1.8E-4	217	5	0.3
4	2.0E-14	1.8E-4	217	2	0.2

2.3.2 Model Domain

The existing 3-D regional aquifer model (Keating et al. 1999) is designed to address site-wide aquifer characterization issues and, as such, has insufficient grid resolution to adequately simulate highly localized behaviors such as drawdowns within tens of meters of a pumping well. To provide the required grid resolution for these pump test simulations, a 1000-m X 10000-m 2-D radial geometry model was developed (see Figure **2-3**). The pumping well (O-1) is at the center of the radial grid; horizontal spacing between grid nodes increases logarithmically from 1m near the well to 3000m at the distant edge of the model domain. Vertical grid spacing is a constant 10m.

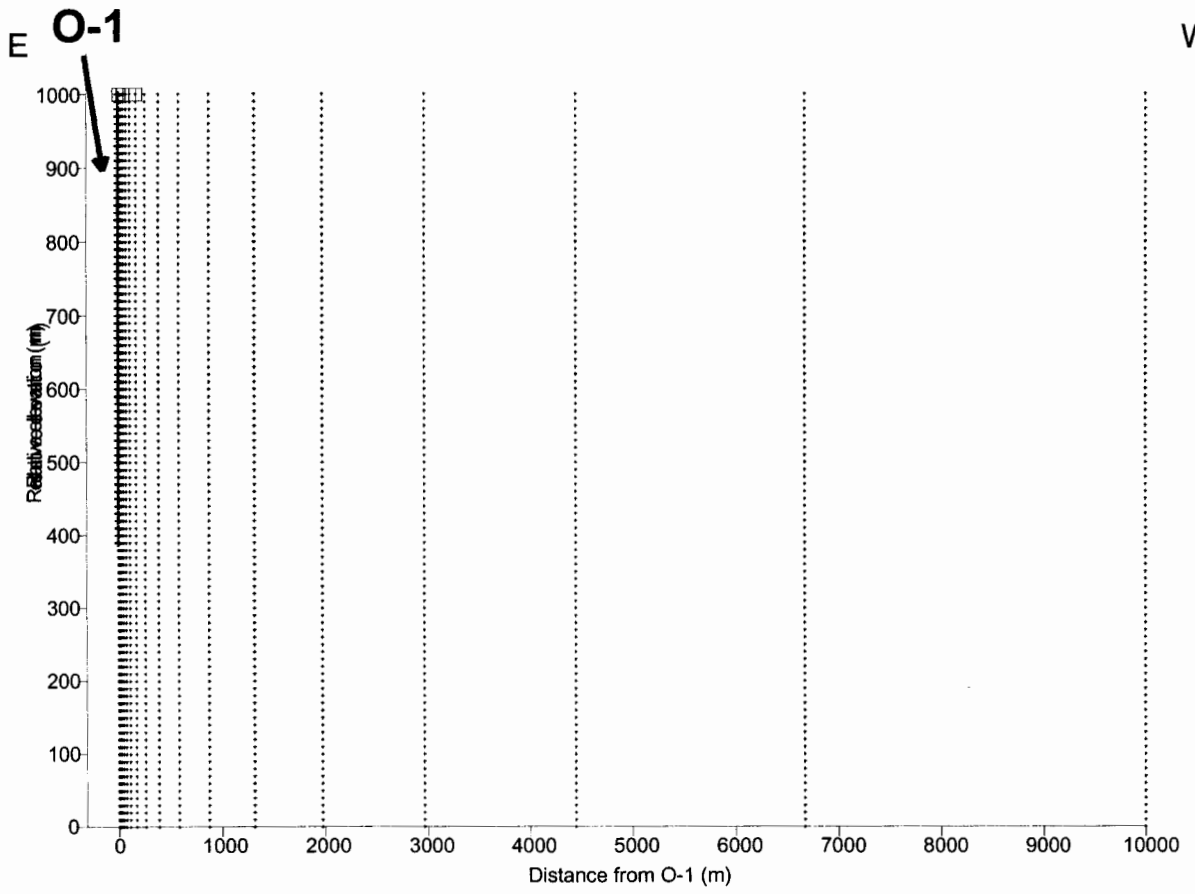

Figure 2-3 Mesh used for 2-D radial slice simulations

2.3.3 Initial and Boundary conditions

The initial condition for all simulations presented in this report is a uniform head distribution. This condition presumes that pre-pumping head gradients near O-1 are unlikely to affect the magnitude or location of drawdowns induced near O-1 during the 30-day pump test.

The upper, lower, and distal edge boundaries are all specified to be no-flow. The distal and lower boundaries are designed to be sufficiently far from the pumping well such that water that might actually move across these boundaries during a pump test would be negligible. Movement of water across the upper boundary (recharge) is not considered in these simulations. The boundary condition along the center axial boundary (the well) is a constant specified flux (water withdrawn during the pump test).

Specified fluxes (withdrawals) are applied to nodes along the center axial boundary that fall within the screened interval of O-1. In a real pump test, it is unknown whether the water is

drawn uniformly from the entire screened interval or, rather, from a small portion of the interval. To explore the sensitivity of model results to this uncertainty, two scenarios were modeled: 1) uniform fluxes along the entire screened interval and 2) fluxes only from the top one third of the screened interval. Total water withdrawn was the same in both cases. The second scenario is meant to mimic conditions that could be caused by either of two. One, that the aquifer is relatively homogeneous but sufficiently permeable such that only the uppermost layers (nearest the pump) are required to satisfy the pump. Or two, that the uppermost layers of the aquifer (say, the Totavi Lentil) are much more permeable than the lower layers and thus produce most of the water to the pump.

3. Parameter sets

Table 2-2 presents the range of selected aquifer parameters that have been reported from well tests across the plateau. Although initial pump test results from O-1 are a useful starting point for these simulations, several cases were simulated using the range of parameters reported in Table **0-2** to bracket the range of possible aquifer responses. Table **2-3** describes eight cases designed to bracket the range of plausible aquifer characteristics and flux conditions along the wellbore that might occur during the pump test. Case 1 is the "base case", which uses T and S values derived from the 1990 pump test, assigned uniformly to all model nodes. Water produced from O-1 during the test is assumed to come from the entire screened interval. Case 2 and 6 differ from the base case by assuming lower and higher values of permeability, according to the range reported in Table 2-1. Case 2-3 differs from Case 1 only by a lower value for S_s (see Table 2-1). Cases 5, 7, and 8 differ from all the other cases by the distribution of fluxes along the wellbore; these cases assume that all the water comes from the upper third of the screened interval.

Table 2-2 Selected aquifer characteristics previously reported

	k (m^2)	S_s (m^{-1})	Reference
O-1 Pump test, 1990	1.98E-13[a] – 2.45E-13[b]	1.6E-4[c] – 2.0E-4[d]	(Purtymun et al. 1990)
Minimum K for plateau	1.45E-13		LA-5, (Purtymun 1995)
Maximum K for plateau	1.16E-11		TW-2, (Purtymun 1995)
Minimum S for plateau		3.53E-06	O-4, (Purtymun et al. 1995)
Maximum S for plateau		1.59E-04	(Purtymun et al. 1990)

[a] derived from T (8803 gpd/ft), assuming b=445m (screened interval of well)
[b] derived from T (8803 gpd/ft), assuming b=849m (water tables to bottom of screen)
[c] derived from S (0.088), assuming b=445m (screened interval of well)
[d] derived from T (0.088), assuming b=445m (screened interval of well)

Table 2-3 Description of simulation cases 1 – 8.

Case	$k_x k_y$ (m^2)	k_z (m^2)	S_s (m^{-1})	distribution of Q
1	2.0E-13	2.0E-15	1.8E-4	full screened interval
2	2.0E-12	2.0E-14	1.8E-4	full screened interval
3	2.0E-13	2.0E-15	3.53E-6	full screened interval
4	heterogeneous[a]	$=K_x,K_y$ except for lower Sf group	1.8E-4	full screened interval
5	2.0E-13	2.0E-15	1.8E-4	upper 1/3 of screen
6	1.44E-13	1.44E-15	1.8E-4	full screened interval
7	1.44E-13	1.44E-15	1.8E-4	upper 1/3 of screen
8	heterogeneous[a]	$=K_x,K_y$ except for lower Sf group	1.8E-4	upper 1/3 of screen

[a] k(Santa Fe group) same as Case 1; k_{xyz} (Puye, Basalts) = $10*k_{xy}$(Santa Fe group)

Cases 4 and 8 differ from other cases in that the aquifer is not assumed to be homogeneous. For these cases, permeability variations were assigned according to aquifer layering as predicted by the FY99 Geologic Model

(see Figure 2-5). Since the 2-D radial geometry cannot accommodate the full 3-D stratigraphy designations, we approximate the geometry by aligning our 2-D slice E-W, with the eastern edge of the model coinciding with the location of O-1. The location of this slice, along with the geology at the water table, is shown in Figure 2-4. The distribution of hydrostratigraphic units amongst grid nodes, as defined by the geologic model, is shown in Figure 2-5. As a simple approximation, all the non-Santa Fe group layers (Puye Formation, Basalts) were assigned a permeability one order of magnitude higher than the Santa Fe group l

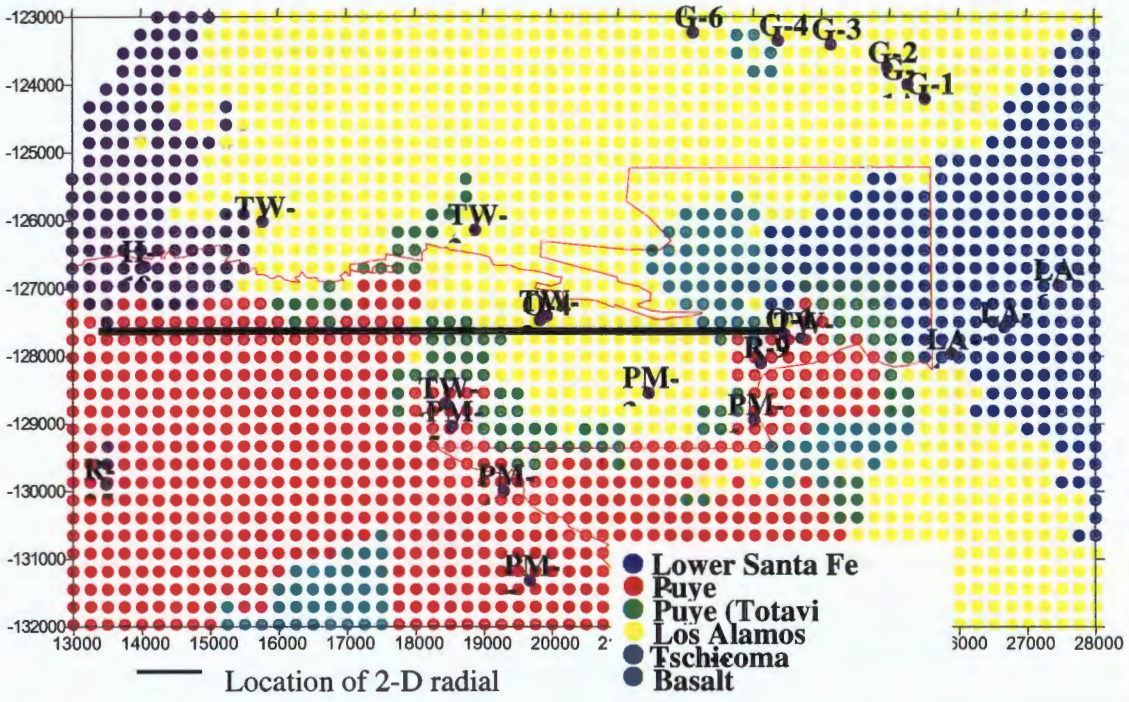

Figure 2-4. Location of 2-D radial slice transect relative to O-1 and hydrostratigraphic units (at the water table)

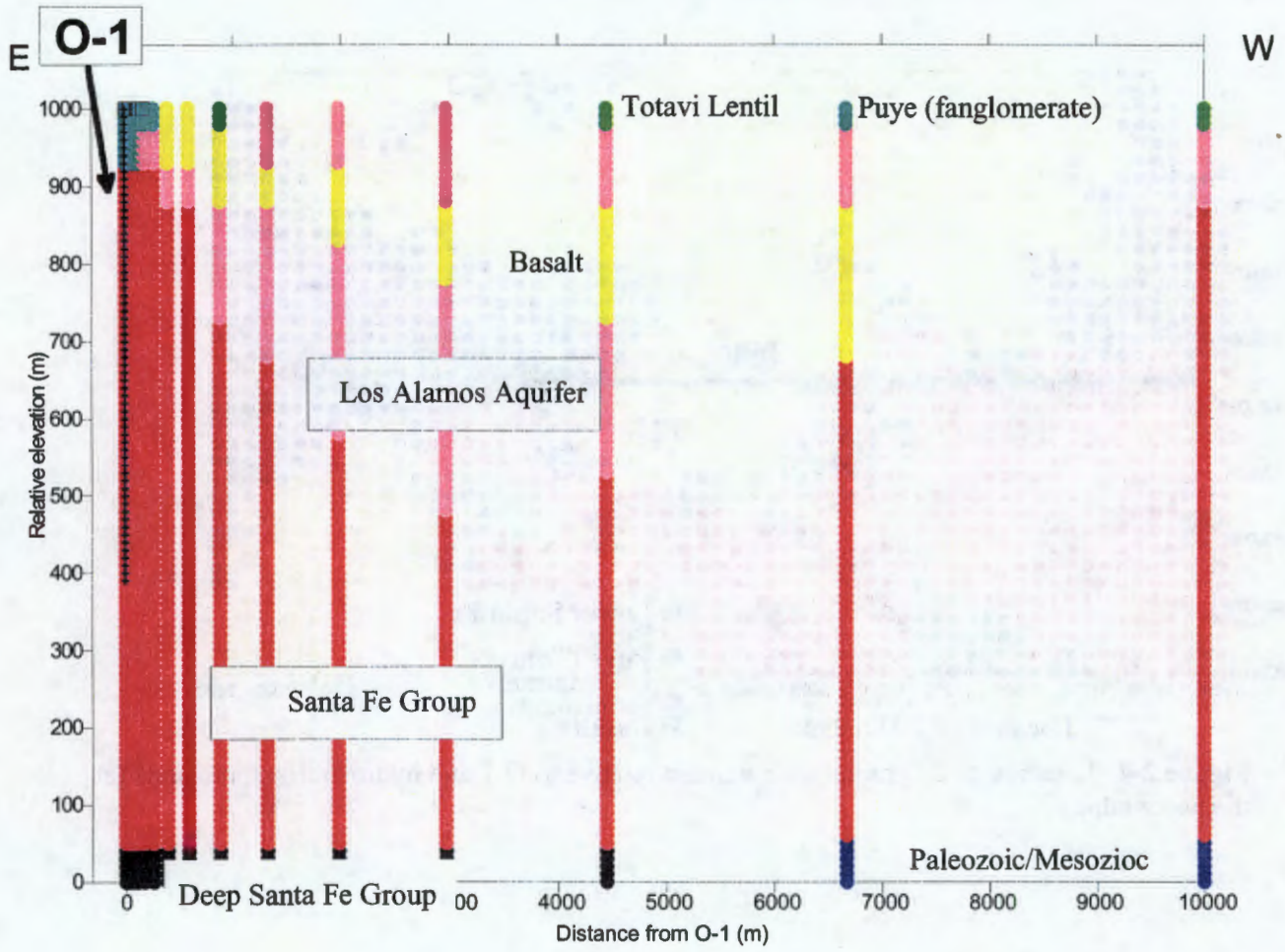

Figure 2-5. Hydrostratigraphic units, interpolated onto radial grid

2.4 Results

Figure 2-6 shows the predicted drawdown (in meters) as a function of distance from O-1 at the end of the 30 days of pumping. For all the cases simulated, most of the drawdown during the pump test occurs within 100m of the well. The largest drawdown predicted near the well were for Cases 5, 7, and 8, the three cases which assumed that

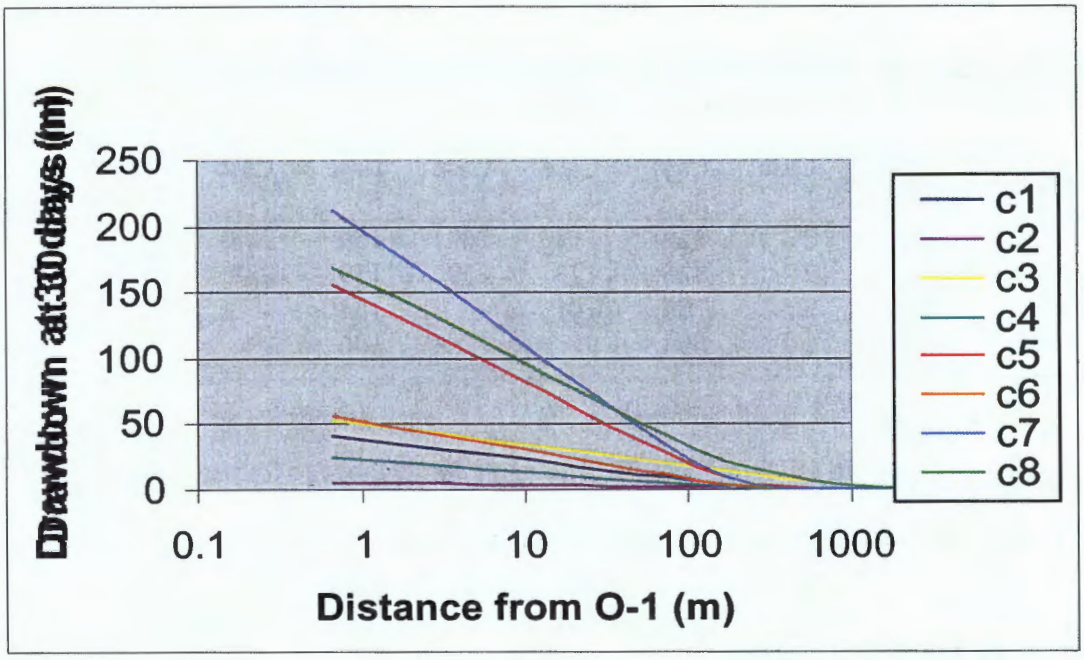

only the upper third of the well produced water. The largest drawdown far from the well (x > 100m) were for Cases 3 and 8, two cases with very little in common. This result highlights the non-uniqueness that is often attributed to pump test analysis.

To obtain useful water level measurements at the observation well, drawdowns of at least 1 – 4m must be evident (McLin, pers. comm., 2000). Tables 2-4 and 2-5 report the distance from O-1 that these critical drawdown levels are predicted to occur, as a function of depth below the water table. All distances are predicted to decrease somewhat with depth, reflecting the fact that the magnitudes of predicted drawdown tend to decrease with depth. This can be explained by a combination of two factors: one, since the well does not fully penetrate the aquifer, upward flow is induced near the bottom of the well and thus head declines at depth are reduced, and two (in Cases 5, 7, & 8), that the largest declines are in the same shallow layers from which most of the water is withdrawn.

Table 2-4 Distance from well (in meters) to 1m drawdown levels at 30 days.
'-' indicates maximum drawdown at any distance is less than 1m.

Depth below water table (m)	Case 1	Case 2	Case 3	Case 4	Case 5	Case 6	Case 7	Case 8
0	304	156	1815	250	378	281	367	380
100	303	154	1814	257	372	281	359	375
400	288	126	1803	287	125	268	68	100
600	235	59	1793	234	-	231	-	-

Table 2-5. Distance from well (in meters) to 4m drawdown levels at 30 days. '-' indicates maximum drawdown at any distance is less than 4m.

Depth below water table (m)	Case 1	Case 2	Case 3	Case 4	Case 5	Case 6	Case 7	Case 8
0	152	2	829	112	249	159	248	185
100	152	2	825	123	239	159	238	191
400	145	2	760	144	-	154	-	-
600	91	1	668	91	-	106	-	-

As shown in Table **2-4**, predicted distances to a one-meter drawdown at the water table range from 156m (Case 2) to 1815-m (Case 3). The range for distance to four-meters of drawdown (Table 2-**5**) is from 112m (Case 4) to 829m (Case 3).

2.5 Implications for R-5 placement

If the top priority for R-5 placement were to be optimal service as a pump test monitoring well, it should be placed close enough to O-1 for 1 – 4 m of drawdown to be measured during the test. Most of these cases predict distances for a 1 – 4m drawdown, in the range of 100 – 400 m's. Case 3, which predicts much larger distances, may not be representative because of its position as an "outlier" in this group of results and its reliance on a very low value of S that was measured at LA-5 (far to the east).

Fully half of the cases (1,5,7, & 8), including the "base case", predict a fairly narrow range of distances: 300 – 380 m for a 1 m drawdown and 150 – 250 m for a 4 m drawdown. Although eight simulations is a small number, the similarity of results for these four cases suggests that these might represent "the most likely" results.

3. Permeability variations within the regional aquifer

Quantifying permeability is a key aspect to the regional aquifer characterization program. Permeability variations within the aquifer play a dominant role in controlling groundwater flow directions, fluxes, and water quantity and quality.

In this section, we summarize information relevant to the permeability of the regional aquifer beneath the Pajarito Plateau. We discuss several categories of information about permeability: (1) permeability estimates derived from bench scale tests on recovered core, (2) permeability estimates derived from short-term pump tests, (3) analysis of long-term (50 years) water level declines in response to pumping, (4) analysis of water level gradients across the plateau. We also discuss the relationship between permeability variations inferred from these various categories of data and hydrostratigraphy of the Pajarito Plateau.

Of the four categories listed above, only the first (core testing) is strictly "model independent", that is, these permeability data do not depend on any particular numerical or conceptual model of groundwater flow. Unfortunately, this advantage is largely offset by the difficulty of deriving representative permeability values for large spatial scales (tens to hundreds of m's) from core-scale data. Permeability estimates for the larger spatial scales are generally derived from pump tests using various idealized models of groundwater flow (e.g. fully penetrating, confined aquifer (Theis solution), partially-confined "leaky aquifer", etc.). Permeability estimates can also be derived from water level data (either short-term or long-term aquifer stress tests on individual wells or steady-state hydraulic gradients at the site-scale) using inverse techniques with numerical groundwater flow models.

3.1 Pump test data for supply and test wells

Purtymun (1995) compiled permeability estimates from pump tests for 28 supply and test wells completed in the regional aquifer on the Pajarito Plateau. These estimates, along with supplementary information about each well, are provided in Table 3-1. The reported values of transmissivity from Table I-A, pg. 31 (Purtymun 1995), were presumably derived from pump test analyses; assessing the validity of these analyses is beyond the scope of this report. It is reasonable to assume, however, that the reported values have significant uncertainty associated

with them, perhaps as large as one order of magnitude. Unfortunately, it is unclear what assumptions were made in the conversion from transmissivity (T) to permeability (K). For each well in Table I-A, we calculated the saturated thickness (b) that was used to convert T to K. These calculated values of b do not correspond to screen length, the sum of reported saturated thicknesses for each stratigraphic unit, or the distance between the water level elevation and the bottom of the screened interval. In light of this discrepancy, we recalculated new values of K from reported values of T using the thickness of the screened interval for each well; for most wells, they are not significantly different from the original values reported.

In general, permeability in the regional aquifer ranges over two orders of magnitude, from $10^{-10.8}$ to $10^{-12.8}$ m^2 (Figures 3-1and 3-2). It is important to note that these measurements are collected in wells completed at various depths and within various hydrostratigraphic units. Nevertheless, there is an apparent spatial trend for permeability to be greatest in wells near the central portion of the plateau, and lowest to the east (Los Alamos well field) and to the north (Guaje well field).

3.2 Relation to stratigraphy

Our initial conceptual model for the regional aquifer is that the primary control on permeability variations is stratigraphy and structural features such as fault zones (Keating et al. 1998; Keating et al. 1999). It is impossible to test this model without numerous measurements of permeability on discreet stratigraphic units. However, one can approximate this test by comparing permeability estimates for wells screened over several stratigraphic units with the percent saturated thickness occupied by any given stratigraphic units.

Carey (pers.comm., 2000) used regression analysis to compare the percent-saturated thickness values for each stratigraphic unit reported by Purtymun (1995) (Table I-A) with permeability estimates for each well. The result of this analysis was that only one (Totavi Lentil) was significantly correlated with permeability; this correlation was weakly positive. Unlike most of the wells for which test results are reported, three wells (TW1, TW2, and TW3) are completed entirely within the Totavi Lentil. These permeability values range from $10^{-11.1}$ to $10^{-12.0}$ m^2.

We repeated this analysis using stratigraphic contact data provided by Cole (pers. comm., 2000), adjusting thicknesses to account only for that portion of any stratigraphic unit that lies within the screened interval of a given well. We also included recent data from pump tests at R-15; the calculated thickness and percentage values for all wells are shown in Tables 3-2 and 3-3. The relationship between stratigraphy and permeability data is illustrated in Figure 3-3. As one would expect from inspecting this figure, regression analysis demonstrated very low or no correlation between most stratigraphic units and permeability. The one exception is the Santa Fe Group, Tsfu. Permeability values in all wells are significantly negatively correlated with the fraction of Tsfu within the saturated interval. This suggests that the presence of any post-Santa Fe Group rock tends to increase the permeability measured in a given well; however, the effects of these various rock types are indistinguishable from one another.

Figure 3- 4 presents permeability estimates for all wells that completed within the Puye Formation and/or the Santa Fe Group. For each stratigraphic unit, we present data from wells completed entirely within that unit and wells completed partially within that unit. Although these data are sparse, they do demonstrate that the range of permeabilities reported for a given stratigraphic unit are smaller than those reported for multi-unit wells, particularly for the Puye Fanglomerate and the Santa Fe Group. In contrast, permeabilities estimated for the Totavi Lentil range nearly as widely as those estimated for wells completed within the lentil and one or more other units.

There are several possible conclusions that might be drawn from these analyses. One is that permeability variations within any given stratigraphic unit are as great or greater than variations between stratigraphic units. This possibility has important implications for parameterization of groundwater flow models, which could be based on the erroneous assumption that stratigraphy is the "first order" control on permeability. A second possibility is that the hydraulic conductivity estimates themselves, which were derived from pump test analyses, have significant errors associated with them. This possibility is examined further in the next section. A third possibility is that the stratigraphic thicknesses used in these analyses, shown in Tables 3-2 and 3-3, are incorrect. This possibility is very plausible, given the uncertainties in our conceptual model of facies within the Puye Formation (Fanglomerate and Totavi Lentil) and our conceptual model of facies within the Santa Fe Group (lower Santa Fe Group and "Chaquehui" formation). Increased attention to formulating and testing hypotheses

concerning facies distributions within these two sedimentary rock units is critical to better characterization of aquifer permeability.

3.3 Long-term trends in water levels due to pumping

Water levels in wells on the Pajarito Plateau have been declining since pumping began in the 1940's. Maximum measured non-pumping water level declines in supply wells range from less than 5 m (G-6) to over 50m (LA-2). Table 3-4 and Figure 3-5 illustrate the wide range in long-term water level response to pumping amongst supply wells on the plateau. Wells in the Guaje and Los Alamos Well Fields have experienced much greater water level declines, given the total amount pumped from these wells, than have wells in the Pajarito Mesa well field.

Many factors may determine the long-term water level declines in supply wells, including hydrologic boundaries (faults, rivers, etc.), recharge rates, pumping in nearby wells, and aquifer properties such as storativity and transmissivity. One advantage of inspecting long-term trends is that these may reflect aquifer properties at a larger spatial scale than would short-term trends, such as those measured during a pump test. To determine the extent to which the hydraulic conductivity values reported by Purtymun (Table I-A) are correlated with trends evident in Figure 3-5, we used regression analysis to compare hydraulic conductivity values to a simple ratio of total cumulative water pumped from a given supply well to maximum drawdown (non-pumping water levels). Figure 3-6 present these data. Excluding PM3 and O4, strong outliers (Figure 3-6a), there is a clear trend for increasing values of hydraulic conductivity to be associated with higher ratios of pumping to long-term drawdowns (Figure 3-6b). Of the 18 supply wells for which these data are available, 15 show a strong linear correlation (r^2=0.9) between hydraulic conductivity (K) and the calculated ratio (best-fit line shown in Figure 3-6b). The remaining four (PM3, PM5, O4, and G6) do not follow this trend. We conclude that for these three wells, either 1) the pump test data are inaccurate or 2) factors other than hydraulic conductivity, such as those mentioned above, control the long-term water level declines.

The strong relationship between hydraulic conductivity and long-term water level responses to pumping for 15 wells on the plateau suggests that the hydraulic conductivity values compiled by Purtymun (Table I-A) are fairly accurate, at least in a relative sense. It is unclear whether the data provided for PM3, PM5, O4, and G6 are reliable. It is also unclear (as

discussed above) whether or not the established stratigraphic designations for rocks within the screened intervals for these wells are meaningful indicators of permeability. These issues are explored further in the section below.

3.4 Groundwater flow model calibration

The process of calibrating a groundwater flow model provides information about large-scale permeability variations in the aquifer. Given a priori information about flux rates (recharge) and observed hydraulic gradients, the groundwater model can be used to determine the permeability of the rocks. If the hydraulic gradient varies spatially, information about spatial variation in permeability can be inferred. Generally, calibration to water levels responding to stress (pumping) provides more information about hydrologic properties of rocks than does calibration to steady-state water levels. The process of model calibration provides information about aquifer permeability at larger scales than do the other methods described above,

Our conceptual model of permeability variation in the aquifer, described above, assumes that stratigraphy is the first order control. The model calibration process using the FY00 Geologic model has generated interesting results. The FY00 Geologic model for the saturated portion of the aquifer differs from previous models in two important ways: one, more discreet basalt flows have been added, and two, the geometry of the "Los Alamos Aquifer" sub-unit of the Santa Fe Group has changed significantly. This unit, previously known as the "Chaquehui", is thought to be a relatively high permeability facies within the upper Santa Fe Group; wells completed within this unit (particularly the PM wells) are much better water producers than wells to the east (LA well field) completed entirely in the lower Santa Fe Group rocks. The "Los Alamos Aquifer" was formerly modeled (FY98, FY99) as a narrow trough, trending northeast/southwest, pinching out just to the north of Guaje Canyon and to the south of Frijoles Canyon (Keating et al. 1998). In the FY00 Geologic model, it is assumed to be correlative with the Cochiti Formation to the south, and, as such, extends a great distance to the south and is crossed by the Rio Grande south of LANL. The FY00 Geologic model also assumes a broader trough, extending east of LANL to the Rio Grande except in the vicinity of the Los Alamos well field. Because of sparse data beneath the plateau and extremely complex stratigraphy within Santa Fe Group rocks (Manley 1976; Ingersoll et al. 1990) there remains a great deal of

uncertainty concerning the geometry, provenance, and hydrologic characteristics of this facies within the Santa Fe Group.

We used automated parameter estimation software, PEST (Watermark Computing 1994), to search for permeability values for each hydrostratigraphic unit defined in the FY00 Geologic model that will provide the best agreement between simulated and observed "pre-development" water levels and fluxes as well as agreement between simulated and observed water level declines due to pumping. Total fluxes to the water table boundary (recharge) are constrained by outflow data (baseflow to the Rio Grande and its tributaries (Keating et al. 1999)) but we use PEST to vary the spatial distribution of recharge to achieve the best fit to water level data. The methods and results of these model calibrations are described in Chapter 5. There are several important conclusions that can be drawn from comparing inverse model estimations of permeabilities and the permeability data, primarily reported by Purtymun (1995). One, because of the relatively large number of water level measurements available from wells completed in the Santa Fe group (both Tsfu and Tsfuv) and the baseflow discharge estimates, which place constraints on recharge, the large-scale permeability of the Santa Fe group can be estimated fairly precisely by the model. One very interesting result apparent in Figure 5–12 is that the permeability of the "Los Alamos aquifer" (as defined by the geologic model) ***cannot*** be, on average, more permeable than the lower Santa Fe group. If there is a large-scale, relatively high-permeability facies within the Santa Fe group, it cannot have the geometry that is defined by the current geologic model. An alternative possibility is that is a large-scale, relatively high-permeability facies does not exist, rather, high-permeability facies within the Santa Fe Group tend to be small-scale, local features. This possibility will be explored in FY01 using facies-based modeling.

The second interesting trend apparent in Figure 5–12 is that the large-scale permeability of the Santa Fe group (both Tsfu and Tsfuv) is significantly lower than pump test data suggest. It has been demonstrated in the literature (Neuman 1990) that the effective properties of heterogeneous media, especially permeability, decrease with the scale of analysis (the so-called "scale effect"). In our case, the most likely cause of this effect is the presence of large-scale low-permeability zones related to north-south trending fault zones that are present in the Santa Fe Group throughout the basin (Kelley 1978). The effect of these large-scale features is not captured in pump-tests. A contributing factor is that pump tests tend to be conducted in the most

permeable zones of the aquifer; this is particularly true for tests conducted in water supply wells. Hopefully as we collect more permeability data for the regional aquifer, we will be able to evaluate these scale effects in more detail.

Table 3-1. Characteristics of wells on the Pajarito Plateau (Purtymun, 1995). Units are feet, unless otherwise indicated.

Well	Ground Surface Elevation	Top of screened interval	Bottom of screened interval	Water level	Year	Screen thickness	Field coefficient of Permeability (gpd/ft^2)	Permeability ($log(m^2)$)
G-1	5979	5697	3999	5784	1950	1698	7.0	-12.5
G-1A	6018	5746	4505	5753	1955	1241	9.1	-12.4
G-2	6058	5777	4098	5799	1951	1679	9.1	-12.4
G-3	6139	5698	4354	5858	1951	1344	5.3	-12.6
G-4	6238	5812	4313	5881	1951	1499	11.3	-12.3
G-5	6317	5617	4807	5903	1951	810	8.7	-12.4
G-6	6438	5868	4438	5857	1964	1430	6.7	-12.5
LA-1B	5628	5302	3934	5662	1960	1368	9.3	-12.3
LA-2	5648	5543	4783	5589	1950	760	3.5	-12.8
LA-3	5672	5567	4807	5575	1950	760	3.3	-12.8
LA-4	5975	5221	4011	5786	1948	1210	5.7	-12.6
LA-5	5838	5398	4098	5769	1948	1300	3.0	-12.8
LA-6	5770	5350	3992	5687	1950	1358	9.1	-12.4
O-1	6396	5379	3919	5723	1990	1460	4.7	-12.6
O-4	6625	5510	4029	5864	1993	1481	30.0	-11.8
PM-1	6497	5552	4018	5751	1965	1534	31.0	-11.8
PM-2	6717	5713	4437	5891	1966	1276	28.0	-11.9
PM-3	6638	5682	4106	5895	1968	1576	179.0	-11.1
PM-4	6920	5660	4066	5870	1982	1594	24.0	-11.9
PM-5	7094	5654	4022	5857	1987	1632	5.3	-12.6
Test Well DT-10	7019	5934	5610	5928	1960	324	111.0	-11.3
Test Well DT-5A	7134	5964	5314	5961	1960	650	17.0	-12.1
Test Well DT-9	6933	5633	5433	5930	1960	200	122.0	-11.2
TW-1	6366	5744	5734	5781	1950	10	4.0	-12.7
TW-2	6645	5885	5845	5886	1949	40	241.0	-10.9
TW-3	6592	5852	5792	5849	1949	60	120.0	-11.2
TW-4	7242	6072	6042	6071	1950	30	19.0	-12.0
TW-8	6878	5908	5778	5910	1960	130	25.0	-11.9

Table 3-2. Total thickness of each stratigraphic unit within the saturated, screened interval of the well.

Well	Tb2	Tb1	Tsfu	Tsfuv	Tpf	Tpt	Tb4	Tt1
TW-8					130			
TW-4								30
TW-3						49		
TW-2						40		
TW-1						10		
Test Well DT-9				146	16	38		
Test Well DT-5A				303	18	52	274	
Test Well DT-10				7	65	46	200	
R15					60			
PM-5	975		292	255	30	80		
PM-4	480			950	44	120		
PM-3	435		445	696				
PM-2	435			430	341	70		
PM-1	587		697	250				
O-4	311		270	900				
O-1		12	1448					
LA-6			1358					
LA-5			1300					
LA-4			1210					
LA-3			760					
LA-2			760					
LA-1B			1368					
G-6		400	516	496				
G-5		637	173					
G-4		651	772	76				
G-3		169	695	480				
G-2			1040	568				
G-1A		6	645	557				
G-1		298	1002	398				

sat_thickness_totals2.xls (sheet1)

Table 3-3. Fraction of the saturated screened interval occupied by each stratigraphic unit.

Well	Tb2	Tb1	Tsfu	Tsfuv	Tpf	Tpt	Tb4	Tt1
TW-8	0.00	0.00	0.00	0.00	1.00	0.00	0.00	0.00
TW-4	0.00	0.00	0.00	0.00	0.00	0.00	0.00	1.00
TW-3	0.00	0.00	0.00	0.00	0.00	1.00	0.00	0.00
TW-2	0.00	0.00	0.00	0.00	0.00	1.00	0.00	0.00
TW-1	0.00	0.00	0.00	0.00	0.00	1.00	0.00	0.00
DT-9	0.00	0.00	0.00	0.73	0.08	0.19	0.00	0.00
DT-5A	0.00	0.00	0.00	0.47	0.03	0.08	0.42	0.00
DT-10	0.00	0.00	0.00	0.02	0.20	0.14	0.63	0.00
R15	0.00	0.00	0.00	0.00	1.00	0.00	0.00	0.00
PM-5	0.60	0.00	0.18	0.16	0.02	0.05	0.00	0.00
PM-4	0.30	0.00	0.00	0.60	0.03	0.08	0.00	0.00
PM-3	0.28	0.00	0.28	0.44	0.00	0.00	0.00	0.00
PM-2	0.34	0.00	0.00	0.34	0.27	0.05	0.00	0.00
PM-1	0.38	0.00	0.45	0.16	0.00	0.00	0.00	0.00
O-4	0.21	0.00	0.18	0.61	0.00	0.00	0.00	0.00
O-1	0.00	0.01	0.99	0.00	0.00	0.00	0.00	0.00
LA-6	0.00	0.00	1.00	0.00	0.00	0.00	0.00	0.00
LA-5	0.00	0.00	1.00	0.00	0.00	0.00	0.00	0.00
LA-4	0.00	0.00	1.00	0.00	0.00	0.00	0.00	0.00
LA-3	0.00	0.00	1.00	0.00	0.00	0.00	0.00	0.00
LA-2	0.00	0.00	1.00	0.00	0.00	0.00	0.00	0.00
LA-1B	0.00	0.00	1.00	0.00	0.00	0.00	0.00	0.00
G-6	0.00	0.28	0.37	0.35	0.00	0.00	0.00	0.00
G-5	0.00	0.79	0.21	0.00	0.00	0.00	0.00	0.00
G-4	0.00	0.43	0.52	0.05	0.00	0.00	0.00	0.00
G-3	0.00	0.13	0.52	0.36	0.00	0.00	0.00	0.00
G-2	0.00	0.00	0.65	0.35	0.00	0.00	0.00	0.00
G-1A	0.00	0.00	0.53	0.46	0.00	0.00	0.00	0.00
G-1	0.00	0.18	0.59	0.23	0.00	0.00	0.00	0.00

sat_thickness_totals2.xls (sheet1)

Table 3-4. Summary of long-term water level response to pumping in water supply wells. An "*" indicates that data from this well was used in the regression analysis.

Well	Maximum drawdown (ft)	Cumulative water withdrawn (kg X 10^9)	Ratio[1]	Permeability (m^2)	Regression
G-1	98	10.3	3.3	3.38E-13	*
G-1a	60	16.7	8.8	4.39E-13	*
G-2	116	14.2	3.9	4.39E-13	*
G-3	94	7.9	2.7	2.56E-13	*
G-4	49	5.3	3.4	5.45E-13	*
G-5	73	14.6	6.4	4.20E-13	*
G-6	14	6.9	15.7	3.23E-13	
LA1b	115	9.4	2.6	4.49E-13	*
LA2	164	6.1	1.2	1.69E-13	*
LA3	142	7.1	1.6	1.59E-13	*
LA4	107	13.7	4.1	2.75E-13	*
LA5	115	12.4	3.4	1.45E-13	*
LA6	133	10.5	2.5	4.39E-13	*
PM1	14	9.9	22.5	1.50E-12	*
PM2	50	31.2	19.8	1.35E-12	*
PM3	36	23.7	20.9	8.63E-12	
PM4	43	17.9	13.2	1.16E-12	*
PM5	21	6.6	9.9	2.56E-13	
O-4	1	3.3	105.6	1.45E-12	

[1] The units of this ratio are ft/(kg/s). Total withdrawals (kg) were converted to (kg/s) by multiplying by a constant.

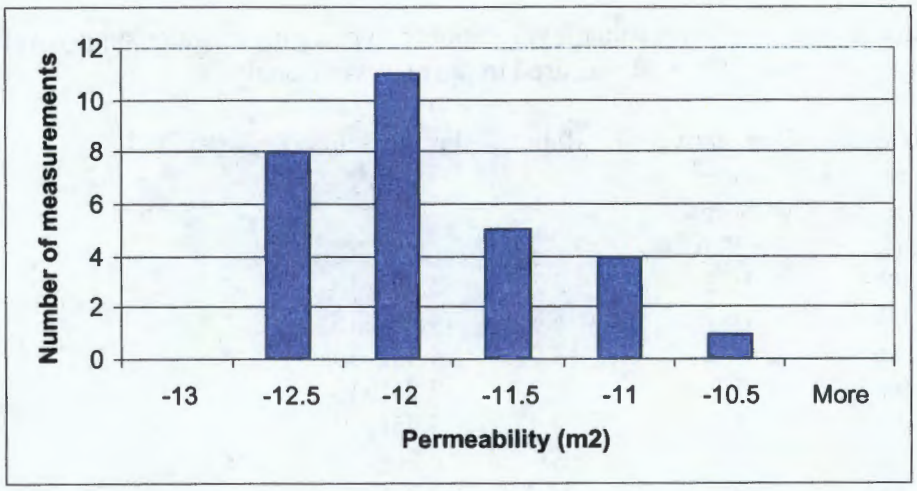

Figure 3-1. Histogram of permeability values for the plateau, derived from pump test analyses. n=29, geometric mean = -12.1.

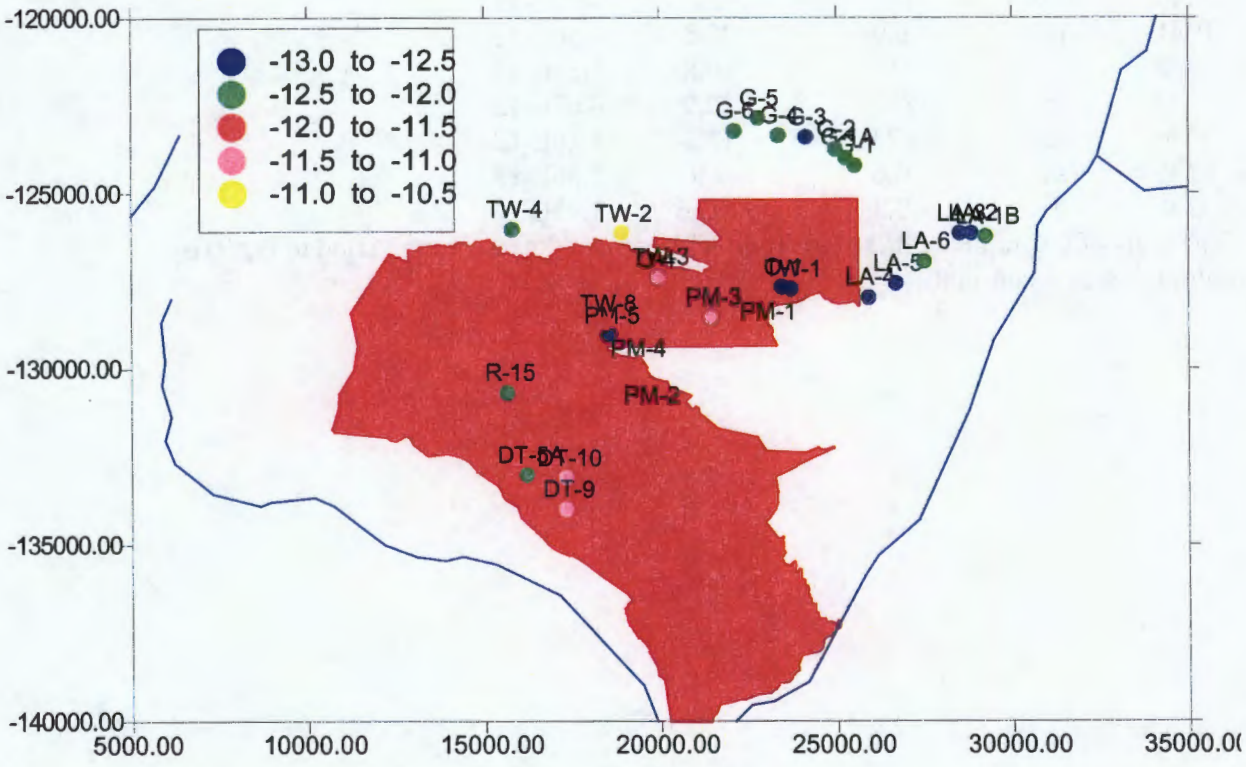

Figure 3-2. Permeability values (log), derived from pump test analyses

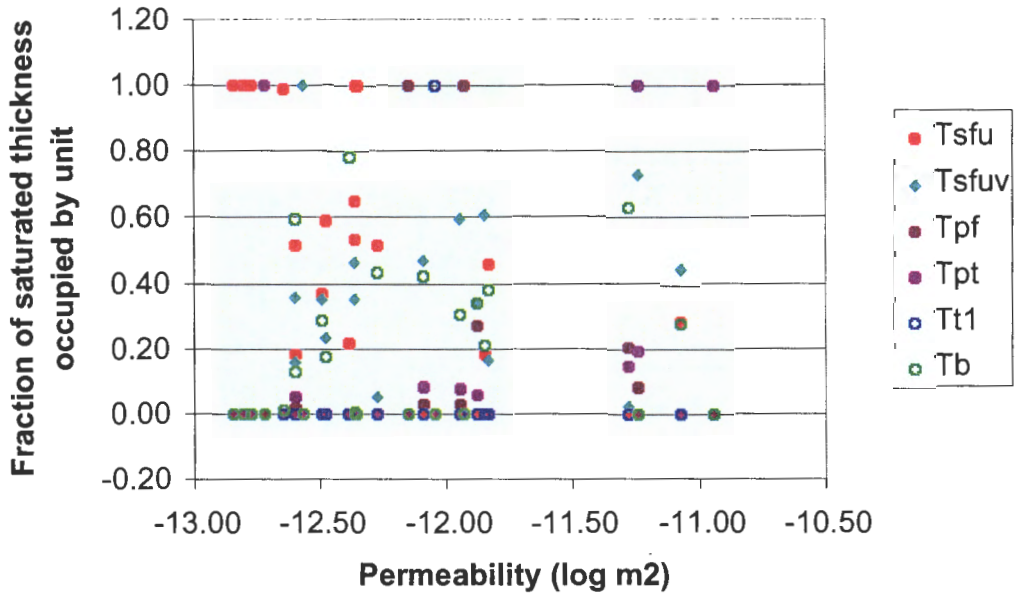

Figure 3-3. Relation between permeability measurement and hydrostratigraphy

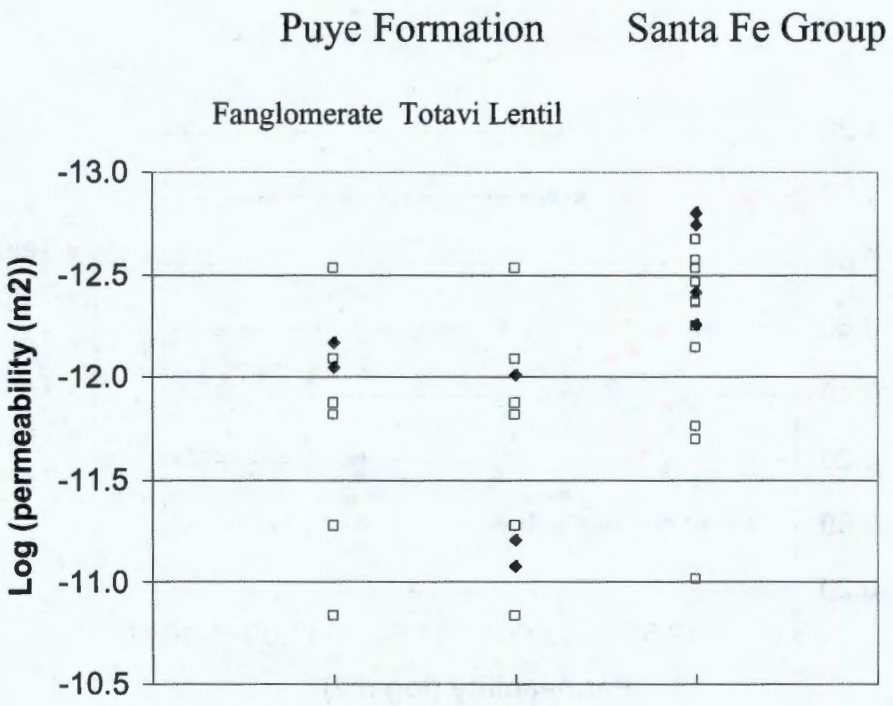

Figure 3-4. Permeability data for 3 hydrostratigraphic units. Blue symbols indicate results from pump tests where well was screened entirely within a given stratigraphic unit; pink symbols indicate results from pump tests where well was screened over multiple units.

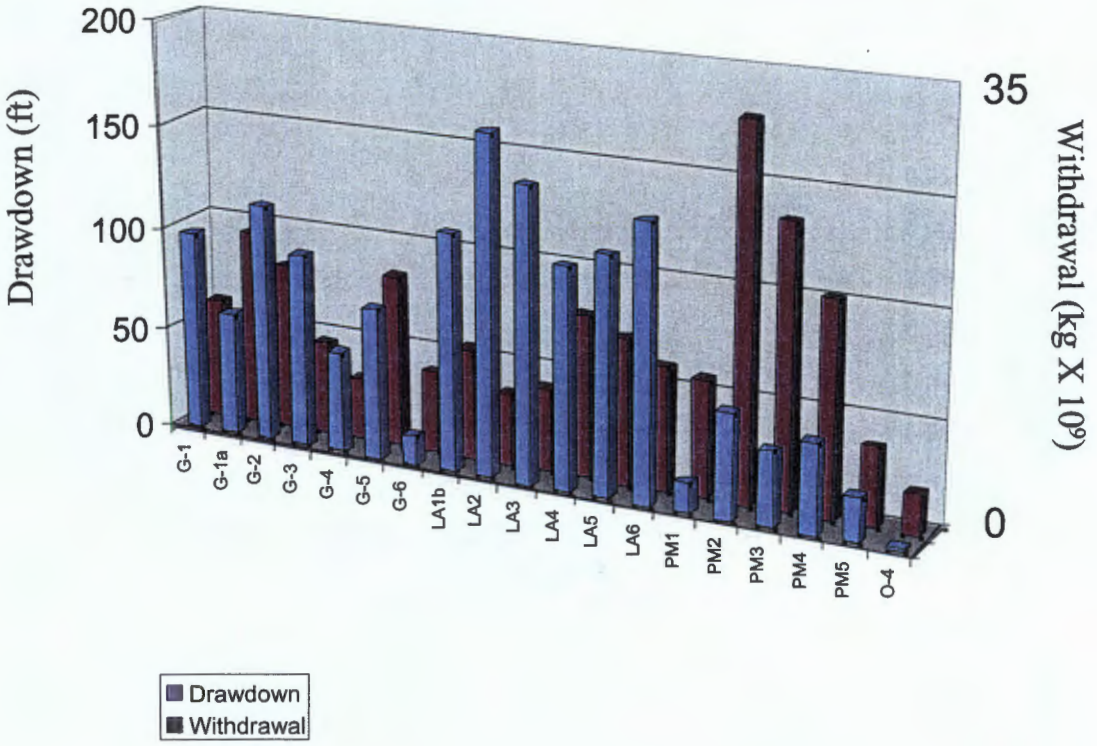

Figure 3-5. Cumulative withdrawal (kg) and maximum water level decline (non-pumping)

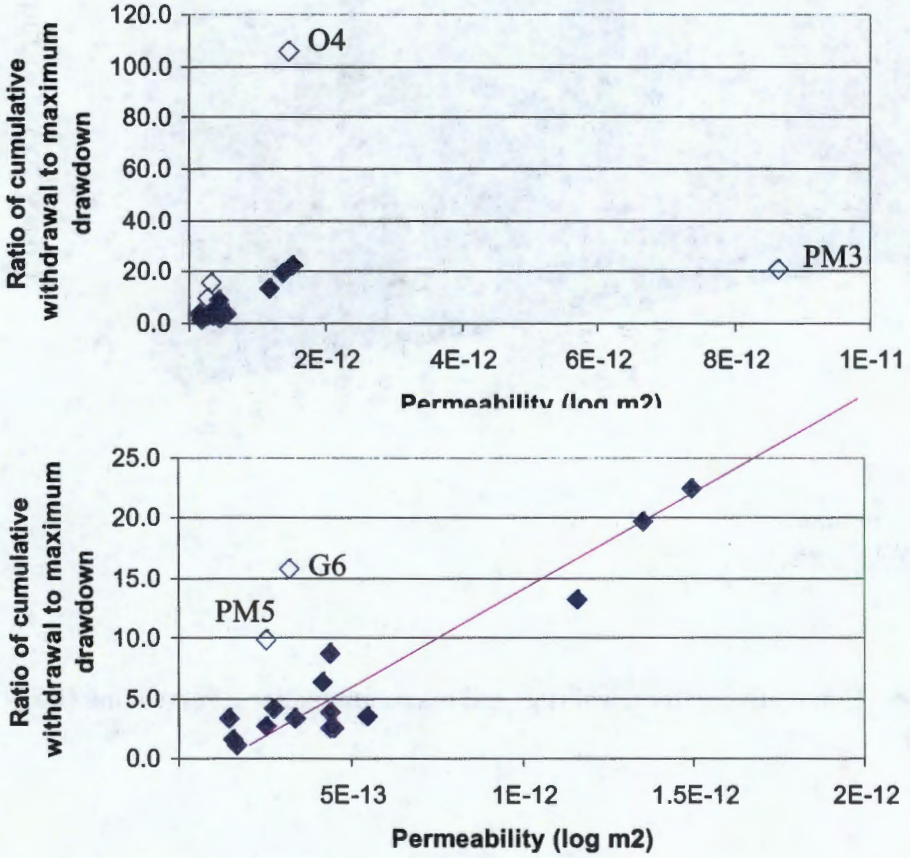

Figure 3-6. Relationship between permeability and ratio of cumulative pumping to maximum drawdown. Open symbols refer to data that was excluded fromregression analysis.

4. Model Development and Hydrologic Datasets

This chapter describes all significant changes to the model framework, to the datasets we use for parameterization, and the datasets we use for model evaluation or calibration since our last report (Keating et al. 1999). In addition, we introduce a new model that has been created for the Pajarito Plateau. This sub-model of the basin model has increased resolution to provide better delineation of hydrofacies within the Puye Formation. Finally, we describe calibration results for both the basin model and for the sub-model and implications for hydrostratigraphy and aquifer permeability.

4.1 Hydrostratigraphy

In January 1999, the FY99 Española Basin geologic model (Carey et al. 1999) was overlain onto the regional flow model mesh. Most changes in this model since the FY98 version were attributable to modifications in the site-wide geologic model. All the regional aquifer flow model results reported in this and subsequent chapters are largely based on definition of hydrostratigraphic boundaries according to this new geologic model.

Three changes to the geologic model in the vicinity of LANL were noteworthy: 1) the spatial extent of the "Los Alamos aquifer" increased, as compared to the FY98 model (see Figure 4-1), 2) basalt flows were modeled with substantially more refinement, and 3) the geometry of the Tschicoma dacite flows were substantially refined. The modification of the geometry of the "Los Alamos aquifer" sub-unit of the Santa Fe Group was based on assumptions about the relationship of this unit and basalt flows Tb1 and Tb2 (within the LANL vicinity) and on assumptions about the relationship between this unit and the Cochiti Formation (to the south). The absence of any outcrop data for this unit and persistent questions regarding the nature of the "Chaquehui Formation" as described and delineated in lithologic logs by Purtymun (1995) contribute to a large degree of uncertainty in the geometry and character of this unit.

As reported in Keating et al. (1999) several hydrostratigraphic units, as defined by the geologic model, are further subdivided in the process of flow model development. This process provides more detail in areas outside the boundaries of the site-wide model. The Santa Fe Group rocks, for example, are sub-divided into 8 units corresponding roughly to facies defined by Kelly (1978). Within the boundaries of the site-wide model, the Santa Fe Group rocks are sub-divided according to the geologic model (Tsf and Tsfuv). This year we have added a few minor new sub-divisions. We sub-divided the Paleozoic-Mesozoic units into a shallow, potentially fractured, hydrostratigraphic unit ($z > 1200$m) and a deeper, potentially less permeable hydrostratigraphic unit ($z < 1200$m). We sub-divided the shallow PreCambrian unit into 3 sub-units, according to geographic location (Sangre de Cristo Mountains, Penasco (south of the Rio Grande), and Ojo Caliente (north edge of model).)

4.2 Model Parameterization

4.2.1 Aquifer Recharge

We use the generalized recharge model described in Keating et al. (1999), assuming that the first order control on recharge rates is elevation. Our conceptual model of recharge in the basin is that most water recharging the aquifer originates in stream channel bottoms. For major channels in the basin, we model this explicitly (either as model input, at specified flux nodes (upper Santa Fe River, upper Pojoaque River) or as model output, at specified-head nodes placed where the water table is thought to intersect the ground surface (Rio Grande and many low-elevation tributaries)). However, for most of the model domain, including the Pajarito Plateau, for simplicity we apply recharge uniformly within any given elevation range ("diffuse" recharge), making no distinction between canyons and mesas. This effectively "spreads" the focused recharge occurring in canyon bottoms over a larger area. This approximation is appropriate for estimating the total amount of water recharging the system in various elevation ranges, for estimating total baseflow discharge to rivers, and for estimating hydraulic gradients in the regional aquifer at scales of kilometers. It is not appropriate for estimation of hydraulic gradients at small scales (i.e. mounding due to local recharge beneath a specific canyon). For the solute transport calculations described in Chapter , we honor our conceptual model by specifying the chemistry of recharge water to be that of stream water. However, because our recharge

model spreads this water evenly across the water table, this approach would not be appropriate for estimation of solute concentration gradients at small scales.

To provide a context for evaluating our generalized recharge model, we have compiled recharge estimates made by Gray (1997) for Los Alamos Canyon and estimates made by Wasiolek (1995) for sub-basins in the Sangre de Cristo Mountains. Figure 4-2 and Table 4-1 presents these comparisons. In general, recharge was estimated to vary from 10 – 26 % of precipitation. These estimates are associated with a large degree of uncertainty, in large e part because of the difficulty in estimating the largest water budget component: evapotranspiration. The recharge estimates made by Wasiolek (1995) have been criticized as being too large (U.S. Department of Justice and New Mexico State Engineer Office 1996). Care should be taken in applying estimates made by Gray (1997) for Los Alamos Canyon to the entire Pajarito Plateau since this is one of the wettest canyon on the plateau; hence these estimated rates are probably larger than the plateau-wide average. In summary, we expect the estimates in Table 4-1 to provide upper limits to basin-scale or plateau-scale rates of recharge.

Table 4-1 Comparison of recharge estimates for 5 basins in the Sangre de Cristos (Wasiolek 1995) and for Los Alamos Canyon (Gray 1997).

	Mean elevation (ft)	ET	Runoff	Recharge	Reduction	Recharge (in/yr)
Santa Fe River	8989	0.69	0.19	0.11	0.01	2.71
Little Tesuque Creek	8786	0.72	0.10	0.19	0.00	4.41
Rio Nambe	9325	0.66	0.20	0.12	0.02	3.03
Tesuque Creek	9197	0.68	0.21	0.10	0.01	2.45
Rio en Medio	9242	0.66	0.15	0.15	0.04	3.73
LA canyon '93	8428	0.71	0.03	0.26	0.00	6.52
LA canyon '94	8428	0.83	0.00	0.17	0.00	4.01
LA canyon '95	8428	0.73	0.02	0.25	0.00	7.33

4.2.2 Aquifer permeability

For most hydrostratigraphic units in the regional aquifer, we are not aware of any new permeability data. Permeability data was derived from core tests at R-9 and R-12 for a basalt flow (Tb4) and from pump tests in R-15, for the Puye-fanglomerate. These values are shown below in Table 4-2. They are included in the discussion of model calibration in the sections below.

Table 4-2. Aquifer property estimates derived from R wells

Parameter	Value	Units	Well	Formation	Comments	K (m^2) or S_s (m^{-1})	log (k)
Hydraulic conductivity	1.1E-06	cm/s	R-9	basalt	Core	1.12E-15	
Hydraulic conductivity	3.9E-10	cm/s	R-12	basalt	Core	3.98E-19	
Hydraulic conductivity	0.00027	cm/s	R-25	Tuff	Core	2.75E-13	
T	218.4	ft2/day	R-15	Puye-fanglomerate	pump test type curve b=60ft	1.31E-12	-11.8826
S	0.0171		R-15	Puye-fanglomerate		9.35E-04	
T	157.9	ft2/day	R-15	Puye-fanglomerate	recovery type curve	9.47E-13	-12.0235
S	0.027		R-15	Puye-fanglomerate		1.48E-03	

4.3 Calibration datasets

4.3.1 Pre-development water levels

We have refined the water level dataset used to calibrate the flow model. In FY99, we used 150 water level measurements to approximate the "pre-development" potentiometric surface. We have added some measurements to this dataset in order to improve spatial coverage, and subtracted some measurements (all relatively far from LANL), because of questions about data accuracy and representativeness. In summary, our criteria for the resulting dataset (93 water levels) are listed in Appendix B.

Water level data from R25 and R31 were added to the predevelopment dataset in order to improve spatial coverage. We assume that water levels in these wells have not been significantly impacted by pumping. Current pumping from supply wells may be affecting water levels in R9 and R12 and so these data were not used.

4.3.2 Discharge estimates

Groundwater discharge to rivers (baseflow) is an extremely important constraint on the regional aquifer model. For this reason, we have continued to examine and refine our baseflow estimates for all reaches within the model. This year, four additional reaches have been added (Santa Clara Creek, Santa Cruz Creek, Rio Madera, Rio Ojo Caliente). In total, we specify 12 river reaches; the model calculates net discharge or recharge to these reaches; see Figure 4-3.

For a subset of these reaches, there is adequate streamflow data and/or reported baseflow estimates to provide independent flux estimates for model validation. Table 4-3 summarizes these estimates.

Table 4-3 Estimated groundwater discharge to river reaches within the basin, with model calibration target values (calibration procedures are described in Chapter 5).

	Reach		Discharge estimates				Calibration	
		Reach length	cfs/mi		Total cfs			
		mi	min	max	min	max	target value	weight
Rio Grande	Above Espanola to Otowi	14.0	0.3	2.2	4.5	31.0	14.5	0.25
	Otowi to Cochiti	26.0	0.5	1.3	13.0	33.8	12.9	1
Tributaries	Rio Chama				19.3		19.3	1
	Lower Pojoaque				4.2	7.5	7.5	1
	Lower Santa Fe				4.4	8.0	8.1	0
	Rio Embudo						24.0	0
	Ojo Caliente						17.2	0
	Santa Clara Creek						3.4	0
	Santa Cruz				-2.6		5.0	0

4.4 Pajarito Plateau Sub-model

One important result from HE transport simulations in the regional aquifer (Keating et al. 1999) was that contaminants traveled primarily within Puye Formation in the shallowest portions of the aquifer. These preliminary simulations were based on the assumption that the Puye

Formation is comprised of two homogeneous facies: the fanglomerate and the Totavi Lentil. The Totavi Lentil was modeled as a continuous coarse gravel unit underlying the fanglomerate. In fact, neither the fanglomerate nor the Totavi Lentil is a homogeneous and alternative model of the Totavi Lentil as a discontinuous facies has been proposed (Reneau and Dethier 1995). A better understanding heterogeneity of this unit and how best to capture this heterogeneity in a numerical model will be very important for future calculations.

To capture fine-scale detail within the Puye and other hydrostratigraphic units on the Pajarito Plateau requires a relatively fine computational mesh. Vertical resolution is particularly important since the coarse gravel layers observed in outcrop may be hydrologically important and are 10 m thick or less. With present computer resources, it was impossible to further refine the basin-scale model sufficiently; instead, we created a separate numerical mesh for the Pajarito Plateau with increased vertical resolution (250m (x direction), 250 m (y direction), and 12 m (z direction)). Development of the flow and transport model for Pajarito Plateau and geostatistical approaches to modeling the Puye Formation was partially funded by the ALDSSR Office; methods and results are described in Robinson et al. (2000).

4.4.1 Boundary conditions

The locations of lateral boundaries for the submodel were specified to be coincident with hydraulic low or no-flow boundaries (topographic divide to the west of LANL; Santa Clara Canyon to the north; Frijoles Canyon to the south, Rio Grande to the east – see Figure 4-4)). These locations were selected so that model errors incurred by under- or over-estimation of fluxes across lateral boundaries would be minimal.

We apply specified fluxes across the northern, western, and southern boundaries; fluxes are specified to be consistent with steady-state basin model results. For all the results reported in the following sections, these fluxes are assumed to be constant over time. We are currently evaluating the validity of this assumption and the sensitivity of transport predictions within the sub-model to this assumption. In addition, we have evaluated the sensitivity of these flux calculations (from the basin model) to basin model parameters. These are described below in Section 5.4.1.

As in the basin model, we apply specified heads along the Rio Grande and the lower reaches of Santa Clara Creek, predicted fluxes along these boundaries is then compared to baseflow estimates described above.

4.4.2 Numerical mesh

The numerical mesh for the sub-model is described in Robinson et al. (Robinson et al. 2000). This mesh, with grid elements colored according to hydrostratigraphic unit, is shown in Figures 4-6a and 4-6b. For all the model results described in the following sections, the Puye formation is sub-divided into the Totavi Lentil and fanglomerate subunits, according to the site-wide geologic model. For a description of a stochastic approach to modeling facies within the Puye, see in Robinson et al. (Robinson et al. 2000).

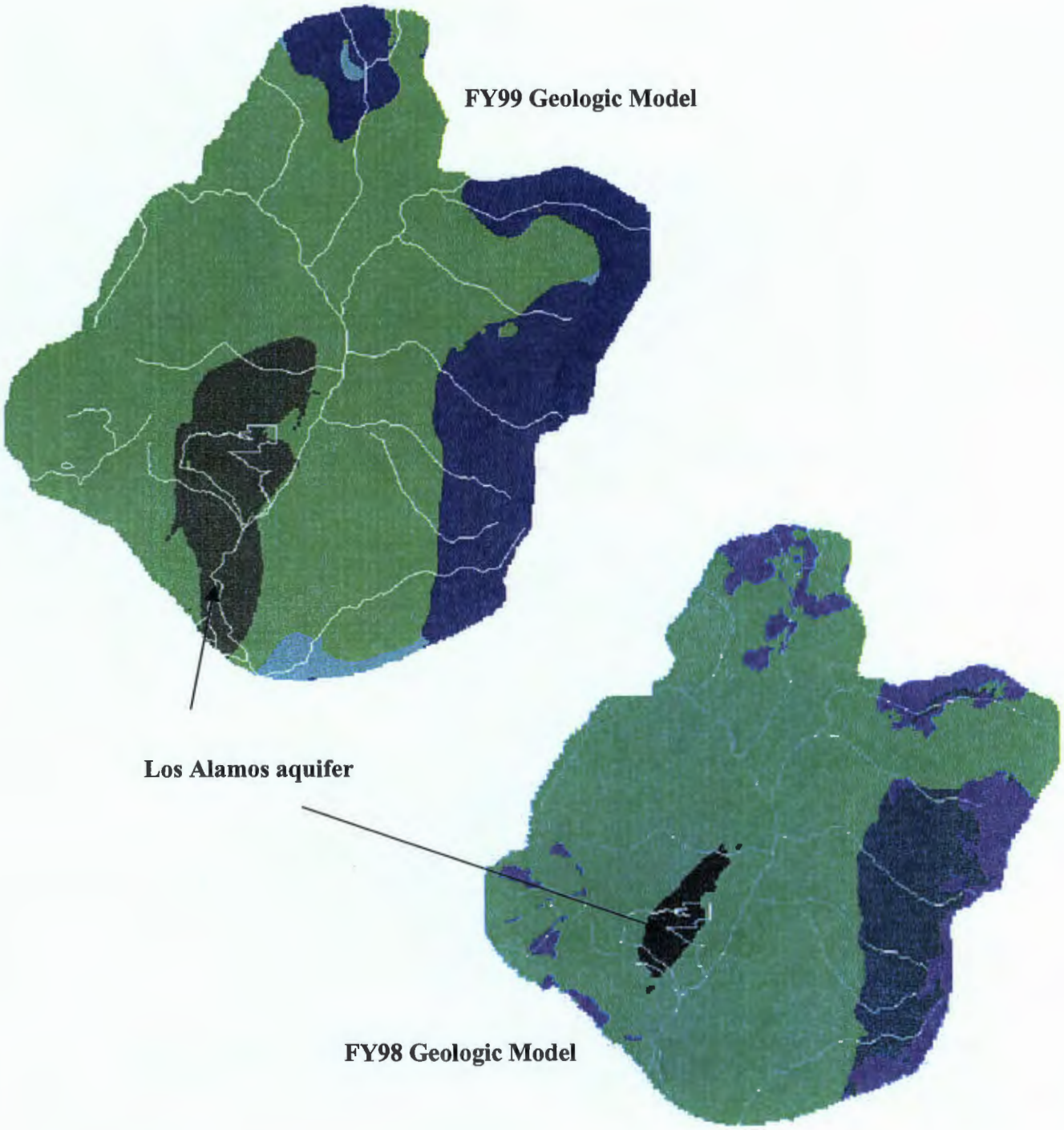

Figure 4-1. Extent of "Los Alamos aquifer", as expressed at the water table, according to the FY98 and FY99 geologic models

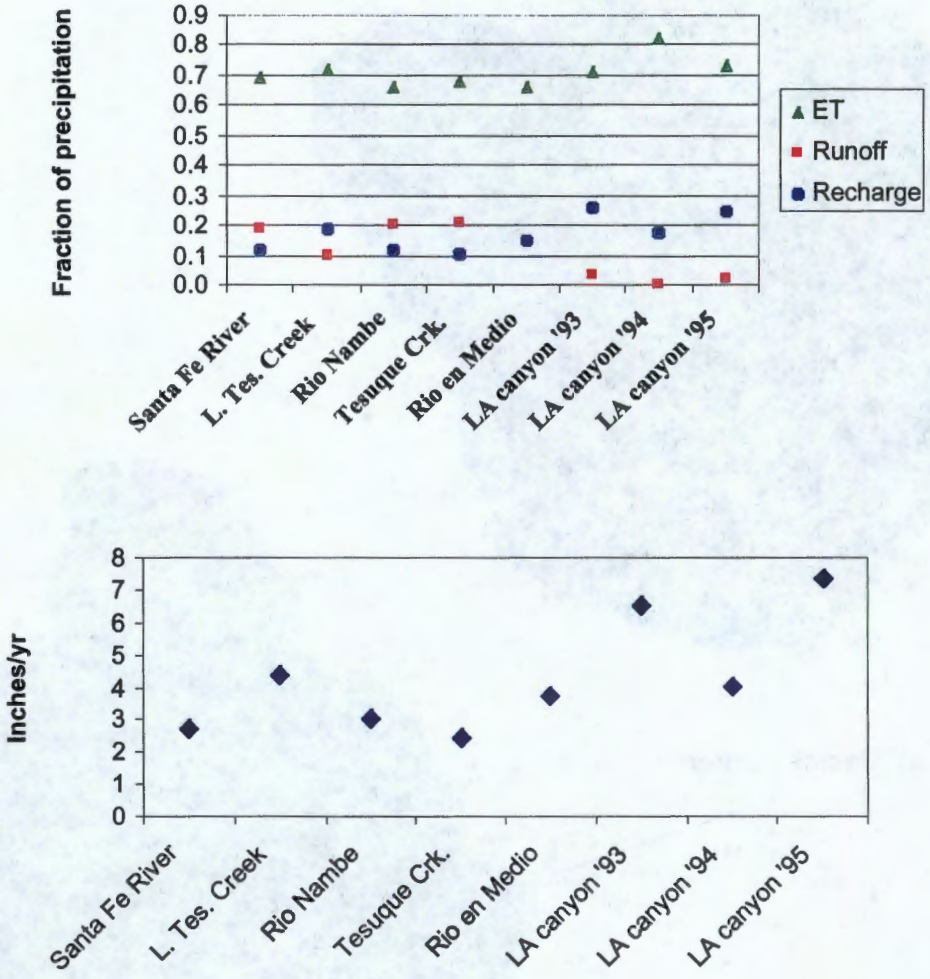

Figure 4-2 . Results from water budget studies from 5 sub-basins within the Espanola Basin a) water budget components (expressed as a fraction of total water) b) recharge estimates.

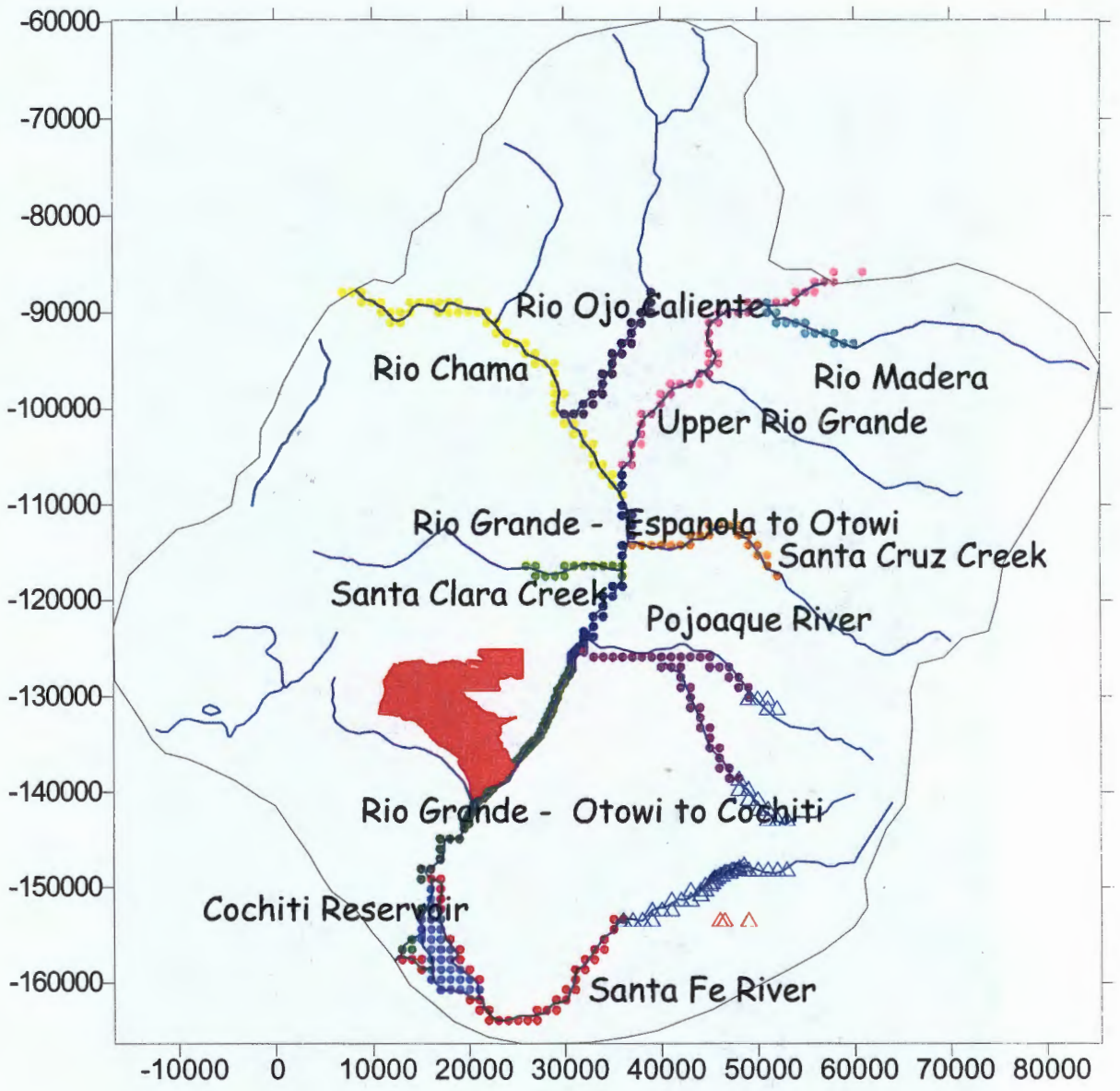

Figure 4-3 . Location of constant head nodes, where groundwater can recharge or discharge. Triangle symbols refer to specified flux nodes, where aquifer recharge is applied.

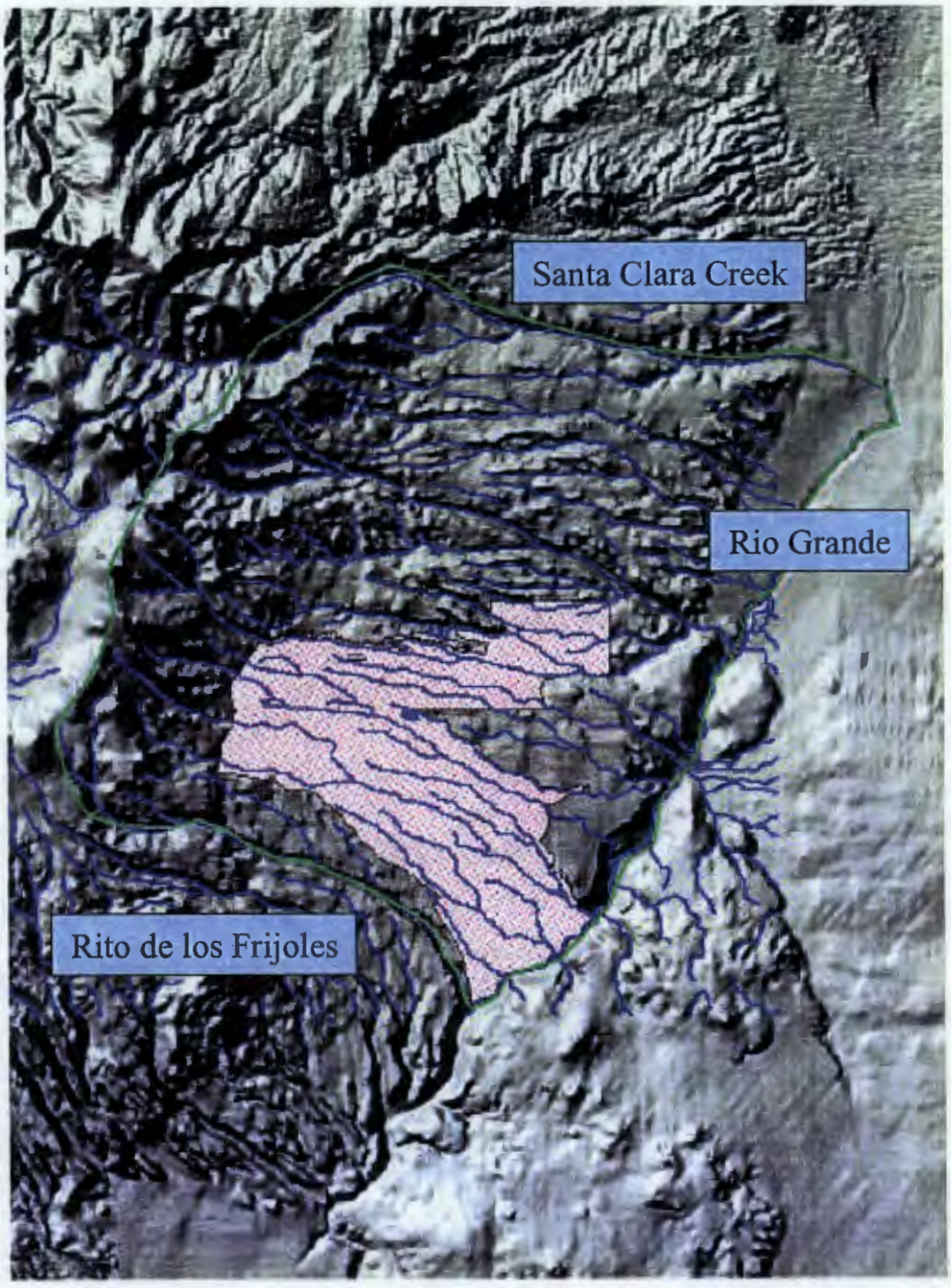

Figure 4-4 . Location of sub-model boundaries (green line)

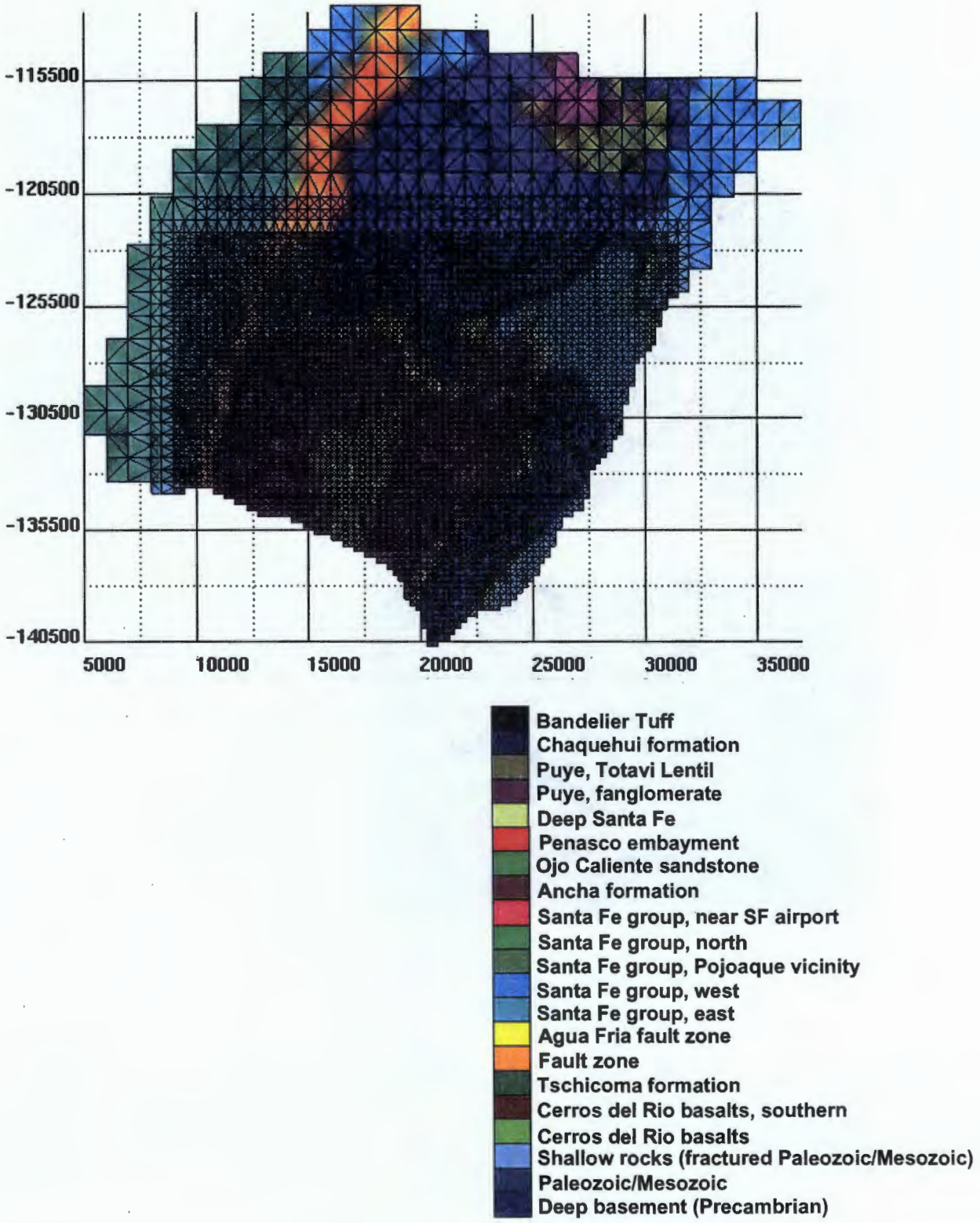

Figure 4-5a . Numerical mesh for sub-model; elements are colored according to hydrostratigraphy

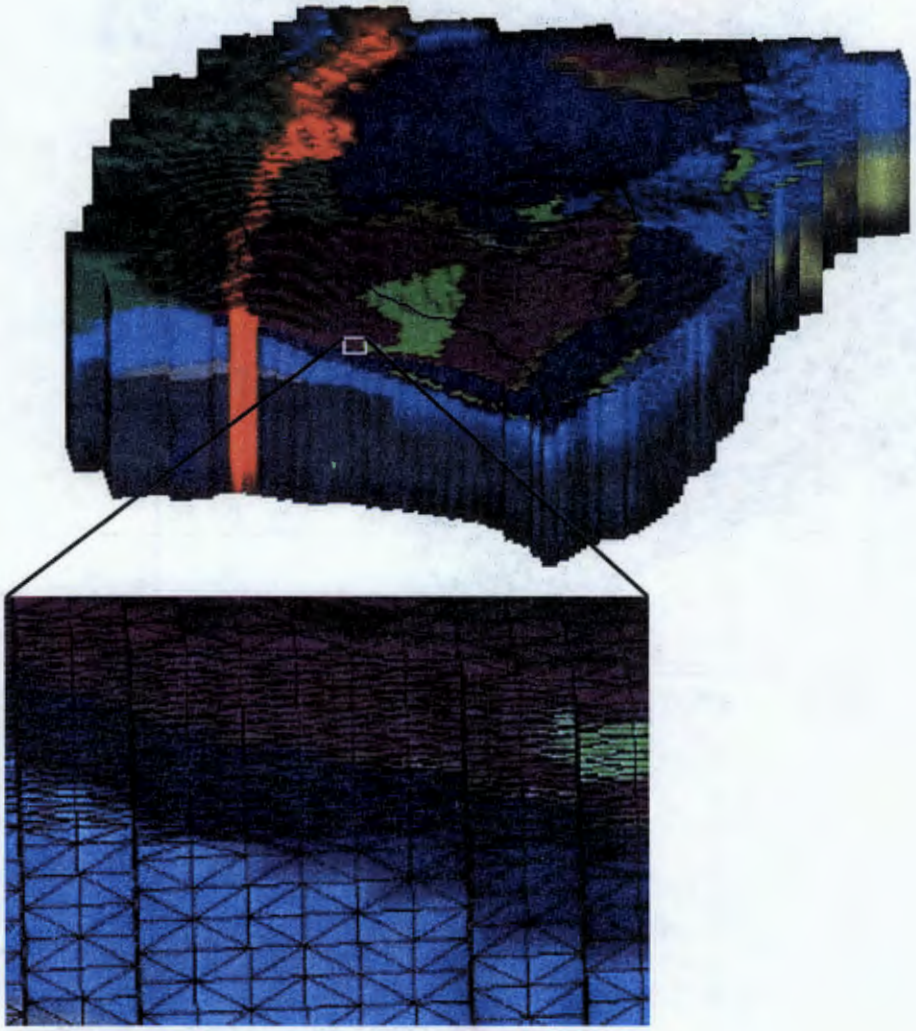

Figure 4-5b . Edge view of numerical mesh for sub-model, looking north

5 Model Calibration and Parameter Uncertainty

The calibration procedures described in this section are necessary because of model parameter uncertainty. The two most important model parameters, permeability and recharge rates, are associated with significant uncertainty. If these parameters were precisely known, then aquifer modeling would consist instead of two "forward" steps: (1) setting model parameters (i.e. permeability and recharge rates) according to known values, and (2) using the model to calculate some quantities of interest (flow rates, directions, concentrations, etc.). Using a strictly "forward" modeling approach can be very misleading if model parameters are uncertain. In this case, it is important to understand in detail the relationship between model parameter uncertainty and model prediction uncertainty. This is a complicated process if the model is complex with many parameters. Fortunately, there are well-established formal mathematical procedures for accomplishing this, which fall within the realm of model calibration, sensitivity analysis, and estimation error analysis. The theoretical basis for these analyses and the computational implementation is described in Appendix C.

The primary tool we use for these analyses is an automated parameter estimation software, PEST (Watermark Computing 1994). PEST is designed to provide detailed analyses of the relation between parameter uncertainty and model results. One way that we use PEST is to *provide information about parameter uncertainty*. In modeling groundwater flow, it is often the case that the quantities the model simulates (e.g. pressure heads) can be measured with far greater accuracy than the quantities that are required to parameterize the model (such as large-scale permeability). This is certainly true for our present model application. As a result, the process of "inverse" modeling (i.e. using observation data (water levels, fluxes) to predict model parameter values (permeability, recharge rates) can be a very powerful way to evaluate parameter uncertainty. Essentially, the inverse model (PEST) creates a large number of parameter value combinations, generates "forward" model results for each combination, compares each result with independent data, and calculates (1) the sensitivity of model results to parameter variations, and (2) the range of values for each parameter that generate "acceptable" model results (i.e. parameter uncertainty). These ranges are a measure of parameter uncertainty that is difficult to obtain using direct methods, such as conducting a large number of pump tests.

This same process provides very useful information about *model sensitivity to parameter uncertainty*. Through inverse modeling, we can discriminate between parameters to which model results are highly insensitive and those that are very sensitive. Further, we can distinguish parameters whose estimation errors are cross-correlated. Data collection efforts should obviously be prioritized toward reducing uncertainty in those parameters which are very insensitive, and those parameters whose estimation errors are cross-correlated. Strong cross-correlation between two or more calibrated parameters indicates that the same calibrated model may be obtained by simultaneously varying the parameters over large ranges. This can be a serious problem if the parameters have a different affect on post-calibration use of model, such as for transport.

5.1 Calibration procedure

As described in Keating et al. (1999), modeling the "pre-development" aquifer (with no significant withdrawals) provides the most straightforward measure of the relation between recharge rates, permeability, and aquifer discharges. For both the basin model and Pajarito Plateau sub-models, we simulated steady state flow, assuming no pumping. We used PEST to evaluate parameter uncertainty and sensitivity, given available data on pre-development water levels (93 basin-wide (Appendix B), 34 of which fall within the sub-model boundaries) and fluxes (see Table 4-3). The weights assigned to all these calibration targets are shown in Table 4-3. Recharge model parameters (α, Z_{min}, and dz ($dz = Z_{max} - Z_{min}$)) and permeability values for each hydrostratigraphic unit were varied, within specified ranges, to achieve optimal calibration to the steady-state "pre-development" dataset. This process, illustrated below in Figure 5-1, comprises our "steady-state" inverse models (basin and sub-model).

We are examining two alternative approaches concerning recharge on the plateau. The first approach is to assume that the process of steady-state basin model calibration will produce the most reliable parameters, since the basin model provides the best possible constraints on global water balance. Thus, recharge model parameters are taken from the basin model calibration results and applied *a priori* to the sub-model. The second approach is to assume that recharge rates on the Pajarito Plateau might be different from "average" rates at the basin-scale and thus recharge model parameters should be allowed to vary independently of those determined by basin-model calibration. Thus, recharge model parameters are varied as part of the sub-model calibration process. Both these approaches are used in the calibration process; results are described below.

As discussed in Chapter 3, water level declines due to pumping provide important information about aquifer permeability. To incorporate this information in the model calibration process, we developed a second type of inverse model: one that optimizes model parameters simultaneously for steady-state, no pumping, models and for subsequent transient models, with pumping; see Figure 5-2. The calibration dataset for the steady-state models is the same as that described above; the calibration dataset of the transient models is the measured water level decline in 14 wells on the Pajarito Plateau. Because of the large number of model runs involved in inverse analysis, we simplified the transient portion of the problem as follows. First, rather than simulating fifty years of pumping (1945 – 1995) using annual time steps, we simulating pumping using 10 year time steps. Ten-year average pumping rates were derived from annual pumping data for all wells in our dataset (Los Alamos, City of Santa Fe (including Buckman well field)) and applied as withdrawals in the model at each well. The transient model, simulating 50 years of pumping, was used to predict the total water level decline at each of 14 wells on the Pajarito Plateau. In total, we calibrated 6 models. These models are described in Table 5-1.

Table 5-1 Numerical inverse models.

Model	Numerical mesh	Recharge model parameters	Steady-state simulation	Transient simulation
Sub- SS1	sub-model	optimized	yes	no
Sub - SS2	sub-model	fixed (from basin model)	yes	no
Sub - SS-TR1	sub-model	optimized	yes	yes
Sub - SS-TR2	sub-model	fixed (from basin model)	yes	yes
Basin – SS	Basin	optimized	yes	no
Basin - TR	Basin	optimized	yes	yes

5.2 Calibration results

For each of the optimized models, PEST reports the model error at each calibration target. The residuals (simulated – observed) for simulated water levels and fluxes are shown in Figure 5–3. The residuals are unbiased (centered around zero). The spatial distribution of residuals, along with simulated pre-development water table elevation contours, is shown in

Figures 5–4 and 5–5. Figure5-6 presents a histogram of residuals for only those water level measurements within sub-model boundaries. From examination of water level simulation errors, it is clear that these three models are roughly comparable in their ability to adequately reproduce pressure heads on the plateau. Most water levels are predicted within 25ft; many are predicted within 10ft. This level of agreement is probably as good as one might expect with relatively coarse hydrostratigraphic definitions and a generalized recharge model.

Table 5–2 presents the simulated and observed fluxes (steady-state) for each of these models. This table demonstrates that allowing the recharge model parameters to differ from optimized values from the basin model produces a much better simulated fluxes to the Rio Grande. Both submodel results (optimized recharge parameters) and basin model results produce reasonable agreement between simulated and measured. Figure 5–7 presents simulated fluxes to 3 boundaries (Jemez, Embudo, and Chama) and 10 reaches within the basin model (steady-state). There are several reaches for which there are significant discrepancies (Lower Santa Fe River, Rio Embudo, Ojo Caliente, and Santa Clara Creek). Of these, only the observation data for the Lower Santa Fe River is measured with high accuracy. For the two boundaries most significant to the aquifer beneath LANL (Rio Grande Otowi to Cochiti and Jemez), agreement is excellent.

Table 5-2 Errors in simulated fluxes, for five models. Numbers are in cfs.

Reach	Estimate	Error (simulated – measured)				
	d	ss1	ss2	tr1	tr2	basin-ss
Rio Grande	10.4[a]	-0.1	-3.6	1.4	-3.9	-2.5
Santa Clara	0.0	0.1	0.1	0.1	0.1	-0.7

[a] this value assumes _ of total discharge to the Rio Grande along this reach originates to the west (Pajarito Plateau).

5.3 Parameter uncertainty

5.3.1 Steady-state basin model

The steady-state basin model requires specification of 37 parameters (recharge parameters and permeability). The inverse model estimates are listed in Table 5–3. The data is presented using ten-based log transformation. Since this presentation is not typical for the recharge parameters, their non-transformed estimates and lower/upper 95% confidence limits are

as follows: dz = 106 ft (fixed), zmin = 6981 ft (6606/7378), alpha = 0.0542 % (0.0429/0.0684). Permeability estimates are also presented graphically in Figure 5–8, along with permeability data (for comparison). Much of the permeability data was derived from pump tests in wells screened over multiple hydrostratigraphic units and it is unclear which unit the permeability data corresponds to (see Chapter 3). In Figure 5–8, data is only included for any given unit that occupies 50% or more of the screen interval in the well. This figure also shows the 95% confidence intervals associated with parameters that were allowed to vary in the inverse model process. The confidence intervals vary widely; for example, the permeabilities of Tsf (east,xy) and Tsf (west, xy) are very well constrained by the model; the permeabilities of Tsfuv, Tpf, and the Ancha formation are very poorly constrained.

Table 5-3 Parameter estimates.

Parameters	Short name	Units	Steady-state basin model		Steady-state submodel		Transient submodel	
			Estimates	Conf. limits	Estimates	Conf. limits	Estimates	Conf. limits
Recharge								
• dz	dz	$\log_{10}$[ft]	2.04	(fixed)	2.04	(fixed)	2.04	(fixed)
• Z_{min}	zmin	$\log_{10}$[ft]	3.84	0.02	3.85	0.05	3.85	0.05
• alpha	alpha	$\log_{10}$[%]	-1.27	0.11	-1.07	0.68	-0.99	0.34
Pemeabilities								
• Deep Basement	Basement	$\log_{10}$[m^2]	-15.30	(fixed)	-15.30	(fixed)	-15.30	(fixed)
• Paleozoic/Mesozoic	P/M	$\log_{10}$[m^2]	-15.45	(fixed)	-15.45	(fixed)	-15.45	(fixed)
• Shallow Paleozoic/Mesozoic (fractured)	Frac. P/M	$\log_{10}$[m^2]	-12.08	0.41	-12.08	(fixed)	-12.08	(fixed)
• Pajarito fault zone	Paj.Fault	$\log_{10}$[m^2]	-14.90	0.73	-14.90	(fixed)	-14.90	(fixed)
• Tschicoma Formation	Tt	$\log_{10}$[m^2]	-12.89	0.45	-12.89	(fixed)	-12.89	(fixed)
• Tschicoma formation - shallow	Frac. Tt	$\log_{10}$[m^2]	-12.82	(fixed)	-12.82	(fixed)	-12.82	(fixed)
• Cerros del Rio basalts	Tb1	$\log_{10}$[m^2]	-11.31	(fixed)	-11.30	15.80	-12.58	0.64
• Cerros del Rio basalts	Tb2	$\log_{10}$[m^2]	-11.30	0.61	-11.00	0.88	-11.50	0.68
• Cerros del Rio basalts	Tb4	$\log_{10}$[m^2]	-13.49	1.87	-13.46	8.67	-13.74	3.99
• Santa Fe group - West	Tsf (west, xy)	$\log_{10}$[m^2]	-13.55	0.19	-13.43	0.42	-13.30	0.27
vertical	Tsf (west, z)	$\log_{10}$[m^2]	-13.24	0.59	-13.22	1.95	-12.99	1.27
• Santa Fe group - deep	Tsf (deep,xy)	$\log_{10}$[m^2]	-15.00	0.70	-15.00	(fixed)	-15.00	(fixed)
vertical	Tsf (deep,z)	$\log_{10}$[m^2]	-16.00	(fixed)	-16.00	(fixed)	-16.00	(fixed)
• Puye fanglomerate	Tpf	$\log_{10}$[m^2]	-14.07	1.72	-14.01	4.71	-14.56	2.32
• Puye Totavi Lentil	Tpt	$\log_{10}$[m^2]	-11.09	3.45	-11.25	0.85	-11.00	1.07
• Chaquehui Formation	Tsfuv (xy)	$\log_{10}$[m^2]	-14.64	2.94	-14.67	1.96	-13.35	0.27
vertical	Tsfuv (z)	$\log_{10}$[m^2]	-15.53	0.50	-15.39	0.71	-15.23	0.97
• Shallow Sangres	Frac. PC (1)	$\log_{10}$[m^2]	-13.64	0.22	N/A		N/A	
• Frac. PC - Ojo Caliente vicinity	Frac. PC (2)	$\log_{10}$[m^2]	-13.24	1.22	N/A		N/A	
• Frac. PC - Penasco vicinity	Frac. PC (3)	$\log_{10}$[m^2]	-13.07	0.15	N/A		N/A	
• Cerros del Rio basalts - south	Tb (south)	$\log_{10}$[m^2]	-15.58	(fixed)	N/A		N/A	
• Agua Fria fault zone	AF fault	$\log_{10}$[m^2]	-15.00	(fixed)	N/A		N/A	
• Santa Fe group – East	Tsf (east,xy)	$\log_{10}$[m^2]	-13.20	0.24	N/A		N/A	
vertical	Tsf (east,z)	$\log_{10}$[m^2]	-14.77	0.99	N/A		N/A	
• Santa Fe group – Airport	Tst (SF, xy)	$\log_{10}$[m^2]	-13.13	0.73	N/A		N/A	
vertical	Tst (SF, z)	$\log_{10}$[m^2]	-13.68	0.81	N/A		N/A	
• Santa Fe group – Pojoaque	Tst (Poj., xy)	$\log_{10}$[m^2]	-12.32	(fixed)	N/A		N/A	
vertical	Tst (Poj., z)	$\log_{10}$[m^2]	-16.52	(fixed)	N/A		N/A	
• Ancha formation	Ancha (xy)	$\log_{10}$[m^2]	-13.74	1.17	N/A		N/A	
vertical	Ancha (z)	$\log_{10}$[m^2]	-13.00	14.86	N/A		N/A	
• Santa Fe group – North	Tsc	$\log_{10}$[m^2]	-13.11	0.36	N/A		N/A	
• Santa Fe - Ojo Caliente sandstone	Tso	$\log_{10}$[m^2]	-13.47	0.22	N/A		N/A	
• Santa Fe - Penasco embayment	Tst (Pen)	$\log_{10}$[m^2]	-13.74	0.37	N/A		N/A	
• Bandelier Tuff	Band	$\log_{10}$[m^2]	-13.00	(fixed)	N/A		N/A	
Specific Storage	Ss	$\log_{10}$[m^{-1}]	N/A		N/A		-3.75	0.29

Table 5-4 Residual statistics.

Residuals (n=33)	Median	min	max
ss1	-11.5	-69.8	144.3
ss2	-3.3	-65.6	127.9
tr1	-9.8	-65.7	82.0
tr2	-6.0	-77.2	89.0
basin-ss	-3.3	-65.6	131.2
basin-tr	-3.3	-72.2	105.0
Residuals (absolute value)			
ss1	20.8	0.8	144.3
ss2	23.0	0.0	127.9
tr1	24.2	0.9	82.0
tr2	29.3	0.5	89.0
basin-ss	19.7	0.0	131.2
basin-tr	26.2	0.0	105.0

For some units, the permeability data are very close to the estimates; e.g. Tb2, Tbt, Frac.PC(1), Tsf(east,xy), and Ancha(xy). There are significant deviations (but within the uncertainty limits) for Tb4, Tpf, and Tsfuv(xy). Inverse estimates for Tsf(west,xy) and Tpf are much lower than the data values. This is very significant result and will be discussed further below. Overall, the permeability data averages are, however, higher than the respective inverse estimates. It is important to note that both estimates represent the rock properties at very different scale. The inverse estimates represent the large-scale effective permeabilities for the whole rock unit, while the permeability data is defined from small-scale field tests representing rock properties in the close vicinity of test boreholes. It has been demonstrated in the literature (e.g. (Neuman 1990) that the effective properties of porous medium, especially permeability, decrease with the scale of analysis (the so called "scale effect"), which is consistent with our results. We should also take into account the fact that the prior permeability data is collected for the existing water supply wells, which are typically screened in highly permeable portions of the aquifer in order to achieve higher pumping rates. Therefore, the prior permeability data might be biased towards higher estimates.

Figure 5–9 shows the log sensitivities of all the model parameters in respect to the simulated observations (red bars). All parameters except Ancha(z), Tst(SF,xy), and Basement demonstrate relatively high sensitivity. The good model sensitivity to the model parameters is important. It allows proper identification of parameter estimates and associated errors (including

the cross-correlations between the estimation errors). The most sensitive are the recharge parameters (dz, zmin, alpha) and the permeabilities of Tsf(west,xy) and Paj.Fault.

Identifying correlations between parameters, and more importantly between their estimation errors, is a important aspect of understanding the effect of parameter uncertainty on model results. If two parameters are correlated, for example, one can achieve the same model responses for the available observations by keeping the same ratio between both parameters. However, different pairs of estimates for the cross-correlated parameters can produce very different model predictions for hydrogeological processes, which have not been considered in the inverse analysis (e.g. contaminant transport). This situation can be caused by either of two factors: (1) too few data with which to test the model, or (2) too few data with which to parameterize the model. In other words, the model has more complexity than the available data can support. Figure 5–10 presents the correlation matrix of estimation errors for all unknown model parameters. It appears that there is a strong correlation between estimation errors for many parameters. For only few of the parameters, the estimation errors are uncorrelated with the rest of parameters; e.g. Frac.PC(2), Ancha(xy), Ancha(z). However, it is important to note that though Ancha(z) estimation errors appear to be uncorrelated, its estimate is highly uncertain (very large 95% confidence intervals; Table 5–3; Figure 5–8); this is due to the model insensitivity to Ancha(z) (Figure 5-9).

The most accurate way to estimate cross-correlation between multiple variables is through eigenanalysis of the covariance matrix of estimation errors, which PEST provides. This analysis is presented in Figure 5–11. The eigenvectors are ordered according to the magnitude of their corresponding eigenvalues; that with smallest eigenvalue is first and numbered 1, and that with highest eigenvalue is last and numbered 37. The components of each eigenvector represent the relative contribution to it by the estimation errors of each parameter. Parameters associated with eigenvectors having small eigenvalues are less uncertain than those associated with eigenvectors having large eigenvalues. Parameters associated with a single eigenvector have uncorrelated estimation errors. Parameters associated with multiple eigenvectors have cross-correlated estimation errors. In Figure 5–11, the first eigenvector (with the smallest eigenvalue) is associated almost entirely with zmin. Therefore, its estimate is the most certain and its error is uncorrelated. The last eigenvector (with the largest eigenvalue) is associated with Tb(south), which is, therefore, very poorly estimated though its error is uncorrelated. Eigenvector 3 is

characterized by a series of parameters (Tsf(west,xy), Tsf(east,xy), Paj.Fault, Tso) which estimation errors are highly correlated. Therefore, we could improve significantly the estimation uncertainty of these parameters if additional data was available. Estimation errors of Tsf(deep,xy) and Tsf(deep,z) are characterized by similar eigenvectors and clearly highly correlated; therefore, their separate estimation based on the available data is not feasible. Further, their eigenvectors are associated with high eigenvalues and, therefore, their estimates are also uncertain. On the other hand, Tst(SF,xy) and Tst(SF,z) errors are independent to each other, but the former is better estimated than the latter. In similar way, we can analyze the estimation uncertainty and the correlation between estimation errors regarding all model parameters. In summary, there are significant uncertainties in the inverse estimates of Basement, P/M, Tt, Frac.Tt, Tb1, Tsf (deep,xy), Tsf (deep,z), Tb (south), AF fault, Tst(Poj., z), Ancha (z), and Band.

5.3.2 Steady-state submodel

Inverse analysis of steady-state submodel includes 20 model (recharge and permeability) parameters and 35 observations. Residuals are presented in Figures 5–3 and 5–6. Similar to the basin model, the residuals are unbiased (centered around zero) but clearly not normally distributed. The inverse estimates are listed in Table 5–3 and some of them also presented graphically in Figures 5–8 and 5–12. Permeability parameter estimates using the sub-model are very similar to those using basin model (Figure 5–8; Table 5–3). The largest differences are for Tb2 and Tpt; the latter estimate is getting close to the prior data, the former is farther. The differences in recharge parameters are significant (alpha, zmin); a higher alpha estimate for the submodel means that significantly more water is recharging the aquifer. Both models provide reasonable estimates for discharge to the Rio Grande and reasonable water level predictions, so it is impossible to discriminate between these two recharge models at this point.

Figure 5–9 shows the log sensitivities of model parameters in respect to all the simulated observations (blue bars). Overall, the sensitivities are consistent with but smaller than the one for the basin model. Basement, Frac.P/M, and Tb1, are the most insensitive parameters. There is relatively high sensitivity to the recharge parameters (zmin, alpha) and the permeabilities of Tsf(west,xy), Paj.Fault, Tb2, and Tsf(deep,xy).

Figure 5-13 presents the correlation matrix of estimation errors for all unknown submodel parameters. All the parameters except Basement and Tb1 appeared to have mutually correlated errors. The strong cross-correlation not only slows down the optimization process, but also could

prevent the reach of global minimum. We also performed eigenanalysis of the covariance matrix of estimation errors (Figure 5–14). As for the basin model, zmin is defined with most certainty. Tsf(west,xy) appears to be well defined but its estimation error is highly correlated with the one of alpha, Paj.Fault, and Tsfuv(z). In contrast with the basin model, Tsf(deep,xy) and Tsf(deep,z) errors are not highly correlated which is an important improvement for the submodel. The same is true for the other rock types where we separate horizontal and vertical permeability components. The last eigenvector (with the largest eigenvalue) is associated with Basement, which is, therefore, very poorly estimated. The inverse analysis produces uncertain estimates for Ratio, dz, Tt, P/M, FracP/M, and Tsf(deep,z).

5.3.3 Steady-state+Transient submodel

For the transient simulation, we have added additional 15 observations representing the non-pumping drawdown after 50-years. The residuals (Figure 5–3; cyan bars) are unbiased (centered around zero), but clearly not normally distributed. More importantly, the steady-state+transient submodel improved the residuals for the steady-state observations (Table 5–4). The spatial distribution of residuals, along with simulated pre-development water table elevation contours, is shown in Figures 5–15 and 5–16. This undoubtedly shows that the steady-state model did converge to a global minimum for our objective function Φ. Most probably, this is a result of high cross-correlation of the estimation errors between some of the parameters (as discussed in the previous section). As will be discussed further below, the addition of transient data resolves the problematic cross-correlations, which were evident in the steady-state calibrations.

All parameter estimates are listed in Table 5–3; permeability estimates are also presented graphically in Figure 5–12. Comparison between the steady-state and steady-state+transient estimates (Figures 5–12 and 5-17) show that the major changes are associated with Tsuv(xy) and Tbl permeabilites.

The estimate of specific storage estimated by the transient inverse model is close to the available prior estimate listed in Table 4–2.

Figure 5–9 presents the log sensitivities of model parameters in respect to all the simulated observations (cyan bars). Overall, the steady-state and steady-state+transient submodel sensitivities are close to each other. Still, Basement and Frac.P/M, are the most insensitive one,

but Tb1 sensitivity increased substantially compared to the steady-state case. Direct comparison between the steady-state and steady-state+transient sensitivities is shown in Figure 5–18.

Figure 5–19 compares the observed and simulated drawdowns at the pumping wells. The obtained match is satisfactory.

Figure 5–20 presents the correlation matrix of estimation errors for all steady-state+transient submodel parameters. Comparing with the respective stead-state analysis (Figure 5–13), we clearly notice significant improvement in terms of computed cross-correlations. The result of eigenanalysis of the covariance matrix of estimation errors is shown in Figure 5–21. Again, the figure demonstrates significant improvement in estimation certainty versus the steady-state case (Figure 5–14). This is also indicated by the significant decrees of the covariance-matrix conditioning number (the conditioning number is defined by the ratio of maximal and minimal eigenvalues). Now, Tsf(west,xy) appears to be extremely well defined and uncorrelated. Still, the model appears to be insensitive to Basement, FracP/M, Ratio, dz, Tt, P/M, and Tsf(deep,z).

5.4 Predictive analysis

Predictive analysis is a tool for estimating the uncertainty associated with a model prediction of interest. Because of parameter uncertainty and correlation between parameters, there may be multiple combinations of parameters that provide equally good calibrations (for example, compare model results in Figures 1–3). Although these models may be equivalent in terms of their ability to reproduce water level and flux data, they may provide quite different estimates of other quantitities of interest (flow rates, solute concentrations, etc.). We use predictive analysis to investigate uncertainty of (1) fluxes into/out of the boundaries of the sub-model and (2) the variation in groundwater flow direction taken by a particle entering the aquifer beneath the western boundary of LANL.

5.4.1 Flux estimates for the lateral boundaries of the sub-model

One of the primary purposes of using a basin scale model to address site-scale questions about groundwater flow is to understand the fluxes into and/or out of the aquifer beneath the site. These fluxes may have significant influence on local flow directions and will certainly have impact on contaminant transport in the regional aquifer. Questions of interest include (1) what is our "best guess", given the available data, of lateral fluxes into/out of the aquifer beneath the

site? (2) how uncertain are these guesses?, and (3) to what model parameters are these estimates most sensitive? These questions can be framed in terms of estimation of fluxes (as predicted by the basin model) into or out of the lateral boundaries of the sub-model.

Optimization and predictive analysis is designed to answer these questions. Optimization, the process of model calibration, has been described above. By optimizing the parameters for the basin model, we estimate the "best guess" for the fluxes into/out of the sub-model. Predictive analysis is aimed at evaluating the role of parameter uncertainty in determining these fluxes. In this case, the estimates we are interested in are the fluxes into/out of the submodel boundaries.

The estimates obtained by the optimal basin model for the North, West, and South boundaries of the submodel region are 2.4, -8.8, and 36.8 kg/s, respectively. In predictive analysis, PEST modified our parameter estimates in a way which will produce maximal/minimal prediction for the fluxes along the three boundaries such that our objective function Φ (the sum of weighted squared residuals) is within a predefined upper limit (Φ = 55,000) which is slightly higher than the one obtained for the optimal basin model (Φ = 47,211). The predictions are listed in Table 5–5. The largest uncertainty is associated with the flux along the West boundary; least uncertain is the flux along the North boundary. It is interesting to note that all three boundaries can be either net inflow or net outflow within the range of uncertainty of the problem. This uncertainty, particularly on the western boundary, points to the need for further understanding of the regional flow field (basin scale).

Figure 5–22 presents sensitivity of all the predicted fluxes in respect to model parameters. Clearly, the flux estimates are most sensitive to recharge parameters (zmin and alpha), and, secondarily to permeability parameters such as Paj.Fault, Tt, Tsf(west,xy), Tso, and Ratio. For all these parameters, the North flux is least sensitive (most certain) compared to the West and South fluxes. Figure 5–23 shows the relative change in parameters as a result of the predictive analysis compared to the optimal basin model estimates. The parameters, which were modified significantly in all cases, are P/M, Paj.Fault, Tt, Tsuv, Tst(Po), and Ratio. Therefore these parameters are not only sensitive to the predicted flow and but also their inverse estimates were uncertain. In most cases, the maximum and minimum prediction estimates produce opposite changes in the estimates which was theoretically expected; the parameter changes in the same directions are most probably as a result of low parameter sensitivities to the prediction.

Table 5-5 Flux predictions for the North, West, and South boundaries of the submodel region.

	North		West		South	
	Max	Min	Max	Min	Max	Min
Flux Predictions	6.7	-4.6	94.3	-5.2	8.1	-33.8

5.4.2 Flow directions

To estimate the sensitivity of our model to the flow directions in the western portion of the aquifer, we have simulated the advective transport from a point at the water table near TA16. As a rough measure of flow direction uncertainty, we ask the model to predict the *y* coordinate of the particle as it reaches the PM well field. Other measures can be examined in the future. We have estimated the sensitivity of this coordinate to all the submodel parameters. Our results are presented in Figure 5–24. Clearly, the transport direction is highly sensitive to zmin and Tpt. However, according to our error analysis (Figures 5–11 and 5–21) these parameters are estimated with relatively high certainty. Of the parameters, which are important to predicting flow direction, we have uncertain estimates for Tt, P/M, FracP/M and Tsuv(z). To a lesser degree, this is also valid for Tb2 and Tb1. Decreasing the estimation uncertainty of all those parameters would decrease the prediction uncertainty of flow direction.

To obtain better estimates of the flow direction uncertainty, we have to perform a predictive analysis, which will take into account the cross-correlations among the parameters and the problem non-linearity. Though this analysis is computationally very intensive (single forward run for this case takes more than an hour, and the complete analysis would require more than 1,000 forward runs), we plan to perform it in the future.

5.5 Conclusions

Our inverse analyses included the basin model and the Pajarito Plateau submodel as well as steady-state and transient simulations. An important question is which model(s) is(are) most important for the characterization of hydrogeological conditions in the region of LANL.

Compared to the submodel, the basin model includes larger amount (~ 3 times) of observation data but also more model parameters (~ 2 times). This allows better definition of overall water balance in the Espanola basin. More importantly, it provides us with estimates for parameters (such as Frac.P/M, Paj.Fault, Tt and Tsf (deep,xy)), which are defined within the submodel but cannot be estimated by the submodel inverse analysis since their estimation errors

are highly correlated. Further, some of these parameters are very important for characterization of flow directions in the vicinity of LANL.

The basin model defines the fluxes along the submodel boundaries. Our analysis demonstrates that there is uncertainty in these fluxes (especially regarding the West boundary) due to uncertainty in the parameter estimates in the basin model. Therefore, we would need to improve the certainty of these parameters. This analysis would not possible without the basin inverse model.

For the submodel, the transient data proved to be very important in the inverse analysis. We plan to incorporate additional transient data (currently available), which we hope to further improve our estimates.

Currently we have different estimates for recharge parameters obtained by submodel and basin-model inversions. The flow directions in the vicinity of LANL are very sensitive to the recharge and, therefore, we should perform further analysis on the recharge estimates and resolve the discrepancy between submodel and basin-model inversions.

For the basin model, there are uncertainties in the inverse estimates of Basement, P/M, Tt, Frac.Tt, Tb1, Tsf(deep,xy), Tsf(deep,z), Tb(south), AF fault, Tst(Poj., z), and Ancha(z). Those are due to both low model sensitivity and cross-correlations among estimation errors. The (transient) submodel significantly improves the estimation quality of Tb1; in a lesser degree, there is also improvement in Tsfuv(xy) estimate. Further development of the inverse estimates would require additional information (pressures, fluxes) about the Espanola basin.

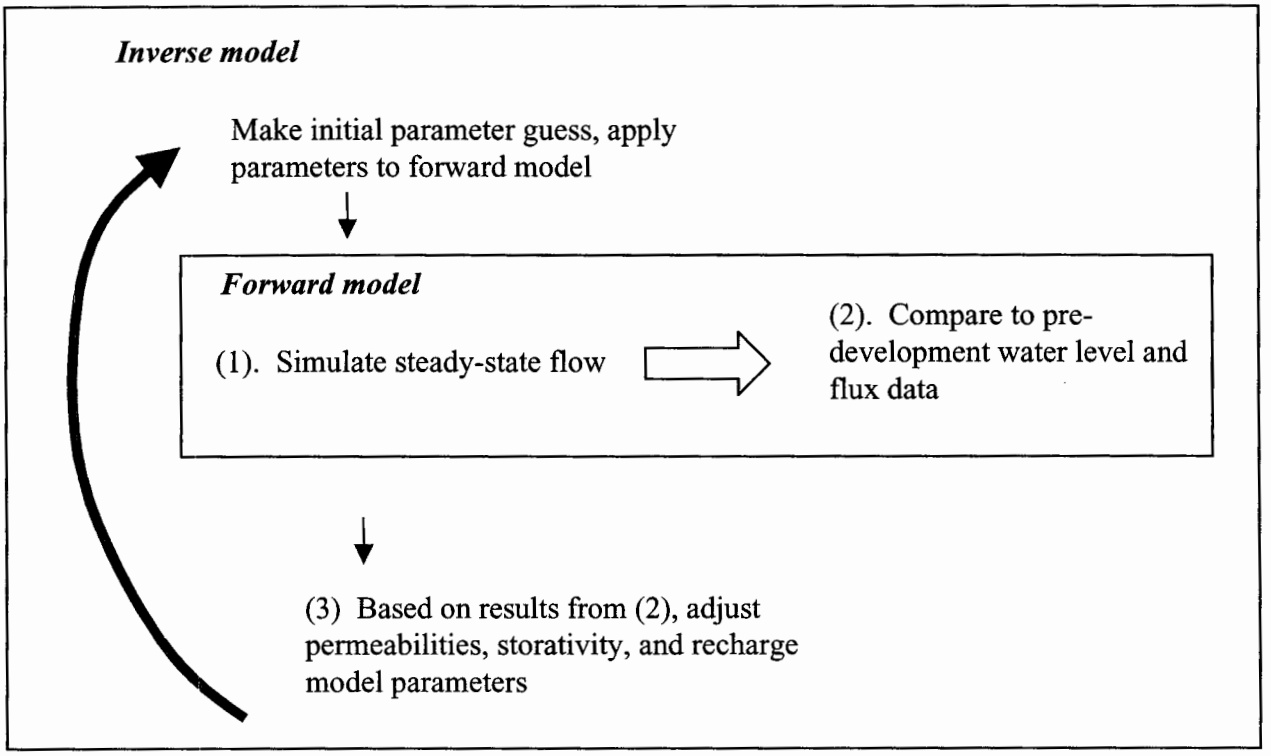

Figure 5-1.. Process for steady-state model calibrations

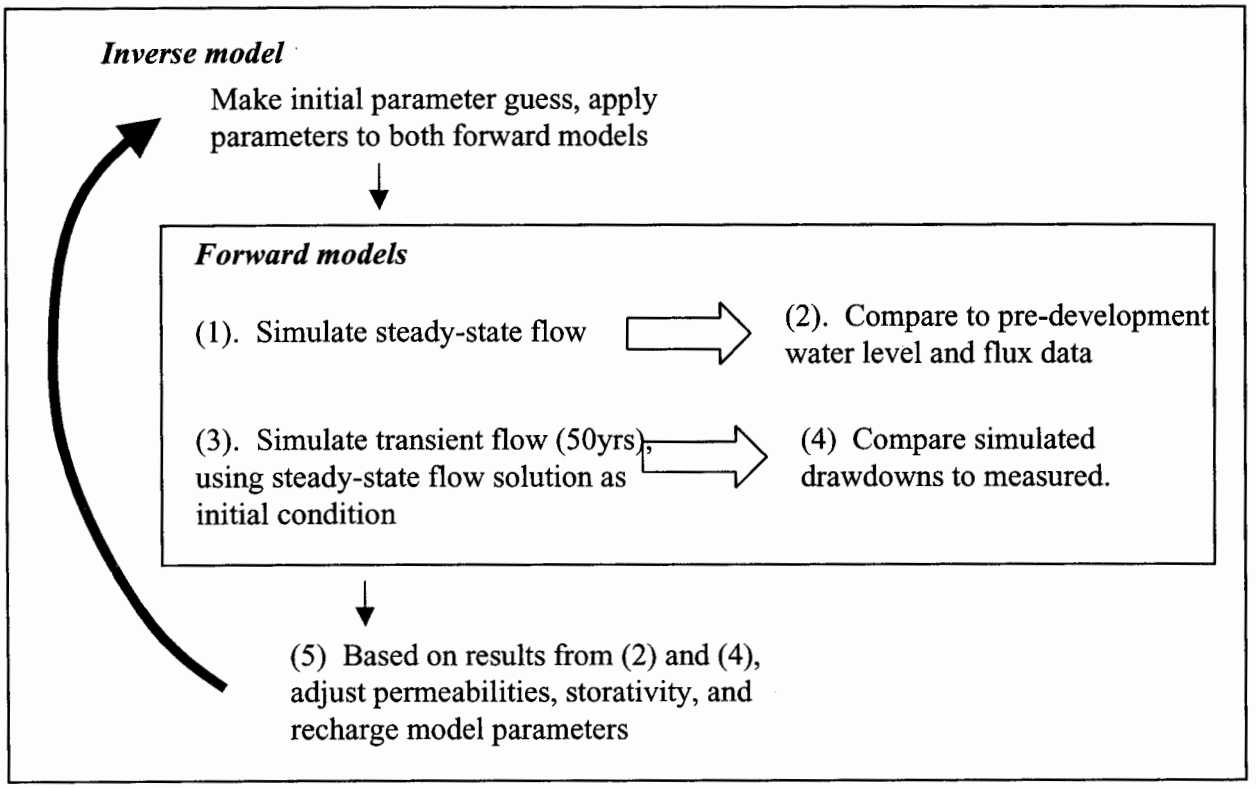

Figure 5-2. Process for steady-state- transient model calibrations

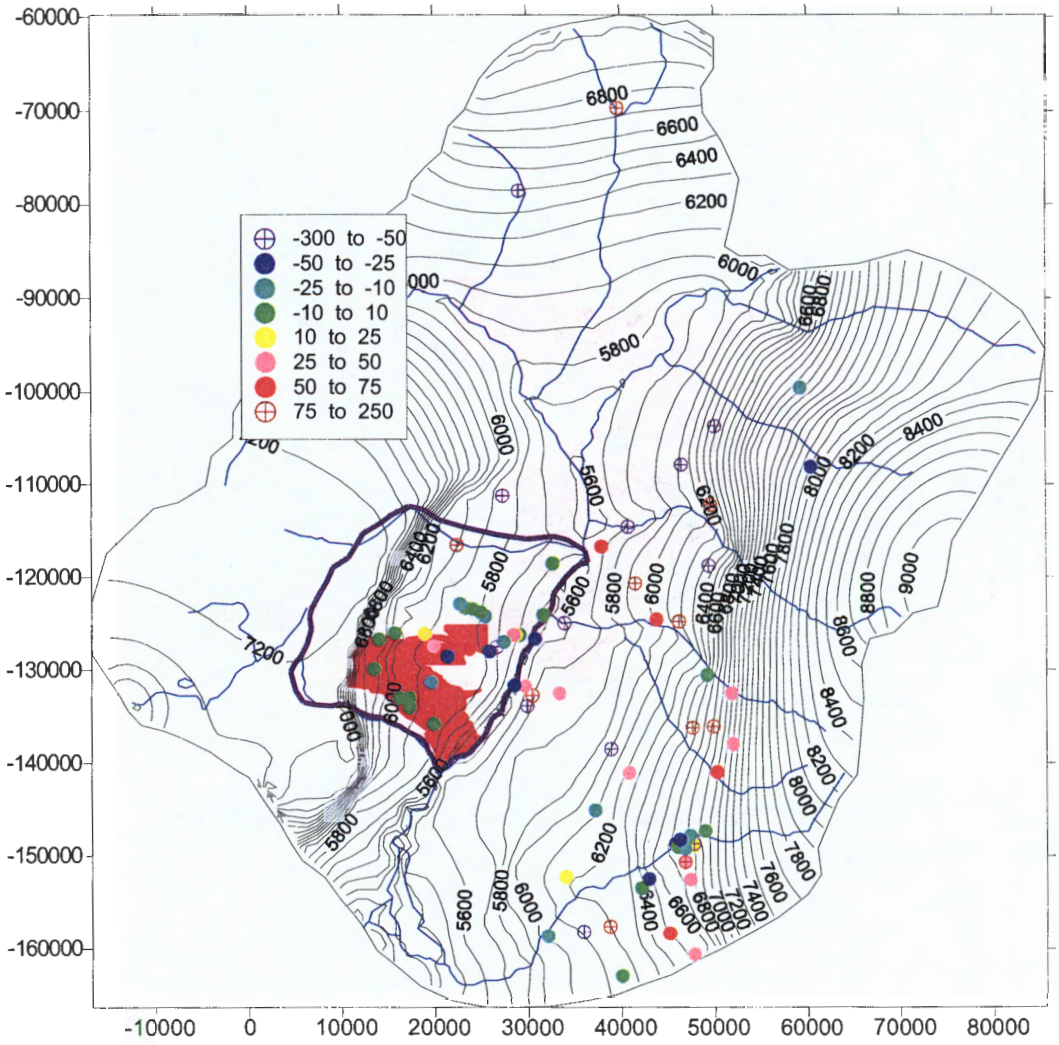

Figure 5-4. Steady-state basin model Water level contours and model error (simulated - observed).

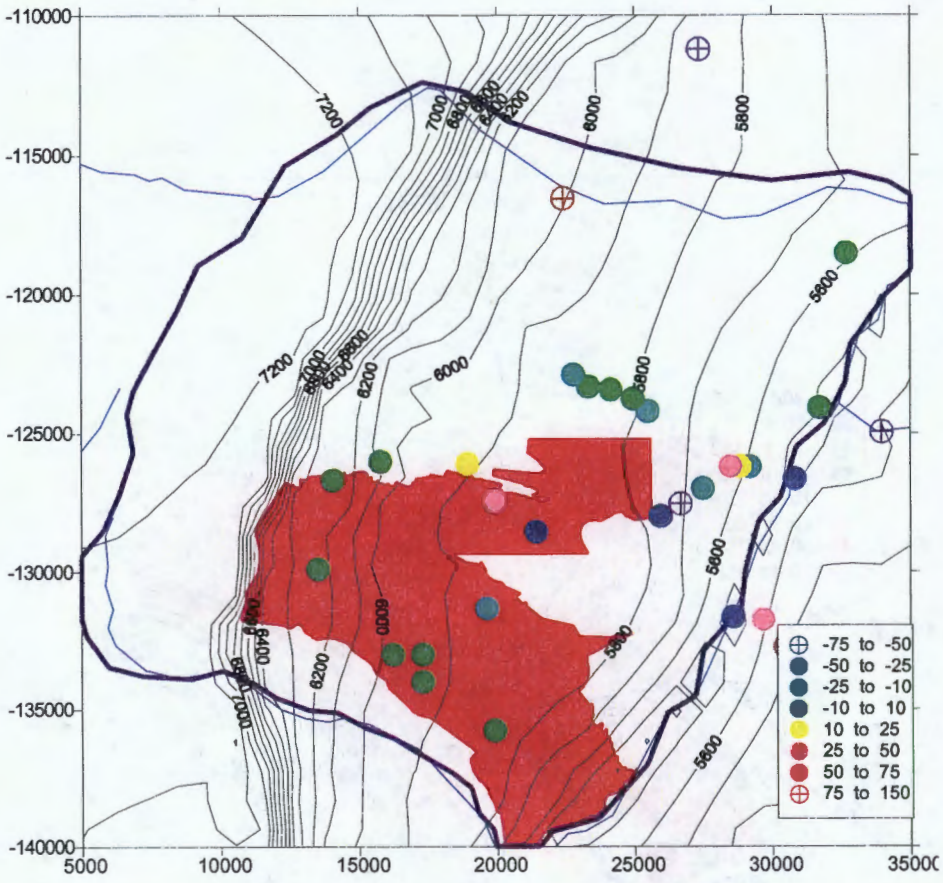

Figure 5-5. Steady-state basin model Water level contours and model error (simulated - observed).

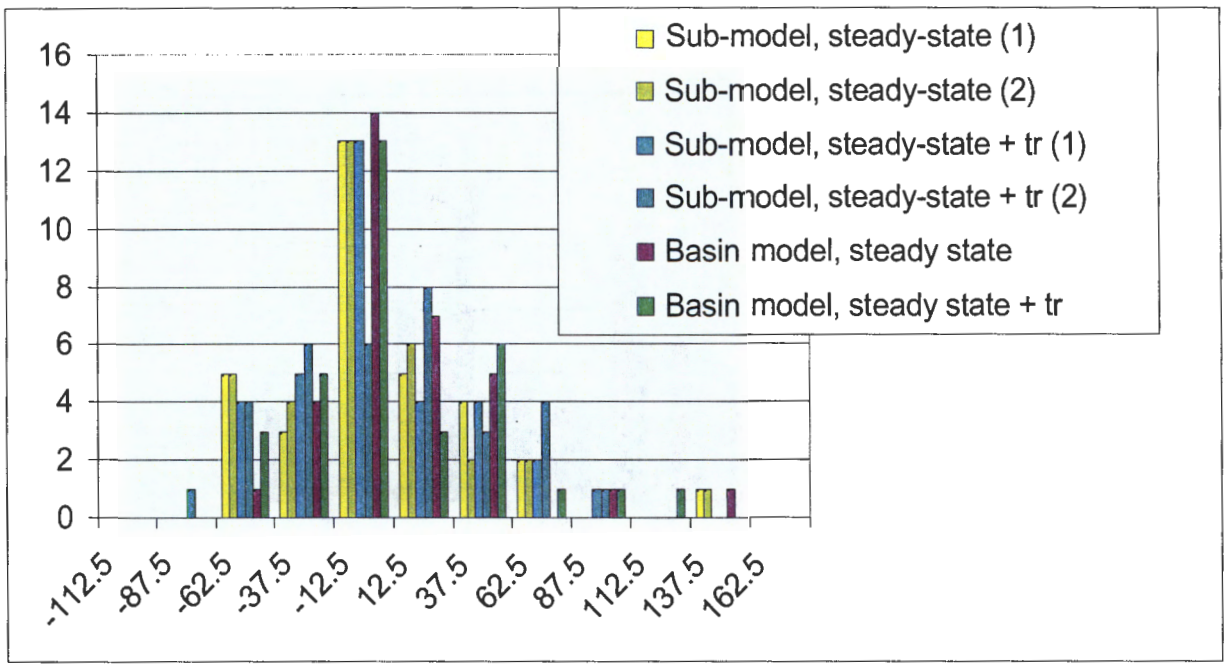

Figure 5-6. Residuals (in feet) for three models, including only water levels within submodel boundaries

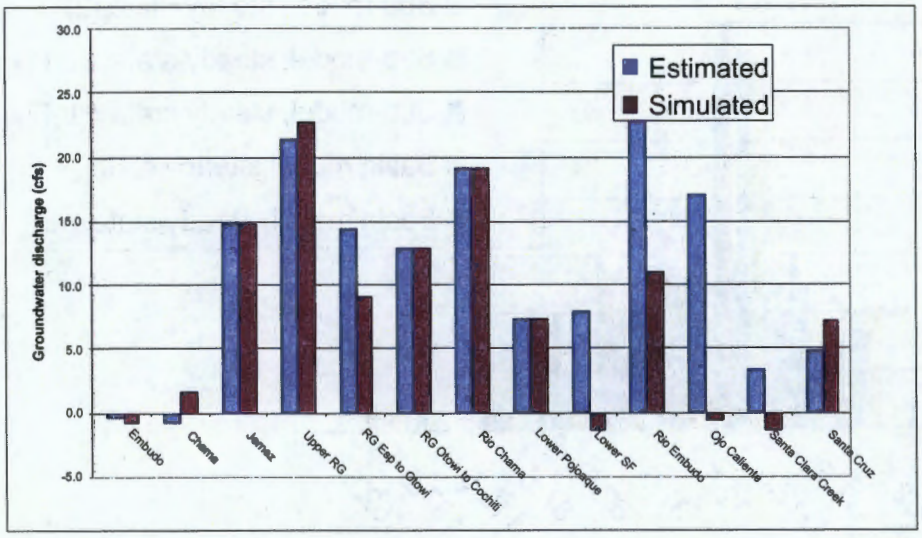

Figure 5-7. Simulated and observed fluxes at 3 model boundaries (lateral) and 10 river reaches

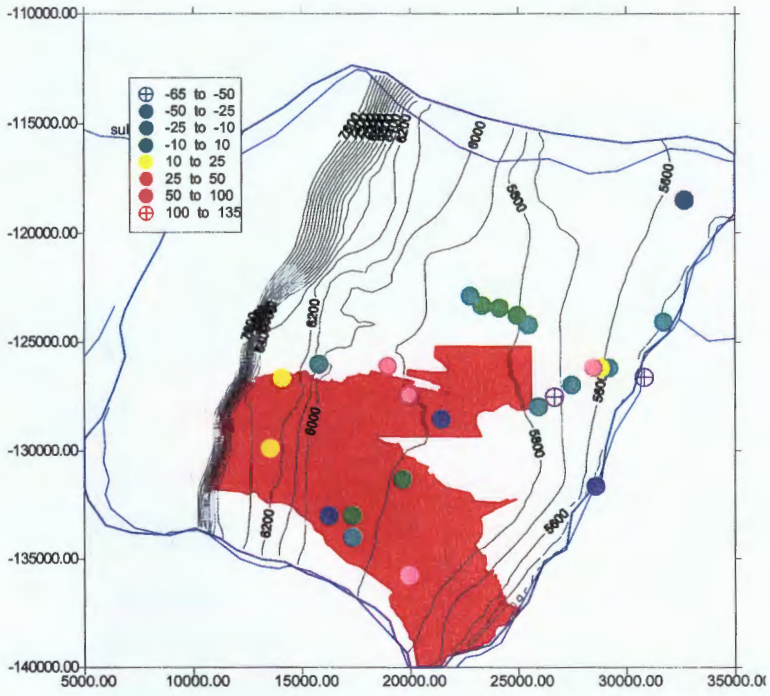

Figure 5-15. Steady-state sub-model (1) Water level contours and model error (simulated - observed).

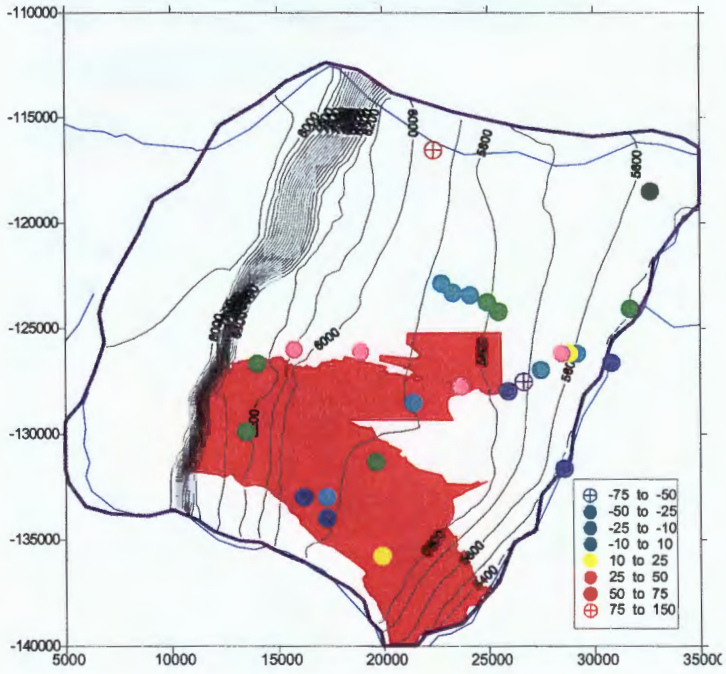

Figure 5-16. Steady-state-tr sub-model (1) Water level contours and model error (simulated - observed).

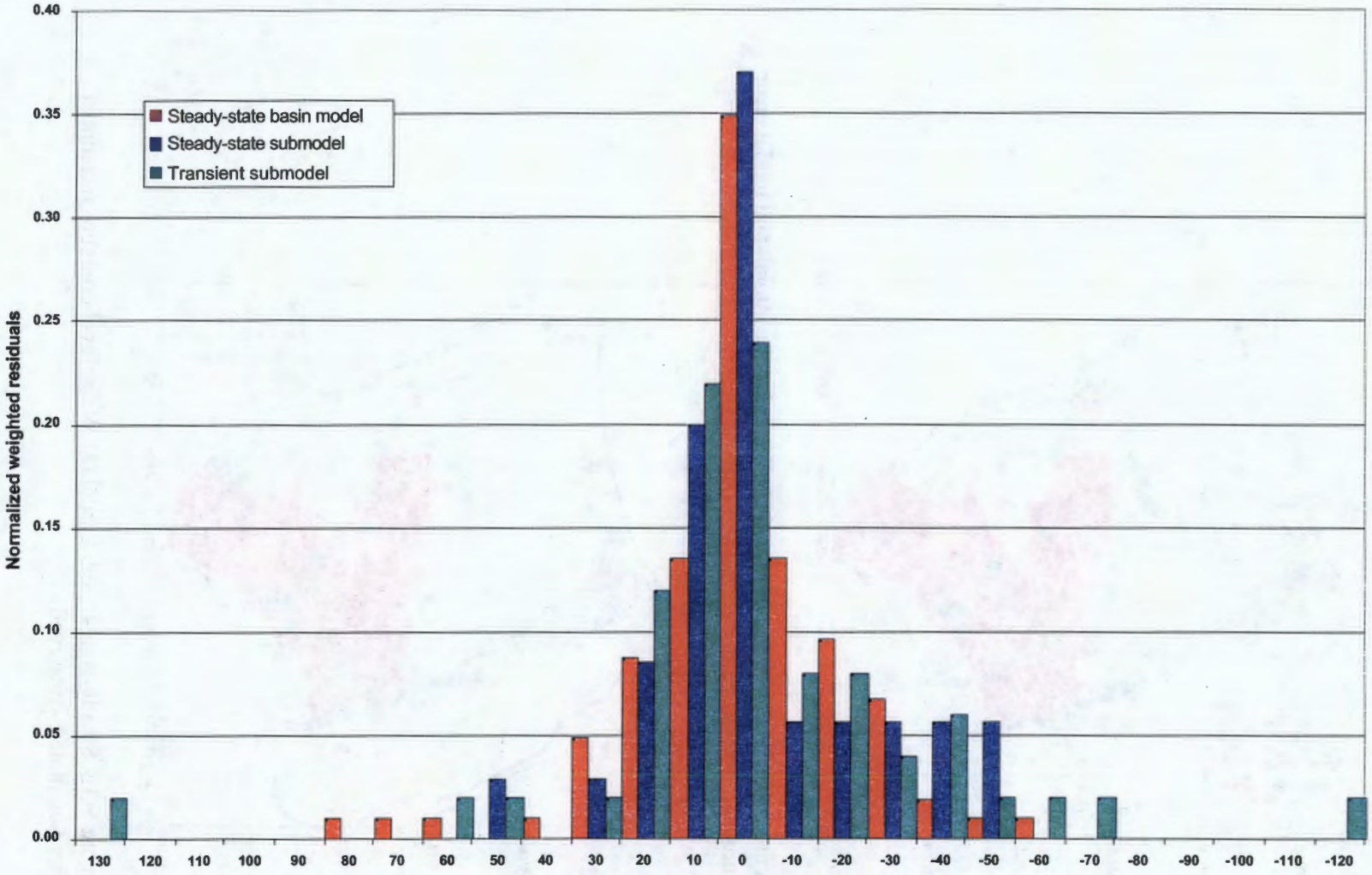

Figure5-3. Normalized weighted residuals obtained for different inverse models.

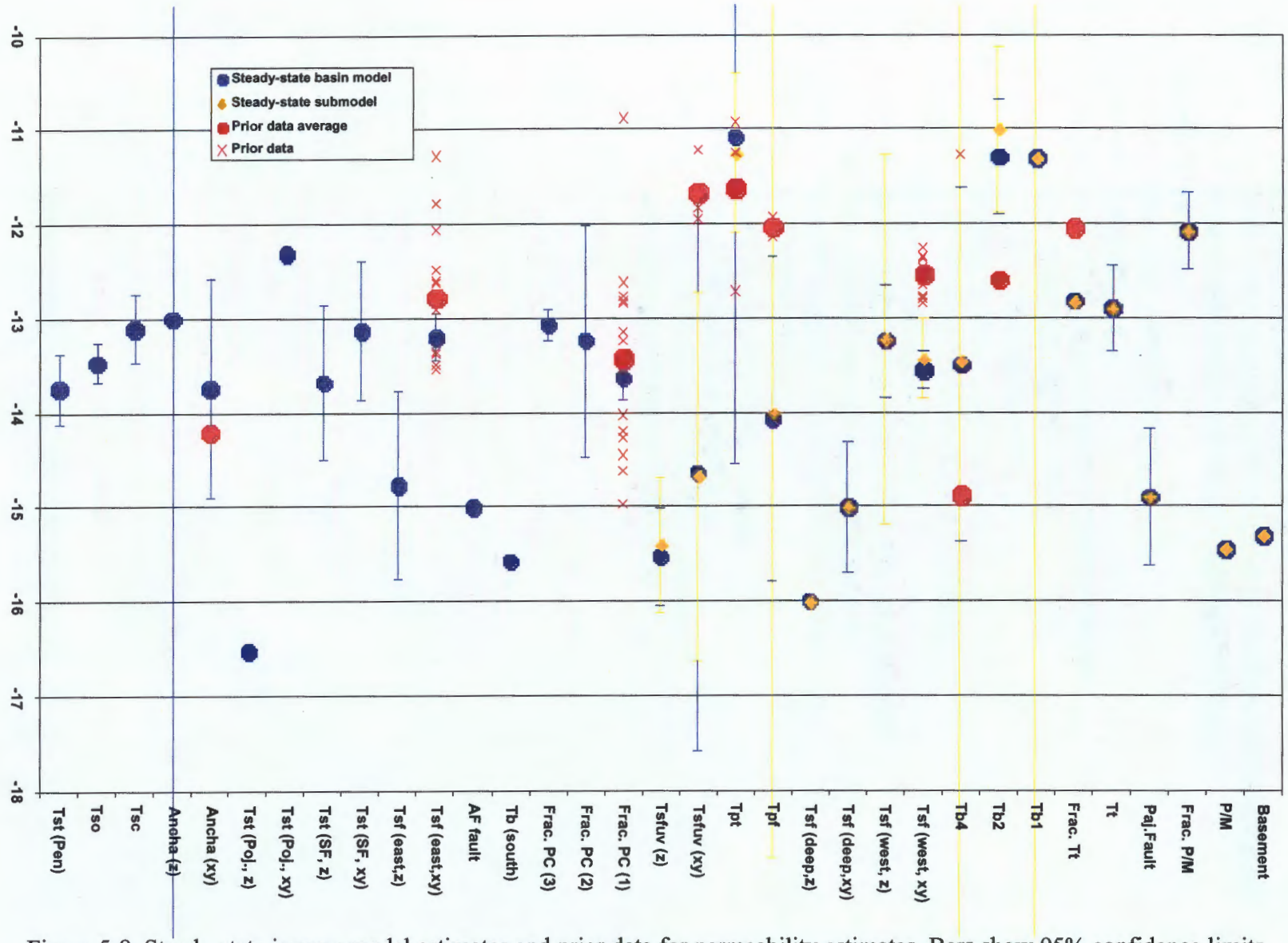

Figure 5-8. Steady-state inverse model estimates and prior data for permeability estimates. Bars show 95% confidence limits.

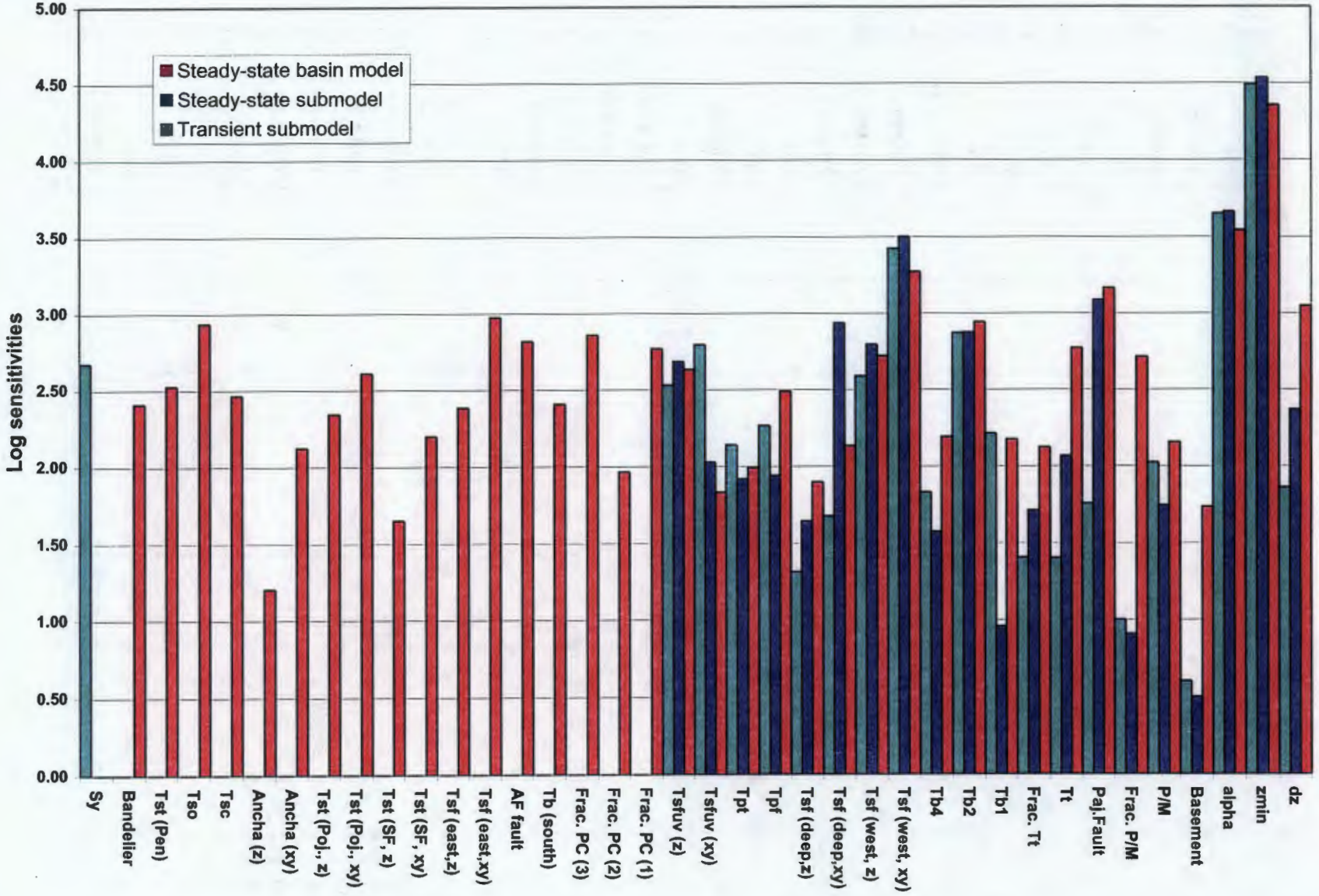

Figure 5-9. Log sensitivities of model parameters to simulated observations for different inverse models.

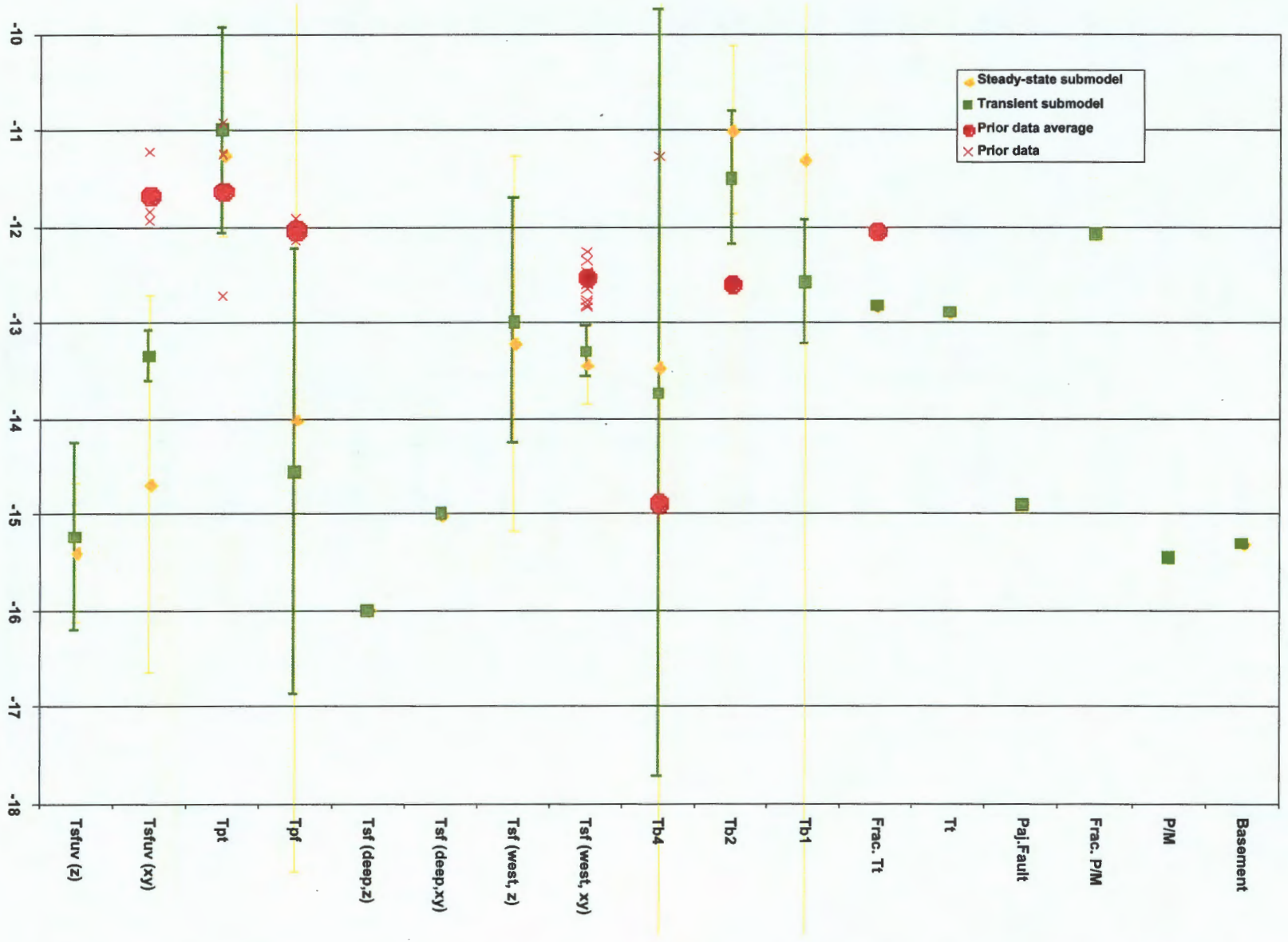

Figure 5-12. Inverse submodel estimates and prior data for permeability estimates. Bars show 95% confidence limits.

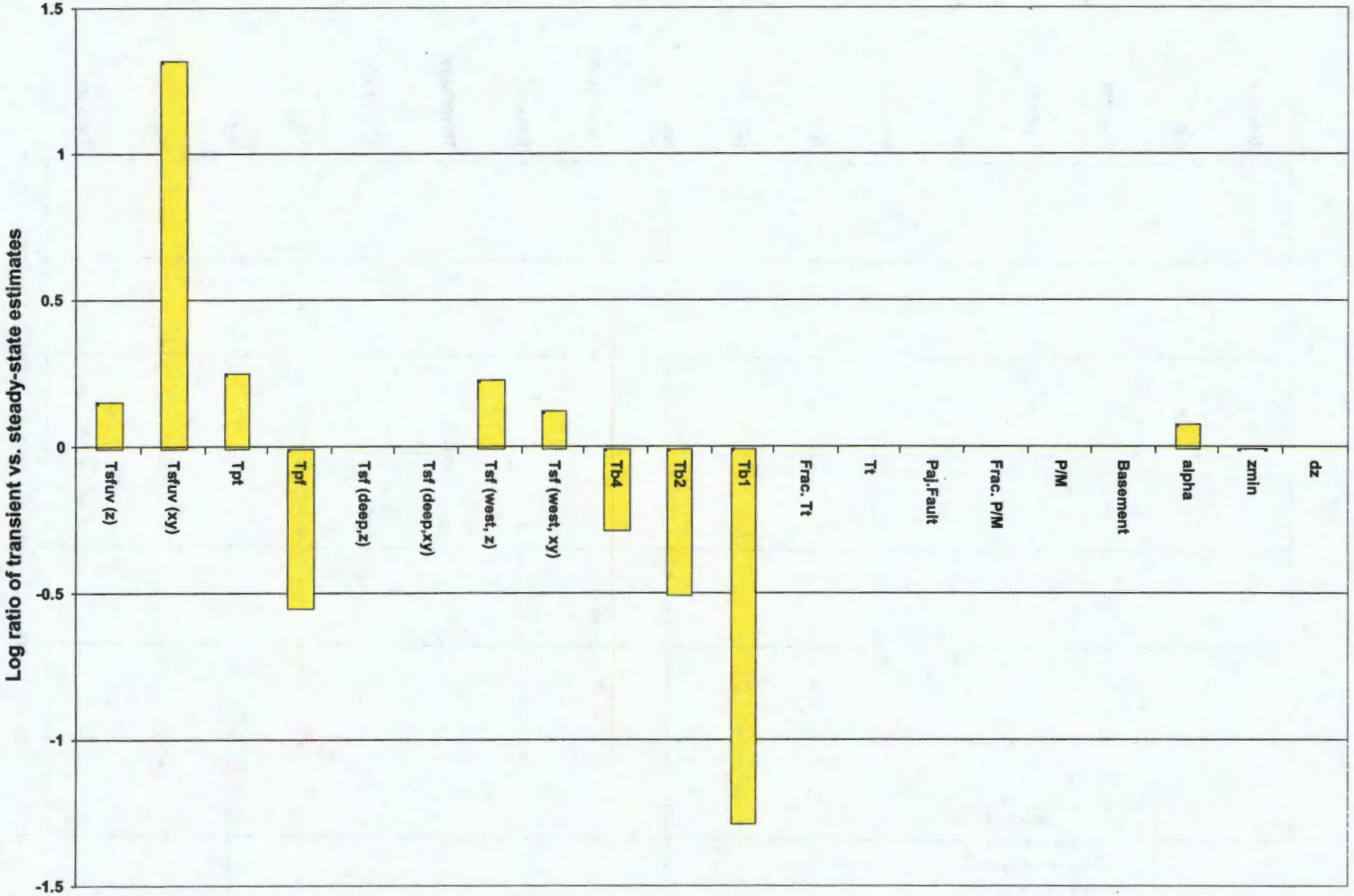

Figure 5-17. Relative change in submodel parameters obtained by transient and stead-state analysis.

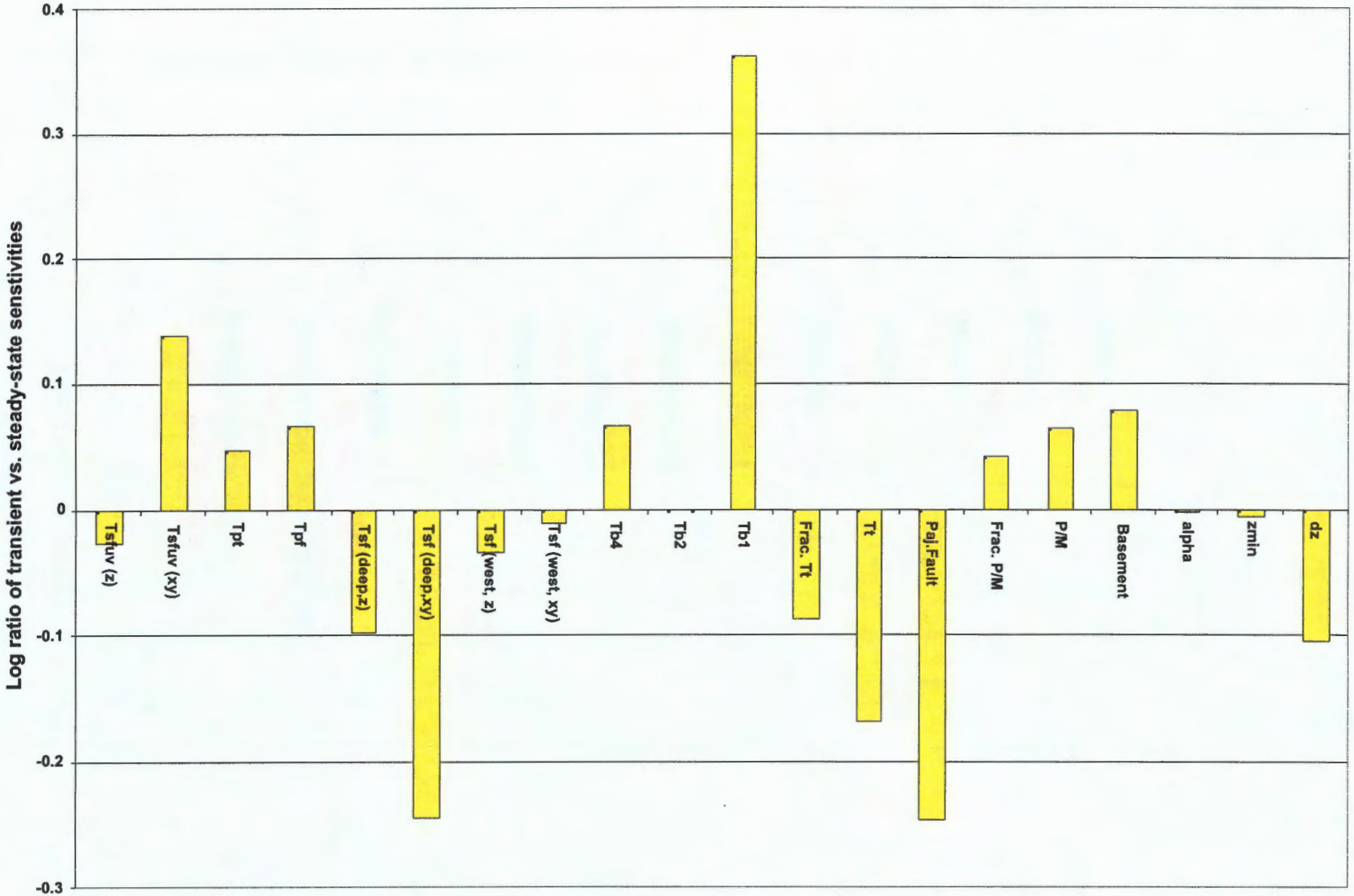

Figure 5-18. Relative change in submodel parameter sensitivity obtained by transient and stead-state analysis.

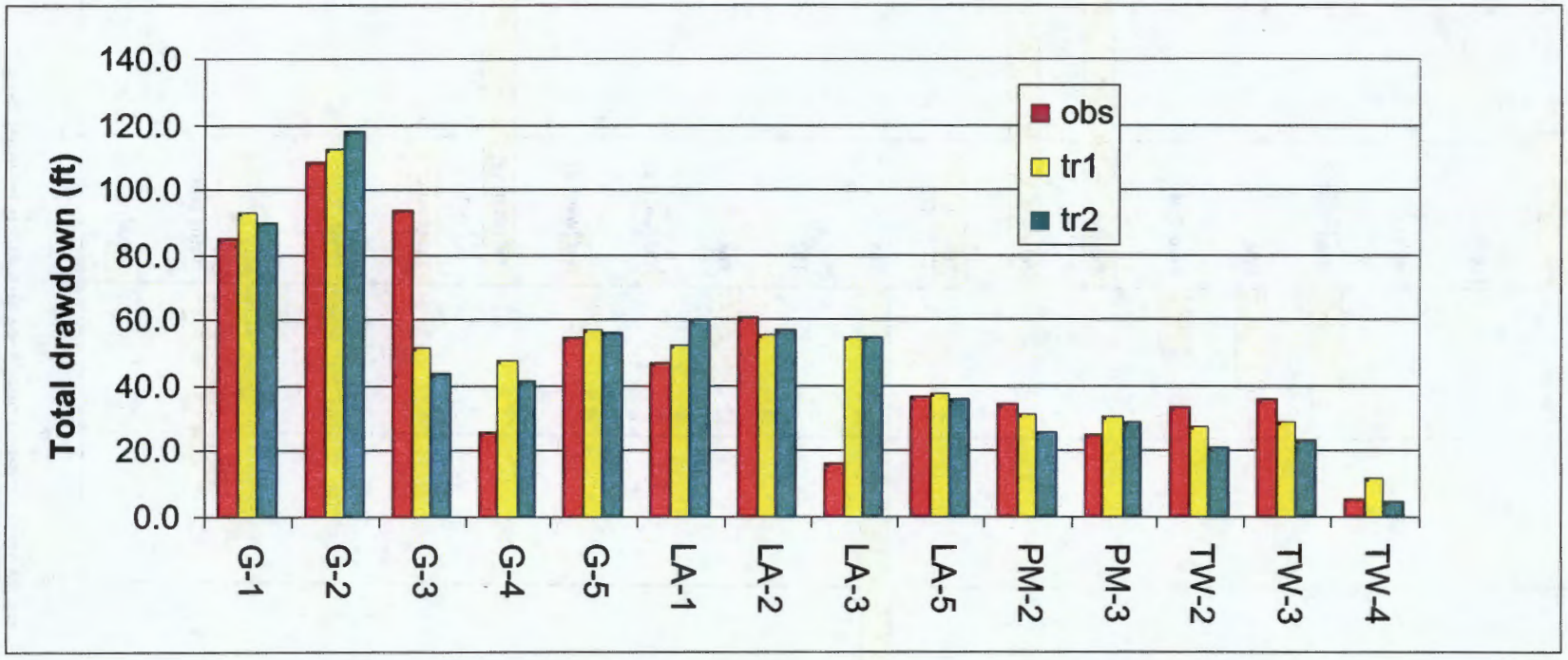

Figure 5-19. Comparison of observed and simulated drawdowns.

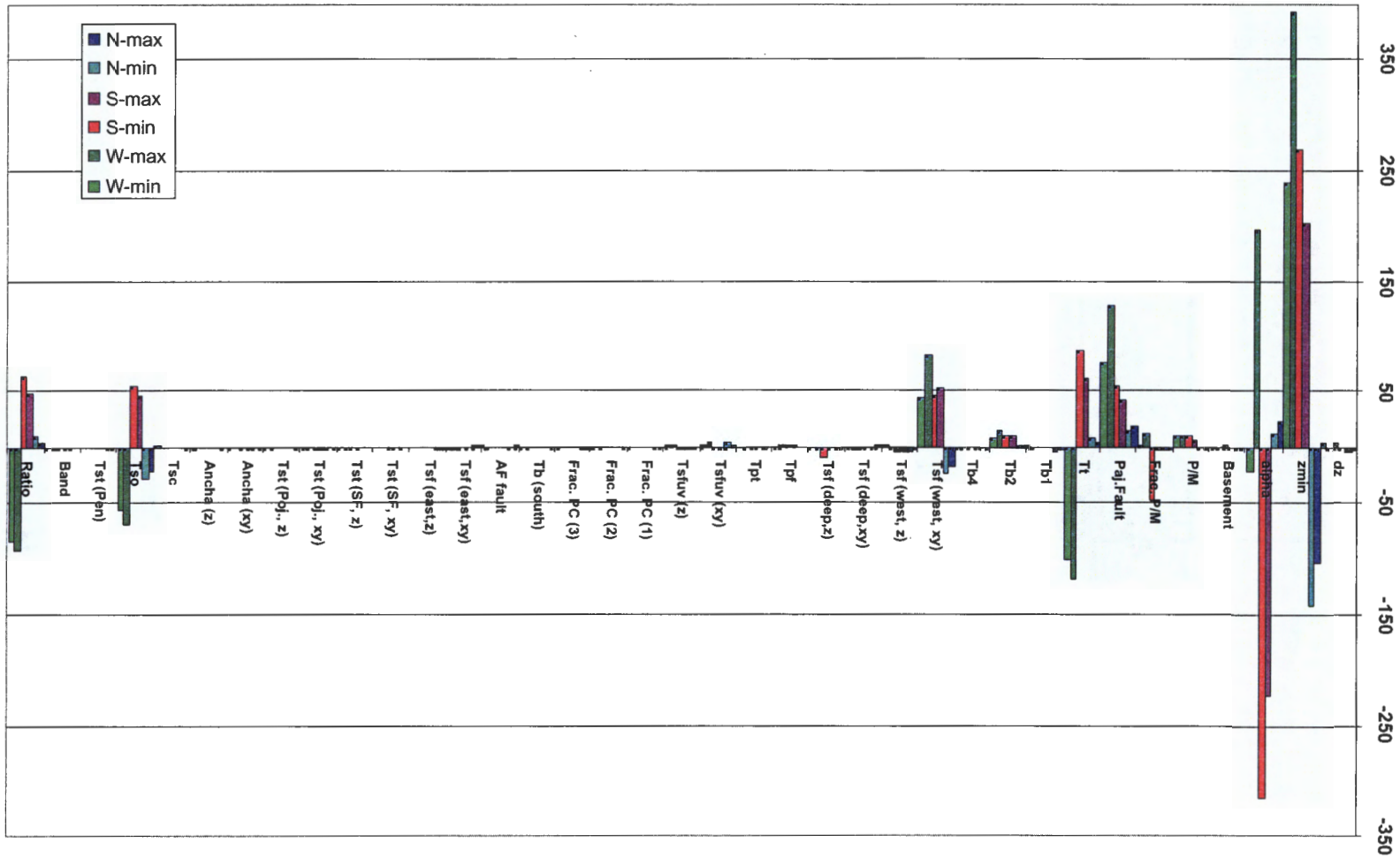

Figure 5-22. Sensitivity of predicted fluxes along submodel boundaries to model parameters.

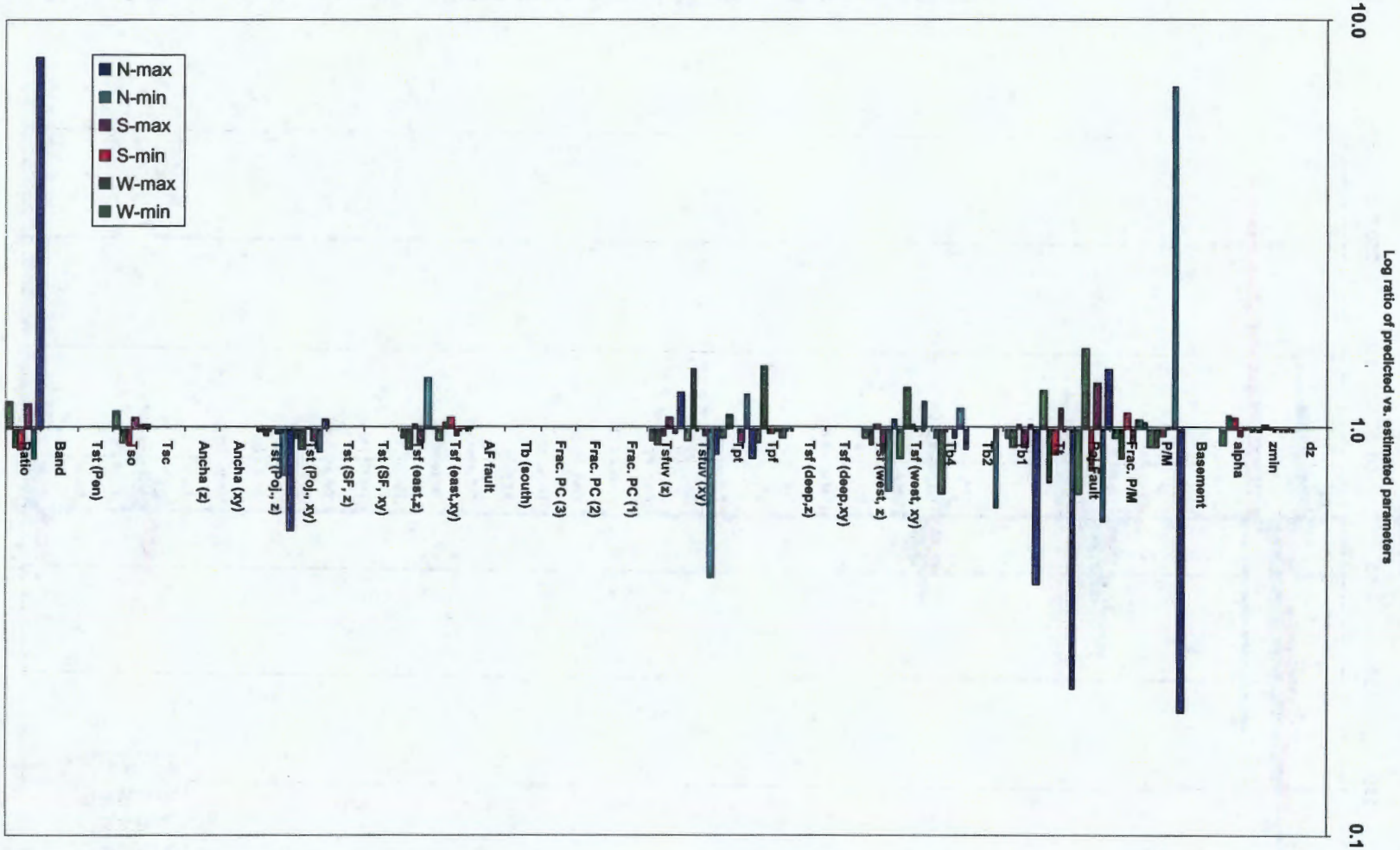

Figure 5-23. Relative change in model parameters obtained by prediction of maximal/minimal fluxes along the submodel boundaries.

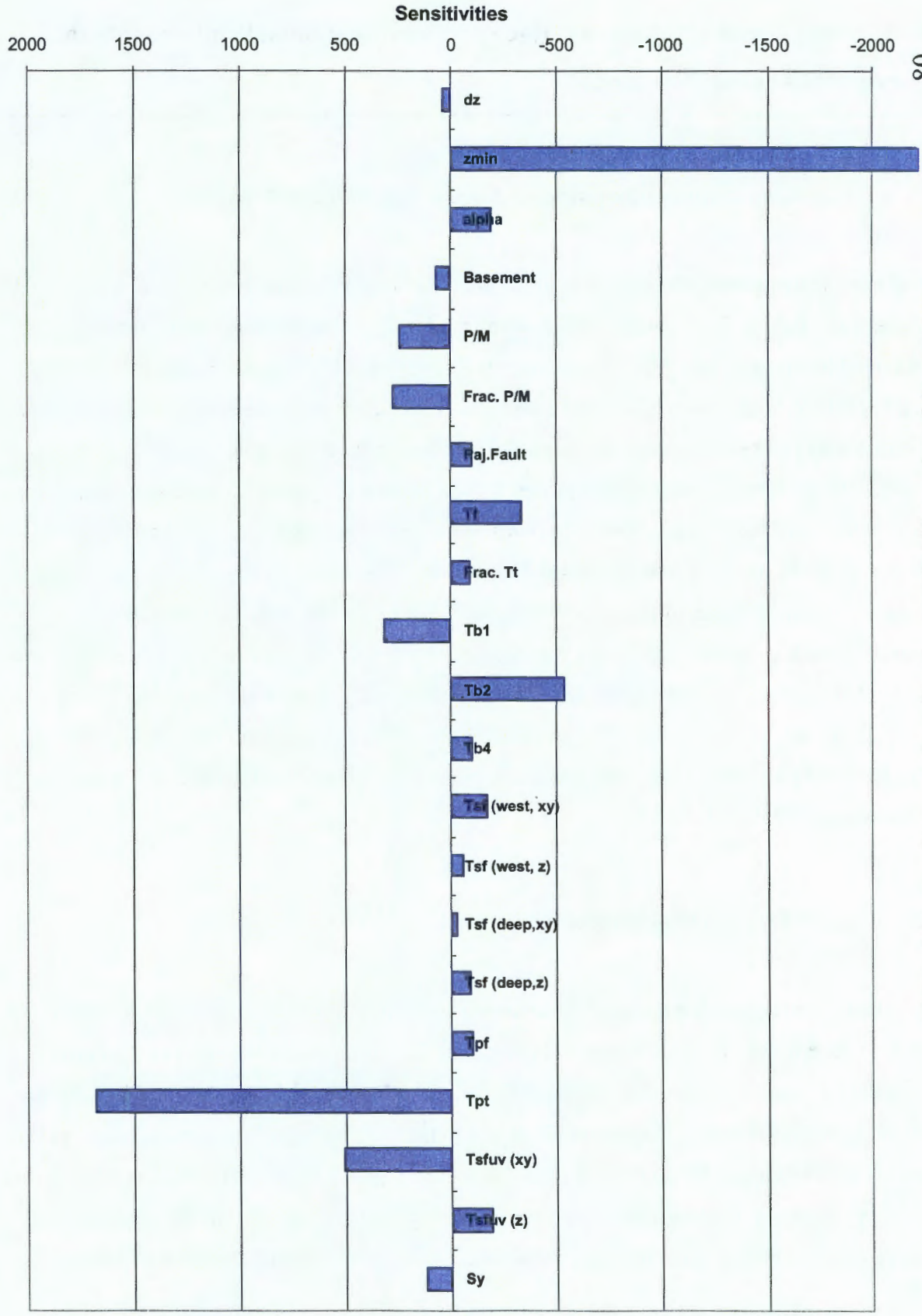

Figure 5-24. Sensitivity of flow direction near TA16 to submodel parameters.

6. Using chemistry data to refine the conceptual model and validate the regional aquifer flow model

6.1. Hydrologic conceptual models for the Los Alamos Area

From the hydrologic data discussed in the previous chapters, a conceptual model for regional groundwater flow in the Espanola Basin has emerged in which groundwater predominantly recharged in relatively wet, high-elevation areas flows toward low-elevation areas, discharging to the Rio Grande and lower reaches of many of its tributaries. Measurements indicating artesian conditions and increases in hydraulic head with depth near the Rio Grande have helped to confirm this picture of regional groundwater flow. Although the general picture of ground-water flow in the Los Alamos area seems to be consistent with this regional conceptual model and has been established for some time (Griggs and Hem 1964); (Cushman 1965), important questions remain concerning details of regional groundwater flow in the Los Alamos Area. These questions relate to (a) the sources of groundwater, (b) groundwater flow rates and directions, and (c) groundwater mixing and dilution in the Los Alamos area. As discussed in the following sections, reliable quantification of the sustainable groundwater supply and of the risk posed by past laboratory activities to groundwater quality in the Los Alamos area depend on a better understanding of these issues.

6.1.1. Sources of Groundwater

The general conceptual model of groundwater water flow in the vicinity of Los Alamos is shown schematically in cross-section in Figure 6-1. The groundwater beneath Los Alamos National Laboratory is potentially composed of water recharged (1) in the Valle Caldera, (2) the Sierra de los Valle, and (3) locally, on the Pajarito Plateau. Although the hydraulic heads, as far as they are known, permit the flow of groundwater recharged in the Valle Caldera and the Sierra de los Valle toward the laboratory, the presence of ring fractures surrounding the caldera and of the Pajarito Fault west of the laboratory have been postulated to restrict flow to the Pajarito

Plateau from the west, based on the absence of elevated temperatures and high trace- element concentrations characteristic of caldera geothermal waters in groundwater east of the caldera (Vuataz et al., 1986, p. 1836, Fig. 2). The hydraulic characteristics of these faults have not been measured, however.

Understanding the relative contributions of the three potential source areas to groundwater beneath the Pajarito Plateau is important for developing estimates of the sustainable groundwater supply for the Los Alamos area: if the faults significantly impede groundwater flow from west of the plateau, the groundwater supply is sustained only by local recharge. Conversely, if the faults are not significant barriers to flow, a potentially much larger catchment area and recharge volume sustains the groundwater supply.

It is clear from Figure 6-1 that a well drilled on the Pajarito Plateau could sample water from one recharge area or another, or possibly water from several recharge areas. The relative amounts of water contributed to a water sample from each recharge area would depend on the depth and length of the sampling interval in the well and on the relative thicknesses of the- flow tubes originating from the different recharge areas. These thicknesses would depend on the relative magnitude of the flow from each of the three potential recharge areas, and hence, on the unknown characteristics of the faults; any permeability variations of the rock intersected by the well would also be expected to influence the relative contributions to the water sample from the three potential source areas.

6.1.2. Flow Rates and Directions

The pre-development potentiometric surface indicates that, in the absence of structures or hydrogeologic units having permeabilities with preferred north-south anisotropy, groundwater flow beneath the Pajarito Plateau should be predominantly eastward toward the Rio Grande. It has also been suggested that the informally designated Chaquehui Formation, a north-south trending unit composed of relatively coarse-grained material deposited in channels incised into the top of the Santa Fe Group sediments by the ancestral Rio Grande, might impart a southerly component to groundwater flow beneath the Pajarito Plateau. However, water levels in wells penetrating the Chaquehui do not indicate a southerly component in the hydraulic gradient.

The flow rates or fluxes of groundwater beneath the Pajarito Plateau depend on the same factors that influence the sources of water beneath the plateau, namely, the magnitude of recharge in the potential source areas and the unknown hydraulic properties of the faults that could potentially impede groundwater flow beneath the plateau from the west.

Linear groundwater velocities depend on the groundwater flux and on the effective porosity of the aquifer. Although the hydraulic characteristics of the basalts near Los Alamos are not well known, based on extensive data from other areas such as the Idaho National Engineering Laboratory (INEL) (e.g. (Magnuson and Sondrup 1998)), it is expected that the basalts would have relatively high permeability and low effective porosity compared to the sedimentary deposits in the Los Alamos area. Thus, linear groundwater velocities are expected to be relatively high in the basalts. Additionally, studies at the INEL (e.g. (Newman 1996)) have determined that sedimentary interbeds similar in composition to the sediments of the Santa Fe Group have a much greater tendency than the basalts to sorb radionuclides such as strontium-90 and plutonium that have been detected in Los Alamos area groundwater. This suggests that transport of radionuclides in the regional aquifer near Los Alamos would be facilitated if these radionuclides reached the aquifer and flowed through the basalts.

6.1.3. Groundwater mixing and dilution

The total flux of groundwater beneath the plateau as well as the relative contributions from the three potential source areas to the groundwater also influence the fate and transport of any contaminants that might have been introduced into the groundwater from past laboratory activities. In general terms, if the flow from west of the plateau is large compared to local recharge, any potentially contaminated recharge on the Pajarito Plateau would tend to remain relatively shallow in the aquifer. In addition, flow from the west would have a relatively large potential to dilute any contamination at discharge locations, such as springs in White Rock Canyon, where the groundwater is likely to become mixed. Conversely, if groundwater beneath the Pajarito Plateau originates predominantly from infiltration on the Pajarito Plateau, any

potentially contaminated water would be transported relatively deep into the regional aquifer and the potential for dilution at the regional discharge zones would be less.

6.2. *Overview of Hydrochemical and Isotopic Data for the Los Alamos Area*

In this section, the existing groundwater hydrochemical and isotopic for the Los Alamos area are presented. Briefly, the data considered in this report are (a) delta oxygen-18 ($\delta^{18}O$), (b) carbon-14 (^{14}C), (c) chloride, and (d) tritium (^{3}H). As discussed in their respective sections, each species potentially contributes information regarding the source, timing and magnitude of recharge, rock/water interaction, flow velocities and directions, or the extent of groundwater mixing. Collectively, these data can help distinguish between competing hypotheses concerning the flow system when hydraulic data alone are ambiguous.

The chemical and isotopic data used in the analyses that follow are listed in Table 6-1. The sampling locations are shown in Figure 6-2. The symbols associated with each area and sample type (well versus spring) in Figure 6-2 are used in later scatterplots to illustrate the differences and similarities in chemical and isotopic characteristics among the different areas.

6.2.1. delta deuterium and delta oxygen-18

The concentrations of the heavy isotopes of hydrogen and oxygen are expressed using the delta (δ) notation:

$$\delta M = [(R_{sample}/R_{standard}) - 1] \times 1000 \text{ permil} \qquad (6\text{-}1)$$

where R_{sample} and $R_{standard}$ are the ratios of the heavier isotope to the more common isotope ($^{18}O/^{16}O$ or $^{2}H/H$) in the sample and reference standard, respectively, and M is either ^{18}O or ^{2}H. The difference in the isotopic ratios in the sample and standard relative to the ratio in the standard is expressed in parts per thousand (permil) difference from the standard, which for ^{18}O and ^{2}H is Vienna Standard Mean Ocean Water (VSMOW).

One of the primary factors affecting the isotopic composition of precipitation is condensation temperature, which is a function of season, elevation and climate. The evidence for elevational trends in isotopic composition of precipitation in the Jemez Mountains and the Española Basin has been discussed in Vautaz et al. (1986) and in Keating and Goff (unpublished report)(1999). Although spring data reported by Vautaz et al. (1986) for the Jemez Mountains imply a strong elevation dependence, precipitation data is more equivocal. Nevertheless, there does appear to be at least a weak correlation between isotope composition and elevation of precipitation within the basin. From the precipitation data, the relation between $\delta^{18}O$ and ground-surface elevation is:

$$\delta^{18}O = -2.99 - 1.043 \times 10^{-3} z_{ft} \qquad (6\text{-}2)$$

where z_{ft} is ground surface elevation, in feet.

Data for $\delta^{2}H$ and $\delta^{18}O$ from springs and wells in the Los Alamos area from Blake et al. (1995) are shown in Figure 6-3 along with the global meteoric water line ($\delta^{2}H = 8\ \delta^{18}O + 10$) (Craig, 1961) and the local meteoric water line for the Jemez Mountains ($\delta^{2}H = 8\ \delta^{18}O + 12$) (Vautez et al., 1986). Most of the data plot close to the global and local meteoric water lines; however, some of the data with heavier isotopic ratios plot to the right of these lines, possibly indicating some effects of evaporation.

Calculated recharge elevations for groundwaters, based on measured isotopic ratios, have been presented in Blake et al. (1995) and in Keating et al. (1999). Isotopic ratios for springs discharging near the Rio Grande area are very similar to groundwater at most wells and springs on the Pajarito Plateau, indicating a similar recharge elevation for groundwater in both areas. Groundwater at a smaller number of wells on the Pajarito Plateau has somewhat lighter $\delta^{2}H$ and $\delta^{18}O$ values that are similar to those found for springs emanating from the eastern slope of the Sierra de los Valles. Isotopic ratios of groundwater from wells east of the Rio Grande have a broad range that encompasses the isotopic ratios of water from other areas. The lightest isotopic values are generally found in wells east of the Rio Grande although groundwater at one well on the Pajarito Plateau also has very light isotopic values.

Based on the factors known to influence the isotopic composition of precipitation and recharge outlined earlier in this section, and on the site-specific relation between isotopic ratios

and elevation given by Equation (6-2), it can be concluded that groundwater at many springs and wells on the Pajarito Plateau and at springs near the Rio Grande contains a component of recharge from precipitation that fell at ground-surface elevations lower than those of the precipitation which recharged the springs on the Sierra del los Valles.

A second observation that can be made, based on Figure 3 and Figure 6 of Keating and Goff (1999), is that the isotopically lightest groundwater found in the Los Alamos area has values that are outside the range of isotopic ratios measured in present-day precipitation, including measurements made at stations high in the Sangre de Cristos. This observation indicates that factors other than elevation have affected the isotopic ratios of the isotopically lightest groundwater. A number of studies worldwide in arid regions have concluded that groundwater that is isotopically much lighter than present-day precipitation is "fossil" groundwater that originated during wetter conditions that prevailed during the Pleistocene. Anderholm (1994) originally proposed a Pleistocene origin for the isotopically light groundwater near the Rio Grande. This interpretation is supported by ^{14}C activities for some of these isotopically light groundwater samples that indicate uncorrected ^{14}C ages of 18,000 to 45,000 years (Rogers et al. 1995). These measurements are discussed in more detail in a later section.

The isotopically heaviest groundwater found in the Wells East of the Rio Grande group of samples has δ^2H values between –80 and –75 permil, values which are similar to the δ^2H of groundwater upgradient from these wells in the Pojoaque area (Anderholm, 1994, plate 2). The isotopically heaviest groundwater in both groups of samples plots below the local meteoric water lines, indicating the water in these areas may have been partly evaporated. Based on numerical modeling by Hearne (1985), shallow groundwater in the Pojoaque area is estimated to undergo a large amount of evapotranspiration because of its proximity to land surface (Anderholm, 1994, p. 34).

The variation of $\delta^{18}O$ for springs and groundwater in the Los Alamos area are shown in map view in Figure 6-4. In map view, the isotopic ratios in a downgradient direction are variable, with (1) predominantly light isotopic ratios in the high-elevation springs in the Valle Caldera and Sierra de los Valle, (2) somewhat heavier isotopic values in springs on the Pajarito Plateau and west of the Rio Grande, and in most wells on the Pajarito Plateau, and (3) isotopically values in some Pajarito Plateau wells close to the Rio Grande that are comparably light to the values of the springs west of the Plateau. These variations are consistent with a

conceptual model of flow in which groundwater recharged at high elevations west of the Pajarito Plateau is supplemented by lower elevation recharge on the Plateau. The lower elevation recharge constitutes most of the discharge of the springs west of the Rio Grande, whereas the higher elevation recharge is tapped by deep wells as it flows toward the Rio Grande.

6.2.2. Carbon-14

The isotopes carbon-13 (^{13}C) and carbon-14 (^{14}C) are useful for identifying the sources of carbon in groundwater and for estimating groundwater age, respectively. A knowledge of the sources of carbon in groundwater is helpful in correcting groundwater ^{14}C ages for water/rock interactions, such as calcite dissolution, in which the groundwater incorporates carbon that is depleted in ^{14}C compared to the water itself. Measurements of groundwater $\delta^{13}C$ and ^{14}C typically reflect the isotopic composition of the dissolved inorganic carbon (DIC), which is composed of $CO_{2(aq)}$, HCO_3^-, and CO_3^{2-}. HCO_3^- is the dominant inorganic carbon species between pH values of 6.4 and 10.3, with $CO_{2(aq)}$ and CO_3^{2-} the dominant species at lower and higher pH values, respectively.

Carbon-14 activities of groundwater can be used to estimate the length of time the groundwater has been isolated from the atmosphere, where ^{14}C is produced by the neutron bombardment of nitrogen and release of a proton. The ^{14}C is subsequently oxidized to $^{14}CO_{2(g)}$, incorporated into plant and animal tissue, and respired by plants in the soil zone. Once isolated from the atmosphere, ^{14}C activities decrease by radioactive decay.

The ^{14}C age (or "residence time") of groundwater can be calculated as:

$$\text{Age} = (t_{1/2}/\ln 2) \times \ln(^{14}A_o/^{14}A) \qquad (6\text{-}3)$$

where $t_{1/2}$ is the half-life of ^{14}C (5,730 years), $^{14}A_o$ is the initial ^{14}C activity of the groundwater sample prior to radioactive decay, and ^{14}A is the ^{14}C activity of the water sample. If no dilution of the ^{14}C of the water sample has taken place because of calcite dissolution, $^{14}A_o$ is taken as 100 percent modern carbon (pmc), which is set as the ^{14}C activity of the atmosphere ($^{14}A_{atm}$) in 1895, prior to substantial dilution of atmospheric ^{14}C caused by the combustion of fossil fuels.

Although evidence from tree rings and marine corals indicates that the ^{14}C activity of the atmosphere has been up to 40% higher at times during the last 30,000 years ((Clark and Fritz 1997), Fig. 8-4), it is generally assumed in groundwater studies that atmospheric ^{14}C activities have remained constant. If evidence indicates that ^{14}C dilution by carbonate minerals (or old $CO_{2\,(g)}$ in thick unsaturated zones) has occurred, $^{14}A_o$ is set to a value less than 100 pmc that reflects the magnitude of that dilution. A number of techniques are available to correct the ^{14}C ages of groundwater for these effects. Most of these techniques make use of the $\delta^{13}C$ of soil gas and carbonate minerals, element mass-balance techniques, or a combination of these approaches, to estimated the amount of mineral carbon in the water sample (Clark and Fritz, 1997, chapter 8).

Carbon-14 data for the Los Alamos area have been published by Rogers et al. (1995), along with calculated minimum and maximum groundwater ^{14}C ages. Maximum ages were calculated using the radioactive decay equation and assuming that no isotopic dilution of the groundwater ^{14}C activity from calcite dissolution had occurred. Minimum ages were calculated by assuming that dilution of groundwater ^{14}C by calcite dissolution had occurred and that the amount of dilution could be estimated from the $\delta^{13}C$ of the water samples.

In appendix D of this report, evidence is presented regarding the need to correct groundwater ^{14}C ages in the Los Alamos area, and the published groundwater ^{14}C ages are re-interpreted in light of this evidence. An areal plot of these $\delta^{13}C$-corrected ^{14}C ages (Fig. 6-5) shows that they are generally two to three thousand years older than the minimum groundwater ^{14}C ages shown in Rogers et al. (1995, Fig. 7), but otherwise, the two maps of groundwater ^{14}C age are very similar. In both maps, groundwater age increases rapidly toward the Rio Grande. This increase in age is possibly the result of the upward flow of groundwater with deep, long flowpaths from the Sierra de los Valle area, or areas further west, toward discharge locations near the Rio Grande (Fig. 6-1).

6.2.3. Tritium

Tritium (^3H) is produced naturally in the atmosphere as a result of the bombardment of nitrogen by neutrons in cosmic radiation. As a result of the continuous natural production of ^3H in the atmosphere and its removal from the atmosphere by precipitation, by diffusion into surface

water, and by decay, a steady-state concentration of 6 to 10 tritium units (1 tritium unit or TU = 1 ^3H atom in 10^{18} hydrogen atoms) existed in the atmosphere prior to atmospheric nuclear weapons tests, depending on latitude. High neutron fluxes associated with atmospheric testing of nuclear weapons in the 1950's and early 1960's resulted in large increases in atmospheric concentrations of ^3H. The peak concentration of ^3H in precipitation measured in the spring of 1963 at Ottawa, Canada, exceeded 6000 TU (Clark and Fritz, 1997, p. 174-178). High concentrations of ^3H are also associated with steam and water releases from nuclear power plants, creating regions of elevated ^3H concentrations in the atmosphere near these facilities.

In the Los Alamos area, naturally occurring background levels of ^3H prior to weapons testing were estimated to average about 6 TU (Blake et al. 1995). Following atmospheric nuclear weapons testing, the mean annual value of ^3H in New Mexico precipitation was as high as 2800 TU in 1963 (Vuataz et al. 1984). Since atmospheric testing of nuclear weapons was halted after the Nuclear Test Ban Treaty in 1963, concentrations of ^3H in precipitation in the northern New Mexico have decreased to about 10 TU (Blake et al, 1995, p. 32).

Tritium has a half life of 12.43 years. Most groundwater ^3H data in the Los Alamos area were collected between 1990 and 1993 (Rogers et al., 1995, Table 2; Blake et al., 1995, Table 4). Because of radioactive decay, groundwater with a ^3H concentration of 6 TU that was recharged prior to 1950 would have had a concentration less than 0.6 TU by the early 1990's. Therefore, groundwater with a ^3H concentration greater than 0.6 TU has likely been mixed with water that was recharged since 1950. Similarly, groundwater recharged in 1963 with a ^3H concentration of 2800 TU would have had a ^3H concentration of about 550 TU by the early 1990's. Thus, groundwater with a ^3H concentration higher than about 550 TU most likely has been contaminated by ^3H from local Laboratory activities. The presence of many local sources of ^3H in the Los Alamos area make it difficult to determine from the ^3H concentration alone whether ^3H concentrations above 0.6 TU (but below 550 TU) are indicative of local contamination or a result of the globally elevated atmospheric concentrations of ^3H existing since 1950. However, in either case, groundwater ^3H concentrations greater than about 0.6 TU indicate a component of recent or "post-bomb" recharge in the groundwater. These calculations assume that recent recharge has not mixed with older water in the aquifer, either as a result of hydrodynamic mixing or mixing in the wellbore during sampling. Groundwater containing some post-1950 recharge

could have a ^3H concentration less than 0.6 TU, depending on the extent of dilution of the recharge by older groundwater in the aquifer.

Tritium data for the Los Alamos area were summarized by Blake et al. (1995) and by Rogers et al. (1995). Rogers et al. (1995) reported that the detection limit for trace-level ^3H measurements is about 1 pCi/kg H_2O or about 0.3 TU (1 TU=3.2 pCi/kg H_2O). Because the actual ^3H concentrations of groundwater with reported ^3H concentrations less than 0.3 TU are statistically not different from zero, these data are not discussed further in this summary.

Elevated ^3H concentrations have been reported in alluvial groundwater and in springs that discharge from perched systems. Tritium concentrations of several tens to thousands of tritium units were measured in perched-water zones at Test Wells 1A and 2A in Pueblo Canyon, LADP-3 and Basalt Spring in Los Alamos Canyon, DP spring in DP Canyon. The perched-water ^3H concentrations at wells TW-2A, LADP-3, and DP spring are substantially in excess of 550 TU (Rogers et al., 1995, Table 2). Rogers et al. (1995, p. 411) suggested that most of the high ^3H concentrations could be attributed to known ^3H sources associated with past or present Laboratory activities. Well LADP-3 is downgradient from the Omega reactor, which is known to have been leaking tritiated cooling water. The interpretation that Laboratory sources of ^3H are responsible for the high ^3H concentrations is, in some cases, supported the presence of other environmental indicators such as sulfate, nitrate, phosphate, chlorate, and lead at concentrations indicative of anthropogenic inputs. Water samples from Basalt Spring and Test Wells 1, 1A, and 2A each had concentrations above background for one or more of these constituents (Blake et al., 1995, Figs. 6-10, Table 3).

Concentrations of tens to hundreds of tritium units, clearly indicative of recent recharge, are also present in the regional aquifer at (1) Test Well 1 (TW-1) in Pueblo Canyon near the confluence with Los Alamos Canyon, (2) Test Well 3 in Los Alamos Canyon, (3) former observation and water supply wells LA-1A and LA-2 (4 TU), located in Los Alamos Canyon near the Rio Grande, and (4) Test Well 8 in Mortandad Canyon (Rogers et al., 1995, p. 411). Trace-level ^3H concentrations between 0.5 and 1 TU were present in groundwater at wells DT-9 and DT-10, located on a mesa between Water and Ancho Canyons (Rogers et al., 1995, Table 2) and at the Guaje 6 (G-6) well in Rendija Canyon (Blake et al., 1995, Table 4). In some cases, an obvious upgradient local source of ^3H was present that likely contributed to the high ^3H concentrations in the groundwater (Rogers et al., 1995, p. 411). Discharge from the radioactive

liquid waste treatment plant about a mile upstream from TW-8 in Mortandad Canyon is a likely source for the high ^{3}H concentrations in groundwater at this well. Springs in White Rock Canyon have ^{3}H concentrations ranging from 0.01 TU at Spring 6a to 5.47 TU at Doe Spring (Blake et al., 1995, Table 4). Springs from the White Rock Canyon area with ^{3}H concentrations of about 0.6 TU or greater include Springs 2, 3, 4a, 6, 7, 8, 8b, 9a and Ancho and Doe Springs. For some of these springs, ^{3}H concentrations greater than 0.6 may be indicating that the water that recharged these springs is less than 50 years old. However, springs 6, 7, 8, 8b, and 9a and Ancho and Doe Springs are downgradient from TA-33, where ^{3}H concentrations in an effluent drain were measured in excess of 1500 TU (Blake et al., 1995, Table 4.) Therefore, it is possible that the slightly elevated ^{3}H concentrations at these springs resulted from the mixing of a small amount of highly tritiated recharge with older, ^{3}H-free groundwater, despite the absence of other evidence for LANL-related contamination (e.g. nitrate, chlorate, etc) at these springs (Blake et al., 1995, Figs. 6 to 10).

Springs and surface water upgradient from LANL in the Valle Caldera and Sierra de los Valle generally have ^{3}H concentrations well above the detection limit of 0.3 TU (Blake et al., 1995, Table 4) indicating that they are sustained by post-1950's precipitation. An interesting exception is Frijoles Spring #49, which is reported as ^{3}H-free.

Wells on the San Ildefonso Pueblo, which includes wells in the "Rio Grande Area Wells" and "Wells East of the Rio Grande" groups of this report, provide several groundwater samples in which ^{3}H concentrations are several to several tens of tritium units (Blake et al., 1995, Table 4). Many of the same wells having groundwater ^{3}H concentrations in this range also have high sulfate or nitrate concentrations which Blake et al. (1995, Figs. 6 and 7) attributed to fertilizer use and livestock grazing. Although a Laboratory source for the ^{3}H concentrations at some of these wells cannot be completely ruled out, the presence of these other constituents indicates that irrigation water may be presently recharging the regional aquifer in the San Idlefonso Pueblo area.

In summary, there are some locations in the regional aquifer beneath LANL where ^{3}H concentrations are much higher than would be expected for pre-1950's recharge. It is likely that the highest ^{3}H concentrations are associated with Laboratory releases of ^{3}H into the environment. Some intermediate groundwater ^{3}H concentrations may also be attributable to Laboratory sources, based on the presence of other indicators of anthropogenic impact. Low-level ^{3}H

concentrations in the regional aquifer above 0.6 TU that may or may not be associated with Laboratory activities are present in some wells beneath the Pajarito Plateau and in springs in White Rock Canyon. Collectively, the ^3H data demonstrate that recharge to the regional aquifer has taken place beneath the Pajarito Plateau in the last 50 or so years. Rogers et al. (1995, p. 411-412) suggested a conceptual model for ^3H transport wherein ^3H from known Laboratory sources seeped through alluvium in the canyon bottoms to intermediate perched zones and, finally, to the regional aquifer. A similar conceptual model for water transport in other canyons on the Plateau seems reasonable.

6.2.4. Chloride

Chloride concentrations in groundwater are primarily controlled by chloride concentrations in recharge, by rock-water interactions, and by geothermal processes. Concentrations in recharge, in turn, can be controlled by evapotranspiration and/or anthropogenic influences. In the absence of anthropogenic and geothermal effects, chloride concentrations in groundwater are generally related to the concentration of Cl^- in precipitation and the concentration increase that infiltrating water undergoes due to evapotranspiration in the root zone before the water reaches the water table to become recharge. The relation between precipitation rates (P), recharge rates (R) and Cl^- concentrations is expressed by the chloride mass-balance equation

$$(P)\ (C_p) = (R)\ (C_R) \qquad (6\text{-}4)$$

where C_P and C_R are the Cl^- concentrations in precipitation and recharge, respectively. The average Cl^- concentration of precipitation in the Santa Fe area between November, 1987 and March, 1989 was calculated to be 0.29 mg/L (Anderholm, 1994, p. 18). Equation (6-4) assumes that the only Cl^- arriving at the ground surface is the Cl^- contained in precipitation at that point. Thus, without further modifications, Equation (6-4) does not consider the Cl^- arriving at or leaving from a particular location because of surface runoff. Redistribution of chloride due to

surface runoff is expected to be a particularly significant process along arroyos and canyon bottoms.

In the Espanola Basin as a whole, anthropogenic influences on chloride in recharge include road salting and septic tank effluent in the Santa Fe area (Anderholm, 1994, p. 31) and agriculture in the San Ildefonso Pueblo area (Blake et al., 1995). Geothermal processes that affect chloride concentrations are evident in the Valles Caldera and Ojo Caliente areas (Goff and Grigsby. 1982; Vuataz et al. 1984). Because of the absence of chloride (Cl^-) bearing minerals in local aquifers, rock-water interactions are presumably negligible and thus Cl^- ions are expected to behave conservatively in groundwater in the basin.

Chloride concentrations of springs in the Valles Caldera and Sierra de los Valle are between about 2 and 14 mg/L (Fig. 6-6). Groundwater on the Pajarito Plateau generally has Cl^- less than 4 mg/L, although groundwater at a few wells and springs in the northeast corner of the LANL has Cl^- concentrations of several tens of milligrams per liter. Based on the high concentrations of trace elements typical of the geothermally heated water in the Valle Caldera, the high Cl^- concentration of groundwater from wells LA-1b and LA-6 have been attributed to the upwelling along faults of geothermally-heated water from deep Paleozoic rocks in the area (Goff and Sayer. 1980). However, this mechanism would not explain the high Cl^- concentrations of perched springs in the area. Springs in the Rio Grande Area of Cl^- have concentrations less than 4 mg/L in the south and between 4 and 8 mg/L further north along the Rio Grande. Groundwater in the Rio Grande Area Wells and Wells East of the Rio Grande has highly variable Cl^- concentrations, ranging from a few to several hundred milligrams per liter. Some of the higher Cl^- concentrations of groundwater in these groups may have been caused by the return flow of irrigation water or leakage of septic tank effluent, as indicated by the high nitrate concentration in some groundwater from these areas (Blake et al., 1995). A similar cause was invoked to explain some of the high Cl^- concentrations of upgradient groundwater in Pojoaque, where evapotranspiration of shallow groundwater might also have increased groundwater Cl^- concentrations (Anderholm, 1994, p. 34).

6.3. Summary and Conclusions

Tritium data from the Los Alamos area show that perched and regional groundwater with tritium concentrations indicative of local sources for the tritium (> 550 TU) exist in the lower reaches of Los Alamos, Pueblo, and Mortandad Canyons. Facilities that produced or used tritium presently exist or formally existed upstream from these areas in the same canyons. Elsewhere, groundwater from perched and regional aquifers having moderately high (< 550 TU) tritium concentrations are associated with nitrate, chlorate and other chemicals that have anthropogenic sources, indicating that Laboratory activities may have been a cause of these elevated tritium concentrations as well. Tritium concentrations are greater than 0.6 TU in low elevation springs near the Rio Grande and in some wells that tap the regional aquifer, indicate that these spring and well waters either contain a small amount of highly tritiated water discharged from laboratory sources or recharged naturally when atmospheric concentrations of tritium were high, or else that these waters are composed water that was dominantly recharged since 1950. The tritium data indicate that recharge along canyon bottoms on the Pajarito Plateau is likely pathway for chemicals associated with Laboratory activities to enter the regional aquifer. Conversely, chloride and stable isotope studies of pore water in the unsaturated zone beneath the mesa tops have indicated low or negligible recharge in these settings (Newman 1996). Therefore, numerical models of the regional aquifer system should include focused recharge along those canyons where stream-gage measurements indicate substantial stream-channel losses or where tritium data demonstrate the presence of recent recharge to the regional aquifer.

Groundwater carbon-14 data were corrected for isotopic dilution by calcite with an assumed $\delta^{13}C$ value of –4.6 permil, similar to the $\delta^{13}C$ value measured for fracture-filling calcite from the unsaturated-zone by Newman (1996). Contour plots of these corrected groundwater ^{14}C ages in plan view appear to show a rapid increase in groundwater age in a downgradient direction in the northeast part of the Laboratory, a trend that could be interpreted as indicating a decrease in groundwater velocity in this area. In this case, if groundwater flow is at steady-state, decreases in groundwater velocity could only be caused by substantial downgradient increases in porosity. More likely, the apparently abrupt rapid increase in groundwater age results from the upwelling of deeper, older groundwater toward the Rio Grande, the greater depth of the wells in this area, and the difficulty of portraying three-dimensional data in just two dimensions.

6.4. *Simulations of Hydrochemical and Isotopic Tracers with FEHM*

6.4.1. Introduction

The flow models described in previous sections were calibrated solely on the basis of hydraulic heads and estimates of groundwater discharge to rivers and streams in the Basin. As a way of evaluating the reasonableness of these models, as well as the generalized recharge model that serves as an important boundary condition, we simulated the transport of several naturally occurring isotopic and geochemical tracers, including ^{18}O, Cl^-, ^{14}C, and ^{3}H. The simulations approximated the steady-state distribution of each of these species at the basin scale. These tracers are particularly useful because they generally do not interact with the aquifer rocks and, therefore, retain the chemical signature of recharge water (in the case of ^{18}O and Cl^-) or, because of radioactive decay, provide some indication of groundwater age (^{14}C, and ^{3}H).

As described earlier, ^{18}O is part of the water in precipitation and naturally enters the groundwater system with recharge. At temperatures less than those associated with geothermal reservoirs, the $\_^{18}O$ of groundwater is generally not measurably affected by water/rock interaction, so it can be considered a conservative tracer once in the groundwater system. As discussed above, the $\_^{18}O$ of precipitation depends on ground-surface elevation, which varies between about 12,500 and 5,400 feet within the Basin. This pronounced topographic relief results in large measured contrasts in the $\_^{18}O$ of groundwater in the Basin, contrasts that potentially can be exploited to evaluate both the assumed elevation distribution of recharge used in the groundwater model and the simulated flow directions taken by the recharge once in the regional aquifer.

In non-geothermal areas and in those areas of the Espanola Basin not affected by human activities, groundwater Cl^- concentrations are assumed to reflect the degree to which infiltrating water in the soil zone becomes concentrated by evapotranspiration before reaching the water table to become recharge (see section "Major Ions"). The Cl^- concentrations in the recharge and precipitation and the precipitation and recharge rates are related through the chloride mass-balance equation. The Cl^- concentration of groundwater therefore indicates the magnitude of the

recharge where the groundwater entered the aquifer and, together with the _^{18}O, provides another check on the assumed distribution of recharge and on flow directions taken by that recharge.

The transport simulations of ^{14}C of provide an indication of the residence times of the groundwater in the regional aquifer as the groundwater moves from the recharge toward the discharge areas. A comparison between groundwater residence times estimated from simulations of ^{14}C transport and corrected groundwater ^{14}C ages based on measured ^{14}C activities provides a check on the simulated rates of groundwater movement, and indirectly, of recharge rates. Unlike the steady-state simulations of _^{18}O and Cl^- transport, however, the steady-state distribution of ^{14}C in the aquifer depends on the effective porosities of the hydrogeologic units encountered along each flow path. This sensitivity arises for ^{14}C transport because ^{14}C undergoes radioactive decay as it moves through the aquifer; the ^{14}C activity at a point in the aquifer thus depends on residence time of the groundwater, which, in turn, is a function of both the water in storage and the groundwater flow rates along the flowpath. Although the transport simulations for ^{14}C are more complex than the simulations of _^{18}O and Cl^- because additional parameters must be considered, the ^{14}C simulations also provide an opportunity to calibrate the porosity values of the aquifer materials, provided that enough confidence has already been gained in the recharge rates and flow directions from the simulations of the other environmental tracers.

Tritium transport was simulated because ^3H is an indicator of very young groundwater and its presence in the aquifer above its detection limit of 0.3 TU indicates that post-1950 recharge has reached the aquifer. In the aquifer beneath LANL, there are three possible sources of tritium in groundwater: atmospheric ^3H, either naturally occurring (6 TU in precipitation) or post-nuclear-weapons testing and local discharges of ^3H from past LANL operations. As a first step, we simulated the expected concentrations of naturally-occurring ^3H to determine if flow rates into and away from recharge areas in the model are realistic. The results of these simulations can be compared to ^3H data from local groundwater only in a qualitative way. For a more comprehensive study of ^3H, these simulations should be extended in the future to include anthropogenic sources of ^3H.

6.4.2. Boundary Conditions for Transport Simulations

Recharge (water table) boundary

A ^{14}C activity of 100 pmc and ^{3}H concentration of 6 TU were chosen to reflect the long-term values of ^{14}C and ^{3}H in precipitation that prevailed prior to the onset of nuclear-weapons testing in the 1950's. These values of ^{14}C and ^{3}H may be reasonable for recharge in many places in the Espanola Basin where the depth to water is small and unsaturated zone residence times are short, such as canyon bottom recharge. However, these values would not be appropriate for mesa top recharge on the Pajarito Plateau, where chemical evidence (e.g. (Newman 1996)) indicates unsaturated zone residences times on the order of several thousands of years. Therefore, our assumed water table boundary conditions are only valid if recharge through mesa tops is negligible compared to canyon bottom recharge.

The largest inflow water budget component of the basin model is diffuse recharge. Therefore, for conservative tracers (^{18}O and Cl^-) the hydrochemical and isotopic characteristics we specify for diffuse recharge will dominate the simulated hydrochemical and isotopic characteristics of the regional aquifer. The _^{18}O of the recharge at each node along the upper surface of the model domain was estimated using the regression equation from Keating and Goff (1999) and the ground-surface elevation at the node. In the Cl^- transport simulations, the Cl^- concentration of the recharge at each node along the upper surface of the model was estimated using the chloride mass-balance equation (Equ. 6-4), the precipitation and recharge rates assumed for the ground-surface elevation at each of these nodes, and the average Cl^- concentration in precipitation of 0.29 mg/L measured by Anderholm (1994) at Santa Fe airport.

The simulations of these environmental tracers assume that their concentrations in the recharge water have been constant for at least as long as the oldest water in the Basin, which has been estimated to be 45,000 years (Table D–1). There is evidence from elsewhere in the southwest (e.g. (Tyler et al. 1996 ; Spaulding 1983; Winograd et al. 1992)) that climatic variations in the past 100,000 years have caused dramatic shifts in temperature, precipitation and recharge rates, with accompanying shifts in the stable isotope composition of precipitation and, presumably, in the Cl^- concentration of recharge. Additionally, there is evidence that in the past 30,000 years the ^{14}C activity of meteoric water has been as much as 40 percent higher and as much as 4 percent lower than modern values (100 pmc) (Clark and Fritz, 1997, Fig. 8-4). The simulations presented in the following sections do not consider these complexities, primarily

because of a desire on the part of the authors to keep these preliminary investigations into the usefulness of these hydrochemical and isotopic data relatively simple. However, potential or likely changes in the values of the simulated environmental tracers due to climate change and other factors will be kept in mind when comparing the simulation results with the data.

Lateral boundaries and rivers

Most of the lateral boundaries of the Espanola Basin are treated as no-flow in the groundwater model either because the model boundary coincides with a topographic divide, or because the boundary of the model domain was drawn parallel to hydraulic gradients in certain areas. For these no-flow boundaries, no chemical boundary conditions need to be specified. Likewise, chemical boundary conditions are not specified at nodes where groundwater discharges, such as most of the river reaches specified in the model and the southern lateral boundary (adjoining the Albuquerque basin).

There are relatively small amounts of water entering the regional aquifer model as inflow along northern boundary and from small areas adjacent to the Chama River and Rio Grande, and from recharge along the channels of the Rio Tesuque and Santa Fe River adjacent to the Sangre de Cristo Mountains. For all these inflow nodes, we assume the following chemical characteristics: (1) ^{14}C activities are 100 pmc; (2) $\delta^{18}O$ values are –12 per mil, except along the northern boundary of the basin, where the $\delta^{18}O$ of inflow equals –16 per mil; (3) Cl^- concentrations are 2 mg/L; and (4) ^{3}H concentrations are 6 TU. The $\delta^{18}O$ and the Cl^- concentrations of surface water and associated shallow groundwater draining the Sangre de Cristo Mountains were estimated to have these values, based on data and analyses presented by Anderholm (1994, Table 4, p.33). These $\delta^{18}O$ values and Cl^- concentrations were extrapolated to other surface water in the basin, as well as to shallow groundwater associated with the Chama River and Rio Grande where these rivers entered the basin. Groundwater inflow along the northern boundary of the model was given a $\delta^{18}O$ of –16 per mil primarily to distinguish this groundwater from other groundwater recharged within the Espanola Basin and allow the movement of the groundwater inflow to be traced as it moved through the Basin.

6.4.3. Results of Numerical Simulations using FEHM

Carbon-14 transport simulations

Carbon-14 transport in the regional aquifer was simulated using the porosity values given in Table 6–1 and an assumed initial ^{14}C activity of 100 pmc. The results of this simulation are given in Figures 6–7a and 6–7b. These figures show that ^{14}C activities are high at the water table in the high elevations recharge areas along the perimeter of the basin and along the lower parts of some streams such as the Santa Fe and Santa Clara Rivers that are predicted by the groundwater model to be recharging the aquifer. Compared to these areas, much lower ^{14}C activities are predicted in the deeper parts of the aquifer (Fig. 6-7B) and near discharge areas at the Rio Grande and along the lower parts of most other streams.

At each node in the model, the simulated ^{14}C activities were converted to age using the radioactive decay law:

$$T_{years} = [T_{1/2}/\ln(2)] \times \ln(100 \text{ pmc}/{}^{14}A_{sim}) \qquad (6\text{-}5)$$

where T_{years} is the groundwater age in years, $T_{1/2}$ is the half-life of ^{14}C (5,730 years), *ln* is the natural logarithm, and $^{14}A_{sim}$ is the simulated ^{14}C activity at the node in pmc. Calculated groundwater ages are shown in Figures 6-8A through 8E. Groundwater ages in the recharge areas are younger than 5,000 years. The simulated groundwater ages are between 5,000 and 15,000 years at the water table near the Rio Grande, but increase to greater than 50,000 with increasing depth beneath the river. Some of the oldest shallow groundwater in the Espanola Basin is predicted to be present beneath the Pajarito Plateau north of Los Alamos National Laboratory (Fig. 6-8D). Beneath LANL, however, the simulated groundwater age at the water table is generally less than 10,000 years, with groundwater age increasing rapidly with increasing depth (Figs. 6-8B, 8D, and 8E).

The pattern of groundwater ages beneath the Pajarito Plateau was examined in the context of the simulated hydrogeologic setting for the Plateau and nearby areas. The distribution of hydrogeologic units and their calibrated permeabilities are shown for vertical cross-sections

along y = -127,000 m and y = -130,000 m in Figures 6-9A and 9B, respectively. The cross-section along y = -127,000 passes along the northern boundary of LANL and through the LA-wellfield, and the cross-section along y = -130,000 m passes through the southern part of LANL A comparison of the groundwater ages shown in Figures 6-8B and 8C with the distribution of the hydrogeologic units and their permeabilities shown in Figures 6-9A and 9B provides an explanation for the complex distribution of calculated groundwater ages beneath LANL.

In the groundwater flow model, the low permeability of the Pajarito Fault Zone greatly impedes groundwater flow from the Valles Caldera and the Sierra de los Valle to the Pajarito Plateau. In cross-sections along both y = -127,000 m and –130,000m, young groundwater recharged west of the Pajarito Fault Zone in the Valles Caldera and upper Sierra de los Valle first moves rapidly downward in the high permeability, low porosity Tschicoma Formation and then moves slowly eastward across the fault zone. Young groundwater recharged along the lower Sierra de los Valle along the western margin of LANL probably results in most of the shallow young groundwater found beneath LANL.

Along y = -127,000 m, the young groundwater recharged along the lower Sierra de los Valle east of the Pajarito Fault Zone moves from the Tschicoma Formation through a wedge of Chaquequi Formation and into the high permeability basalt units Tb1 and Tb2; generally, relatively older shallow water is associated with the lower permeability Chaquequi Formation and the western Santa Fe Group sediments. The high groundwater velocity through the basalts is a function of both their high permeability and low porosity. Where the relatively young water that had been channeled through the basalts encounters the Santa Fe Group sediments at the eastern margin of the basalts, the water spreads out vertically throughout the upper part of the sediments and the groundwater flux slows, as indicated by the relatively rapid increase in groundwater age between this point and the Rio Grande. West of the Rio Grande, most of the oldest water (> 50,000 years) is associated with the deep, low permeability Paleozoic/Mesozoic Formations beneath a 1200 m elevation, the deep low permeability Santa Fe Group sediments beneath a 600 m elevation, and the lower part of the Chaquequi Formation, whose calibrated permeability is quite low (2.31×10^{-15} m^2). East of the Rio Grande, the oldest water is within the deep Paleozoic/Mesozoic Formation and deep Santa Fe Group sediments. Along this cross-section, most of the groundwater discharging to the Rio Grande seems to be originating from the eastern part of the Basin, as indicated by the young age for the groundwater east of and just

beneath the river. This conclusion is consistent with the approximately seventeen times greater permeability estimated for the Pojoaque area Santa Fe Group sediments compared to the Santa Fe Group sediments located west of the river (Fig. 6-9A).

Along cross-section y = -130,000 m, the Puye Formation extends eastward from the Pajarito Fault Zone along the top of the regional aquifer. The approximately four times higher permeability estimated for the Puye Formation compared to the Chaquequi Formation facilitates the eastward movement of young groundwater from the Sierra de los Valle and causes the shallow groundwater beneath LANL to have a somewhat younger simulated age near the river than in the cross-section along y = -127,000, where the Puye Formation was absent. Otherwise, many features of the age distribution along y = -130,000 m are similar to those found along y = -127,000 m and have similar causes. Along y = -130,000 m, the contrast in the ages of groundwater found east and west of the Rio Grande is not as pronounced as it was for Y=-127,000 m, probably because in this area of the model, the Rio Grande is contained entirely within the western Santa Fe Group sediments; the high permeability Pojoaque area Santa Fe Group sediments do not drain directly to the Rio Grande along the southern cross-section.

The anomalously old water found at the water table north of LANL on the Pajarito Plateau (Fig. 6-8D) may be due to the greater modeled thickness of fault zone in this area. The greater modeled thickness of the fault zone in this area (2.5 km) compared with areas west of LANL (< 1 km) results in a greater hydraulic impedance for the fault zone north of the LANL, with accompanying decreases in the amount of flow across the Pajarito Plateau from areas west of the fault zone. The increase in the modeled width of the Pajarito Fault Zone north of LANL is related to changes in nodal spacing and in the trend of the fault zone north of LANL, rather than reflecting actual changes in fault zone width

Comparison of simulated and measured groundwater ages

Simulated groundwater ages calculated with the ^{14}C transport model were compared with the uncorrected ^{14}C ages and the ^{14}C ages corrected with the _^{13}C method (_$^{13}C_{calcite}$ = -4.6 per mil) (Fig. 6-10). The simulated ages were calculated using the radioactive decay law and the ^{14}C activities of nodes in the model that corresponded to the screened intervals of the wells in which groundwater ^{14}C was measured. Because the ^{14}C transport simulations did not consider chemical

reactions such as calcite dissolution that would have diluted the simulated groundwater ^{14}C activities, the simulated ages essentially represent the corrected ages and are more directly comparable to the _^{13}C-corrected groundwater ^{14}C ages calculated from the measured ^{14}C activities rather than the uncorrected ages. However, since the ^{14}C-age correction model also involves some uncertainty, these uncorrected groundwater ^{14}C ages are also shown for comparison with the simulated groundwater ages.

For several of these wells (O-4, PM-3, PM-1, and PM-5), the simulated ages at various depths corresponding to the screened intervals showed considerable variability. Direct comparison between the simulated and measured ages is difficult for these wells because the average simulated age of water entering the well would depend on the relative volumes of water contributed by different depth intervals to the well. Likewise, the groundwater ages calculated from the measured ^{14}C activities probably also reflect the relative amounts of different-aged groundwater flowing to the well. In the previous section, it was shown that more permeable hydrogeologic units generally had younger groundwater ages than low permeability units at comparable depths. Based on this observation, it is likely that if flow to each well had been simulated to determine the flux-weighted average age, the resulting flux-weighted age would be shifted toward the younger simulated ages in each screened interval. Based on this reasoning, the simulated results for wells PM-5, DT-5A, O-4, PM-3, PM-1 are considered to be consistent with the corrected and uncorrected ages calculated from the measured ^{14}C activities. The simulated groundwater ^{14}C ages for wells G-5 and LA-1A are slightly older than the corrected ages calculated from the measured ^{14}C activities. In contrast, the simulated groundwater ages at the Eastside and Westside Artesian Wells, and at well LA-1B underestimate the groundwater ages estimated from the measured ^{14}C activities. Based on its high concentrations of Cl^- and of trace elements associated with geothermal water in the Valle Caldera, Goff and Sayer (1980) hypothesized that the groundwater at well LA-1B had risen up from great depths along faults in the area of the well (see section "Trace Elements"). Similarly, upwelling of deep, old groundwater along faults might explain the large ages of groundwater at the Westside Artesian Well, where the measured Cl^- concentration was 354 mg/L. If upwelling of deep groundwater along faults is the cause of the great ages of the groundwater at well LA-1B and the Westside Artesian Well, it is likely that the groundwater model would require a transmissive fault in the vicinity of these wells in order to match the large ^{14}C age of groundwater at these wells.

Results of delta oxygen-18 transport simulations

The results of the _^{18}O transport simulations are shown in Figures 6-11A through 6-11F. At elevations above about 6,900 feet, the patterns in the _^{18}O at the water table (Figs. 6-11A and 6-11D) reflect the _^{18}O of the recharge, as determined from the linear regression between elevation and _^{18}O. At elevations below 6,900 feet, active recharge is absent and the _^{18}O patterns reflect the mixing of recharge from up gradient areas and, near the discharge areas along the streams and rivers in the Basin, the re-emergence of deep groundwater recharged at relatively high elevations (Figs. 6-11C and 6-11D). The lightest _^{18}O values are present in the recharge at the highest locations in the Sangre de Cristo Mountain and in the inflow along the northern boundary of the model. The inflow along the northern boundary was given a _^{18}O of –16.0 per mil in order to distinguish this water from other water in the Basin and allow this water to be traced as it moved through the Basin. Most of the water entering along the northern boundary of the model is discharged to the Chama River and the Rio Grande (Figs. 6-11D and 6-11E).

East-West cross-sections through the model indicate that much of the deep groundwater beneath the Pajarito Plateau at LANL with _^{18}O values between –13 and –12 originates from the Sierra de los Valle west of the Pajarito Fault Zone (Figs. 6-11B and 6-11C). Lower elevation recharge with _^{18}O values between –11 and –10 is locally prominent, but becomes diluted and mixed as it moves toward the Rio Grande by the larger amounts of high elevation recharge with light _^{18}O values. The results of the _^{18}O simulations along an east-west cross-section north of LANL, where the model simulations predicted that very old groundwater (> 50,000 years) is present at the water table beneath the Pajarito Plateau (Fig. 6-8D), indicate that, as speculated earlier, very little groundwater moves east across the Pajarito Fault Zone in this area (Fig. 6-11F) compared to areas farther south (Figs. 6-11B and 6-11C). The east-west cross-sections each indicate a very abrupt transition beneath the Rio Grande between groundwater with light _^{18}O originating from relatively high elevations in the Sangre de Cristo Mountains and groundwater with somewhat heavier _^{18}O flowing from the Sierra de los Valle and Pajarito Plateau (Figs. 6-11B, 6-11C and 6-11F).

West of the Rio Grande, some of the deepest groundwater has simulated _^{18}O values that are lighter than shallow groundwater in the area (Figs. 6-11B, 6-11C, and 6-11F) and thus have no obvious source. Most likely, these very light values continue to reflect the initial value for _^{18}O of –15 permil assumed for all groundwater in the model, indicating that chemical steady-state in some low permeability areas deep in the model was not attained even after a simulation time of 10^6 years.

Comparison of simulated and measured groundwater delta oxygen-18 values

The average _^{18}O value of nodes in the groundwater model that correspond to the screened intervals of wells near LANL are compared to the average measured values at the wells in Figure 6-12A. The average measured and simulated _^{18}O values at most wells are within a range of –12 to –10 permil, suggesting that recharge distribution and source areas for groundwater at wells near LANL is being reasonably approximated by the model. However, the model is not sufficiently refined to explain the variability in _^{18}O values within this range.

The measured _^{18}O of groundwater at the Eastside Artesian Well and well LA-1B is considerably lighter than the simulated _^{18}O values at these wells. The corrected groundwater ^{14}C ages for these wells (Table D–1) indicate that the water was recharged approximately 20,000 years ago, or about the time of the last glacial maximum as recorded in the _^{18}O of ice cores from Greenland and Antarctica and foraminifera in deep-sea sediments (see data summarized in Winograd et al., 1992, Fig. 3). In the southern Great Basin, a continuous half-million-year long record of groundwater oxygen-18 variations ending 60,000 years ago was recorded in calcite deposited at a regional discharge area (Winograd et al., 1992, Fig. 2). This record indicates that the _^{18}O of groundwater in the southern Great Basin is about 2 permil lighter during the coldest parts of the glacial periods than during the warmest parts of the interglacial periods. As shown in Figure 6-12A, a shift in _^{18}O of 2 permil in groundwater recharged 20,000 years ago would explain most of the departure of the Eastside Artesian Well and well LA-1B simulation results from the one-to-one line. Although these arguments do not prove climate change is responsible for the poor match between the simulation results and the data at the Eastside Artesian Well and

well LA-1B, shifts in the $\delta^{18}O$ of recharge with changes in climate should be recognized as a strong possibility in view of the cited studies.

The differences, or residuals, between the average simulated and average measured $\delta^{18}O$ of groundwater within the screened interval of the wells near LANL are shown in plan view in Figure 6-12B. The most negative residuals are found for groundwater at wells near the northeast corner of LANL, indicating that the proportion of high elevation to low elevation recharge flowing to this area is too large in this area of the model. Conversely, the relatively large positive residuals at wells DT-9 and DT-5a are indicating that the proportion of high elevation to low elevation recharge flowing to these wells is too small.

It is not clear if the inferred excess or deficit of low elevation recharge in the certain areas of the model indicates whether adjustments to the recharge model or to the hydrogeologic unit permeabilities are required. The application of additional low elevation recharge in areas of the model corresponding to several canyons in the northeast corner of LANL might improve the match between the simulated and measured groundwater $\delta^{18}O$ values in this area. These canyons (and wells) include: (1) Guaje Canyon (wells G-4, G-5, and G-6); (2) Pueblo Canyon (well TW-1); (3) Los Alamos Canyon (wells LA-1, LA-5 and O-4); and (4) Sandia Canyon (wells PM-1 and PM-3). Well PM-5 is located on a mesa top and decreasing the magnitude of its residual would require changes other than the application of additional recharge along canyon bottoms.

Results of chloride transport simulations

The boundary conditions assumed for $\delta^{18}O$ and Cl^- in the diffuse recharge are related by their mutual dependence on elevation (Fig. 6-13A). For $\delta^{18}O$, this dependence is expressed directly by the linear regression equation presented by in Keating and Goff (unpublished report)(1999). For Cl^-, the dependence with elevation arises from the relation between recharge and elevation identified from the model calibration, and the relation between recharge rates and the Cl^- concentration of the recharge determined from the chloride mass-balance equation. To help evaluate the validity of the recharge model, the relation between $\delta^{18}O$ and Cl^- estimated from the diffuse recharge model is plotted against the groundwater $\delta^{18}O$ and Cl^- data from springs and wells in the Los Alamos area in Figure 6-13B and for wells in the Santa Fe/Pojoaque area in Figure 6-13C. The data for the Santa Fe/Pojoaque area are from Anderholm (1994)

The shape of the relation between _^{18}O and Cl^- shown in Figures 6-13B and 6-13C is a consequence of the parameters identified for the recharge model. These parameters specify that the fraction of precipitation that becomes recharge is 0.0 below 6,981 feet, a constant fraction (0.054) of precipitation above a ground-surface elevation of 7,090 feet, and increases linearly from 0 to 0.054 between these elevations. From the chloride mass-balance relation, the Cl^- in the recharge is constant above 7,090 feet where recharge rates are a constant fraction of the precipitation rates, and increases rapidly with decreasing elevation between 7,090 and 6,981 feet. Below 6,981 feet, recharge rates are zero and Cl^- concentrations are undefined. The _^{18}O of the recharge at elevations of 7,090 and 6,981 feet is estimated from the regression equation to be –10.38 and –10.27, respectively, so that there is a rapid increase in Cl^- concentrations over a very narrow range in _^{18}O. A different set of parameters for the recharge model would yield a different relation between the _^{18}O and Cl^- concentration of the recharge.

It is worth noting that the relation between _^{18}O and Cl^- in the recharge implicitly assumes that the Cl^- concentration of precipitation is changing because of evapotranspiration in the soil zone, but that the _^{18}O of the precipitation is not enriched by fractionation during evapotranspiration. The selective increase in the Cl^- concentration without accompanying enrichment in _^{18}O is possible only if transpiration of water by plants comprises most of the total evapotranspiration. As mentioned earlier (see Section 6.2.1), although Cl^- becomes concentrated in the residual soil water during transpiration, _^{18}O in the residual soil water is unchanged because fractionation of _^{18}O during transpiration does not occur. The dominance of the transpiration component of the overall evapotranspiration rates in the basin is indicated by the fact that most of the groundwater and springs samples in the Los Alamos area do not show pronounced departures from the meteoric water line that would indicate substantial evaporation (Figure 6–3).

Comparison of simulated and measured groundwater chloride concentrations

The parameters of the recharge model estimated from the groundwater model calibration result in a Cl^- versus _^{18}O curve that fits most of the spring and well data from west of the Rio Grande (Fig. 6-13B). The Cl^- versus _^{18}O curve derived from the recharge model also predicts the relative absence of groundwater with measured _^{18}O values greater than about –10.3 per mil.

However, many of the groundwater data, particularly from east of the Rio Grande, plot above and to the left of the Cl^- versus $\delta^{18}O$ curve determined from the recharge model (Figs. 6-13B and 6-13C). There are several possible explanations for the departure of these data from the curve: (1) These groundwater samples represent a mixture of high- and low-elevation recharge found along the flat and steep portions of the curve, respectively; (2) The chloride concentrations of the groundwater data that lies above and to the left of the curve has increased since it was recharged because of the addition of Cl^- to the groundwater from septic systems, irrigation water, and road salt (Anderholm, 1994); (3) Shallow groundwater in some areas, such as Pojoaque, has become concentrated with Cl^- since it was recharged because of transpiration by deep-rooted vegetation downgradient from the recharge area (Anderholm, 1994); and (4) The Cl^- concentrations of groundwater at some wells (for example, well LA-1B, have increased as a result of mixing with deep, saline groundwater that has risen from great depths along faults (Goff and Sayer, 1980).

It has not yet been possible to identify all of the groundwater data that may have been affected by anthropogenic inputs of Cl^- or by mixing with deep, saline groundwater. Evaluation of the importance of anthropogenic inputs of Cl^- would involve examination of the concentrations of other species, such as nitrate, that would likely be present in groundwater receiving septic tank effluent or recharge from irrigation water. Similarly, Cl^- concentration increases caused by the upwelling of deep, warm water along faults would be also likely to have elevated concentrations of trace elements characteristic of hydrothermal waters. Although such an evaluation of the Cl^- data would be useful, it has not yet been undertaken.

The simulated steady-state distribution of Cl^- at the water table (Fig. 6-14) shows that the only area in the model that has Cl^- concentrations much larger than about 6 mg/L is a thin, northeast-trending zone along the western edge of the Pajarito Plateau where the ground-surface elevation is between 6,981 and 7,090 feet. Elsewhere in the basin, the surface area and the total recharge associated with this range of ground-surface elevations is too small for the high-chloride water to exert a discernible effect on Cl^- concentrations in downgradient areas. The small amount of high-chloride water that is recharged between 6,981 and 7,090 feet is readily diluted by the much larger amount of low-chloride, high-elevation recharge, indicating that mixing of high- and low-elevation recharge cannot explain the data that plot above and to the left of the Cl^- versus $\delta^{18}O$ curve (Figs. 6-13B and 6-13C) using the current recharge model. Vertical cross-sections through LANL (not shown) also indicate that the small amount of high-chloride

water at the water table is quickly diluted at depth. The most dilute groundwater in the model (about 2 mg/L) is derived from inflow along the northern boundary of the model, which discharges to the Chama River and Rio Grande, and groundwater derived from recharge applied along the upper parts of the Santa Fe River and Tesuque Creek in the southeast corner of the basin.

Results of tritium transport simulations

The results of the ^{3}H-transport simulations (Figs. 6-15A and 6-15B) indicate that groundwater ^{3}H concentrations above the detection limit of 0.3 TU would be found near the water table in the recharge areas just from natural ^{3}H production alone. However, this naturally-produced ^{3}H would probably not be found at depth or beneath areas that are not currently sites of recharge because of the short half-life of ^{3}H (12.43 years) and the relatively slow rates of groundwater movement.

Comparison of simulated and measured groundwater tritium concentrations

As described earlier in the introduction to this section, the ^{3}H-transport simulations were done in a way that reflects only the long-term distribution of ^{3}H in the aquifer that results from natural ^{3}H production alone. The simulations were not intended to replicate the observations of high ^{3}H concentrations in the Los Alamos area, many of which can only be explained by elevated concentrations of ^{3}H in rainfall following nuclear-weapons tests or by local Laboratory sources of ^{3}H (see section "Tritium"). Substantially higher input concentrations of ^{3}H for the recharge based on reconstructions of the ^{3}H content of New Mexico precipitation since 1950 (Vautez and Goff, 1986, Fig. 12) and records of ^{3}H-releases by the Laboratory would need to be used if the current groundwater model were to attempt to explain the present distribution of ^{3}H in the vicinity of the Laboratory.

The simulated distribution of ^{3}H also indicates that some modifications to the recharge distribution used in the model, as well as in the ^{3}H source term, may be necessary to match the measured ^{3}H values in the vicinity of the Laboratory. The simulated distribution of ^{3}H (Figs. 6-

15A and 6-15B) does not indicate the presence of ^3H above the detection limit of 0.3 TU beneath LANL except for a very small area along its western margin. This result suggests that if the measured ^3H concentrations of a few to several tens of tritium units found near the eastern margin of the Laboratory at wells LA-1A, LA-2, and TW-1 (Rogers et al., 1995, Table 2) are to be matched by the model in future simulations, the application of some additional lower elevation recharge, perhaps as focused recharge at nodes in the model corresponding to canyon bottoms, should be considered. Additional lower elevation recharge may also be necessary to explain presence of ^3H at elevations above the detection limit at several of the San Ildefonso Pueblo wells (Blake et al., 1995, Table 4).

The present ^3H simulations also indicate that the vertical grid resolution in the vicinity of the water table needs to be refined if quantitative comparisons between measured and simulated ^3H concentrations are to be made. Because of the radioactive decay of ^3H, the maximum ^3H concentrations at the water table (Fig. 6-15A) reflect the residence time of the recharge within the uppermost grid cells, as well as input ^3H concentrations. For a constant ^3H input concentration, the maximum ^3H concentration at the water table in the simulation is inversely related to the residence time (t_{res}) in the grid cells at the water table and, hence, also to grid cell thickness (Δz). For vertical flow at the water table

$$t_{res} = \phi \, \Delta z/q \qquad (6\text{-}6)$$

where ϕ is the porosity and q is the recharge flux in meters per year. The ^3H concentration at the water table ($^3H_{wt}$) can then be calculated from the input ^3H of the recharge ($^3H_{rech}$), the calculated value of t_{res}, and the law of radioactive decay:

$$^3H_{wt} = {}^3H_{rech} \exp(-\lambda t_{res}) \qquad (6\text{-}7)$$

where λ is the radioactive decay constant for ^3H (5.58×10^{-2} years^{-1}).

In the present model grid for the Espanola Basin, the grid cell thickness at the water table is 50 m. As an example calculation, for a recharge rate of 1 inch/year (0.0254 m/year) and a porosity of 0.30, t_{res} in the uppermost grid cell is 591 years and the value of $^3H_{wt}$ corresponding to

a value for $^3H_{rech}$ of 6 TU after 47 half lives is only 2.9 x 10^{-14} TU, or zero. Thus, we would not expect to see any ^3H at the water table in the model for this combination of ϕ, Δz, and q, which is typical of certain low-elevation areas in the model. Conversely, for a recharge rate of 2 inches/year (0.0508 m/year) and a porosity of 0.02, t_{res} in the uppermost grid cell is 19.7 years and the value of $^3H_{wt}$ corresponding to a value for $^3H_{rech}$ of 6 TU after 1.6 half lives is 2 TU. These values of ϕ, Δz, and q are typical of parameters in the model corresponding to the Sangre de Cristo Mountains and the Valles Caldera. Undoubtedly, therefore, the simulated distribution of ^3H shown in Figures 6-15A and 6-15B has been influenced by grid thickness near the water table. In summary, the simulated distribution of ^3H at the water table is a function of ϕ, Δz, and q as well as the input ^3H concentration of the recharge, a factor that should be considered in future grid design if the groundwater model is to be used to characterize ^3H transport near the Laboratory.

6.4.4. Summary and conclusions of environmental tracer simulations

The calibrated model of groundwater flow in the Espanola Basin was used to simulate the steady-state transport of several naturally occurring environmental tracers, including ^{14}C, $_^{18}O$, Cl^- and ^3H. The simulations results were compared with measurements of these environmental tracers in groundwater in the basin to help evaluate the groundwater model and indicate what modifications to the model, if any, might be necessary. The simulations of tracer transport also helped to illustrate aspects of the groundwater model that were not previously obvious from analyses of the flow simulations and the measured hydraulic data alone. These aspects of the groundwater model pertained to the location of groundwater source areas, groundwater flow rates and directions, possible geologic controls on groundwater movement, and groundwater mixing behavior near the regional discharge areas.

The ^{14}C transport simulations were used to calculate the ages of groundwater in the model, which could be compared to the groundwater ages, estimated from ^{14}C measurements. The simulation results indicated that, as expected, young groundwater is present at shallow depths beneath the recharge areas in the mountains and groundwater becomes progressively older as its

moves toward the discharge areas and at depth. The groundwater model predicts that some of the oldest groundwater in the basin exists beneath the Pajarito Plateau, partly because the Pajarito Fault Zone impedes eastward groundwater movement from high elevation areas west of the Plateau, and because the recharge model used in the transport simulations predicts that recharge is significant only along the western margin of the Plateau. Because of these factors, most of the groundwater discharge to the Rio Grande east of the Laboratory in the model originates from the eastern part of the Espanola Basin. The simulation results indicate that groundwater ages increase rapidly with depth beneath the Plateau and eastward toward the Rio Grande. These trends in groundwater age are in qualitative agreement the corrected groundwater ages calculated from the measured groundwater ^{14}C data. A detailed comparison between simulated groundwater ages and ages estimated from the ^{14}C data indicated fair agreement at several wells on the Plateau, but simulated ages were too young compared to ages estimated from the ^{14}C data at several wells near the Rio Grande. Although the groundwater model predicts the presence of very old groundwater at depth beneath the Rio Grande, in the model this old water becomes mixed with younger, shallow water as it rises toward the river. The groundwater model also predicts that because basalt flows Tb1 and Tb2 have a high permeability and low porosity, these basalt layers will provide a conduit for the rapid movement of water beneath the Pajarito Plateau.

Because the $\delta^{18}O$ of recharge is strongly negatively correlated with elevation in the model, the simulations of $\delta^{18}O$ transport provide an especially useful method for tracking the movement and subsequent mixing of recharge in the groundwater model. These simulations indicate that although the Pajarito Fault Zone slows the eastward movement of groundwater from areas west of the fault zone, much of the old groundwater deep beneath the Pajarito Plateau in the LANL area originates from the upper part of the Sierra de los Valle west of the fault zone. The simulations predict that the $\delta^{18}O$ of groundwater becomes lighter with increasing depth beneath the Plateau, but that the lightest $\delta^{18}O$ is found in groundwater east of the Rio Grande because of the high elevation of the recharge areas in the Sangre de Cristo Mountains. An abrupt transition in the $\delta^{18}O$ of groundwater is predicted by the model beneath the Rio Grande where the groundwater recharged in the eastern and western parts of the basin converges. A comparison between the simulated and measured $\delta^{18}O$ values at wells on the Pajarito Plateau indicates that both the simulated and measured values are within a range of –12 to –10 per mil, indicating that the recharge model may be reasonably approximating the actual recharge elevations of

groundwater beneath the Plateau. However, the measured variability in $\delta^{18}O$ within this range is not reproduced by the model simulations. An analysis in the trends of the differences in the simulated and measured $\delta^{18}O$ suggests that, in general, a relatively larger proportion of isotopically heavy, low elevation recharge at wells in the northern part of LANL and a relatively larger amount isotopically light, high-elevation recharge at wells in the southern part of LANL in the model would improve the comparison. Whether adjustments should be made to the recharge model, to the permeabilities of the hydrogeologic units in the model, or both, has not yet been determined.

The simulations of Cl^- transport use the chloride mass-balance equation to estimate the concentration of Cl^- in the recharge. The current model of recharge estimates that above a ground-surface elevation of about 7100 feet, recharge is a constant fraction of precipitation. As a result, the simulated Cl^- concentration of most groundwater recharge in the Basin is about 5 to 6 mg/L using the current recharge model. The small amount of recharge with somewhat higher Cl^- concentrations estimated to be present at elevations where recharge becomes very small is easily diluted in the model by the much larger volume of high elevation recharge with a Cl^- concentration of 5 to 6 mg/L. Because of the uniformity of groundwater Cl^- concentrations in the model, Cl^- is not a particularly useful groundwater tracer for the combination of recharge parameters currently used to distribute recharge in the groundwater model. However, the $\delta^{18}O$ versus Cl^- relation predicted for recharge using the current recharge parameters is in good agreement with $\delta^{18}O$ and Cl^- data for most spring and well samples west of the Rio Grande, and may be more consistent with $\delta^{18}O$ and Cl^- data from wells east of the Rio Grande than is first apparent if one accepts the hypothesis of Anderholm (1994) that many of the high Cl^- concentration in groundwater east of the Rio Grande are the result of septic tank effluent and other human effects.

Tritium transport simulations done thus far have examined only the steady-state distribution of ^3H in groundwater that would be expected for the natural ^3H-production rates in the atmosphere that existed prior to nuclear weapons development and testing. Development of source terms for the ^3H concentration of recharge that reflect the effects of atmospheric nuclear weapons tests and local Laboratory activities are underway which will allow a more detailed evaluation of the significance of groundwater ^3H measurements near LANL for groundwater model development.

Table 6-1. Porosity values assumed for hydrogeologic units in transport simulations.

Hydrogeologic Unit	Porosity (fraction)	Hydrogeologic Unit	Porosity (fraction)
Deep basement	0.02	Shallow Sangres de Cristo rocks	0.02
Deep Paleozoic /Mesozoic rocks	0.10	Shallow Paleozoic /Mesozoic rocks	0.10
Pre-Cambrian Rocks – Ojo Caliente area	0.02	Pre-Cambrian Rocks – Penasco Area	0.02
Cerros del Rio basalt (Tb1)	0.05	Cerros del Rio basalt (Tb2)	0.05
Cerros del Rio basalt (Tb4)	0.05	Cerros del Rio basalts in south	0.05
Deep Tschicoma Formation	0.05	Shallow Tschicoma Formation	0.05
Pajarito Fault Zone	0.10	Agua Fria Fault	0.10
Eastern Santa Fe Group sediments	0.25	Western Santa Fe Group sediments	0.25
Pojoaque area Santa Fe Group sediments	0.25	Santa Fe airport area Santa Fe Group sediments	0.25
Ancha Formation	0.25	Northern Santa Fe Group sediments	0.25
Ojo Caliente area Santa Fe Group sediments	0.25	Penasco sediments	0.25
Deep Santa Fe Group sediments	0.15	Puye Formation	0.25
Totavi Lentil member of the Puye Formation	0.30	Chaquehui Formation	0.30
Bandelier Tuff	0.30	---	---

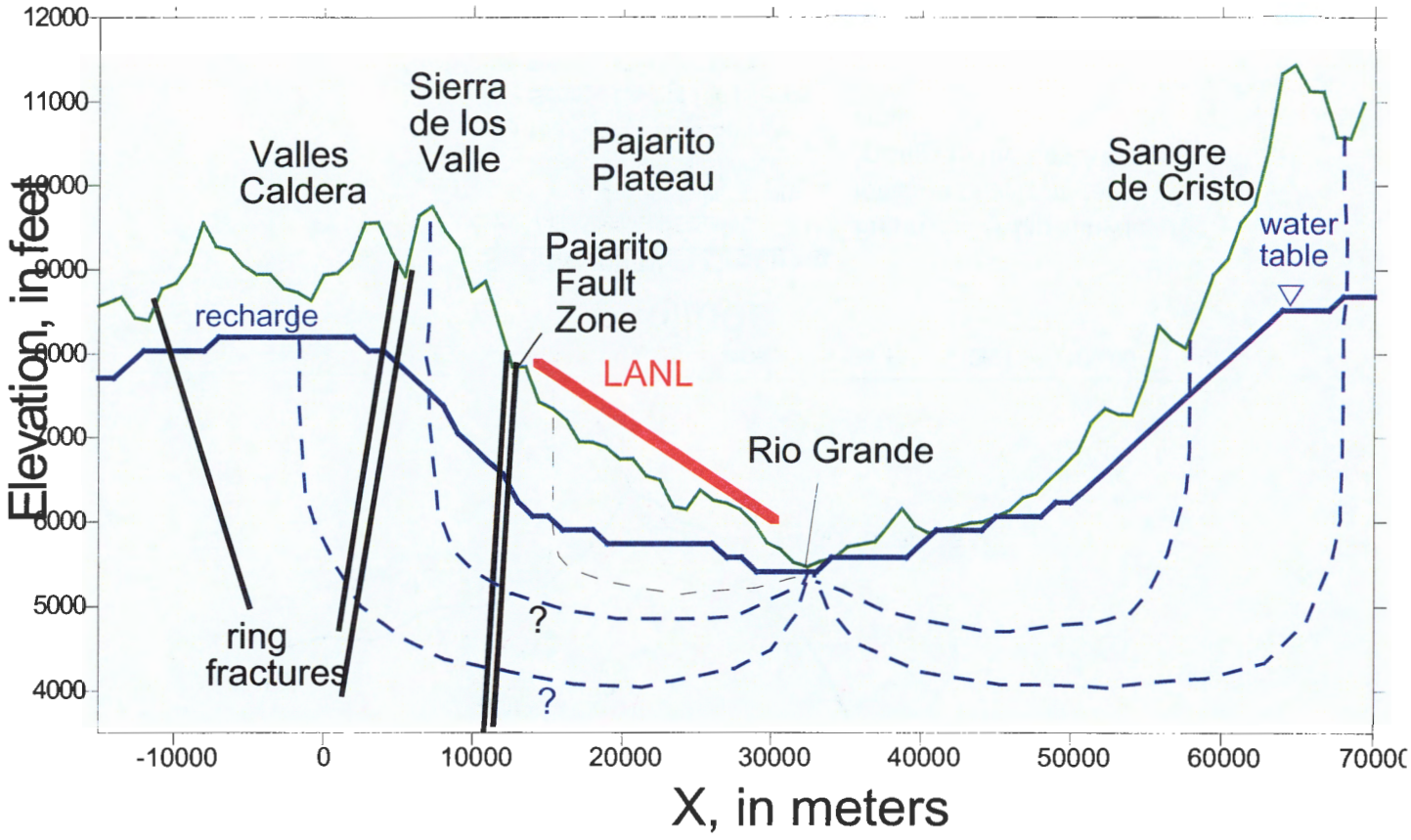

Figure 6-1. Conceptual model of groundwater flow in the Los Alamos area.

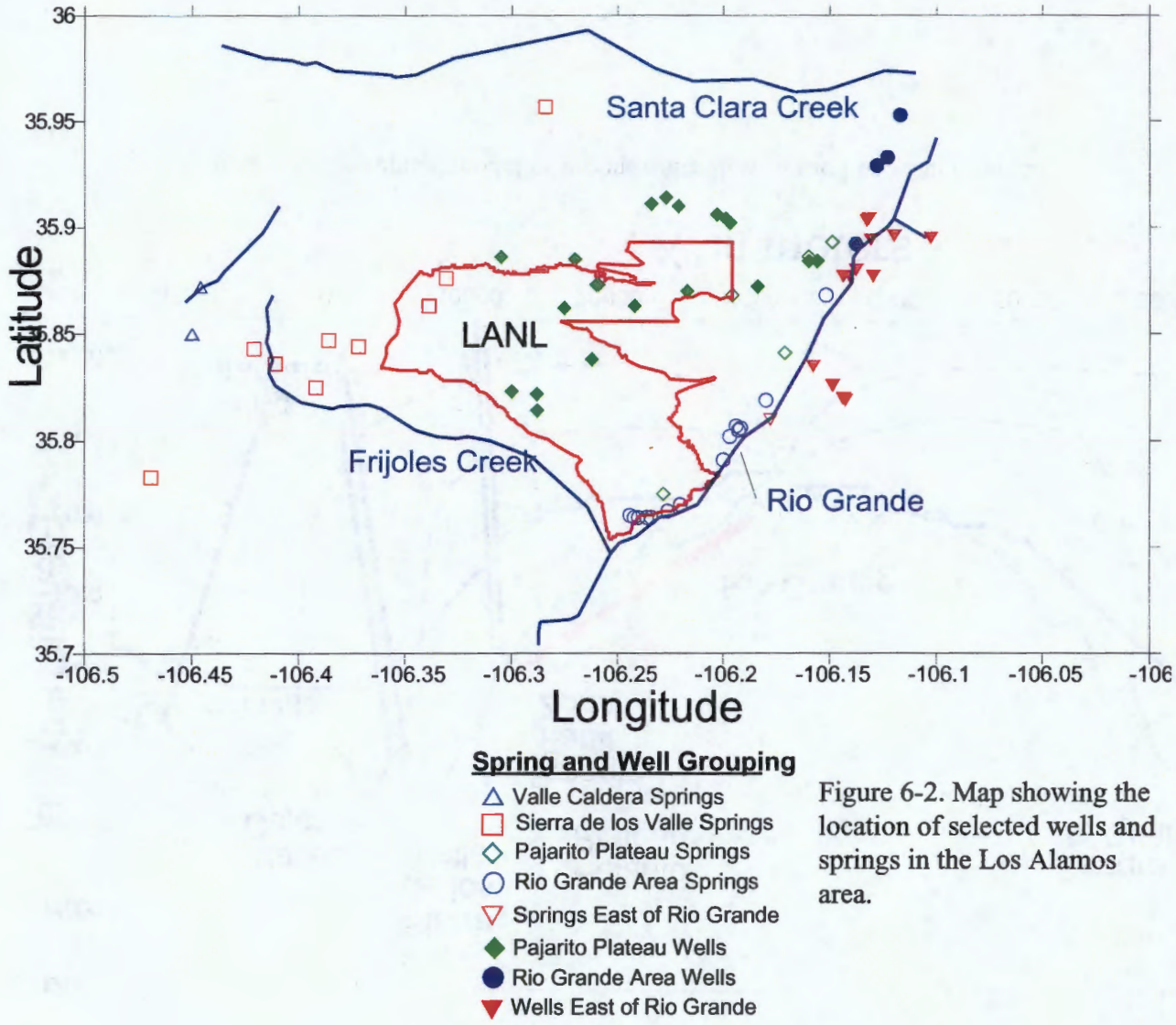

Figure 6-2. Map showing the location of selected wells and springs in the Los Alamos area.

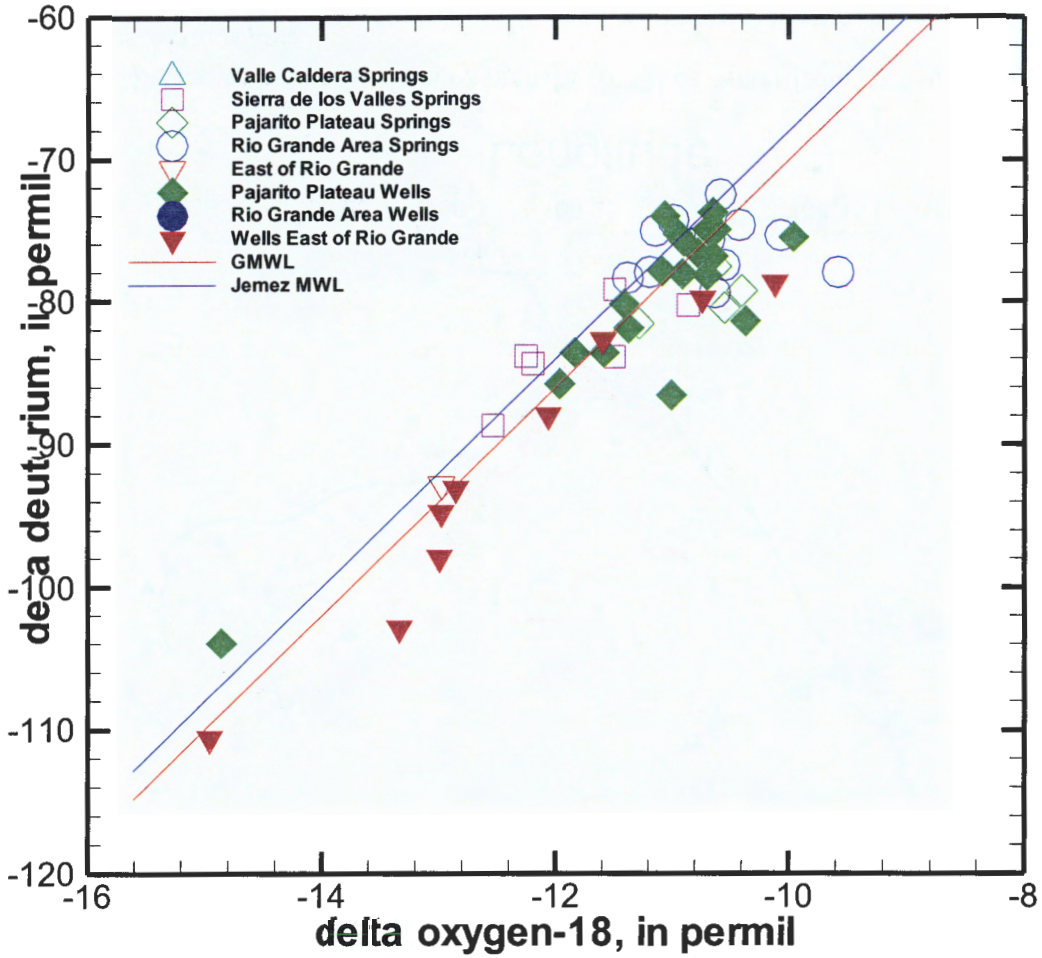

Figure 6-3. Relation between delta deuterium (δ^2H) and delta oxygen-18 ($\delta^{18}O$) of groundwater and springs in the Los Alamos area.

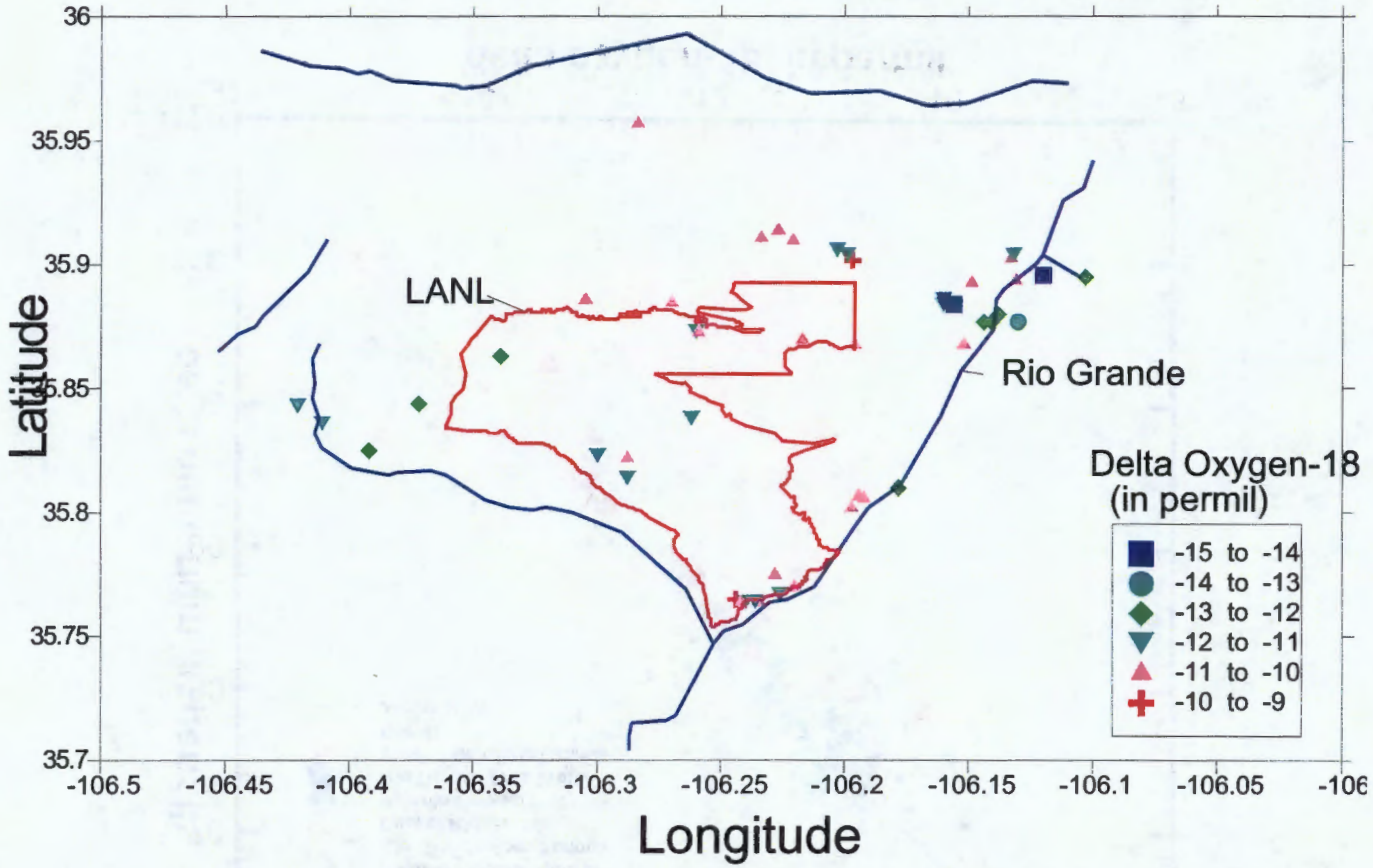

Figure 6-4. Map showing the delta oxygen-18 ($\delta^{18}O$) of water from springs and wells in the Los Alamos area.

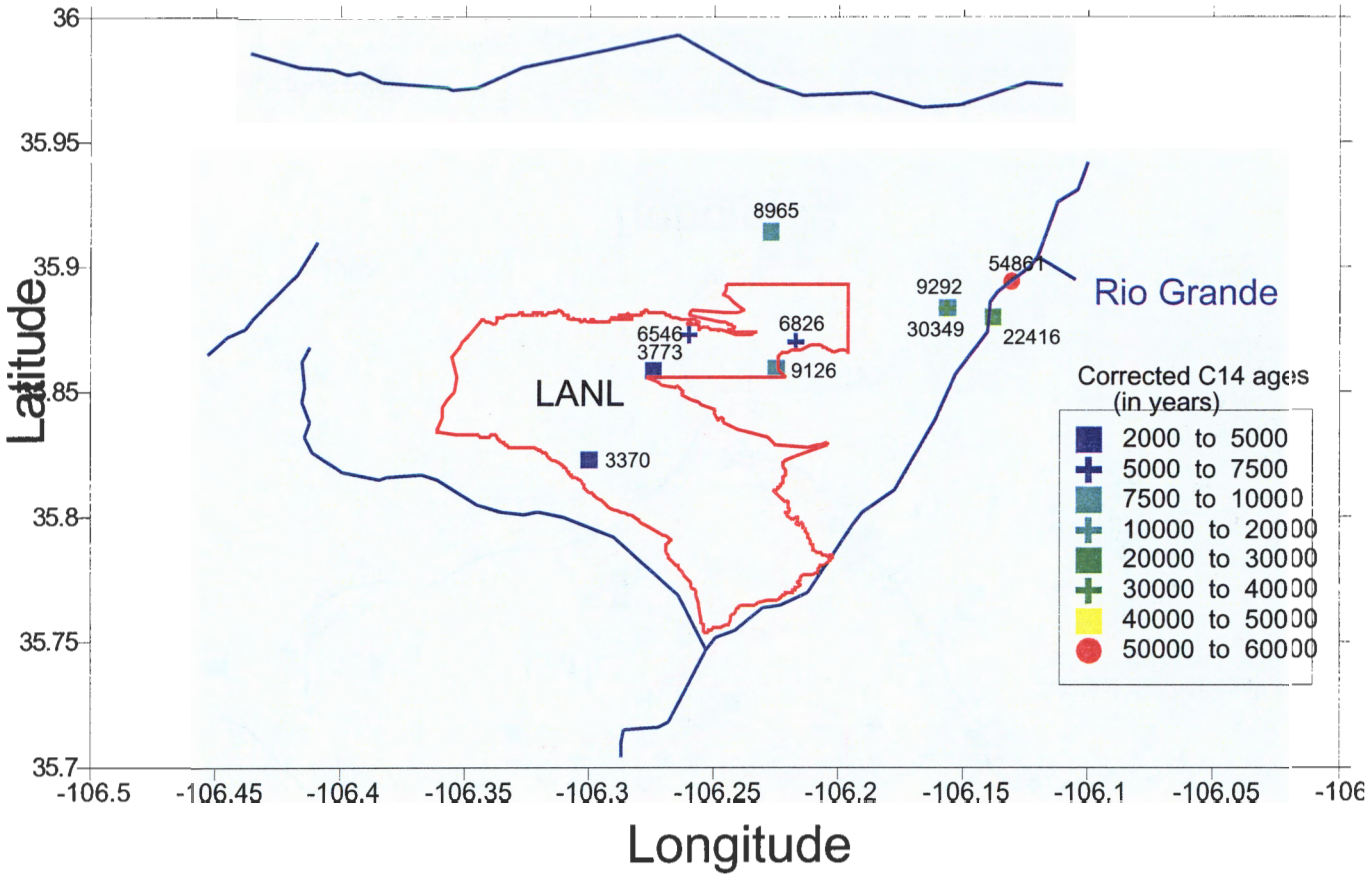

Figure 6-5. Map showing the corrected groundwater carbon-14 (^{14}C) ages in the Los Alamos area.

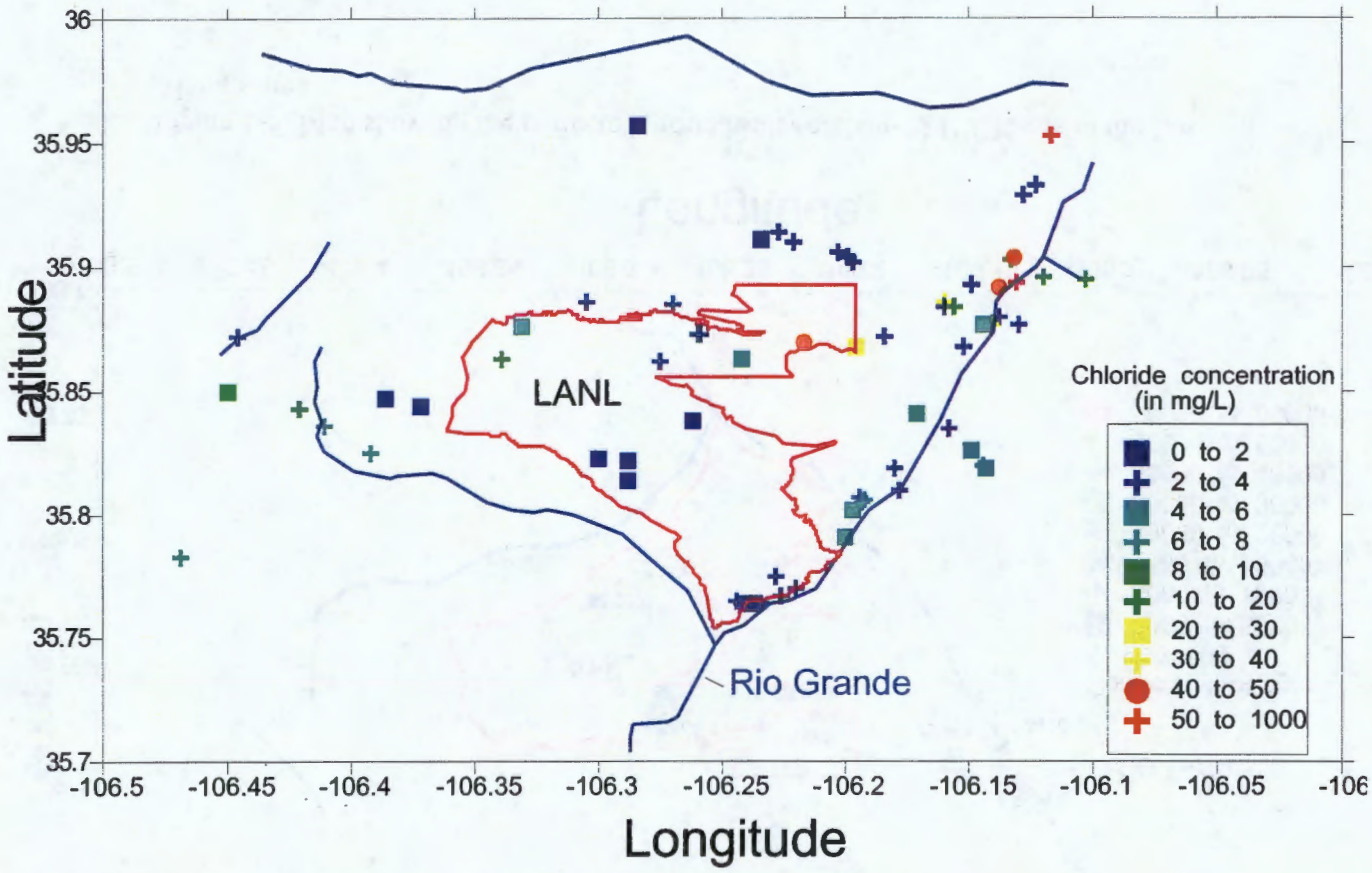

Figure 6-6. Map showing the chloride concentrations of water from springs and wells in the Los Alamos area.

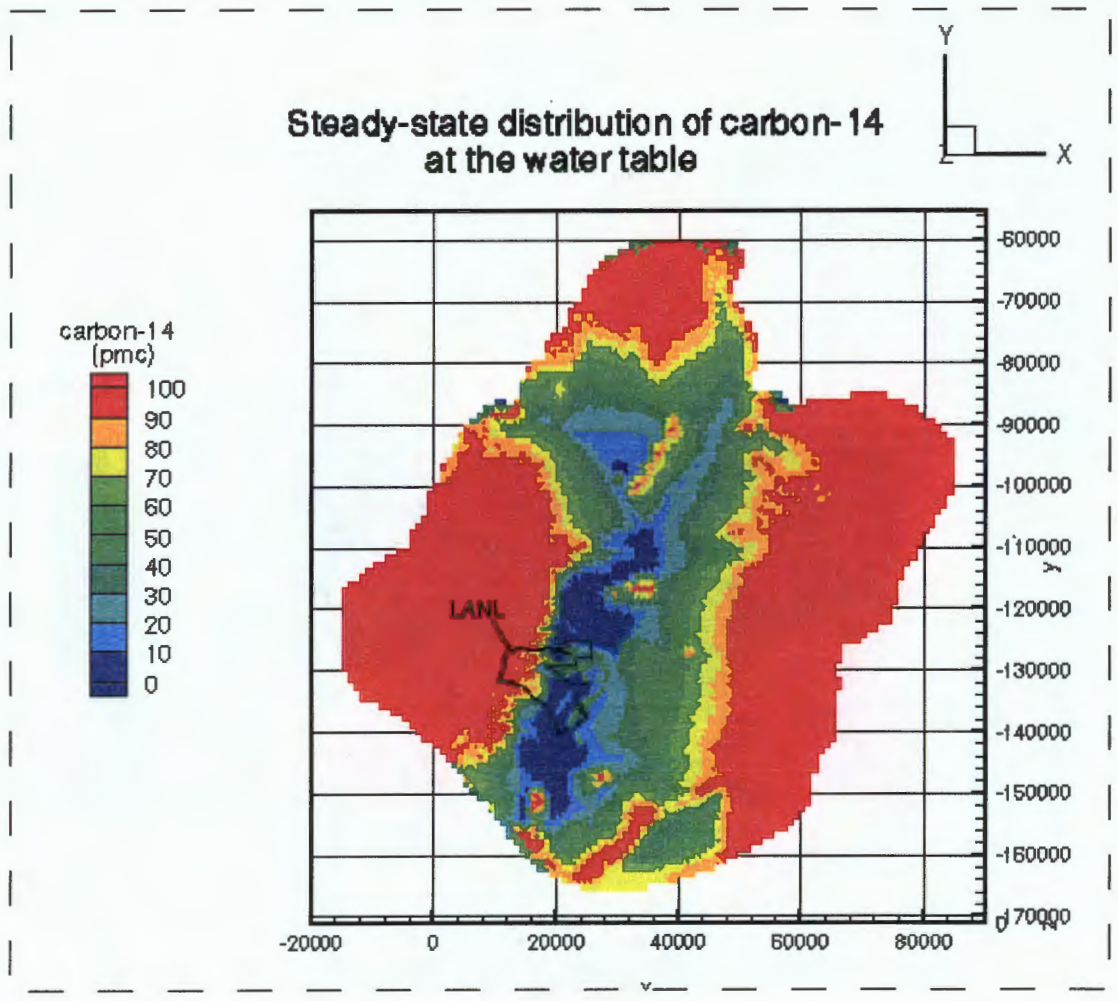

Figure 6-7(A). Simulated steady-state distribution of groundwater carbon-14 activities at the water table.

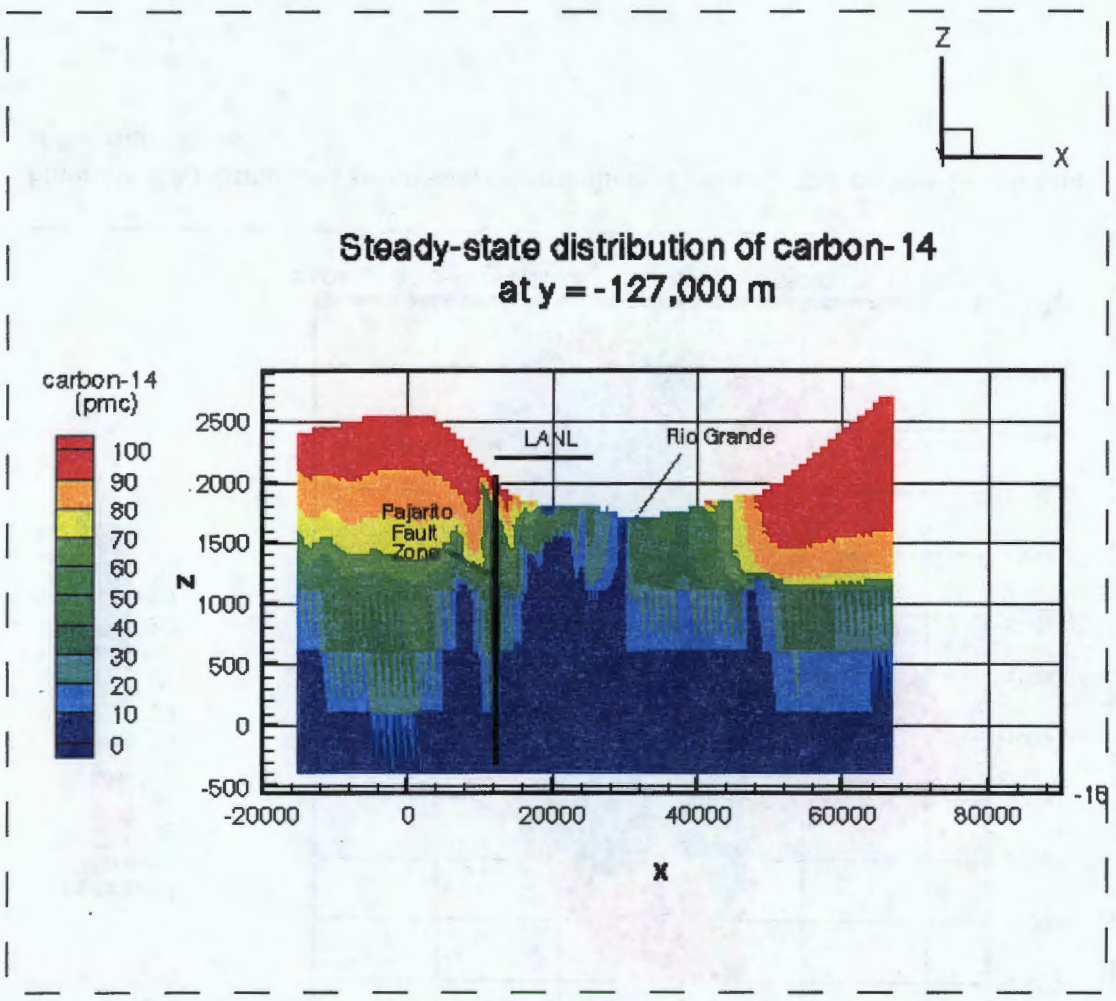

Figure 6-7(B). Simulated steady-state distribution of groundwater carbon-14 activities along y=-127,000 m.

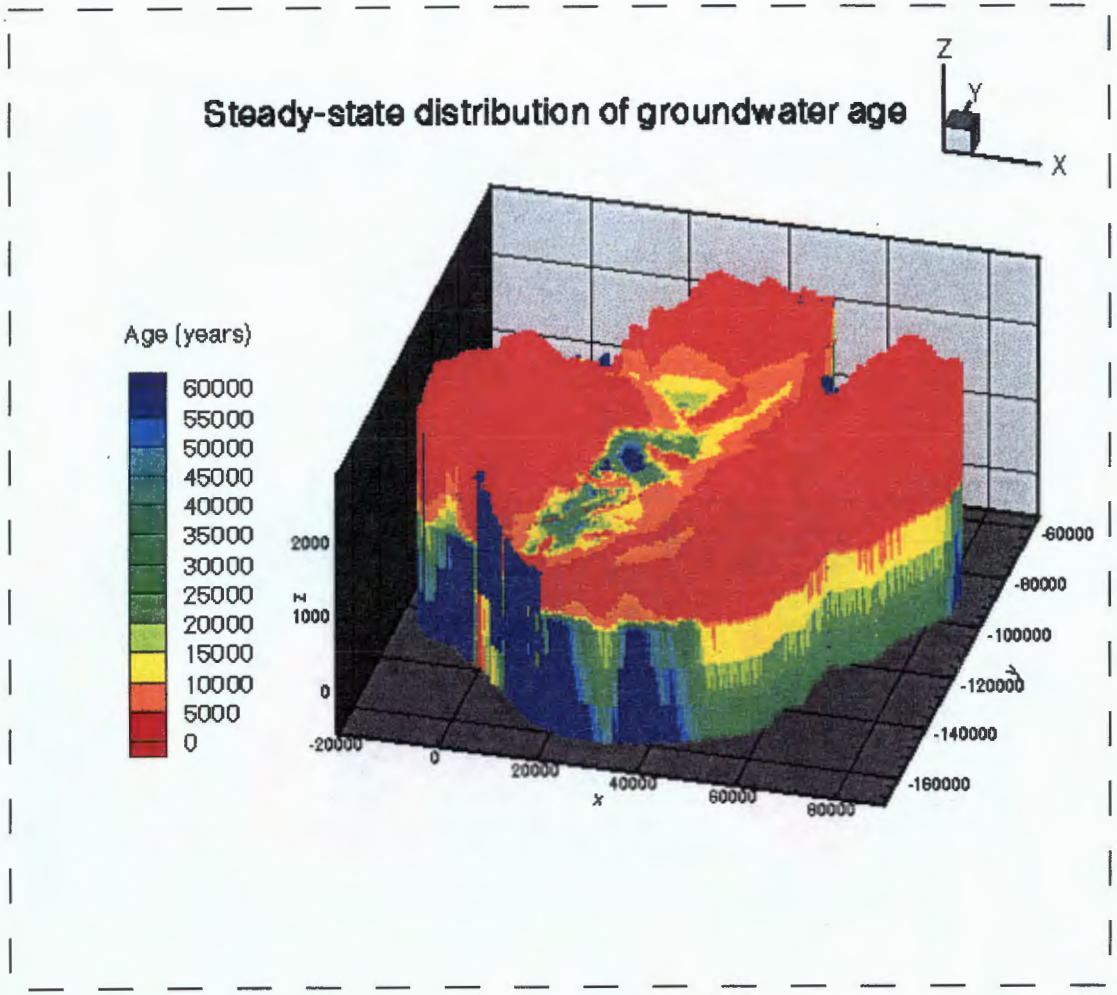

Figure 6-8(A). Three-dimensional view of simulated steady-state distribution of groundwater carbon-14 ages.

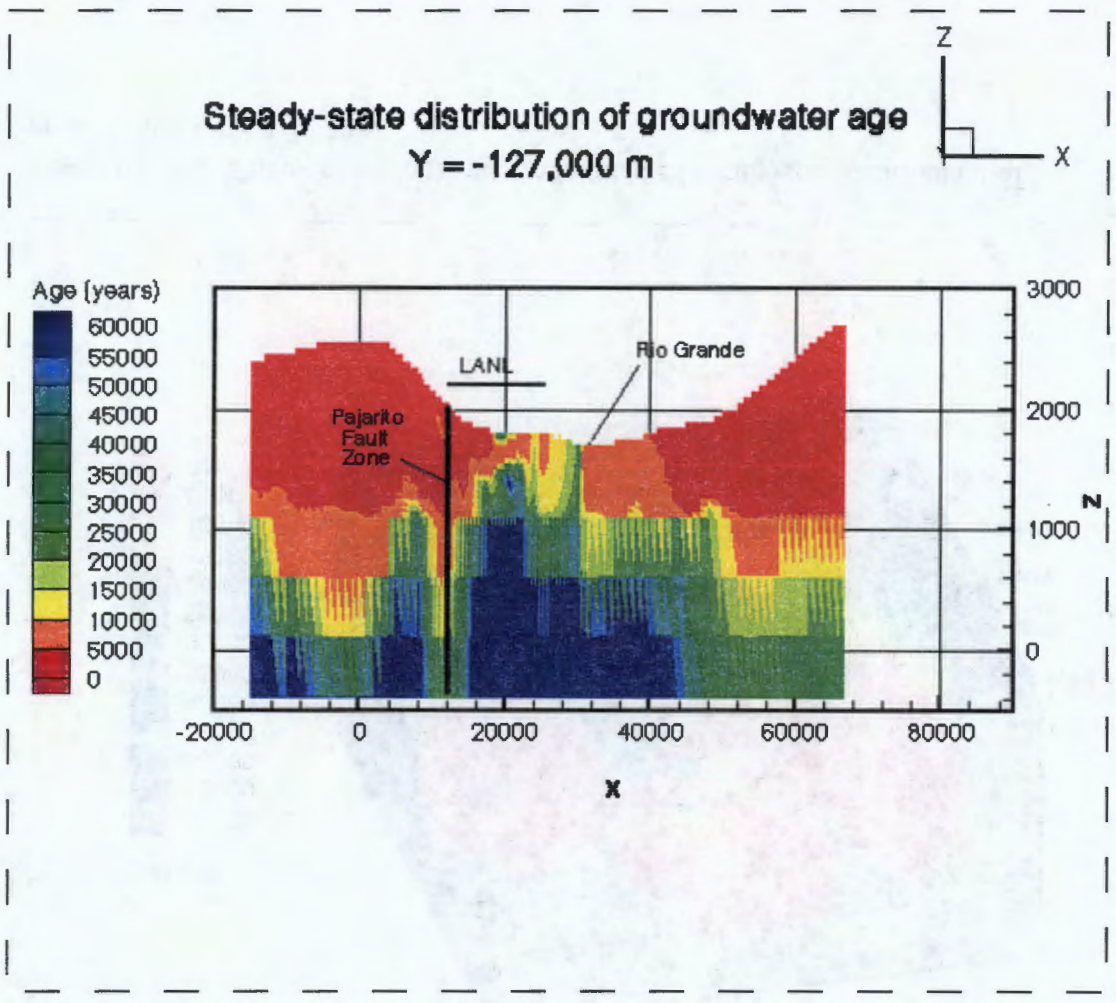

Figure 6-8(B). Simulated steady-state distribution of groundwater carbon-14 ages along y=-127,000 m.

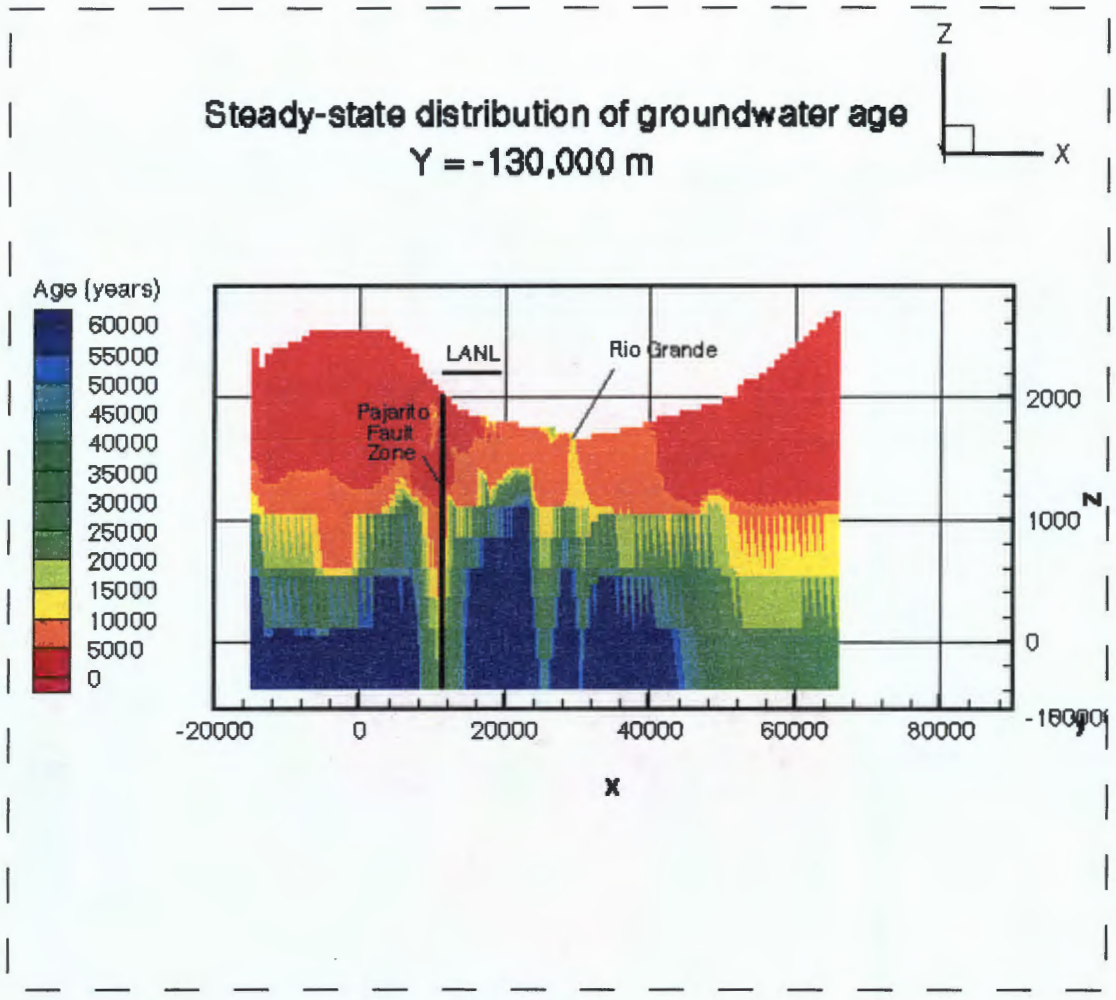

Figure 6-8(C). Simulated steady-state distribution of groundwater carbon-14 ages along y=-130,000 m.

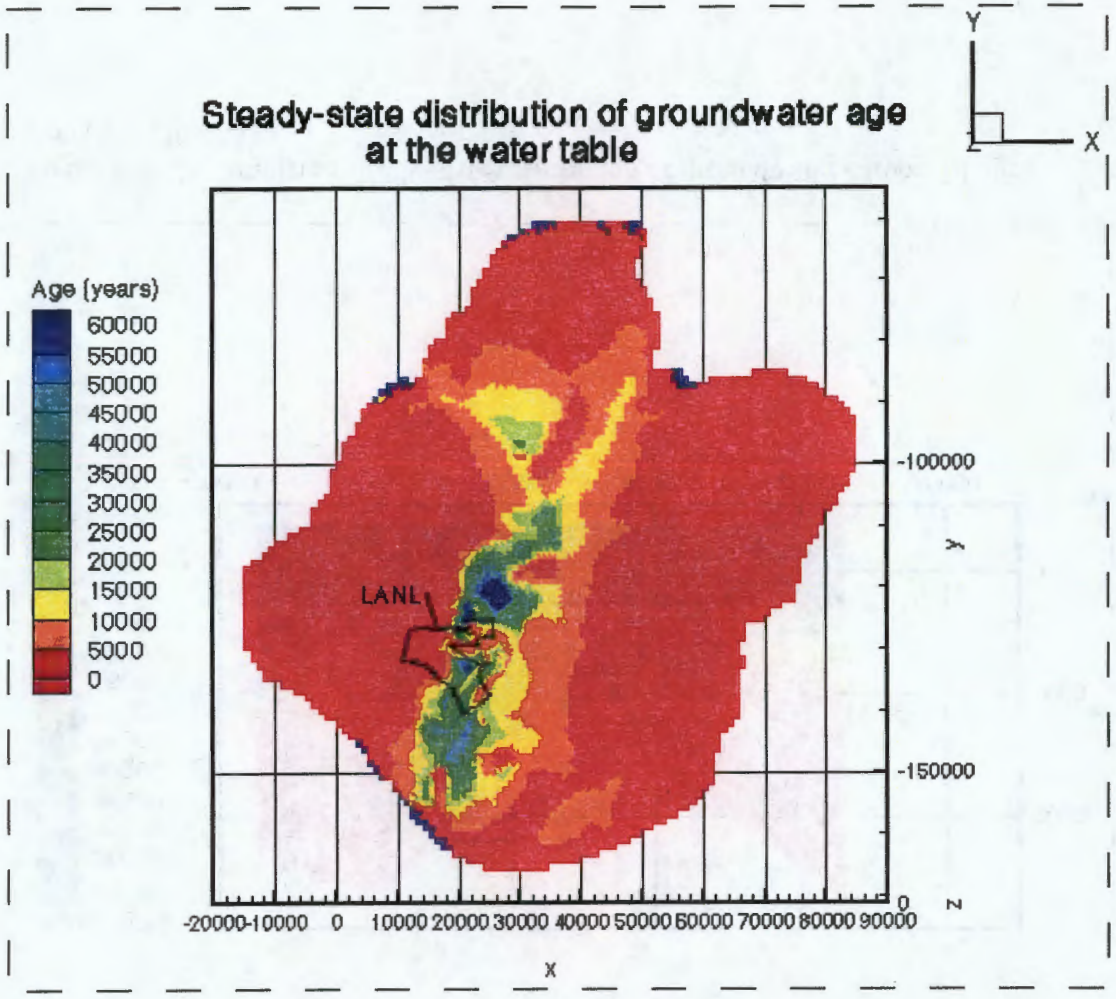

Figure 6-8(D). Simulated steady-state distribution of groundwater carbon-14 ages at the water table.

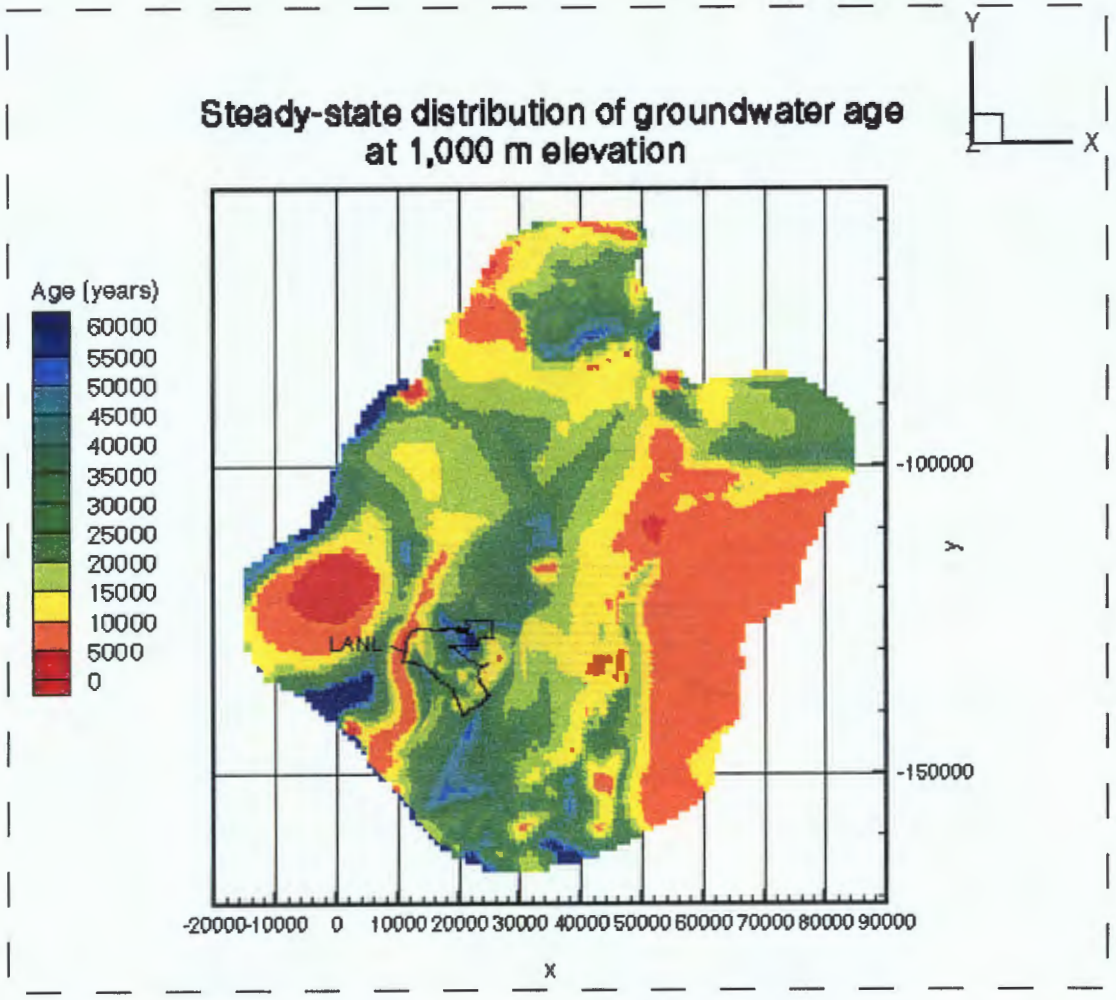

Figure 6-8(E). Simulated steady-state distribution of groundwater carbon-14 ages at the 1,000 m elevation in the basin.

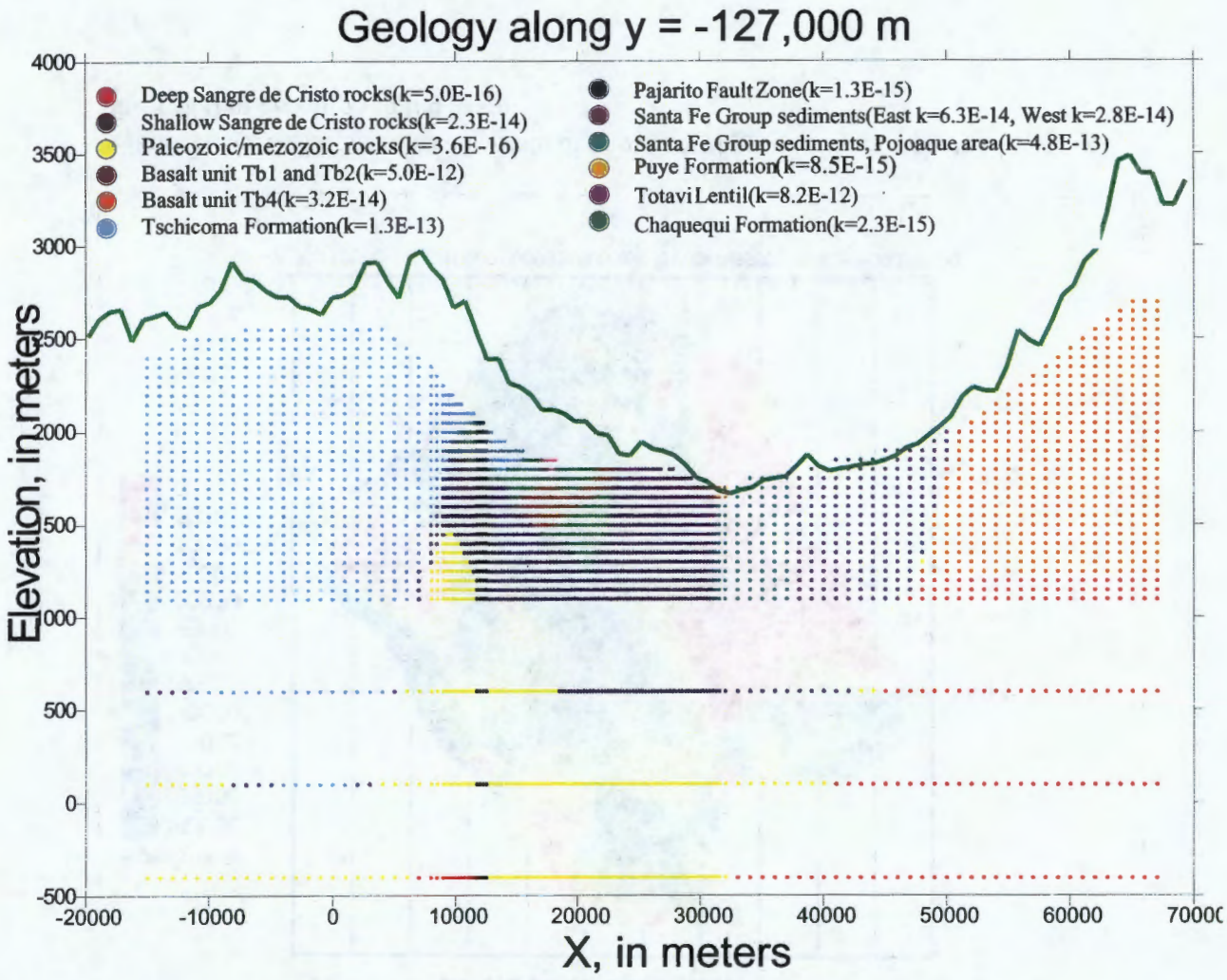

Figure 6-9(A). Distribution of hydrogeologic units and their permeabilities (unit: m^2) along y = -127,000 m

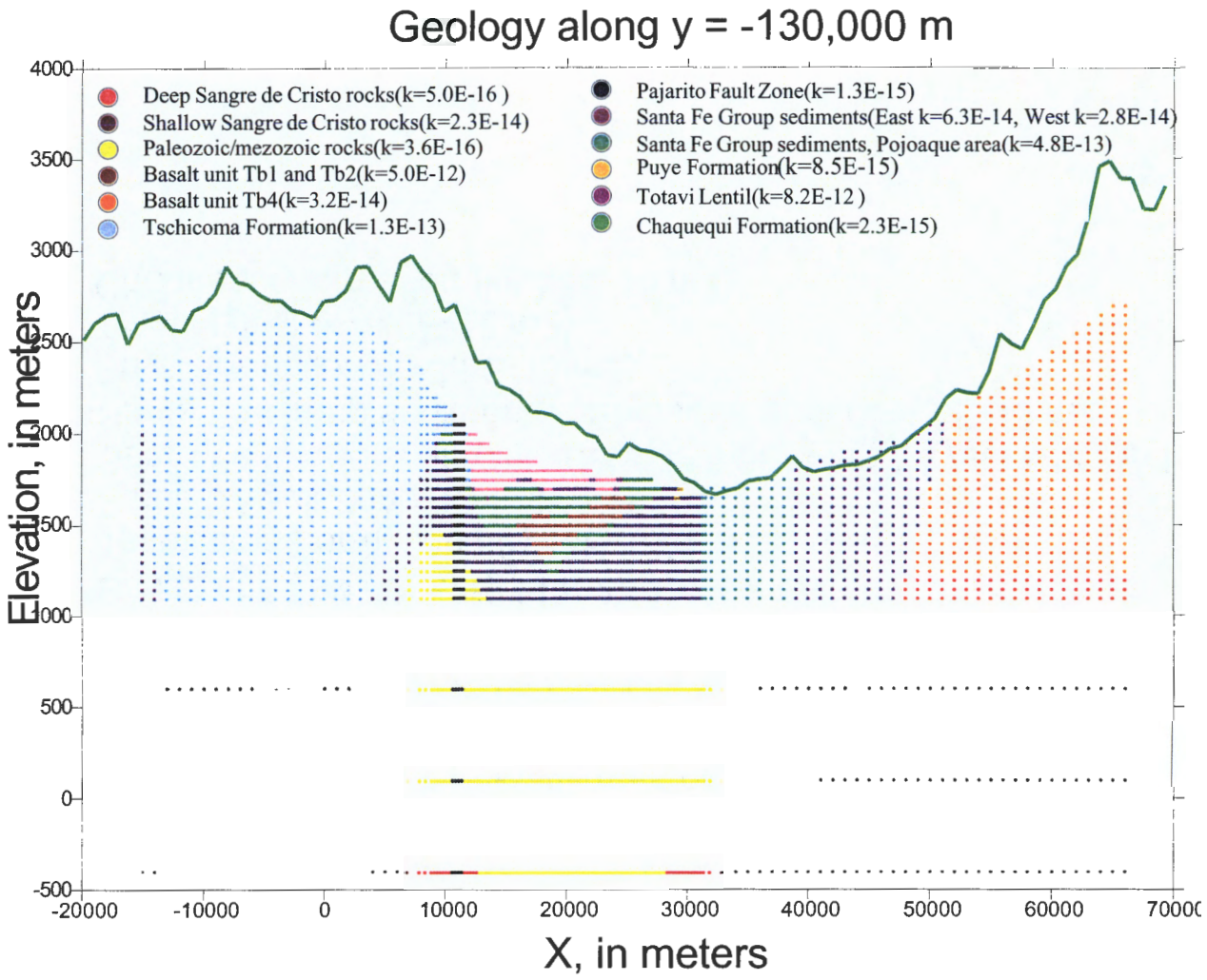

Figure 6-9(B). Distribution of hydrogeologic units and their permeabilities (unit: m^2) along y = -130,000 m

Legend

- Deep Sangre de Cristo rocks (k=5.0E-16 m2)
- Shallow Sangre de Cristo rocks (k=2.3E-14 m2)
  Paleozoic/Mezozoic rocks (shallow k=8.4E-13 m2, deep k=3.6E-
- Basalt units Tb1 and Tb2 (k=5E-12 m2)
  Basalt unit Tb4 (k=3.2E-14 m2)
- Tschicoma Formation (k=1.3E-13 m2)
- Pajarito Fault Zone (k=1.3E-15 m2)
- Santa Fe Group sediments (East k=6.3E-14 m2, West k=2.8E-1
- Santa Fe Group sediments - Pojoaque area (k=4.8E-13 m2)
- Puye Formation (k=8.5E-15 m2)
- Totavi Lentil (k=8.2E-12 m2)
- Chaquequi Formation (k=2.3E-15 m2)

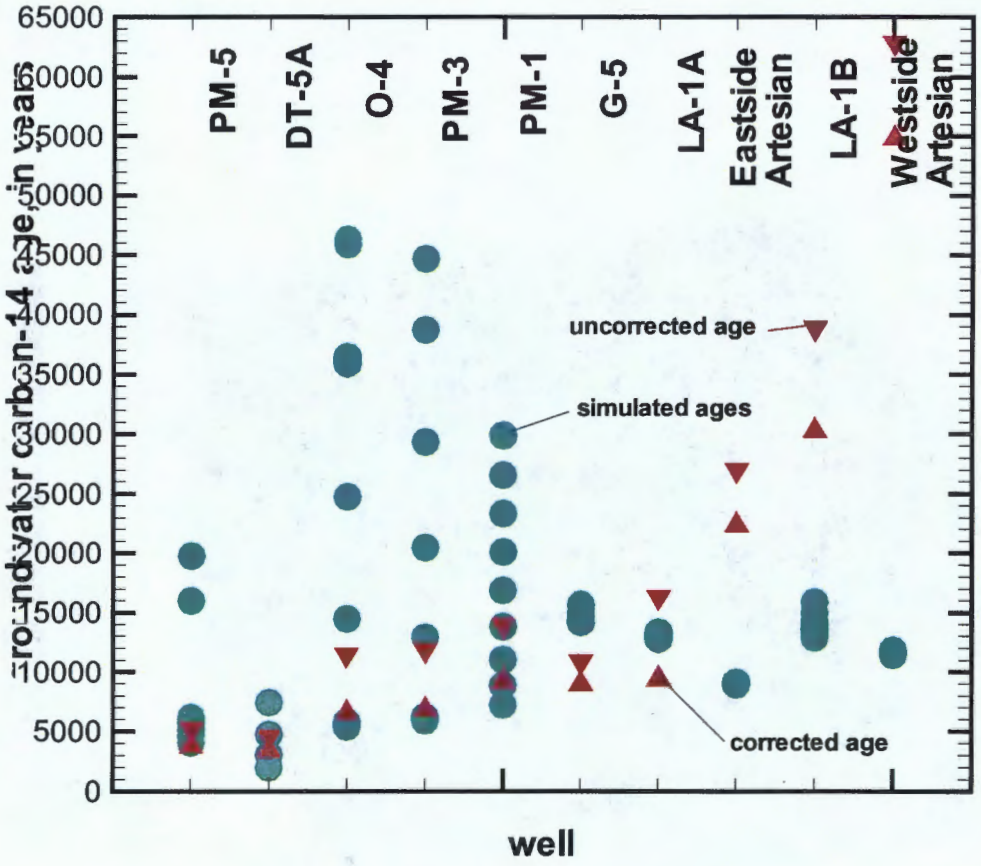

Figure 6-10. Comparison of simulated groundwater carbon-14 ages at nodes within the screened depths of wells with the corrected and uncorrected groundwater ages estimated from measured carbon-14 activities

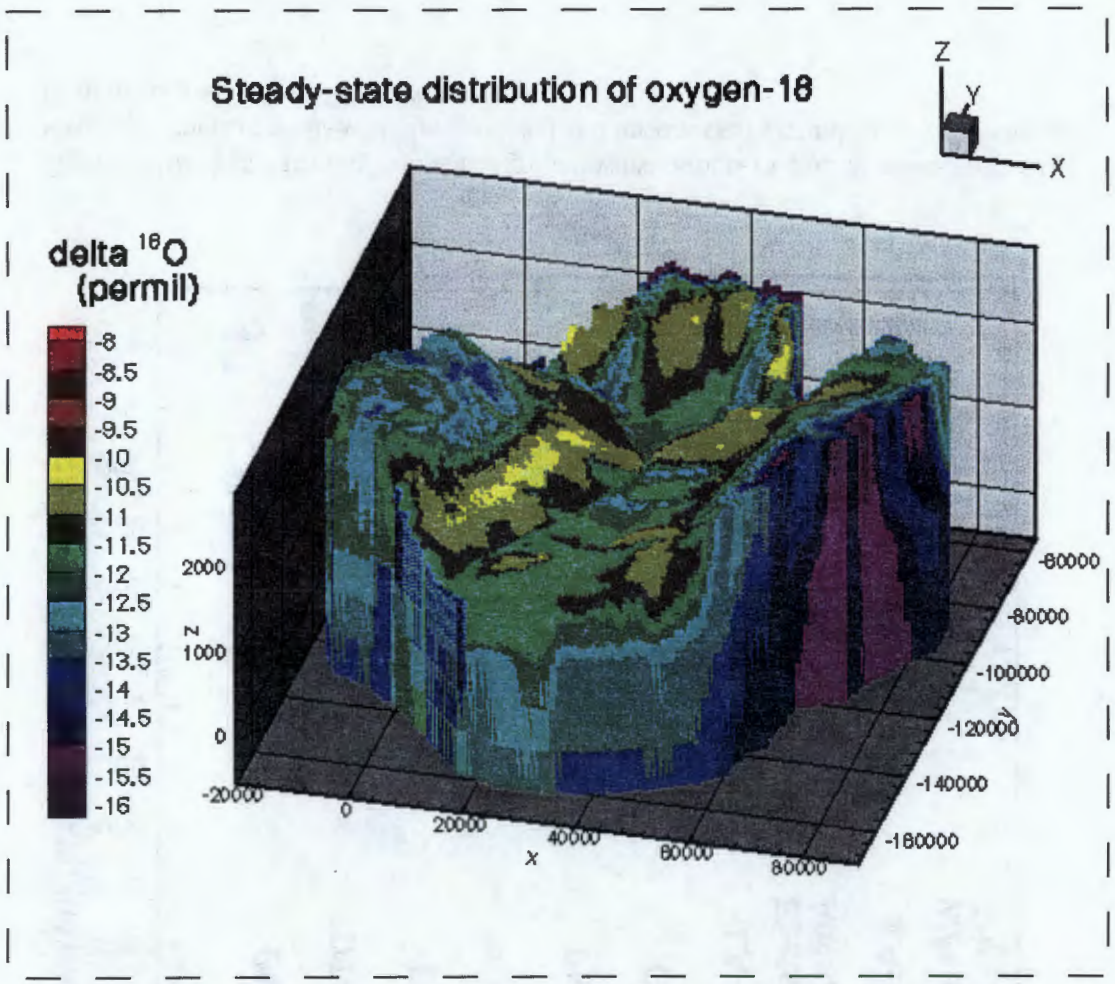

Figure 6-11(A). A three-dimensional view of simulated steady-state distribution of groundwater delta oxygen-18 values.

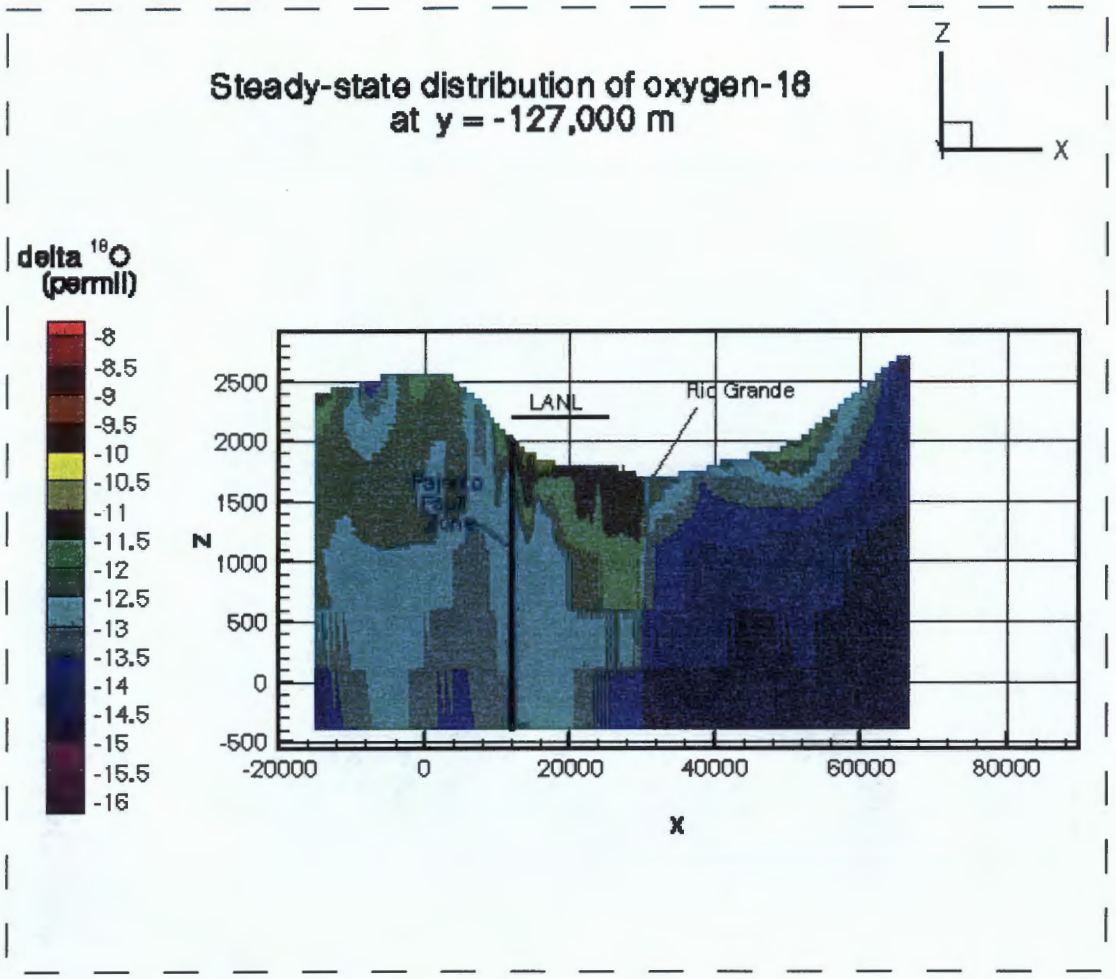

Figure 6-11(B). Simulated steady-state distribution of groundwater delta oxygen-18 values along y=-127,000 m.

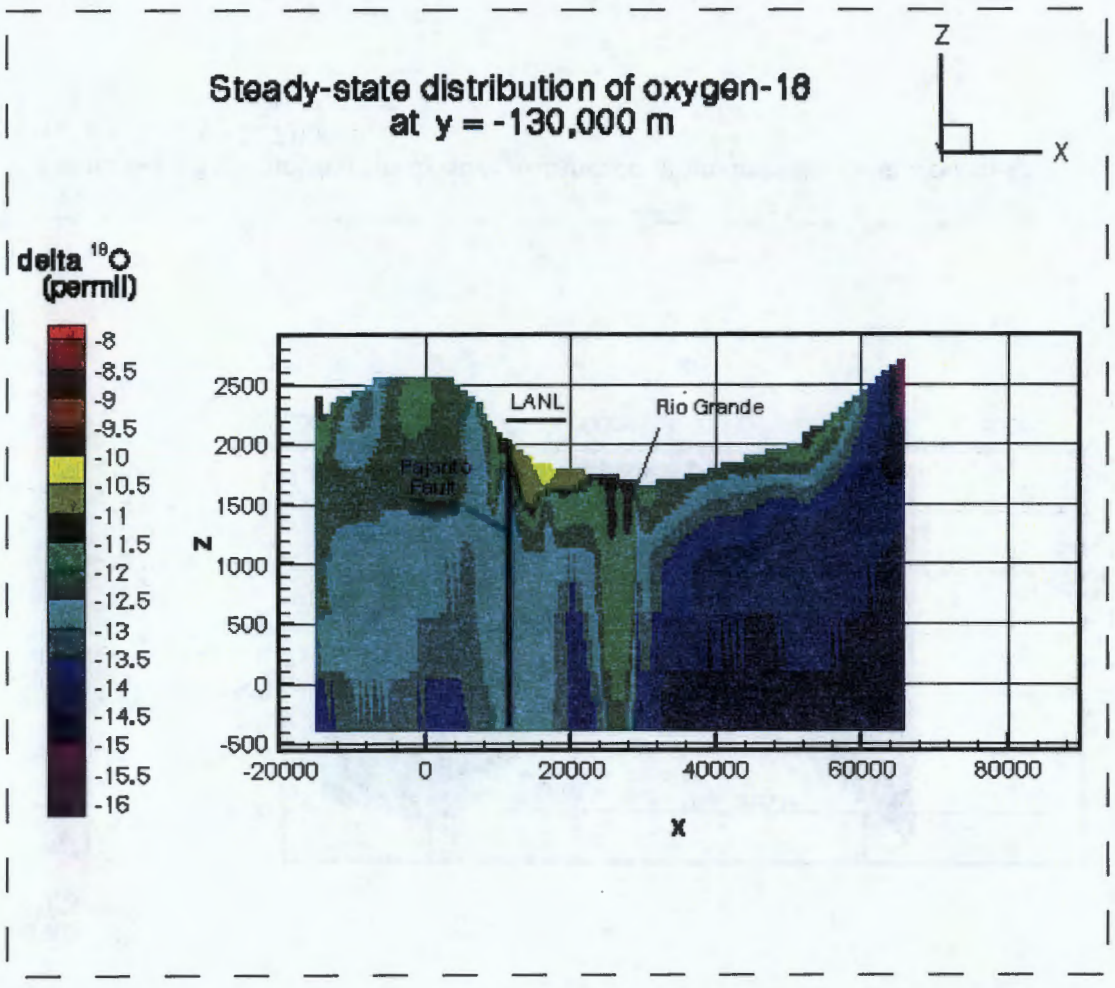

Figure 6-11(C). Simulated steady-state distribution of groundwater delta oxygen-18 values along y=-130,000 m.

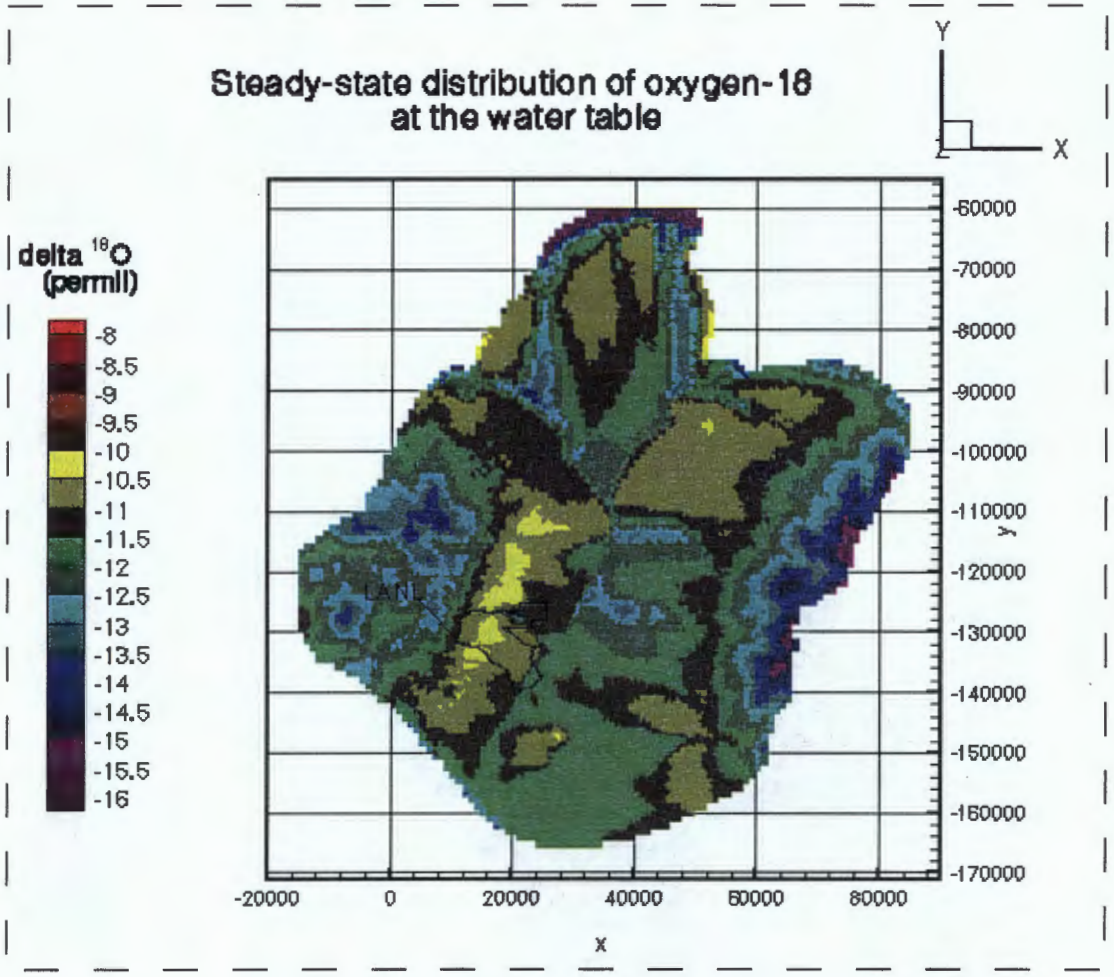

Figure 6-11(D). Simulated steady-state distribution of groundwater delta oxygen-18 values at the water table.

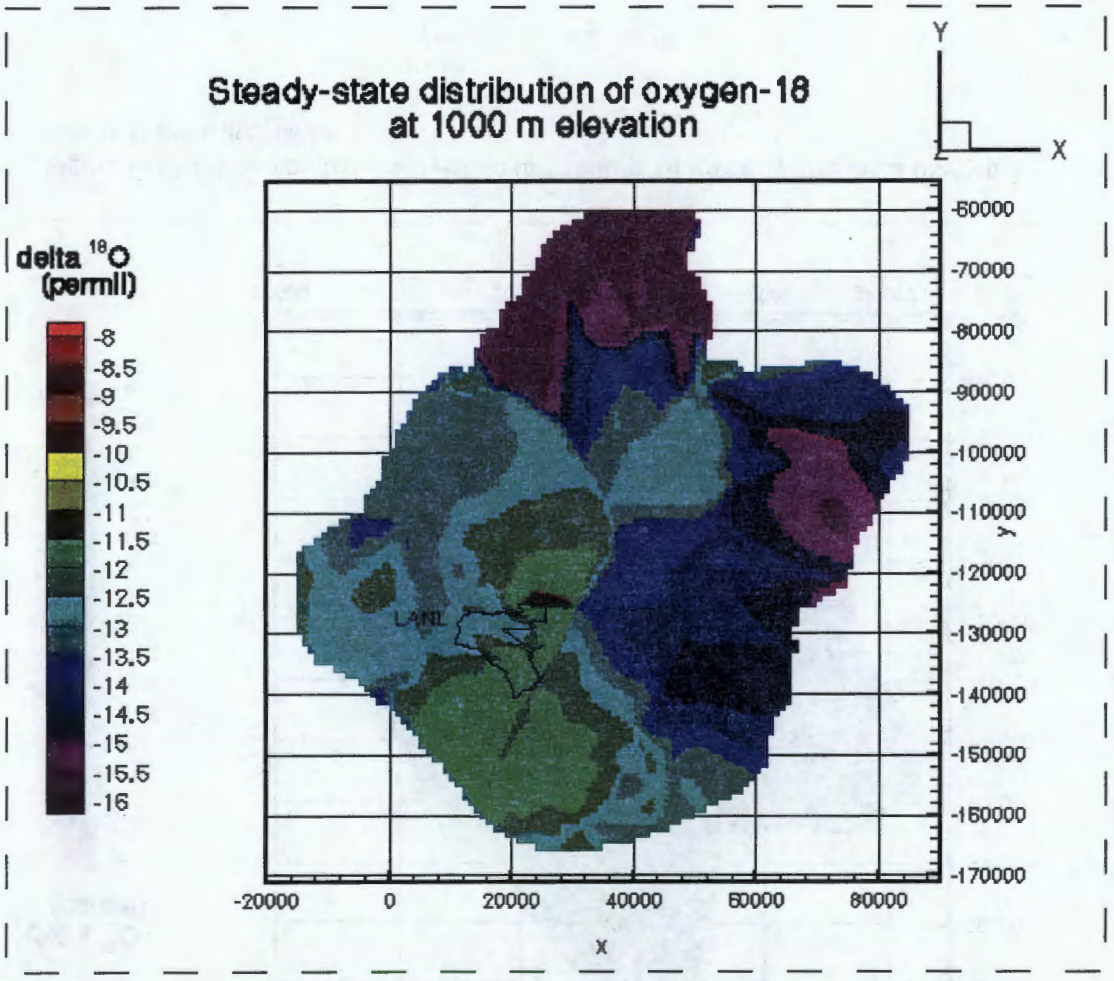

Figure 6-11(E). Simulated steady-state distribution of groundwater delta oxygen-18 values at the 1,000 m elevation in the basin.

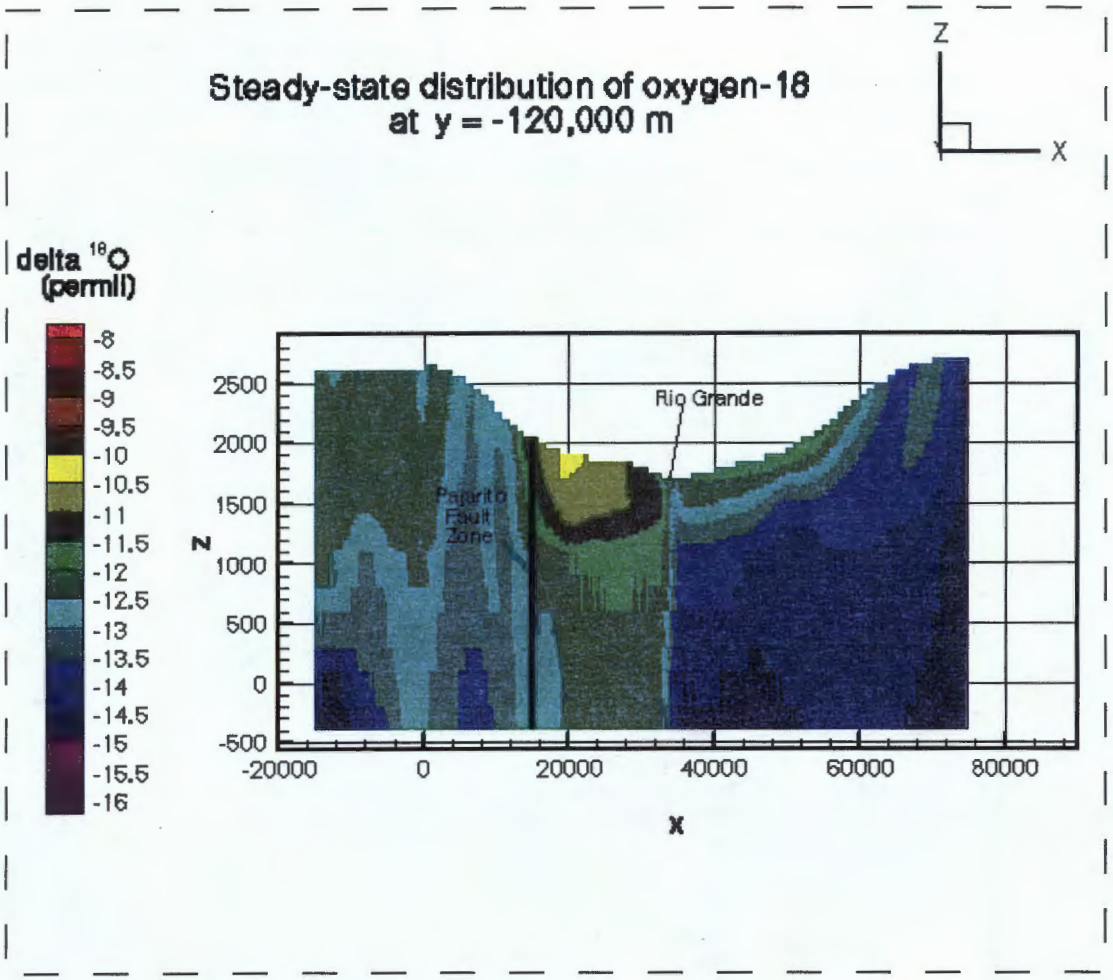

Figure 6-11(F). Simulated steady-state distribution of groundwater delta oxygen-18 values along y=-120,000 m..

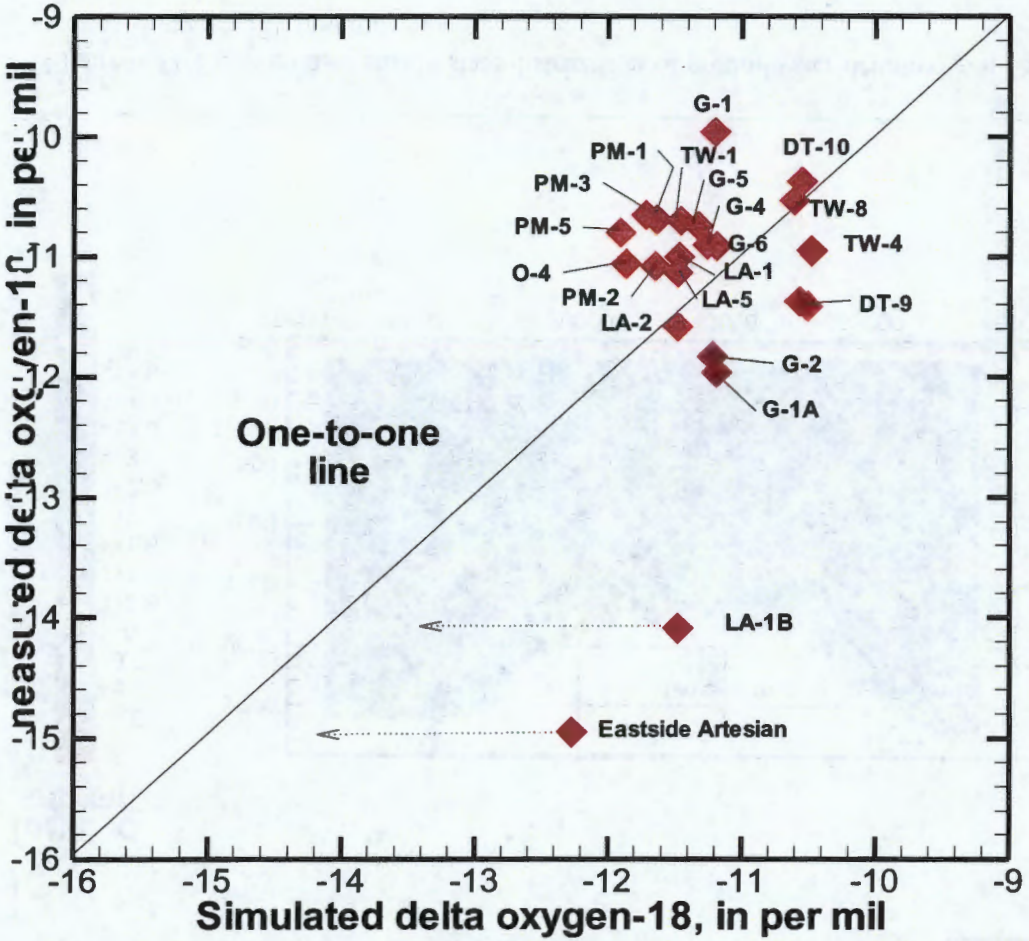

Figure 6-12(A). Comparison of mean measured delta oxgyen-18 values at individual wells ($\delta^{18}O_{mm}$) with mean simulated delta oxygen-18 values at nodes within the screened depth of the well ($\delta^{18}O_{ms}$)

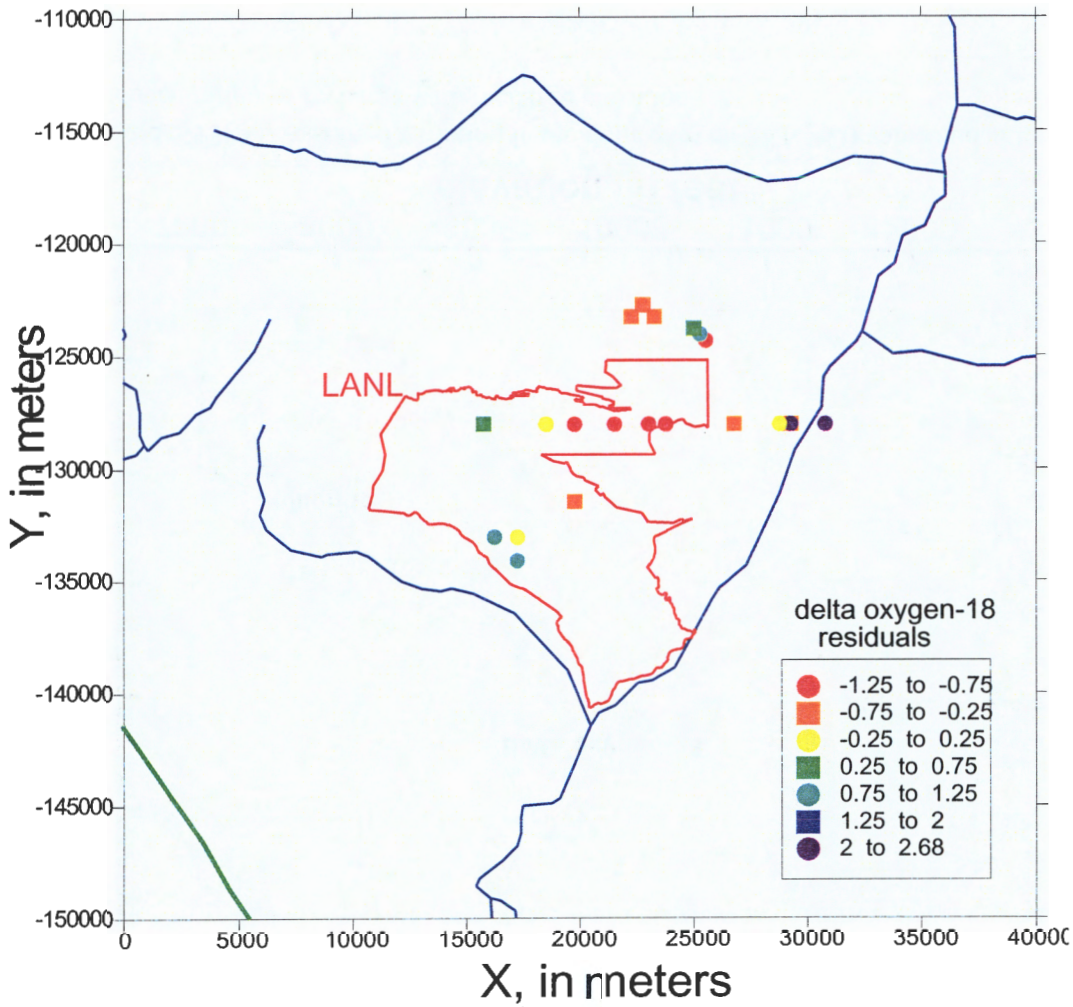

Figure 6-12(B). Residual of $\delta^{18}O_{ms} - \delta^{18}O_{mm}$ as a function of well location.

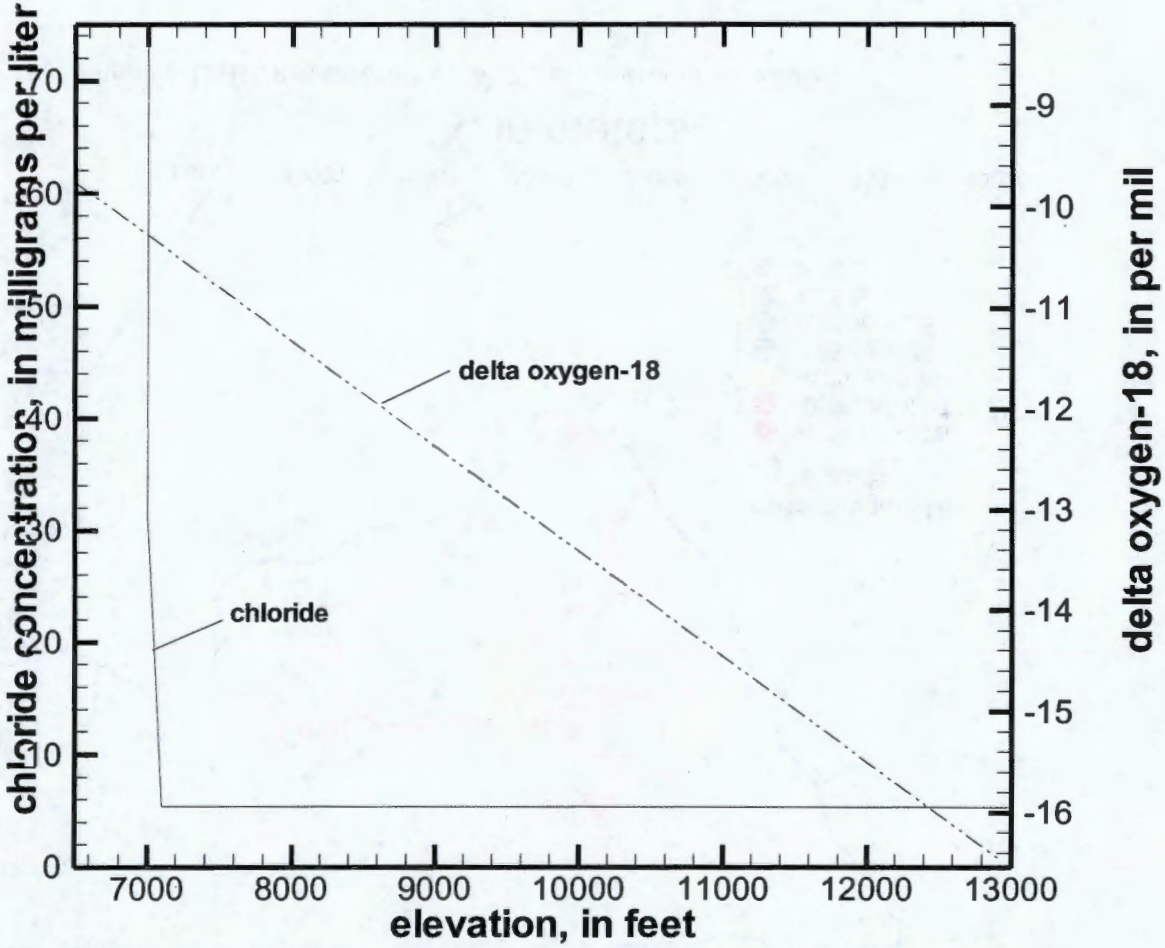

Figure 6-13(A). Assumed variation in the delta oxgyen-18 ($\delta^{18}O$) value and chloride (Cl^-) concentration of recharge with recharge elevation.

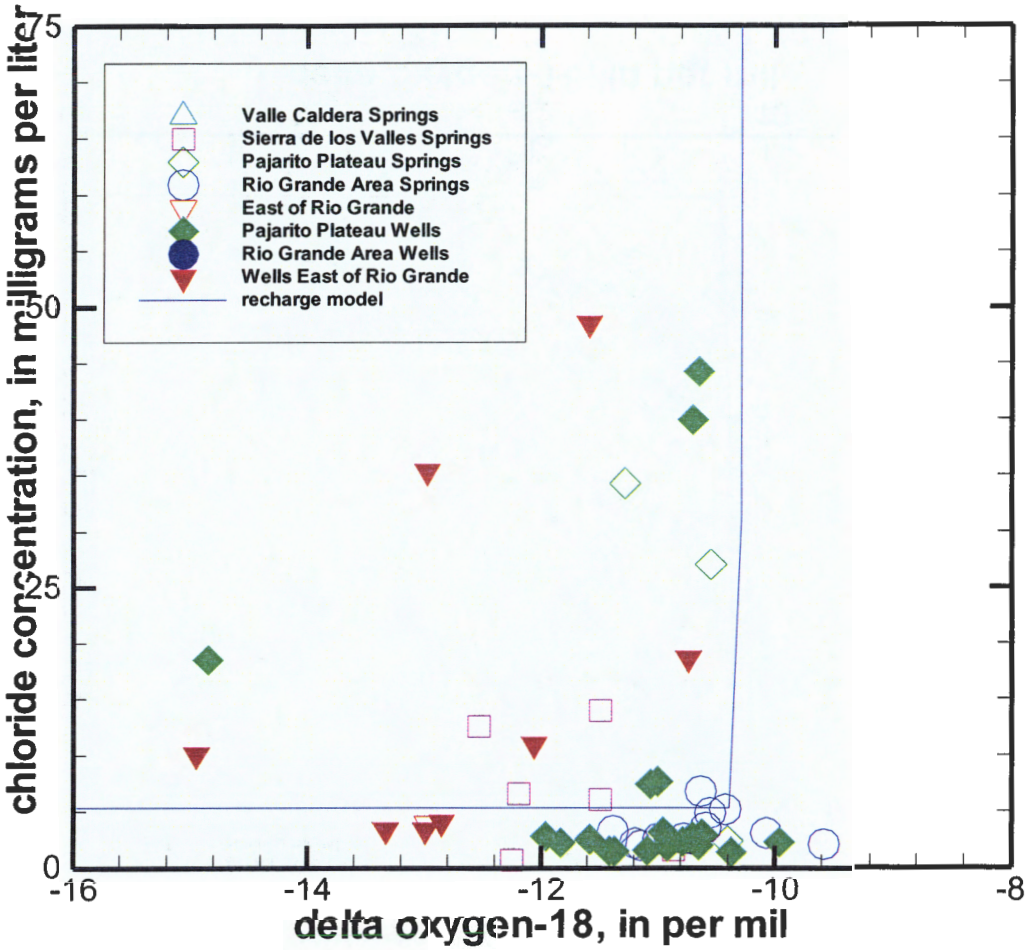

Figure 6-13(B). Comparison of the Cl^- versus $\delta^{18}O$ relation derived from the recharge model with groundwater data from springs and wells in the Los Alamos area.

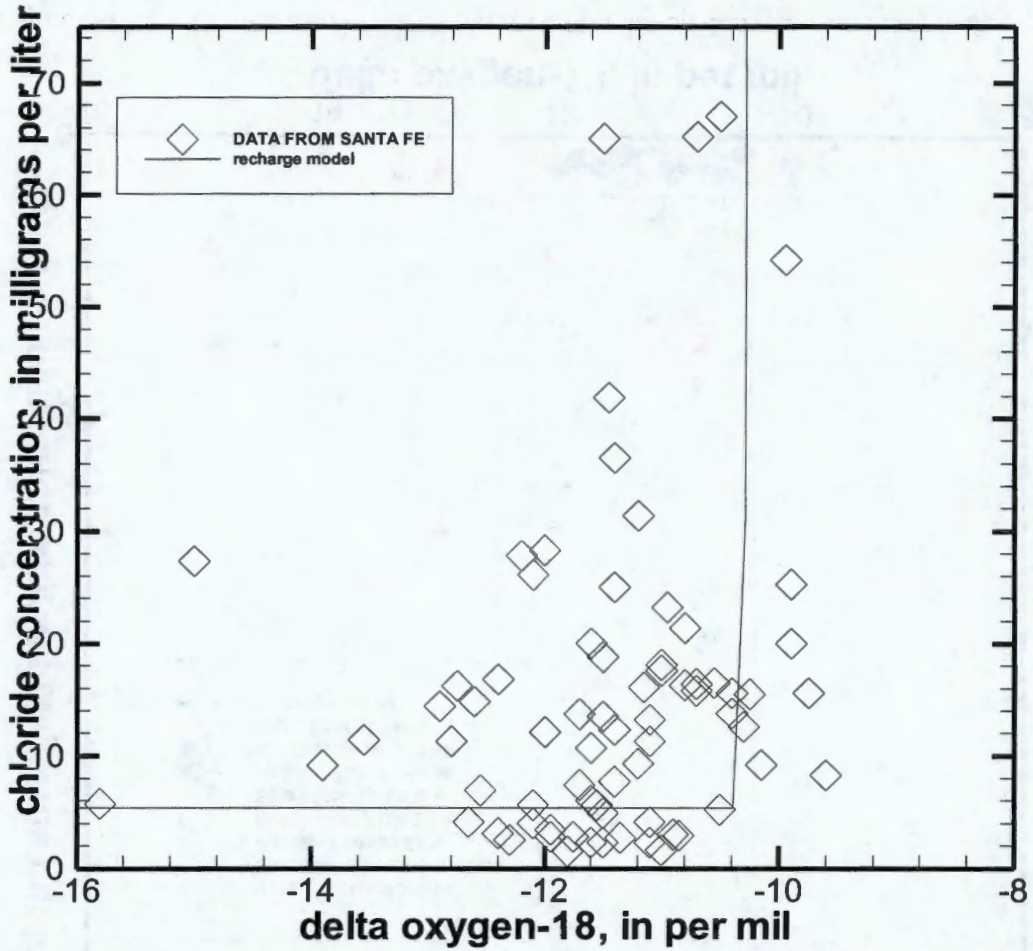

Figure 6-13(C). Comparison of the Cl^- versus $\delta^{18}O$ relation derived from the recharge model with groundwater data from wells in the Santa Fe/Pojoaque area.

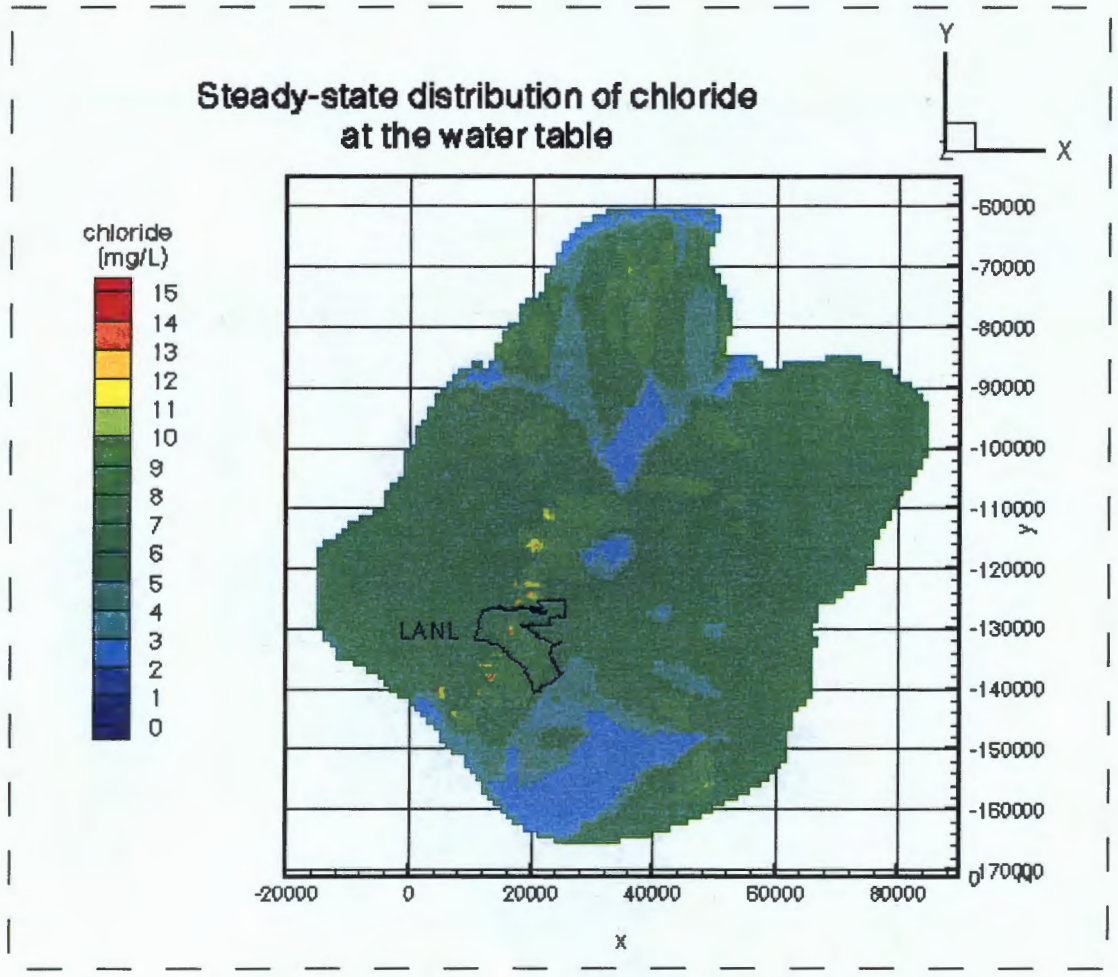

Figure 6-14. Simulated steady-state chloride concentrations at the water table.

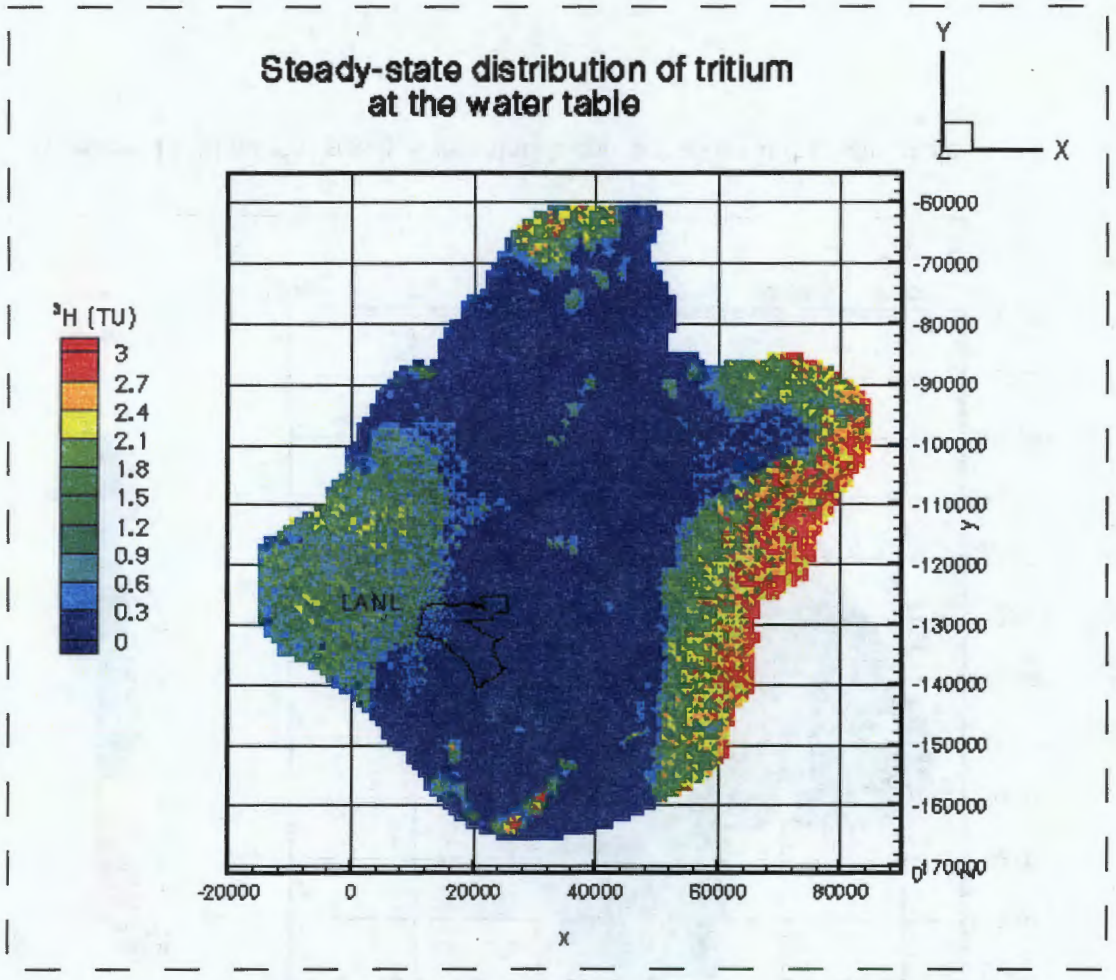

Figure 6-15(A). Simulated steady-state tritium concentrations at the water table.

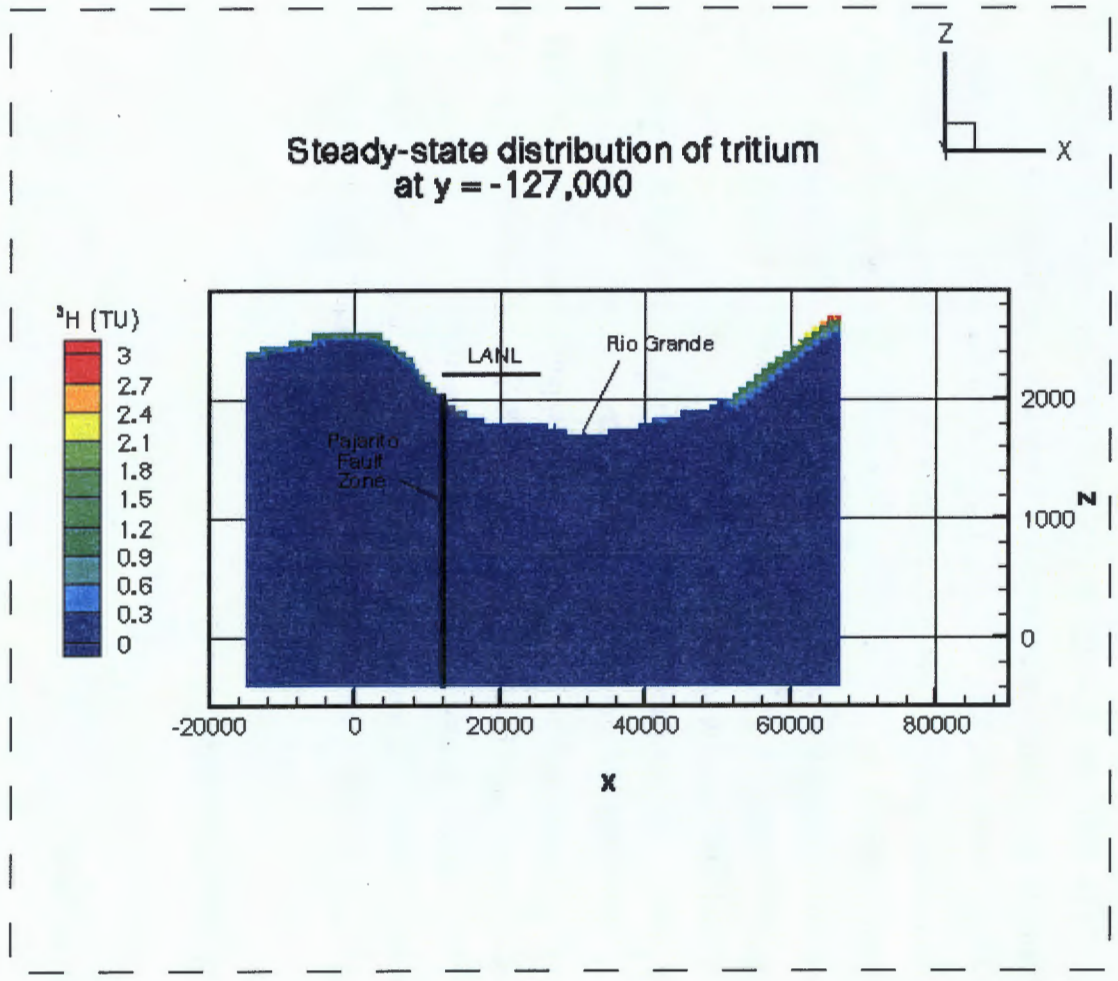

Figure 6-15(B). Simulated steady-state tritium concentrations along y=-127,000 m.

7. Geology and hydrofacies of the Puye Formation

7.1. Geologic History of the Puye Formation

The Puye Formation is a volcanogenic-alluvial fan deposited approximately 2-5 Ma. The Plio-Pleistocene alluvial fan sediments were deposited in response to rift-margin volcanism of the Rio Grande Rift and the development of the Tschicoma volcanic center located in the northeastern Jemez Mountains (Figure 7-1). Progradation of the alluvial fan developed to the east of the Tschicoma volcanic center and advanced continuously with grabben development and establishment of the Rio Grande in the Espanola Basin. Fan migration diminished due to waning sediment supply as a result of ceasing volcanic activity and development of basin-wide pedimentation by the Rio Grande. The Puye is estimated to be a 200km^2 fan which contains >15km^3 of coarse-grained volcaniclastic sediments.

Puye sedimentation is characterized by sediment deposition as stream channel deposits, sheet flood deposits, flood flows, and sediment gravity flows. These sediments are interbedded with primary and reworked pyroclastic units such as pumice falls, pumiceous ignimbrites, block-and-ash flows, rhyolitic deposits, and basaltic ash. Lacustrine deposits, formed by damming of the Rio Grande by Cerros del Rio basalts, constitute a significant portion of the distal facies of the fan. The Puye exhibits great lateral and vertical variation, although many of the pyroclastic facies display distinct cyclicity related to volcanic activity (Waresback and Tuberville 1990).

7.2. Deposit Types found within the Puye Formation

7.2.1. Alluvial Fans

Alluvial fans are cone shaped deposits formed by sedimentation that is enhanced when flows laterally confined by narrow drainages expand rapidly when discharged into a flat valley. Dominant flow processes are stream flows, gravity flows, mudflows, and flood flows. They are generally triangular or fan shaped in map view, wedge shaped in cross section, and are limited

laterally (Figure 7-2). Alluvial fans are usually poorly sorted conglomerates and breccias exhibiting crossbedding, reverse and crude grading, and lenticular bedding. Grain size can range from silt and sand to pebbles, cobbles and large boulders. Fan development occurs in rifting continental grabbens, basins, and areas of rapid uplift.

7.2.2. Stream Channel

Stream channel deposits are generally clast-supported conglomerates exhibiting imbrication and lenticular bedding, crossbedding, ripples and dunes. Depositional processes are rapid discharge, traction flow, open channel flow, saltation, and unidirectional flow. Common macroforms seen in channel deposits are longitudinal, transverse, and point bars. Deposits are generally tabular, elongate and straight with lenticular or sheet-like sand bodies. Stream channels can develop in the upper reaches of alluvial plains and are associated with rapid down dropping basins.

7.2.3. Debris Flow

Debris flows are a poorly sorted assortment of clay, silt, sand, pebbles, cobbles, and boulders. There is usually no stratification unless sequences of debris flows have been emplaced on top of each other. Debris flows are matrix-supported, reversely graded, and are generally tabular and lobate bodies of uniform thickness. In alluvial fans, they usually occur in the upper section of the fan. Debris flows are caused when a dense mass of mud and debris becomes saturated and the force of gravity causes the mass to flow down steep slopes and canyons. Volcanic terrains with large amounts of pyroclastic material, such as the paleo-terrain of the Puye fan, are particularly susceptible to debris flows. Volcanic debris flows are typically clay-poor, and can contain boulder- and cobble-rich zones aligned parallel to flow direction or have more random matrix-supported deposition. Overall, there is not a significant difference between debris flows generated in volcanic and non-volcanic terrains.

7.2.4. Sheetflood/Hyperconcentrated flood flow

Sheetflood deposits form during flood periods when excess water spills over a channel bank and spreads out across the alluvial fan depositing a shallow sheet of sand or gravel with no fines. These deposits are well sorted, well stratified, laminated and crossbedded.
Hyperconcentrated flows represent the transition from debris flow to stream channel deposition. They are generally sand size, massive or crudely stratified, cross bedded and can be normally graded. They usually occur at the top of debris flows and exhibit erosional scours into underlying deposits.

7.2.5. Lacustrine

Dominant flow processes in lacustrine deposits are sediment gravity flows, wave action and suspension settling. Lake deposits are typically laminated mudstones and sandstones displaying ripple marks, hummocky cross stratification, desiccation cracks, soft sediment deformation structures, rootlets, and coarsening upward sequences. Sand body geometry is usually circular to elongate. Lakes generally form in fault grabbens and areas of internal drainage.

7.2.6. Volcaniclastic Sediments

Volcaniclastic rocks are both sedimentary and igneous. They are derived from when pyroclastic material, which is material ejected during a volcanic eruption, is deposited by sedimentary processes.
The following are some of the most common types of volcaniclastic deposits.
Tephra. Tephra is defined as material of any size or composition ejected by volcanic explosions. There are three general classes: 1) vitric tuff and ash dominated by pumice and glass shards 2) crystal tuff and ash dominated by crystals 3) lithic tuff and ash dominated by rock fragments.
Pyroclastic Air Fall. Pyroclastic air fall deposits are derived when ejecta is thrown into the air and settles onto the surface. These deposits tend to rapidly coarsen and thicken toward the

source. Air fall deposits contain large, poorly sorted, angular blocks and bombs immediately adjacent to the center of the eruption. Fine ash is deposited down wind. Air fall deposits tend to form uniformly thick blankets of material on all surfaces regardless of topography.

Volcaniclastic Flow. Volcaniclastic flows form when tephra is remobilized and moves downslope. There are three basic types: 1) pyroclastic flows, which also produce ignimbrites 2) pyroclastic surges 3) lahars.

Ignimbrites. Ignimbrites are the most lithified portion of an ash flow deposit. They are produced by hot density currents, which are gravity-propelled clouds of ground hugging tephra and gas. Ignimbrites tend to have poor internal organization, upward coarsening, and alter to welded tuffs. Deposition follows drainages and does not mantle topographic divides.

Pyroclastic Surge. A pyroclastic surge is a rapid, episodic, or discontinuous downslope movement of pyroclastic material, gas, and/or water. Individual deposits are thinner and finer than ignimbrites and richer in crystals and rock fragments. They exhibit well-defined internal organization, planar- and trough- crossbedding. Surge deposits are usually thicker in valleys and thinner over topographic divides.

Lahars. Lahars are mudflows formed of water saturated volcanic material and can be very voluminous and extensive.

Base Surge. Base surges are sediment gravity flows that form when steam saturated eruption columns collapse and travel outward across the surface as a turbulent mix of water vapor or condensed droplets and solid particles. The deposits are moderately to poorly sorted with a rapid decrease in grain size and thickness away from the source. There is commonly crossbedding and fine laminations.

7.3. Hydrofacies of the Puye Formation

The Puye is made up of three distinct units: the Puye fanglomerate, lacustrine facies, and the Totavi Lentil member (Table 7-1). The Puye fanglomerate can be divided into three main facies and nine subfacies. The three main facies are: clast-supported conglomerates which are further divided into channel deposits and sheet deposits; matrix-supported conglomerates which consist of clast-rich deposits and matrix-rich deposits; pyroclastic facies which can be broken down into

block-and-ash flows, lower tephra group, middle tephra group, upper tephra group, and phreatomagmatic basalts. The facies observations and descriptions below are taken from (Tuberville et al. 1988; Waresback et al. 1990; Turbeville 1991)

7.3.1. Puye Fanglomerate

Clast-Supported Conglomerates. The clast-supported conglomerates are the dominant lithofacies within the Puye Formation. These deposits are divided into two subfacies based on differences in external structure.

The channel deposits change considerably with grain size, geometry, thickness, internal structure, and position within the fan. Proximal to medial-fan exposures tend to exhibit broad channel-form geometries with individual channel sequences ranging from 30 cm to >6 m thick and showing upward thickening and coarsening with abrupt thinning downfan. Coarse grained, poorly sorted deposits that display normal and reverse grading tend to dominate proximal exposures. Clasts are generally angular to subrounded cobbles and pebbles. Some of the stream-channel deposits are capped by a pebbly sandstone, which forms discontinuous lensoid bodies with horizontal to low-angle stratification.

Distal stream-channel exposures are notably much thinner, 10 cm to 3.5 m; better sorted; and finer grained. They tend to be laterally extensive lenticular bodies, which are commonly polymodal and normally graded with better developed stratification than in other exposures.

Sheet deposits form sandy-pebble conglomerates and pebbly sandstones that are laterally continuous throughout the Puye. Proximal deposits are confined to lower parts of the section while medial and distal deposits can be found throughout the fan sequence. Sheet deposits range in thickness from 10 cm to 3.5 m and are laterally extensive for several hundred meters with only minor thinning. Stacked sand and gravel couplets are common and range from 1 cm to 5 cm in thickness.

Sheet deposits are very similar to braided stream deposits but can be distinguished by laterally extensive sheet-like geometry, absence of deep scours, laterally continuous with uniform horizontal stratification, and lack of apparent grading.

Matrix-Supported Conglomerates. Matrix-supported conglomerates are fluidized sediment-gravity flows produced by a variety of debris-flow deposits. These debris flows are divided into clast-rich deposits and matrix-rich deposits, also referred to as clast-poor deposits.

Clast-rich deposits are sandy-cobble and boulder conglomerates that are more dominant in proximal exposures and upper parts of the fan sequence. Deposits range from 20 cm to >4 m thick, are laterally continuous, exhibit tabular geometry parallel to flow direction, and can continue downfan for several kilometers. Clast-rich deposits are characterized as being unstratified, polymodal, poorly sorted, and having a wide grain-size distribution from clay size particles to boulders >3.5 m in diameter. Coarser grained conglomerates contain reversely graded basal layers and overall reverse coarse-tail grading.

Matrix-rich deposits are generally muddy-sandy pebble conglomerates and pebbly-muddy sandstones which predominate medial and distal fan exposures. Deposits tend to be polymodal, massively bedded, lack basal shear zones or well developed reverse grading, locally exhibit more abrupt decreases in grain size downfan, lack traction structures and erosional scours, and commonly exhibit coarse-tail normal grading. Thickness ranges from 20 cm to >3m. Subaerially emplaced deposits form laterally continuous deposits truncated by sheetflood or braided stream deposits.

Pyroclastic Facies. Primary pyroclastic facies consist of clast-supported dacitic, rhyodacitic, and rhyolitic pumice falls, poorly sorted ignimbrites and block-and-ash deposits.

Block-and-ash flow deposits are dense, nonvesicular lava blocks set in an ash matrix with subordinate amounts of poorly vesicular pumice. These deposits are confined to proximal exposures in the fan.

Tephra deposits in the Puye have been divided into three groups based on distinctive changes in clast type, deposition environment, and source. The three groups are the lower tephra group, middle tephra group, and the upper tephra group. The lower tephra group includes widespread pumice-fall and thin ash flows, thin ignimbrites and tephra redeposited as pumiceous clast-poor debris flows.

The middle tephra group consists of lithic-rich nonwelded ignimbrites, coarse-grained lithic-rich pumice falls and fine-grained capping ash falls. Two large dacite pumice blocks and pumice flow deposits have also been observed in this group.

The upper tephra group is made up of several rhyodacitic pumice fall deposits, abundant lake-deposited pumice and ash, and water lain basaltic ash. Two distinct rhyolite pumice falls are located in the upper tephra group at the top part of the fan sequence. In the central portion of the fan, they have been observed to overlie a red clay horizon.
Phreatomagmatic basalts derived from Cerros del Rio volcanic activity interfingers with Puye fluvial gravels and lacustrine sediments in distal portions of the fan.

7.3.2. Lacustrine Facies

Lacustrine deposits, resulting from damming of the Rio Grande by Cerros del Rio basalts, dominate distal fan exposures. Lake deposits are characterized by subaqueously emplaced mudflows, horizontal laminations, abundant tephra, micaceous muds and clays, and lateral grading to stacked pumiceous clast-poor debris flow and sheetflood deposits that form a prominent apron around the perimeter of the Puye fan. Lake sediments generally lack particles larger than small pebbles. The apron ranges from 2 m to 10 m thick.

7.3.3. Totavi Lentil Member

The Totavi Lentil is a pebble to cobble axial stream gravel deposited by the ancestral Rio Grande. Gravel units range from 1.5 ft to 10 ft thick, exhibit cross and planar bedding, and are interbedded with 1ft to 5 ft thick sand lenses. Imbrication and long axis orientation indicate paleoflow direction to the southwest. Total thickness varies from 16 ft to 150 ft. Fills channels in and locally interbedded with the Puye Fanglomerate. In some areas, the Totavi overlies the Santa Fe group.(Dethier 1997). A photograph of an outcrop of the Totavi Lentil is shown in Figure 7-3.

7.4. Permeability

Very few field-scale measures of permeability for the Puye Formation are available. Table 7-2 summarizes these data, both for five tests conducted in wells screened entirely within the Puye and for six tests in wells screened in multiple units including the Puye. For the latter six tests, the contribution of the Puye Formation to test results is unknown. Lithologic logs from these wells that were tested provide thickness estimates for two facies within the Puye: the "fanglomerate" and the Totavi Lentil. Permeability measurements indicate the fanglomerate is, on average, less permeable than the Totavi Lentil.

A crude estimate of permeability has been done for each of the deposit types found within the Puye Formation (Table 7-3). There are plans for a more detailed study of permeability in the future.

Channel deposits within the fan are dominated by well-sorted pebble-cobble gravels. They are clast-supported conglomerates with medium to coarse sand matrixes and little to no cementing. Based on this, permeability is estimated to be high to medium.

Sheet deposits are also gravel rich with minor to no fines and are estimated to have high to medium permeability. Clast-rich debris flows are matrix-supported, but because they are clast rich, the permeability is estimated to be medium to low. Clast-poor debris flows, however, are dominantly made up of fines and would most likely have low permeability. Block-and-ash flows and tephra deposits have a varying permeability dependent on the permeability properties of ash and how extensively the ash has been weathered to clays. Fractured basalts have high permeability. Axial stream gravels are made up of thick sequences of pebble-cobble gravel beds, similar to other channel deposits in the Puye. They would also have high permeability. Lacustrine deposits are dominantly silt to coarse sand, indicating medium to low permeability. When applied to large-scale hydrofacies, the Fanglomerate would have medium permeability, Totavi Lentil permeability would be high, and permeability of Lacustrine facies would be medium to low.

7.5. Size and Geometry

The gravel beds of the Totavi Lentil are defiantly the most permeable unit of the Puye Formation. This makes understanding the size, geometry and continuity of the Totavi very important since those beds will have a great effect on increasing the groundwater flow rate. East-West and North-South dimensions, thickness, and elevation at the top of the bed of Totavi Lentil outcrops were estimated using *Geology of White Rock quadrangle, Los Alamos and Santa Fe Counties, New Mexico* (Dethier 1997) in order to better understand the size and continuity of the Totavi. Table 7-4 shows the minimum and maximum estimates of outcrops in Ancho, Water, Mortandad, Sandia, and Los Alamos canyons.

7.6. Lateral Facies Variations

The following descriptions of lateral facies variations in the Puye are taken from Waresback and Turbeville (1990). Proximal facies are dominated by coarse-grained ignimbrites and block-and-ash sequences which grade downfan to coarse, better sorted clast-rich debris flow deposits (Table 7-5). The debris flow deposits then locally grade laterally to hyperconcentrated flood-flow deposits, which gradually change to sheetflood and stream-channel facies interbedded with ash-rich clast-poor debris flow deposits. Downfan thinning and fining trends were also observed within these sequences.

Debris flow deposits and lithic-rich ignimbrites show marked lateral variability. Lake deposits interbedded with flow deposits contain abundant pumice and ash. Transitions from inversely graded, clast-rich deposits to fine-grained matrix supported deposits occur in as short a lateral distance as 200 m.

Stream channel deposits compose up to 50% of some sequences in proximal exposures and were observed to decrease in abundance progressively downfan and are replaced volumetrically by better-sorted, thinner, and finer-grained distal braided-stream and sheetflood deposits.

Sheetflood deposits volumetrically dominate in outcrop over distal braided-stream deposits and are approximately proportional to clast-poor debris flow deposits. Downfan, sheetflood deposits exhibit decreases in thickness, improved sorting, better-developed horizontal

stratification, and decreases in grain size and angularity. Proximal deposits tend to be more massive while distal deposits show increases in cross-stratal, planar bedsets and horizontally laminated sands and mud.

Several meters of conglomerates and mudstones commonly separate pumice falls in proximal exposures. Distally they become more closely spaced and converge to form thick sequences of primary and reworked pumice and ash.

7.7. Cyclic Facies Variations

The following observations of cyclic facies variations were made by Waresback and Turbeville (1990). Majority of the alluvial fan's development is characterized by the stacking of distinctive eruption related depositional sequences on the 5-m to 30-m scale. Cyclic facies resulted from tephra and volcanic-debris flows generated during explosive eruptions and reworking by fluvial processes during inter-eruptive periods.

Proximal exposures contain cyclic sequences of one or more tephra deposits overlain by pumice and ash-rich debris in the lower portions of the fan and by very coarse-grained block-and-ash flow deposits toward the top of the section. Between eruptive events, unconsolidated lava and pyroclastic material was redistributed as clast-rich debris flows emplaced in stacked assemblages.

Clast-supported conglomerates also developed above individual coarse-grained mass-flow sequences, where the upper parts of the debris flow deposits were partially reworked by braided streams. Coarsening or fining upward trends in fluvial conglomerates indicate individual flood cycles. Sheet-like geometries, poor sorting, common normal grading and horizontal bedding of some conglomerates represents periods of intermittent aggradation.

Medial exposures consist of one or more airfall units overlain by ashy debris flow deposits. Thick sequences of alternating clast-rich and matrix-dominated conglomerates developed as debris flows episodically infilled stream channels following eruptions.

In distal exposures, primary pyroclastic deposits are nonexistent or thin and interbedded with stacked pumiceous clast-poor debris flows and sheetflood deposits. Fine-grained, braided stream and intermittent sheetflood conglomerates separate individual clast-poor debris flow deposits.

Inter-eruptive depositional sequences are more complex than in proximal exposures. Clast-rich debris flow deposits and coarser-grained stream-channel deposits are lacking in distal fan exposures except toward the top of the overall succession, indicating abrupt fan-wide progradation.

A depositional megasequence is observed in the Puye defined by a large-scale coarsening- and thickening- upward sequence. This is most evident in proximal exposures where the fan is thickest. The megasequence reflects nearly continuous emplacement of the Puye between ~4.0 to 1.7 Ma. The Puye megasequence is capped in proximal and medial exposures by stacked stream-channel deposits. The overall succession in areas where the megasequence is incomplete can be described by at least two coarsening- and thickening- upward sequences. The lower 70-m of the fan exhibits progradation of coarse-grained streamflow and clast-rich debris flow conglomerates over finer-grained braided-stream, sheetflood and clast-poor debris flow deposits. The other sequence is observed in the 70 m to 110 m interval which consists primarily of stacked deposits of subaqueously emplaced clast-rich debris flow and clast-poor debris flow deposits that grade upfan to subaerially emplaced debris-flow deposits and locally to hyperconcentrated flood-flow conglomerates. In medial exposures, the upper sequence is characterized by rapid vertical transition from coarse clastics to fine-grained mudstone, which is overlain by stacked conglomeratic mudstones that occur as uniform, laterally continuous, sheet-like beds ranging from 20 cm to 2.6 m thick. The overall succession is then capped by a thick sequence of channel-fill gravels.

7.8. Heterogeneity

The Puye Formation has great variability. Understanding the changes that occur throughout the Puye is very important in order to model water flow throughout the formation. To achieve this understanding, the heterogeneity can be broken down into three scales: large, medium, and small (Table 7-6).

7.8.1. Large Scale

Large scale heterogeneities represent the overall changes throughout the Puye Formation (Figure 7-4, Table 7-7. In this scale, the west to east changes are more significant than vertical change as the units vary from the fanglomerate to lacustrine and Totavi units. Heterogeneity occurs at this scale horizontally from 1-10km (.6-6mi) and vertically from .5-4km (.3-2.5mi). On a more detailed level, the fanglomerate can extend horizontally 3-8km (2-5mi) and vertically .4-3.4km (.2-2mi), the Totavi Lentil can extend horizontally 2-7km (1-4mi) and vertically .2-2.4km (.1-1.5mi), and the lacustrine units can extend horizontally 1-6km (.6-3.5mi) and vertically .2-2km (.1-1.2mi). Another observation that can be made on the large scale is whether the Totavi Lentil extends as a continuous sheet or "pancake layer" below the fanglomerate or if it "stair-steps" down west to east. These two theories are currently under debate. Proximal fan is dominated by the fanglomerate. Medial fan contains all three units, and distal portions of the fan are dominated by lacustrine and Totavi Lentil units.

7.8.2. Medium Scale

Medium scale heterogeneities are the larger bedding features seen in outcrop (Figures 7-5 and 7-6). The scale that these transitions occur is horizontally .6-61m (3-200ft) and vertically .6-30m (2-100ft). Some of the heterogeneity that is observed at this scale is the difference between pyroclastic facies such as pumice and ash falls, ignimbrites, block-and-ash flows. These can extend horizontally and vertically 1-5m (3-16ft). Other observations that can be made are gravel beds 1.5-9m (5-40ft), sand beds .6-2m (2-6ft), and boulder rich zones .6-1m (2-4ft). The differences between stream-channel, debris flow, sheetflood, and mudflow deposits are also made at this scale. Some larger sedimentary structures such as lenses, planar bedding, and cross stratification can be observed on a medium scale. Stream channel, sheetflood, mudflow, and tephra deposits occur throughout all portions of the fan. Block-and-ash flows and clast-rich debris flows are restricted to proximal fan. Clast-poor debris flows occur in medial and distal portions of the fan. Basalts strictly occur in the distal fan.

7.8.3. Small Scale

Small scale heterogeneities are the details seen within the beds of an outcrop (Figure 7-6). They may be too small to be significant in affecting ground water flow, but they are very useful in determining deposit type on a medium scale. These features can be seen horizontally from 0-5ft and vertically from 0-2ft. Heterogeneities observed on this scale are: differences in grain size, silt vs. fine to coarse sand, pebbles, cobbles; grading, normal vs. reverse and massive bedding; matrix vs. clast supported conglomerates; matrix properties such as material, size, cementing agent (silica or calcite), well indurated vs. friable; lithic type, which is very important in determining the difference between fanglomerate stream channel deposits and the Totavi Lentil. Lithic clasts in the fanglomerate channel deposits are volcanic, usually rhyolite and dacite in composition. While Totavi Lentil lithic clasts are dominantly quartzite and other Precambrian material from the Sangre de Cristos. One clay layer was observed in Mortandad Canyon extending horizontally ~2ft and vertically 0-1.5ft. Sedimentary structures that can be observed at this scale are crossbedding, horizontal and ripple laminations, soft sediment deformation features, and erosional scours.

7.9. Field Observations

To further understand the changes throughout the Puye, field studies were done in five locations to observe heterogeneity on large, medium and small scale. Field studies were restricted because proximal and medial exposures of the fan were located in areas either burned by the Cerros Grande fire or were located on pueblo land. As a result, access to Puye outcrops was very limited and mostly distal portions of the fan were observed. Outcrops in Guaje and Rendija canyons represent proximal-medial and medial facies. Truly proximal exposures have yet to be studied. Field notes and photographs representative of the overall appearance of the outcrops were taken at all five locations.

7.9.1. Mortandad Canyon

In Mortandad Canyon, thick outcrops of the Totavi Lentil were observed. In some places, lacustrine deposits are overlying the Totavi and are interbedded with Cerros del Rio basalts. The Totavi Lentil contains massive pebble to cobble gravel beds ~3-15ft thick. The gravel beds are clast-supported conglomerates interbedded with fine to coarse sand lenses and planar bedded sand units 2-5ft thick. Lithic clasts are dominantly quartzite and Precambrian material. Matrix material is very ash-rich and poorly consolidated. Lacustrine deposits located in the top section of the outcrop are finer grained and exhibit horizontal laminations. Crossbedding and normal grading was observed within the sand units. Gravel beds exhibited minor crossbedding, good sorting and basaltic ash was seen throughout the gravel but was not seen in the sand beds. Total outcrop thickness ranges from 20-100ft (Dethier, 1997), majority of the outcrops in Mortandad Canyon are 60-80ft thick.

The gravel units range from 3-15ft thick and are continuous the entire length of the outcrop. Interbedded in the gravels are 1-5ft thick sand lenses, and near the bottom of the sections is a tabular sand body ~2-3ft thick that continues down the canyon. Overlying the Totavi are 2-4ft thick lacustrine units interbedded with Cerros del Rio basalts.

7.9.2. Los Alamos Highway (SR 502)

Outcrops of the Totavi Lentil were studied along Los Alamos Highway, also referred to as Hwy 502 or SR502. The gravel beds here are very similar to those observed in Mortandad Canyon. The overall outcrop thickness is noticeably thinner than the Totavi outcrops in Mortandad. Total outcrop thickness ranges from 20-100ft (Dethier, 1997). Gravel beds were generally 10-15ft thick and interbedded with cross-stratified medium to coarse sand units. Boulders were present up to 3ft in diameter. Capping the gravel beds, a ~20ft thick finer unit of sediment was observed. This unit is medium grained interbedded with granule sized sand lenses ~1/2 ft thick. At first glance, it was thought that this finer unit was lacustrine, but lenticular bodies imply stream channel deposition. Just east of the gravel pit along the highway, the Totavi

Lentil appears to interfinger with either the finer sediment units or possibly the Santa Fe Group. On the side of the highway across from the gravel pit, Cerros del Rio basalts cap the Totavi.

7.9.3. Bayo Canyon

Distal fanglomerate and lacustrine facies were observed near the mouth of Bayo Canyon. The fanglomerate showed great variability between and within outcrops. Generally, the fanglomerate can be described as poorly sorted, silt to boulders up to 3ft in size; deposit types are dominantly debris flow/mud flow, hyperconcentrated flood flow, and stream channel. Cross-stratification and planar bedding was observed in hyperconcentrated flows and stream channel deposits. In one outcrop, a mudflow is overlain by a reversely graded pumiceous ignimbrite. Outcrops can be dominated by one deposit type or exhibit many different deposit types throughout a section.

The lacustrine units are fine to medium sand, silt and clay size, well sorted, horizontally laminated. Ripple laminations, soft sediment deformation structures and crossbedding were observed. Lacustrine facies were interbedded in some outcrops with subaqueously emplaced debris flows, basaltic ash, and very fine-grained tephra deposits. In some areas, there was yellow alteration of lacustrine sediments.

7.9.4. Guaje Canyon

Proximal-Medial fanglomerate outcrops in Guaje Canyon are high up above the canyon floor and may not be relevant to fanglomerate below ground. Proximal exposures in the very western portion of Guaje Canyon may have more accessible exposures representative of Puye at groundwater level; however, we did not go up that far in the canyon. The outcrops we did look at were dominantly clast-rich debris flow and hyperconcentrated flood flow deposits with minor clast-poor debris flow and stream channel deposits. Debris flow deposits contain pebble/cobble clasts to boulder up to 4ft in diameter supported by a fine ashy matrix. They are very poorly sorted, and exhibit some reverse grading. Debris flow deposits were from 1-4ft thick and would often pinch out or transition into hyperconcentrated flood flow deposits. There was also an

angular pumice deposit that appeared to have been reworked by a debris flow. The hyperconcentrated flood flows were medium to coarse sand, ash-rich, moderate to well sorted, exhibiting cross and planar bedding. Some hummocky stratification was also observed.

7.9.5. Rendija Canyon

Some of the best and most accessible proximal-medial exposures of the fanglomerate occur in Rendija Canyon. As in Guaje, Puye fanglomerate in Rendija Canyon is dominated by clast-rich debris flow and hyperconcentrated flood flow deposits. Stream channel deposits seemed more significant in this canyon than in the outcrop looked at in Guaje. There were little to no clast-poor debris flow deposits. Ash flows were interbedded with the debris and hyperconcentrated flows in some outcrops. Many pumice falls were also observed. In one outcrop a pumice fall had weathered to a ~6in thick section of pink clay-like material with white pumice lapilli floating in the matrix. Hornblende crystals were seen within the pumice lapilli. As in Guaje Canyon, hyperconcentrated flows are coarse to granular sand size and exhibit crossbedding.

7.9.6. Well Data

We examined well log data from R-25, R-19, R-12, R-9, R-31, and older wells (Purtymun 1995) wells. Unfortunately, we discovered that well data have many limitations with respect to the information we were hoping to get from the well logs. Purtymun (1995) shows the depths and thickness of the Puye fanglomerate and Totavi Lentil but provides no lithologic descriptions. The R-wells provided depth, thickness, and lithologic information, however in some cases the boundary between what was fanglomerate and what was Totavi was not defined. The lithologic information was useful in showing sand/pebble verse cobble/boulder bed layers and in identifying boulder and argillic clay horizons. Deposit type is near impossible to determine from the log data. Geophysical log data is available for some of the wells and could provide useful sedimentary structure information; however, there is a severe lack of qualified personnel to interpret the data.

Table 7-1. Facies summary

Facies	Sub-facies	Location	Description	Macroforms	Thickness
Clast Supported Conglomerates	Channel Deposits	proximal to mid-fan exposures	thicker & coarser grained upward in the fan	broad channel-form geometries	individual channel: 30cm- >6m sequences
		proximal deposits	coarse grained, very poorly sorted, normal & reverse grading some conglomerates capped by pebbly sandstones which form discontinuous lensoid bodies		
		distal deposits	much thinner, better sorted, finer grained polymodal, normally graded, stratification better developed	laterally extensive, lenticular bodies	10cm- 3.5m
	Sheet Deposits		sheet-like sandy- pebble conglomerates & pebbly sandstones absence of deep scours, uniform horizontal stratification, lack of apparent size grading	laterally continuous with only slight thinning up to hundreds of meters	10cm- 3m individual scours rarely exceed 15cm stacked sand-gravel couplets 1-5cm
		proximal deposits	confined to lower parts of the succession		
Matrix-Supported Conglomerates	Clast-rich Deposits	most prevalent proximally and in upper parts of the succession	sandy-cobble & boulder conglomerates, unstratified, polymodal, coarser grained cong. contain reversely graded basal layers & overall reverse coarse-tail grading, very poorly sorted	laterally continuous tabular bodies	20cm - >4m
	Matrix-rich Deposits	predominate in mid- and distal fan outcrops	lack basal-shear zones or well developed reverse grading, more abrupt decreases in max particle size downfan, lack traction structures, polymodal, muddy-sandy conglomerates & pebbly-muddy sandstones, commonly coarse-tailed normally graded, lack erosional scours	subaerially emplace: laterally continuous, sheet-like bodies interbedd w/ and truncated by clast supported sheetflood or braided stream conglomerates, most beds are massive	20cm - >3m
		distal exposures	predominance of lacustrine deposits, subaqueously emplaced mudflows		
Pyroclastic	Block-and-ash	confined to	dense, nonvesicular lava blocks		

Facies	flows	proximal exposures	set in an ash matrix with subordinate amounts of poorly vescular pumice		
	Lower Tephra Group		widespread pumice-fall and thin ash-flows, thin ignimbrites, redeposited tephra		
	Middle Tephra Group		lithic-rich nonwelded ignimbrite, coarse- grained lithic-rich pumice falls & fine grained capping ash falls, pumice flow deposits, 2 large dacite pumice blocks		
	Upper Tephra Group		several rhyodacitic pumice falls, abundant lake-deposited pumice and ash, water lain basaltic ash 2 Rhyolite Pumice Falls in @ top part of the fan overlies red clay horizon in central portion of the fan		
	Phreatomagmatic Basalts	distal fan	interfinger with Puye fluvial gravels and lacustrine sediments, derived from Cerros del Rio eruptions		

Facies	**Sub-facies**	**Location**	**Description**	**Macroforms**	**Thickness**
Lacustrine Facies		distal fan	subaqueously emplaced mudflows, horizontal laminations, abundant tephra and grades laterally to stacked pumiceous CPDF and sheetflow deposits that form a prominent apron around the perimeter of the Puye fan		apron: 2- 10m

Totavi Lentil Member

Facies	Sub-facies	Location	Description	Macroforms	Thickness
axial stream deposits from ancestral Rio Grande		distal fan	pebble to cobble gravel, lithics dominantly quartzite and other metamorphic rocks, cross and planar beds, sand lenses, fills in channels of and locally interbedded with the fanglomerate, some areas overlies Santa Fe group		gravel beds: 1.5- 10ft sand lenses: 1- 5ft total: 16- 150ft

Table 7-2. Permeability data for the Puye

Well	Permeability (log 10, m^2)	Hydrostratigraphic Unit
TW-8	-12.1	Fanglomerate
R-15	-12.2	Fanglomerate
TW-3	-11.2	Totavi Lentil
TW-2	-11.1	Totavi Lentil
TW-1	-12.0	Totavi Lentil
Test Well DT-9	-10.8	Multiple units including Puye
Test Well DT-5A	-12.1	Multiple units including Puye
Test Well DT-10	-11.3	Multiple units including Puye
PM-5	-12.5	Multiple units including Puye
PM-4	-11.9	Multiple units including Puye
PM-2	-11.8	Multiple units including Puye

Table 7-3. Generalized permeability estimates for facies within the Puye

Deposit Type	Permeability
Channel deposits	high to medium
Sheet deposits	high to medium
Clast-rich debris flow	medium to low
Clast-poor debris flow	low
Block-and-ash flow	medium to low
Tephra	medium
Basalts	high (if fractured)
Axial stream deposits (Totavi Lentil)	high
Lacustrine	medium to low

Table 7-4. Totavi Lentil Outcrop Information (m)

Out crop Name	North-South Dimensions		East-West Dimensions		Thickness		Top Elevation
	Minimum	Maximum	Minimum	Maximum	Minimum	Maximum	
Ancho Canyon	20.1	244	80.7	264	18.3	30.5	1755.6
Water Canyon	20.4	223	61	122	12.2	18.3	1524
Mortandad Canyon	61	223	41	548.6	18.3	24.4	1774
Sandia Canyon	41	142	41	771.8	6.1	18.3	1792
Los Alamos Canyon	41	893.7	41	1097.3	6.1	30.5	1823

Table 7-5. Lateral Facies Variations of the Puye Formation

Proximal	Medial	Distal
dominated by coarse-grained ignimbrites & chaotic block-&-ash sequences	grade down fan to coarse, better sorted clast rich debris flows (CRDF)	CRDF locally grade laterally & vertically to hyperconcentrated flood flow deposits & eventually to sheet flood & stream channel dominated facies interbedded with ash-rich clast poor debris flows (CPDF)
stream channel deposits more abundant (as much as 50% of exposures), coarse-grained, poorly sorted, normal & reverse grading	decrease in abundance progressively downfan	replaced volumetrically by better-sorted, thinner, & finer- grained braided stream & sheetflood deposits
	downslope increase in the proportion of sheetflood deposits	volumetrically dominate over braided stream deposits & become proximal to CPDF deposits
	progressive downfan decreases in the thickness of sheetflood deposits are accompanied by improved sorting, horizontal stratification	
more massive & structureless		downfan increase in cross-stratal, planar bedsets, horizontal laminated sands & muds
pumice falls commonly separated by several meters of conglomerates and mudstones		more closely spaced & eventually converge to form thick sequences of primary & reworked pumice & ash lacustrine sediments more dominate (as much as 70% of exposures)
	increase in lacustrine deposits	
transitions from inversely-graded, clast rich deposits to fine grained ungraded or normally graded, matrix-dominated deposits occur in short lateral distances (as short as 200m)	matrix-rich deposits predominate in medial and distal exposures (as much as 50%)	
block-and-ash flows confined to proximal exposures		

Table 7-6. Heterogeneity of the Puye Formation

Large Scale
overall facies changes throughout the entire Puye Formation
Transitions dominantly occur west to east
Scale[1&2]: Horizontal: 1-10km (.6- 6mi)
Vertical: .5- 4km (.3- 2.5mi)
Heterogeneity
Fanglomerate 3- 8km (2- 5mi)
Totavi Lentil 2- 7km (1- 4mi)
Stair-stepping vs. pancake layer
Lacustrine Facies 1- 6km (.6- 3.5mi)
Location within the fan[2-4]
Proximal: dominated by fanglomerate
Medial: dominantly fanglomerate interbedded with lacustrine and Totavi Lentil
Distal: Lacustrine and Totavi Lentil with minor fanglomerate

Medium Scale
Larger features seen in outcrop
Transitions occur vertically and horizontally throughout outcrop
Scale[1&2]: Horizontal: .9- 61m (3- 200ft)
Vertical: .6- 30m (2- 100ft)
Heterogeneity
Pyroclastic facies 1- 5m (3- 16ft)
Pumice flows, pumice and ash falls, ignimbrites, block-and-ash flows
Gravel beds 1.5- 9m (5- 40ft)
Sand beds .6- 2m (2- 6ft)
Boulder rich zones .6- 1m (2- 4ft)
Clastic deposits .6- 24m (2- 80ft)
Stream-channel, debris flow, sheetflood, mudflow
Sedimentary structures
Lenses, planar bedding, cross stratification
Location within the fan[2-4]
Proximal: channel deposits, sheet deposits, clast-rich debris flow, block-and-ash flows, tephra deposits
Medial: channel deposits, sheet deposits, matrix-rich debris flow, tephra deposits
Distal: channel deposits, sheet deposits, matrix-rich debris flow, tephra deposits, phreatomagmatic basalts, lacustrine deposits, Totavi Lentil

Small Scale
Details within the beds of an outcrop
Transitions occur vertically and horizontally throughout bedding
Scale[1]: Horizontal: 0- 5ft
Vertical: 0-2ft

Heterogeneity
Grain size
Fine to medium sand, pebble, cobble
Grading
Normal vs. reverse
Matrix vs. clast supported conglomerates
Matrix properties
Fine vs. coarse sand, ash
Cementing
Indurated vs. friable
Calcite vs. silica, etc.
Lithic type
Volcanic vs. quartzite
Pumice, fine ash deposits
Clay layers 0- 1.5ft
Sedimentary structures
Crossbedding, horizontal and ripple laminations, soft sediment deformation features, erosional scours
Location within the fan:
Seen throughout the entire fan

Table 7-7. Variations within the Puye according to distance from source

PROXIMAL

DEPOSIT TYPES

- Channel deposits
- Sheet deposits
- Clast-rich debris flows
- Block-and-ash flows
- Tephra deposits

Characteristics

- Single, large-scale coarsening upward, fan wedge is thickest
- Overall upward decrease in sheetflood gravels and CPDF deposits that dominate lower parts of the succession
- Capped by stacked stream channel deposits
- Dominated by coarse-grained ignimbrites and chaotic block-and-ash sequences
- Stream channel deposits more abundant: coarse grained, poorly sorted, normal and reverse grading
- More massive and structureless
- Pumice falls commonly separated by several meters of conglomerates and mudstones
- Transitions from inversely-graded clast-rich deposits to fine-grained ungraded or normally graded
- Matrix dominated deposits occur in short lateral distances (as short as 200m)
- One or more tephra deposits overlain by pumice and ash-rich debris in the lower portions of the fan and by very coarse grained, block-and-ash flow deposits toward the top of the section
- Clast-supported conglomerates also commonly developed above individual coarse-grained massflow sequences where upper parts of debris-flow deposits were partly regraded by shallow braided streams

MEDIAL

Deposit Types

- Channel deposits
- Sheet deposits
- Clast-poor debris flows
- Tephra deposits
- Lacustrine facies (minor)
- Totavi Lentil (minor)

Characteristics

- Capped by stacked stream channel deposits
- Rapid vertical transition form coarse clastics to fine-grained mudstone
- Fine-grained units overlain by stacked conglomeratic mudstones that occur as uniform, laterally continuous, sheet-like beds ranging from 20cm to 2.6m
- Grade down fan to coarse, better-sorted clast rich debris flows
- Decrease in stream channel abundance progressively downfan
- Progressive down fan decreases in the thickness of sheetflood deposits are accompanied by improved sorting, horizontal stratification
- Increase in lacustrine deposits
- Matrix-rich deposits (CPDF) dominate in medial and distal exposures
- One or more airfall units overlain by ashy debris-flow deposits
- Thick sequences of alternating clast-rich and matrix-dominated conglomerates developed as debris flows episodically in filled stream channels following eruptions

DISTAL

Deposit Type

- Channel deposits
- Sheet deposits
- Clast-poor debris flows
- Tephra deposits
- Lacustrine facies
- Totavi Lentil

Characteristics

- CRDF locally grade laterally and vertically to hyperconcentrated flood flow deposits and eventually to sheet flood and stream channel dominated facies interbedded with ash-rich clast-poor debris flows (CPDF)
- Stream channel deposits replaced volumetrically by better-sorted, thinner, and finer-grained braided stream and sheetflood deposits
- Sheetflood deposits volumetrically dominate over braided stream deposits and become proximal to CPDF deposits
- Downfan increase in cross-stratal, planar bedsets, horizontal laminated sands and muds
- More closely spaced and eventually converge to form thick sequences of primary and reworked pumice and ash
- Lacustrine sediments more dominate
- Primary pyroclastic deposits are thin and interbedded with stacked pumiceous CPDF and sheetflood deposits
- Individual CPDF deposits separated by fine-grained, braided stream and intermittent sheetflood conglomerates
- Inter-eruptive depositional sequences more complex than in proximal exposures

7.10. Development of a stochastic model of heterogeneity within the Puye Formation

As described in Robinson et al. (Robinson et al. 2000), we generated a preliminary stochastic model of heterogeneity within the Puye Formation using a Gaussian sequential simulator, GCOSIM (Gomez-Hernandez 1991). This model requires specification of correlation lengths (x, y, and z directions). Correlation length is a measure of how spatially continuous any given facies is, on average. We estimated correlation lengths based on outcrop-based estimates of geometries for the coarse Totavi Lentil (Table 7-4). Because of the uncertainty associated with these estimates, we generated stochastic fields corresponding to three different sets of correlation lengths. These are shown in Table 7-8. Figure 7-7 shows three of these cases in map view; Figure 7-8 shows three cases in cross-section. Because we set correlation lengths in x and y directions equally, our facies trend southeasterly. These facies are intended to mimic the type of heterogeneity found in alluvial fans. A more rigorous model of facies within the Puye will be developed in FY01, using a Markov-chain approach developed for alluvial fan sediments in California.(Fogg et al. 1998).

Table 7-8. Combinations of correlation lengths (λ), mean (<f>) and variance σ_f^2 of hydraulic conductivity, and porosity (ϕ) used to simulate stochastic conductivity fields.

Case numbers	<f>	σ_f^2	λ_x	λ_y	λ_z	ϕ
0	-11.793	0	500	500	20	0.1
1		0.276				
2		0.5				
3		1.0				
4	-11	0.276				
5	-13					
6	-11.793		250	250		
7			1000	1000		
8			500	500	12	
9					30	
10					20	0.15
11						0.20
12						variable

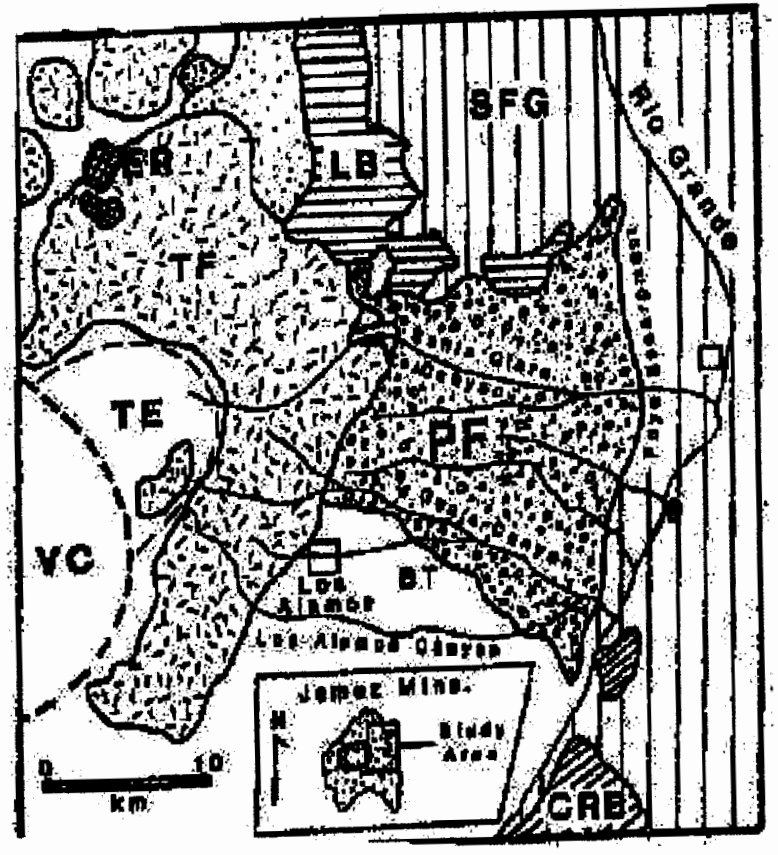

Figure 7-1. Location of the Puye Formation (PF) (Waresback and Turbeville, 1990).

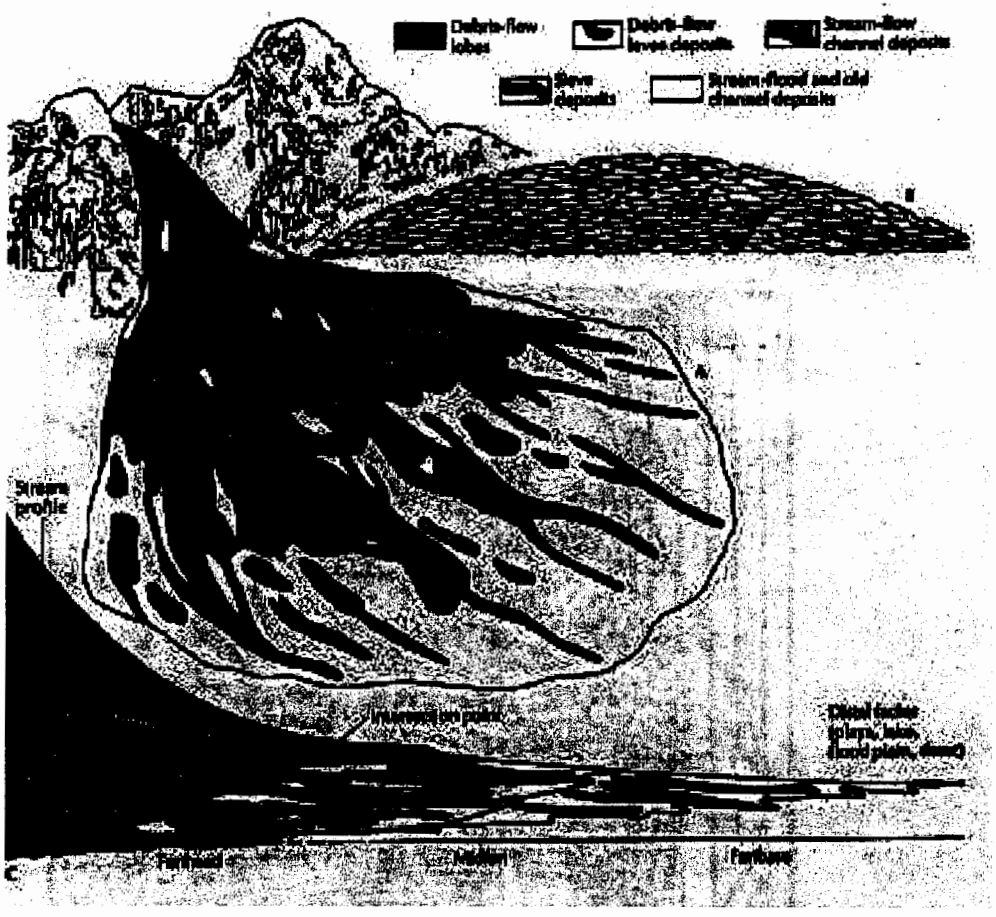

Figure 7-2. Model of alluvial fan sedimentation. (A) Fan surface; (B) Crossfan profile; (C) Radial profile. Vertical profiles are greatly exaggerated (reproduced from Prothero and Schwab, 1996).

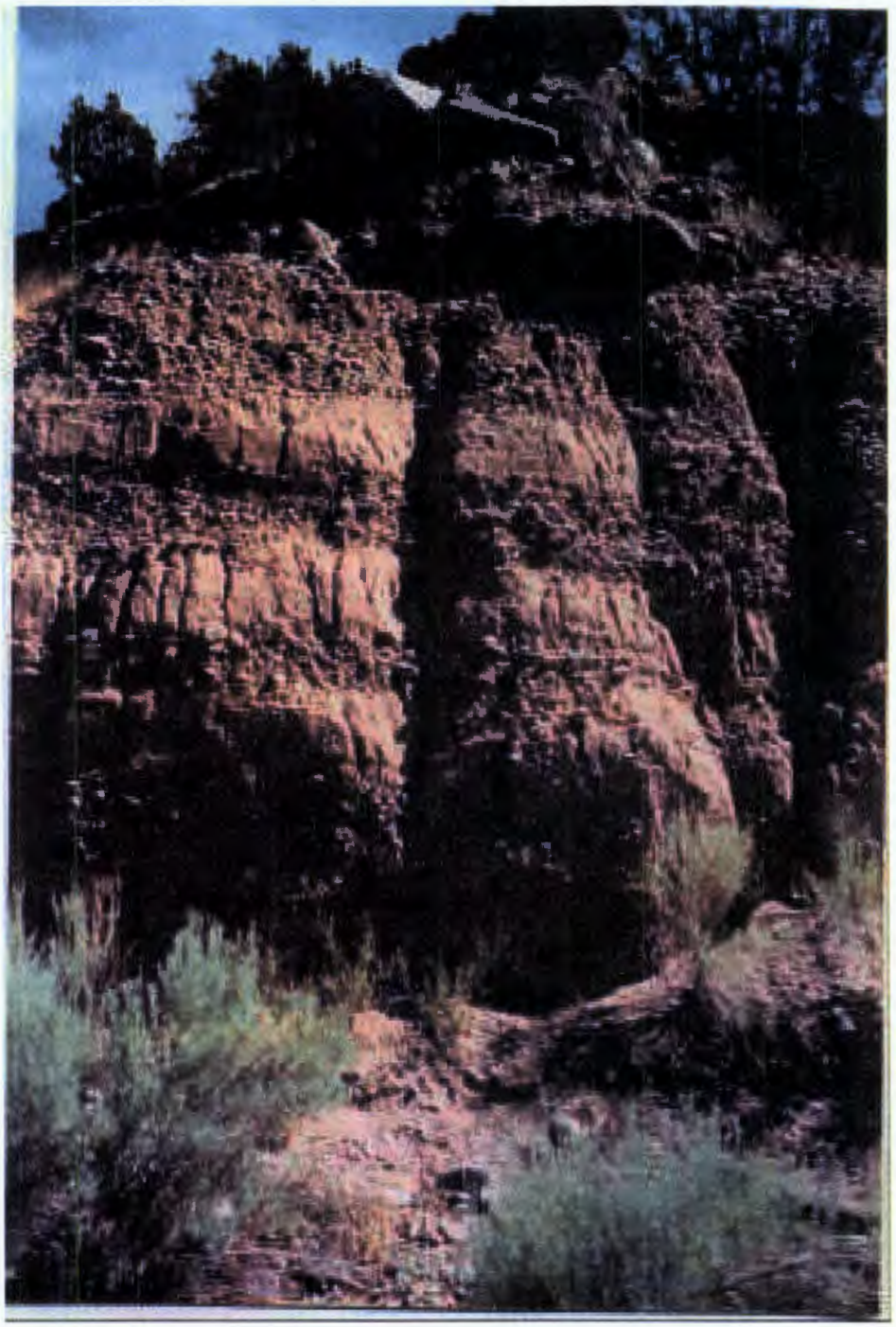

Figure 7-3. Photograph of an outcrop of the Totavi Lentil

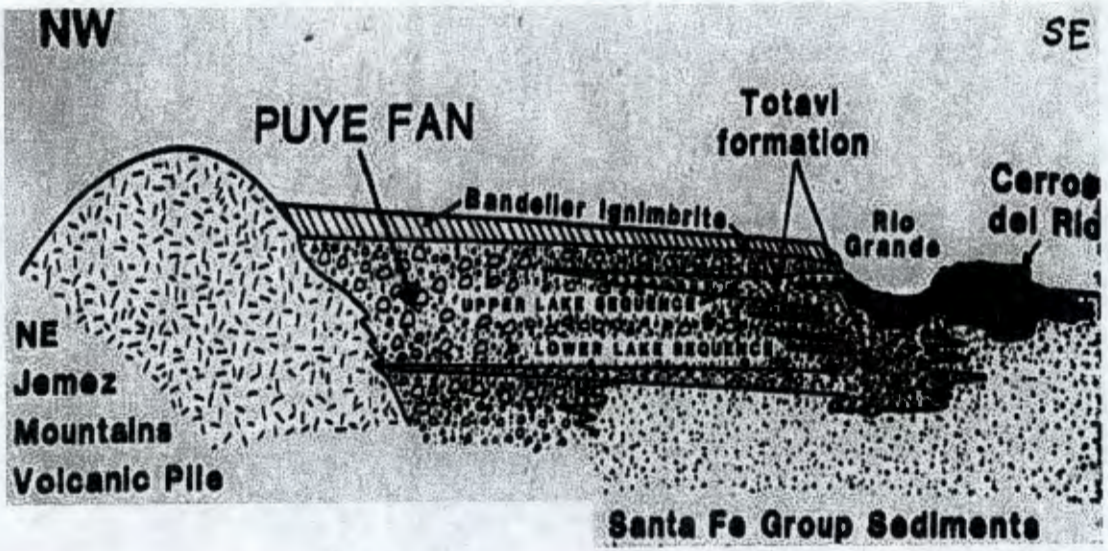

Figure 7-4. Large scale heterogeneity (Waresback and Turbeville, 1990).

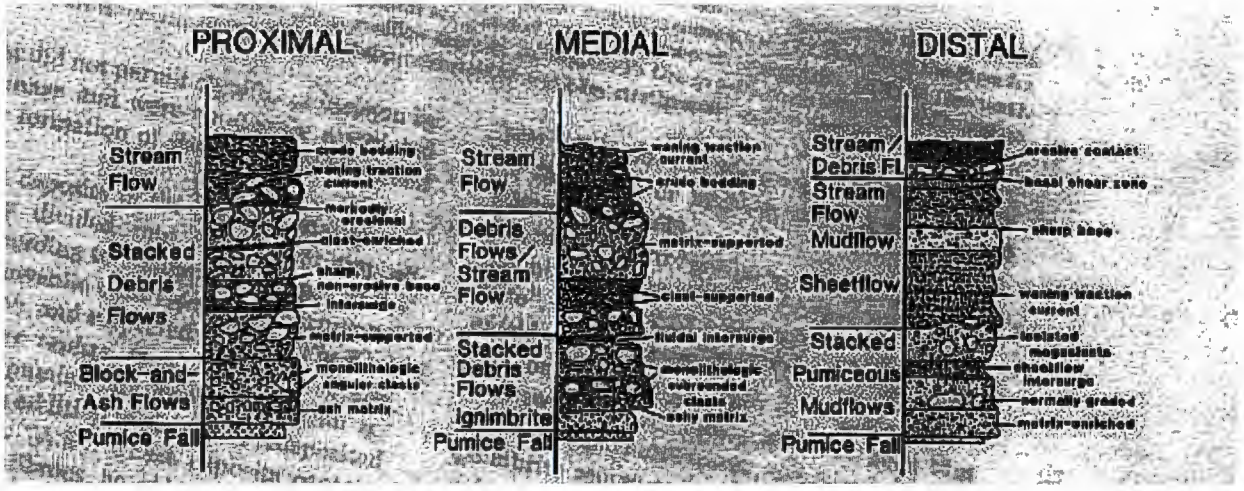

Figure 7-5. Medium scale heterogeneity (Waresback and Turbeville, 1990).

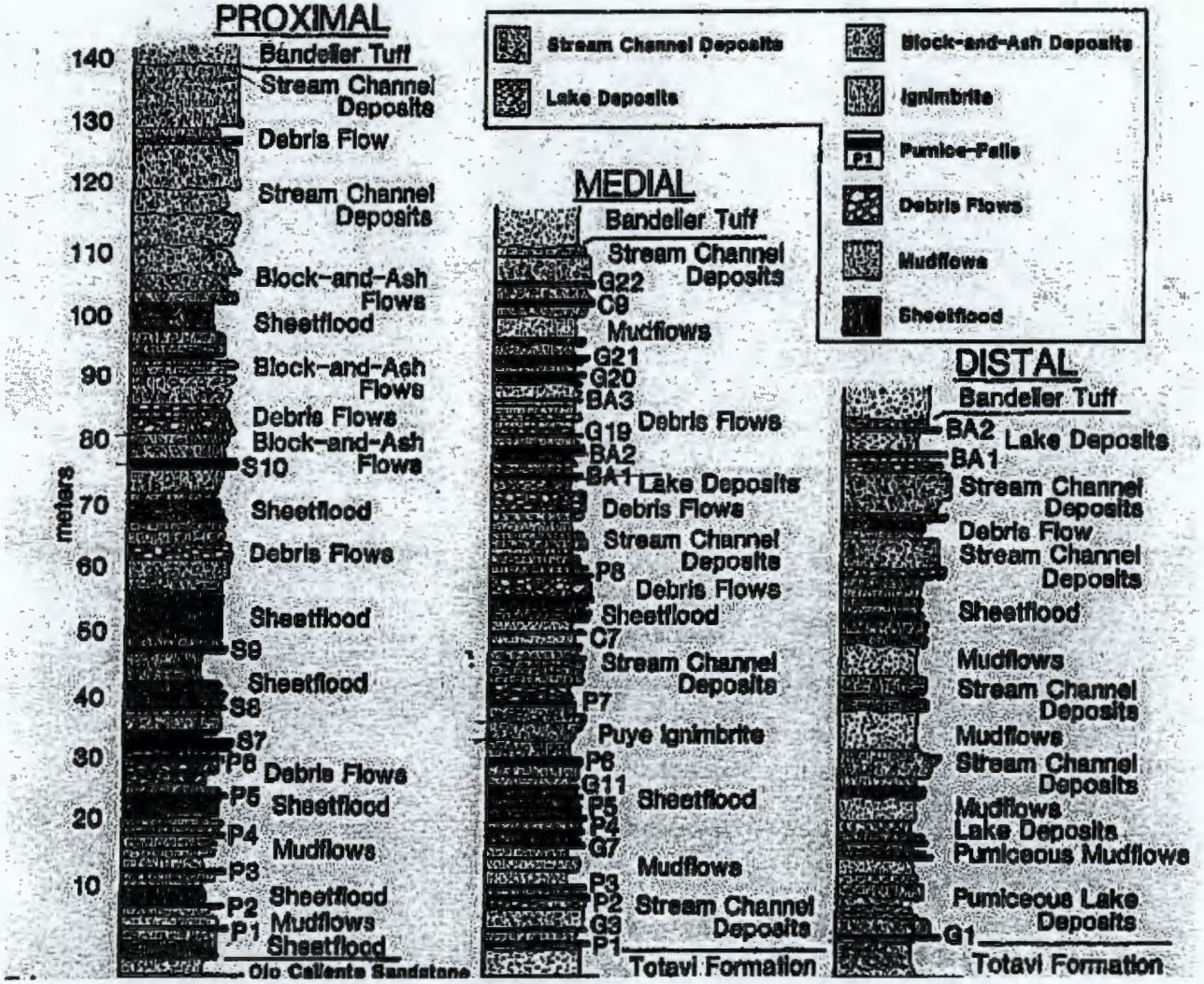

Figure 7-6. Medium and small scale heterogeneity (Turbeville, 1991).

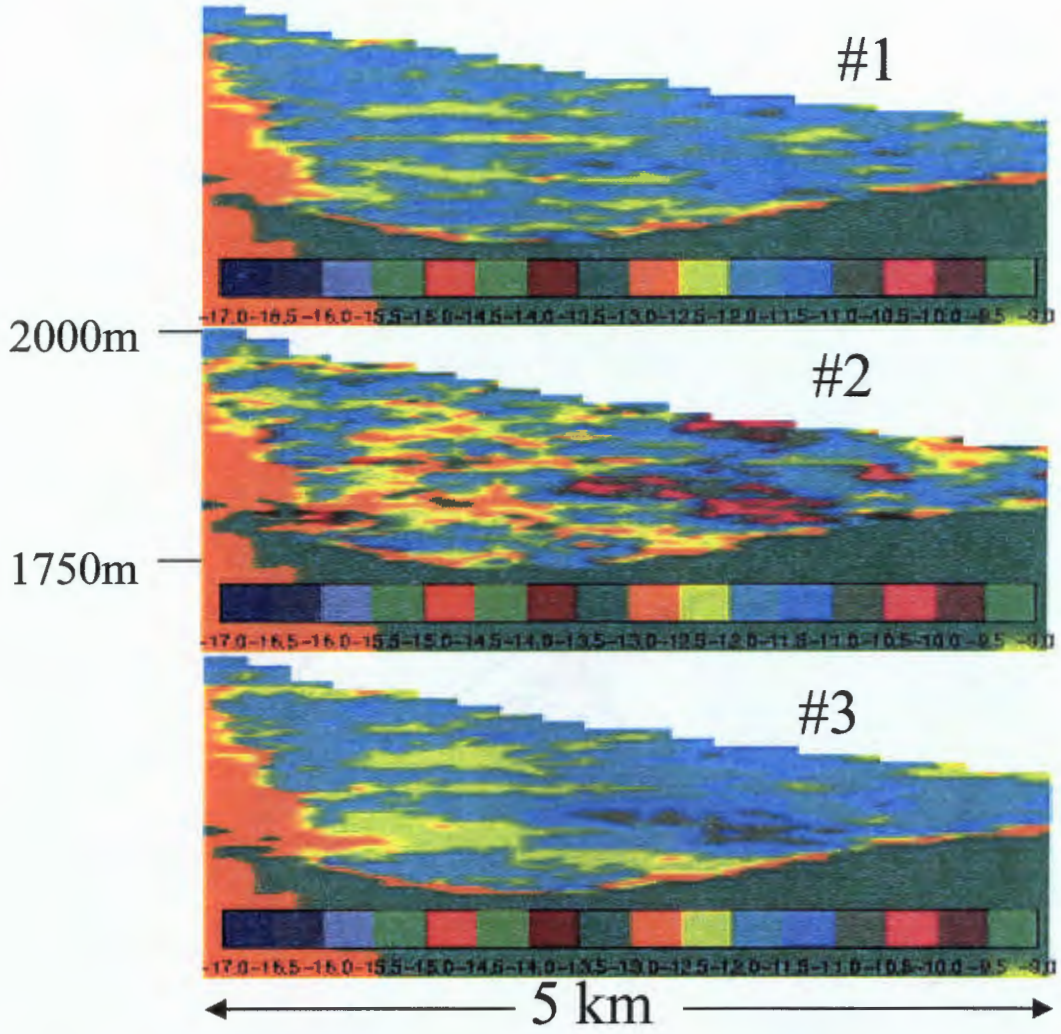

Figure 7-7. Hydraulic conductivity (m2) in cross-sections through the Puye formation, according to three different stochastic models. 5X vertical exaggeration.

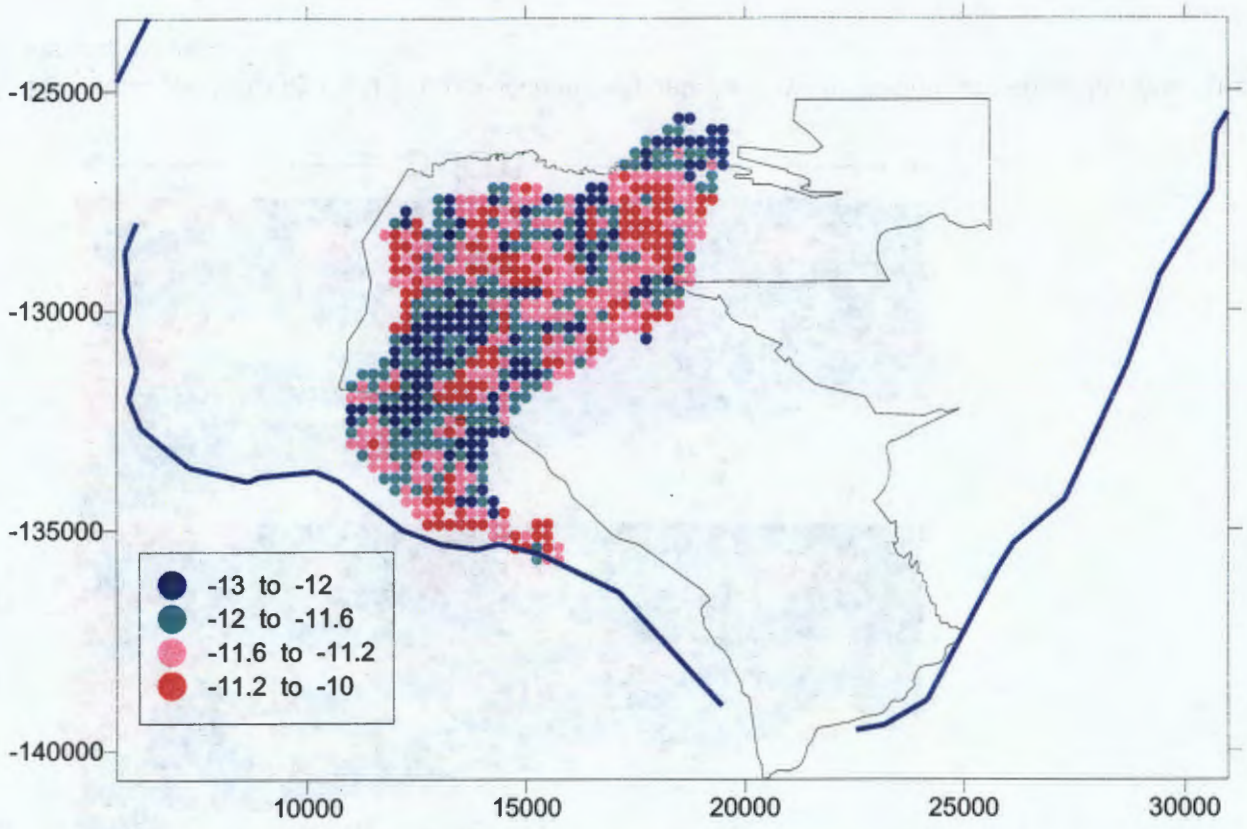

Figure 7-7a. A plan view of generated log hydraulic conductivity field (Case 1: $\lambda x = \lambda y = 500$ m) for Puye Formation at a 1000 m elevation.

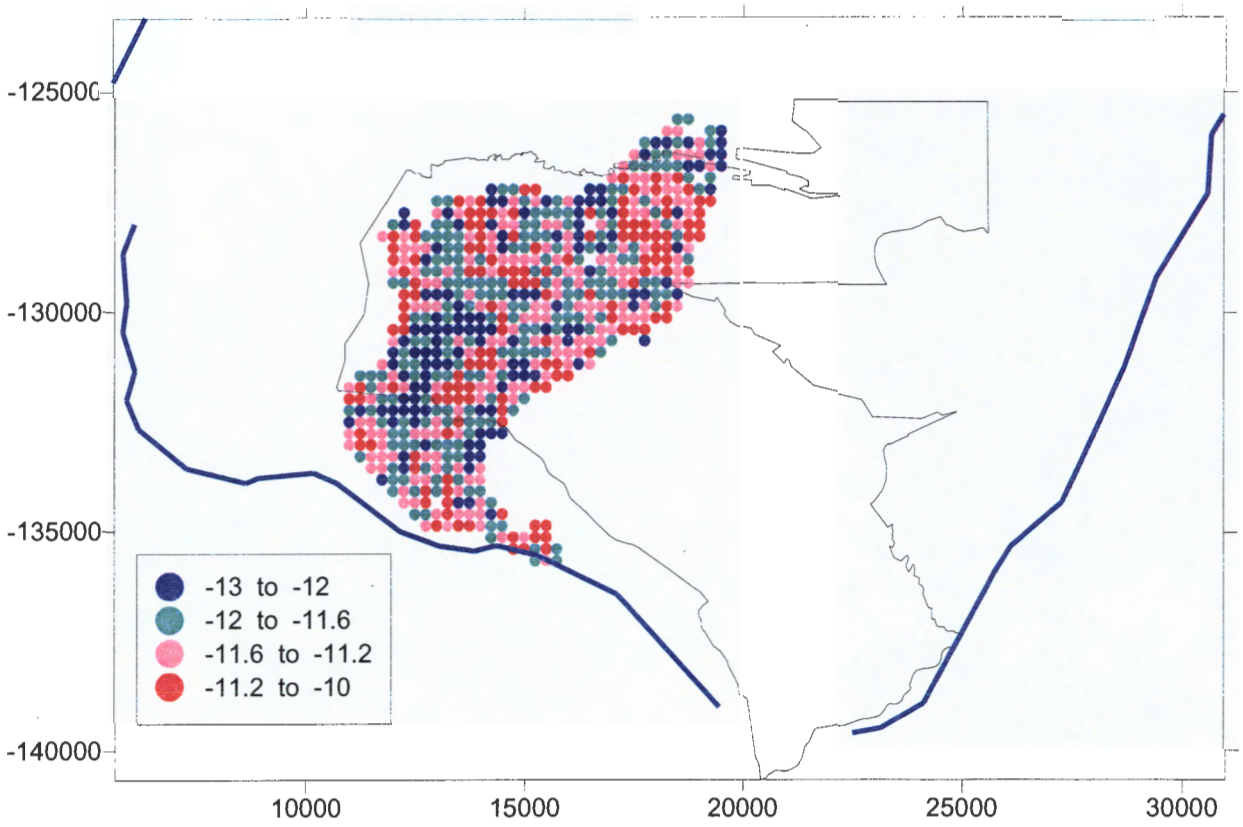

Figure7-7b. A plan view of generated log hydraulic conductivity field (Case 4: $\lambda x = \lambda y = 500$ m) for Puye Formation at a 1800 m elevation.

In conclusion, both the basin model and the Pajarito Plateau submodel are important for the characterization of hydrogeological conditions in the region of LANL.

References

Anderholm, S. K. (1994).Ground-water recharge near Santa Fe, north-central New Mexico.94-4078.

Bear, J. (1972). Dynamics of fluids in porous media. New York, Dover Publications, Inc.

Blake, W. D., F. Goff, A. I. Adams and D. Counce (1995).Environmental Geochemistry for surface and subsurface waters in the Pajarito Plateau and outlying areas, New Mexico.LA-12912-MS.Los Alamos National Laboratory.

Carey, B., G. Cole, C. Lewis, F. Tsai, et al. (1999).Revised site-wide geologic model for Los Alamos National Laboratory
(FY99).LA-UR-00-2056.

Carrera, J. and S. P. Neuman (1986). "Estimation of Aquifer Parameters Under Transient and Steady State Conditions: 1. {Maximum} Likelihood Incorporating Prior Information." Water Resources Research **22**: 199-210.

Cerling, T. E. (1984). "The stable isotopic composition of modern soil carbonate and its relationship to climate." Earth and Planetary Science Letters **71**: 229-240.

Clark, I. and P. Fritz (1997). Environmental isotopes *in* hydrogeology. Boca Raton, Fl, Lewis Publishers.

Cushman, R. L. (1965).An evaluation of aquifer and well characteristics of municipal well fields in Los Alamos and Guaje Canyons, near Los Alamos, New Mexivo.1809-D.U.S. Geological Survey.

Dethier, D. P. (1997). Geology of White Rock quadrangle, Los Alamos and Santa Fe Counties, New Mexico., New Mexico Bureau of Mines & Mineral Resources.

Doherty, J. (1997). Parallel {PEST}. Brisbane, Australia, Watermark Computing.

Fogg, G. E., C. D. Noyes and S. F. Carle (1998). " Geologically-based model of heterogeneous hydraulic conductivity in an alluvial setting." Hydrologeology Journal **6**(1): 131-143.

Goff, F. and Grigsby (1982). "Valles caldera geothermal systems, New Mexico, USA." Journal of Hydrology **56**: 119-136.

Goff, F. and S. Sayer (1980).A geothermal investigation of spring and well waters of the Los Alamos region, New Mexico.LA-8326-MS.

Gomez-Hernandez, J. J. (1991). A Stochastic Approach to the Simulation of Block Conductivity Fields Conditioned Upon Data Measured at a Smaller Scale. *Stanford, California, Stanford University.*

Gray, R. N. (1997). Hydrologic budget analysis and numerical simulations of groundwater flow in Los Alamos Canyon near Los Alamos, New Mexico. Earth and Planetary Sciences. Albuquerque, NM, University of New Mexico: 202.

Griggs, R. L. and J. D. Hem (1964).Geology and groundwater resources of the Los Alamos Area, New Mexico.1753.U.S. Geological Survey.

Harr, L., J. Gallagher and G. S. Kell (1984). NBS/NRC Steam Tables, Thermodynamics, and Transport Properties and Computer Programs for Vapor and Liquid States of Water, Hemisphere Press.

Hearne, G. A. (1985).Mathematical model of the Tesuque aquifer system underlying Pojoaque River basin and vicinity, New Mexico.2205.U.S. Geological Survey.

Ingersoll, R. V., W. Cavazza, W. S. Baldridge and M. Shafigulla (1990). "Cenozoic Sedimentation and Paleotectonics of North-Central New Mexico: Implications for Initiation and Evolution of the Rio Grande Rift." GSA Bull. **102**(9): 1280-1296.

Keating, E., E. Kwicklis and B. Robinson (1999).Simulated transport of HE in the regional aquifer from TA-16.LANL.

Keating, E. and R. Warren (1999).Geochemistry of the regional aquifer. LANL.

Keating, E., G. Zyvoloski, C. Gable, M. Witkowski, et al. (1998).A Steady-state regional flow model for the saturated zone in the Espanola Basin. Los Alamos National Laboratory.

Keating, E. H. and F. Goff (1999). "Overview of the Hydrogeology and Geochemistry of the Espanola Basin." .

Keating, E. H., E. Kwicklis, M. Witkowski and T. Ballantine (1999).A Regional Flow Model for the Regional Aquifer beneath the Pajarito Plateau.LA-UR-00-1029.

Kelley, V. C. (1978). Geology of the Espanola Basin.

Magnuson, S. O. and A. J. Sondrup (1998).Development, calibration, and predictive results of a simulator for subsurface pathway fate and transport of aqueous- and gaseous-phase contaminants in the subsurface disposal area a the Idaho National Engineering and Environmental Laboratory.INEEL/EXT-97-00609.

Manley, K. (1976). The Late Cenozoic History of the Espanola Basin, New Mexico, UC-Boulder.

Neuman, S. P. (1990). "Universal Scaling of Hydraulic Conductivities and Dispersivities in Geologic Media." Water Resources Research **28**(8): 1749-1758.

Newman, B. D. (1996). Geochemical investigations of calcite fracture fills and mesa-top water dynamics on the Pajarito Plateau, New Mexico. Socorro, NM, New Mexico Institute of Mining and Technology.

Newman, M. E. (1996).Evaluation of the mobility of Am, Cs, Co, Pu, Sr, and U through INEL basalt and interbed materials, Summary report of the INEL/Clemson University Laboratory studies.WAG7-82, INEL-95/282.

Purtymun, W. D. (1995).Geologic and hydrologic records of observation wells, test holes, test wells, supply wells, springs, and surface water stations in the Los Alamos area.LA-12883-MS.

Purtymun, W. D., S. McLin and A. Stoker (1990).Water supply at Los Alamos during 1990.LA-12471-PR.Los Alamos National Laboratory.

Quade, J. and T. E. Cerling (1990). "Stable isotopic evidence for a pedogenic origin of carbonates in Trench 14 near Yucca Mountain, Nevada." Science **250**: 1549-1552.

Quade, J., T. E. Cerling and J. R. Bowman (1989). "Systematic variations in the carbon and oxygen isotopic composition of pedogenic carbonate along elevation transects in the southern Great Basin, United States." Geological Society of America Bulletin **101**: 464-475.

Reneau, S. L. and D. P. Dethier (1995). Pliocene and quaternar history of the Rio Grande, White Rock Canyon and vicinity, New Mexico. NM Geol.Soc.Guidebook, 47th Field conference, Jemez Mountains Region.,. F. Goff, NM Geological Society: 484.

Robinson, B., E. Keating, B. Newman, K. Birdsell, et al. (2000).Process-Level and Systems Models of Groundwater Flow and Transport Beneath the Pajarito Plateau: Migration of High Explosives from Technical Area 16.LANL.

Rogers, D. B., A. K. Stoker, S. G. McLin and B. M. Gallaher (1995). Recharge to the Pajarito Plateau regional aquifer system. NM Geol.Soc.Guidebook, 47th Field conference, Jemez Mountains Region.,.

Spaulding, W. G. (1983).Vegetation and climates of the last 45,000 years in the vicinity of the Nevada Test Site, South-Central Nevada. 83-535.U.S. Geological Survey.

Tuberville, B. N., D. B. Waresback and S. Self (1988). "Lava-Dome Growth and Explosive Volcanism in the Jemez Mountains, New Mexico: Evidence From the Plio-Pleistocene Puye Alluvial Fan." Journal of Volcanology and Geothermal Research **36**: 267-291.

Turbeville, B. N. (1991). "The influence of ephemeral processes on pyroclastic sedimentation in a rift-basin, volcaniclastic-alluvial sequence, Espanola basin, New Mexico." Sedimentary Geology **74**: 139-155.

Tyler, S. W., J. B. Chapman, S. H. Conrad, D. P. Hammermeister, et al. "Soil-water flux in the southern Great Basin, United States: Temporal and spatial variations over the last 120,000 years." Water Resources Research **32**(6): 1481-1499.

U.S. Department of Justice and New Mexico State Engineer Office (1996).Selection of a hydrogeologic model for water-rights administration in the Pojoaque River Basin Santa Fe County, New Mexico.

Vautaz, F. D., F. Goff, C. Fouillac and J. Y. Calvez (1986). "Isotope geochemistry of thermal and nonthermal waters in the Valles Caldera, Jemez Mountains, northern New Mexico." J. Geophysics Res. **91**: 1835-1853.

Vuataz, F. D., J. Stix, F. Goff and C. F. Pearson (1984).Low-temperature geothermal potential of the Ojo Caliente warm springs area, northern New Mexico.LA-10105-OBES.Los Alamos National Laboratory.

Waresback, D. B. and B. N. Tuberville (1990). "Evolution of a Plio-Pleistocene Volcanogenic-Alluvial Fan: The Puye Formation, Jemez Mountains, New Mexico." GSA Bulletin **102**(3): 298-314.

Wasiolek, M. (1995).Subsurface recharge to the Tesuque Aquifer system from selected drainage basins along the western side of the Sangre de Cristo Mountains near Santa Fe, New Mexico.94-4072.U.S. Geological Survey.

Watermark Computing (1994).PEST Model-Independent parameter estimation: user's manual, Watermark Computing.

Winograd, I. J., T. B. Coplen, J. M. Landwehr, A. C. Riggs, et al. (1992). "Continuous 500,000-year climate record from vein calcite in Devils Hole, Nevada,." Science **258**: 255-260.

Zyvoloski, G. A., B. A. Robinson, Z. V. Dash and L. L. Trease (1997).Summary of the Models and Methods for the {FEHM} Application --- A Finite-Element Heat- and Mass-Transfer Code.LA-13306-M.Los Alamos National Laboratory.

Appendix A. Useful conversions

Type of measurement	To Obtain	Multiply values reported in these units	By this factor:
Permeability/hydraulic conductivity	ft/day (hydraulic conductivity)	gpd/ft^2 (specific capacity)	0.134
	m^2 (permeability)	ft/day	3.6E-13
Flux	kg/s	cfs	28.32
	cfs	gal/min	2.23E-3

Appendix B. Refinement of the pre-development water level dataset

The comprehensive water level database includes data gathered by a variety of agencies and spans the period of the early 1940's to the present. We imposed several criteria for selecting representative data, to 1) exclude wells that might be in perched water systems and 2) to exclude data from wells that might be influenced by significant pumping. The specific criteria we used were as follows:

1) remove all wells identified by the USGS as "alluvial"
2) remove any water levels measured before 1955, unless the water level would substantially improve the spatial distribution of the dataset (especially providing better vertical coverage), using the following criteria:

a) the data point is at least 5km (horizontal distance) from any well with a pre-1955 water level measurement (note: this criteria generally ensures that water levels taken in the vicinity of pumping fields will be excluded)

OR,

b) the data point is at least 1 km from any well (horizontal distance) AND 33m vertical separation with any pre-1955 water level measurement

In addition to the above criteria, we removed a few additional water level measurements that we felt were probably taken from perched systems, based on careful examination of water level trends and river elevations. Additionally, several measurements were removed because of extremely low reported water levels, hundreds of feet below nearby wells and/or river levels. One measurement, north of Santa Clara Creek, was removed from the calibration procedure because it fell directly within the Pajarito Fault zone (as defined by the geologic model). Because the current model represents the fault zone as a relatively wide, homogeneous hydrostratigraphic zone, calibration to fine scale data (such as water levels within the zone) is inappropriate.

Appendix C. Numerical Inverse Analyses

A major task of our field of study is to understand and predict the fluid flow and contaminant transport through natural hydrogeological systems. This requires the definition of a conceptual model and corresponding model parameters, which represent adequately hydrogeological processes of interest. For a given model, the identification of model parameters and associated uncertainties is called an inverse problem. Numerical inverse methods have been used widely in hydrogeological research and, more recently, application. The applied inverse methodology follows the principles and definitions established by the milestone papers of (Carrera and Neuman 1986).

Water flow in porous medium is governed by the following partial differential equation over a three-dimensional domain Ω with boundary Γ (Bear 1972),

$$\nabla \cdot \left(\frac{k\rho}{\mu} \nabla p \right) - \frac{\partial}{\partial z} \left(\frac{gk\rho^2}{\mu} \right) - q_m = \phi \frac{\partial \rho}{\partial t} \qquad \text{(C-1)}$$

subject to initial and generalized boundary conditions

$$p = p_0 \qquad \text{on } \Omega \text{ at } t = 0 \qquad \text{(C-2)}$$

$$\left(\frac{k\rho}{\mu} \nabla p \right) \cdot \mathbf{n} = \nu \left(p_f - p \right) + q_b \qquad \text{along } \Gamma \qquad \text{(C-3)}$$

where p is absolute liquid pressure [M/LT^2], ρ is liquid density [M/L^3], μ is liquid dynamic viscosity [M/LT], k is permeability [L^2], ϕ is porosity [–], q_m is a source term [M/L^3T], $\mathbf{n}$ is unit vector normal to the boundary Γ, q_b is prescribed air mass flux [M/L^2T] normal to Γ, ν is a parameter controlling the type of boundary conditions (first or second type if $\nu = 0$ or $\nu \to \infty$, respectively; third type otherwise) [T/L], and g is acceleration due to gravity [L/T^2; 9.8 m/s^2]. The absolute liquid pressure p and liquid density ρ are related through the equation of state

$$\rho = \rho_0 \exp(Cp) \tag{C-4}$$

where C is liquid compressibility [LT^2/M]. Rational-function approximations are used to estimate these properties in FEHM, where the rational functions are a ratio of polynomials (Harr et al. 1984).

The governing liquid pressure p depends on initial and boundary conditions as well as on the spatial distribution of medium properties (in our case permeability k and porosity ϕ) throughout model domain Ω. The forward problem can be defined formally as follows

$$p = \Psi(\mathbf{a}) \tag{C-5}$$

where $\mathbf{a}$ is a vector [$M \times 1$] of the unknown model parameters and the forward operator Ψ is a functional that maps $\mathbf{a}$ into p through the governing equations. The inverse problem can be defined as solving the last equation for $\mathbf{a}$ based on a knowledge of the state variable p

$$\mathbf{a} = \Psi^{-1}(p) \tag{C-6}$$

where Ψ^{-1} is an inverse operator. A well-posed mathematical problem is one for which a solution exists, is unique and stable. Although the forward problem is generally well-posed, the corresponding inverse problem tends to be ill-posed. This is due to lack of sufficient information about the state of the system (pressures, fluxes), measurement and interpolation errors, as well as computational errors associated with solving the forward problem. This can lead to non-unique and unstable inverse solutions (Carrera and Neuman 1986). Following to maximum likelihood approach proposed by Carrera and Neuman [1986a], the solution of the inverse problem can be defined as a weighted square-difference problem where we minimize the objective function $\Phi(\mathbf{a})$,

$$\Phi(\mathbf{a}) = [\mathbf{o}(\mathbf{a}) - \mathbf{o}^*]^T \mathbf{W} [\mathbf{o}(\mathbf{a}) - \mathbf{o}^*] \tag{C-7}$$

where $\mathbf{o}^*$ and $\mathbf{o}(\mathbf{a})$ are vectors [N × 1] of respectively observed and simulated responses (pressures, fluxes) of the hydrogeologic system, $\mathbf{W}$ is a diagonal weight matrix [N × N]. The computation of $\mathbf{o}(\mathbf{a})$ is performed by the code FEHM; the minimization of objective function is performed by the code PEST, which implements the Levenberg-Marquardt (second-order optimization) algorithm. The latter requires the computation of a sensitivity (Jacobian) matrix $\mathbf{J}$ representing the sensitivity (partial derivatives) of each simulated response $\mathbf{o}(\mathbf{a})$ in respect to each model parameters $\mathbf{a}$ ($\partial[\mathbf{o}(\mathbf{a})]/\partial\mathbf{a}$).

In the inverse methodology, the analysis of estimation errors is of critical importance. Here we follow the linearized analysis of estimation errors proposed by (Carrera et al. 1986). It assumes that the forward model Ψ is linear close to the obtained parameter estimates and parameter estimation errors are multi-Gaussian. If this is the case, the estimation errors are fully characterized by their mean (equal to zero) and covariance matrix $\boldsymbol{\Sigma}$. It is proved that $\boldsymbol{\Sigma}$ is such that $\boldsymbol{\Sigma} - \mathbf{F}^{-1}$ is semi-positive definite, where $\mathbf{F}$ is the Fisher information matrix. Therefore, $\mathbf{F}^{-1}$ defines "a lower bound" for the covariance matrix of estimation errors, and we can define $\boldsymbol{\Sigma} \approx \mathbf{F}^{-1}$.The Fisher information matrix $\mathbf{F}$ is a measure of information about the parameters that is contained in the inverted data, and $\boldsymbol{\Sigma}$ is a measure of estimation uncertainty. The more information is contained in the data, the less uncertain are the parameter estimates. In our case, F is defined as

$$\mathbf{F} = \mathbf{J}^T\mathbf{C}\mathbf{J} \qquad \text{(C-8)}$$

where $\mathbf{C}$ is the covariance matrix of observation errors. $\mathbf{F}$ may become singular when some of the parameter estimates are highly correlated. If $\mathbf{F}$ is not singular, the covariance matrix of estimation errors $\boldsymbol{\Sigma}$ can be estimated as

$$\boldsymbol{\Sigma} = [\mathbf{J}^T\mathbf{C}\mathbf{J}]^{-1} = s^2[\mathbf{J}^T\mathbf{W}\mathbf{J}]^{-1} \qquad \text{(C-8)}$$

where s^2 is a scaling factor of covariance matrix $\mathbf{C}$, and $\mathbf{J}^T\mathbf{W}\mathbf{J}$ is the so-called "normal matrix". If s^2 is unknown (as typically is the case) it can be estimated *a posteriori* by dividing the objective function estimate Φ by the number of degrees of freedom (i.e. N – M).

The simplest way to present the uncertainty in parameter estimates (i.e., the estimation errors) is through 95% confidence intervals that are proportional to the respective diagonal terms

of Σ. To estimate what is causing these uncertainties, parameter insensitivities or cross-correlations among estimation errors, we should perform further analysis. From Σ, we can calculate a correlation matrix, which represent the direct (one-to-one) correlation coefficient between estimation errors of respective parameters. We can also perform an eigenanalysis of Σ, which allows better identification of parameter uncertainties and cross-correlations among the estimation errors. Since by definition the covariance matrix is positive definite, the eigenvalues are real and the eigenvectors are mutually orthogonal, representing the axes of an M-dimensional covariance ellipsoid defined by Σ. The components of each eigenvector represent the relative contribution to it by the estimation errors of each parameter. Parameters associated with eigenvectors having small eigenvalues are less uncertain than those associated with eigenvectors having large eigenvalues. Parameters associated with single eigenvectors have uncorrelated estimation errors. Parameters associated with multiple eigenvectors have cross-correlated estimation errors.

We should note again that the error analysis described above is based on the assumptions that (1) the measurements $\mathbf{o}^*$ are mutually uncorrelated ($\mathbf{W}$ is diagonal), (2) the measurement errors are Gaussian (3) the forward model $\Psi(\mathbf{a})$ is linear in the close vicinity of the optimal parameter estimates, and (4) the estimation errors of parameters are multi-Gaussian. In practice, none of these assumptions are typically fulfilled, and therefore the computed statistics are approximate. Still the estimation error analysis as well as the analysis of sensitivity matrix $\mathbf{J}$ provide us will important insights about the inverse model estimates and their estimation errors.

Enhanced computational efficiency of the Levenberg-Marquardt algorithm can be achieved by parallelizing the evaluation of the sensitivity (Jacobian) matrix. Doherty (1997) created a parallel UNIX version of PEST. We have modified this parallel version so as to better utilize the computational resources of a standard UNIX multi-processor environment. We have further altered PEST to allow efficient restarting of the optimization process, if and when it terminates prematurely, so as to virtually eliminate loss of computational time. The parallelized version of the inverse model was run on the SGI Origin 2000 multi-processor supercomputer.

Appendix D. Corrections to groundwater carbon-14 ages in the Los Alamos area

In discussing the processes that influence the values of the carbon isotopes, it is helpful to distinguish between "open" systems, in which carbon isotope exchange between the gas and liquid phases takes place continuously and "closed" systems, in which the water is isolated from the soil gas. Generally, in open systems, changes in the values of the $\delta^{13}C$, ^{14}C, and pH of the water that might occur from water/rock interactions, including calcite dissolution, are buffered by the presence of an essentially unlimited volume of soil gas in which the partial pressure of $CO_{2(g)}$ (P_{co2}) is constant. Under closed system conditions, the amount of $CO_{2(g)}$ available for reaction is limited to the amount dissolved in the water at the time it passed from open system to closed system conditions. Because the rates of gas diffusion through water are quite low compared to the water flux under all but nearly stagnant conditions, the transition from open to closed system conditions is generally assumed to take place at the water table.

The isotopic ratio ($^{13}C/^{12}C$) is expressed in the δ-notation (Equation 6-1), with Pee Dee Belemnite (PDB) forming the reference. Studies of Holocene pedogenic carbonates in the Great Basin (Quade et al. 1989; Quade and Cerling 1990) have shown that the $\delta^{13}C$ of these carbonates are negatively correlated with elevation. The $\delta^{13}C$ of pedogenic carbonates reflect the $\delta^{13}C$ values of CO_2 in soil gas, which increases at lower elevations in the Great Basin because (1) the proportion of plants that follow the C4 and CAM rather than C3 photosynthetic pathway increases at the more arid, low-elevation sites, and (2) plant respiration rates are lower at these water-stressed sites, permitting the downward diffusive flux of ^{13}C from isotopically heavy, atmospheric CO_2 to have a greater effect on the overall isotopic composition of the soil gas. The average $\delta^{13}C$ of C4 plants is –12.7 permil, the average $\delta^{13}C$ of C3 plants is –27.1 permil, and the average of CAM plants is intermediate and depends on the local environmental conditions (Cerling 1984).

Holocene pedogenic carbonates both in Great Basin (Quade et al., 1989; Quade and Cerling, 1990) and worldwide (Cerling, 1984), have $\delta^{18}O$ values that reflect the $\delta^{18}O$ of the local precipitation, which, as discussed above, tends to become lighter with increased elevation. In the Great Basin, it was shown (Quade et al., 1989, Fig 9)) that the observed $\delta^{18}O$ values of pedogenic carbonate were correlated with, but somewhat heavier than, the local meteoric water, a relation

that was attributed to the preferential deposition of pedogenic carbonates by isotopically heavy summer rains or to partial evaporation of the water in the soil zone.

Detailed elevation profiles of $\delta^{13}C$ and $\delta^{18}O$ in pedogenic carbonates similar to those described for the Great Basin do not exist for the Los Alamos area. Fracture-filling calcite from unsaturated Tshirege Member of the Bandelier Tuff had average $\delta^{13}C$ and $\delta^{18}O$ values of –4.6 permil PDB and 21.8 permil SMOW, respectively, and a ^{14}C age between 23,300 and 25,300 years (Newman, 1996, p. 10). The $\delta^{13}C$ of this calcite is somewhat heavier than the values typical of Holocene calcite in pinyon-juniper-sage zones at the same elevation in the Great Basin (-7.4 +/- 0.8 per mil; Quade and Cerling, 1990, p. 1550). Based on the temperature-dependent fractionation factors listed in Clark and Fritz (1997) and an assumed temperature of 15 degrees Celsius, the equilibrium $\delta^{13}C$ of the soil gas and the equilibrium $\delta^{18}O$ of the water precipitating the calcite were calculated. The estimated $\delta^{13}C$ for the soil gas of –16.4 permil PDB is slightly heavier than would be expected for the sample elevation of 6,600 feet (2,012 m), based on a comparison with modern trends between the $\delta^{13}C$ of soil gas and elevation in the Great Basin (Quade et al, 1989, Figs. 6 and 7). The estimated equilibrium $\delta^{18}O$ of –9.3 permil is only slightly heavier than the $\delta^{18}O$ of about -10 permil estimated for precipitation at the land-surface elevation of the calcite samples, based on the correlation between $\delta^{18}O$ and ground-surface elevation given by Equation (6-2). The limited data provided by the calcite fracture coating suggests that 25,000 years ago, the climate on the Pajarito Plateau was not substantially cooler or wetter than the modern climate.

In map view, the $\delta^{13}C$ values of water from springs and wells in the Los Alamos area do not show evidence of systematic variations (Fig. D-1). Only one value for $\delta^{13}C$ (-15.0 per mil) exists for springs in the Sierra de los Valle. The values for wells and springs on the Pajarito Plateau range between –15.0 and –6.0 per mil, and a similar range of values exist for springs in the Rio Grande areas. In some locations, such as near the southernmost springs in the Rio Grande area, waters discharging in close proximity have very different $\delta^{13}C$ values.

From the elevation trends established for pedogenic carbonates in the Great Basin, it might be expected that if the recharge water acquires a the dominant fraction of its dissolved inorganic carbon from pedogenic carbonate in the recharge area, the $\delta^{13}C$ of the recharge water might reflect the effects of land-surface elevation in a similar way as the $\delta^{18}O$ of the water. Thus, a positive correlation might be expected between the $\delta^{13}C$ and $\delta^{18}O$ values in groundwater.

However, the data for springs and wells in the Los Alamos area do not show evidence of a positive correlation.

The absence of a correlation between $\delta^{13}C$ and $\delta^{18}O$ values in groundwater may be the result of one or more of several factors. The first is that the enrichment factor associated with fractionation of ^{13}C between the DIC and $CO_{2(g)}$ ($\varepsilon_{DIC\text{-}CO2(g)}$) is highly dependent on the relative proportions of the dissolved carbon species present in the infiltrating water and, hence, on the pH of the water, as it passed from open to closed-system conditions. Once under closed system conditions, the $\delta^{13}C$ of the DIC is fixed unless additional sources of carbon, such as calcite, are encountered by the groundwater. Enrichment factors between DIC and $CO_{2(g)}$ range from zero at a pH of about 5.5 to a value of about 7.9 at near-neutral pH values (Clark and Fritz, 1997, Fig.5-5). Thus, the $\delta^{13}C$ of recharge water in equilibrium with $CO_{2(g)}$ having a $\delta^{13}C$ of –16.4 per mil could range from –16.4 to –8.5 per mil, depending on pH. The pH of springs in the Valle Caldera and Sierra de los Valle ranges from 5.5 to 7.2 (Blake et al., 1995), so that the effects of pH on $\varepsilon_{DIC\text{-}CO2(g)}$ may be responsible for at least some of the variability in $\delta^{13}C$ values.

A second possible reason for the absence of a correlation between groundwater $\delta^{13}C$ and $\delta^{18}O$ values is that the $\delta^{13}C$ of the groundwater is modified along its flowpath by deeper calcite in the regional aquifer whose $\delta^{13}C$ values, which are presently unknown, have no relation to modern surface topography. Secondary calcite has been identified on thin sections of rocks from the Santa Fe Group and the Puye Formation (R. Warren, written communication, 1999). Calcite dissolution is described by the equation

$$CaCO_{3(s)} + CO_{2(g)} + H_2O = Ca^{2+} + 2HCO_3^- \qquad \text{(D-1)}$$

During calcite dissolution, the dissolved $CO_{2(g)}$ and calcite contribute equal amounts of carbon to HCO_3^-. Under closed-system conditions, neither the total DIC nor the isotopic composition of the DIC changes as a result of the conversion of dissolved $CO_{2(g)}$ (H_2CO_3) to HCO_3^-. For closed-system conditions, the additional DIC is derived from the calcite alone and has the $\delta^{13}C$ value of the dissolving calcite. Thus, if calcite dissolution were taking place continuously along a flow path in the saturated zone, the $\delta^{13}C$ values of the DIC would shift from light values typical of the recharge area toward heavier values typical of the calcite as additional HCO_3^- (the predominant form of DIC at neutral pH) is added to the groundwater.

At most sites, the pH of the water is neutral or alkaline and the alkalinity and DIC values are similar. For many springs in the Sierra de los Valle, however, DIC concentrations are much higher than alkalinity because of the low pH values at these sites. Because of their high DIC concentrations, springs in the southern part of the Sierra de los Valle cannot be representative of the source of the lower elevation waters unless a substantial amount of de-gassing of $CO_{2(g)}$ takes place as these spring waters percolate through the unsaturated zone to the water table. Springs in the Valle Caldera have low alkalinity and DIC compared to other subsurface water in the Los Alamos area. Groundwater in the Rio Grande Area Wells, Wells East of the Rio Grande, and Springs East of the Rio Grande groups have generally high values of alkalinity and DIC compared with water from the Pajarito Plateau Wells, Pajarito Plateau Springs, and the southern Rio Grande Area Springs. Springs on the Pajarito Plateau also have high alkalinity and DIC compared to groundwater from most Pajarito Plateau Wells and the Rio Grande Area Springs.

The degree of saturation of water with respect to a mineral is indicated by the saturation index (SI_{min}) for the mineral, where $SI_{min} = \log (IAP/K_{min})$, K_{min} is the dissociation constant for the mineral, and IAP is the ion activity product of the ions that result from dissolution of the mineral. When the water is saturated with respect to a mineral, $SI_{min} = 0$; conversely, $SI_{min} > 0$ and $SI_{min} < 0$ when the water is oversaturated and undersaturated with respect to a mineral. Calculations of the calcite saturation indices (SI_{cal}) of water in the Los Alamos area are of interest because these values indicate the potential of water in different areas to dissolve calcite. These SI_{cal} are shown in plan view in Figure D-2. Water samples from springs in the Valle Caldera and Sierra de los Valle have low alkalinity and are undersaturated with calcite; Springs on the Pajarito Plateau are generally also undersaturated with calcite, except for Sandia Canyon and Indian Springs close to the Rio Grande. Groundwater from wells on the Pajarito Plateau and from springs in the Rio Grande area have values of SI_{cal} that range from about –2 to 0, indicating variable degrees of saturation of the water with calcite. Generally, groundwater at wells in the northern part of the Pajarito Plateau has higher SI_{cal} values than groundwater at wells in the southern part. Groundwater in the Rio Grande Area Wells, East of the Rio Grande Wells, and Springs East of the Rio Grande groups is saturated or slightly supersaturated with calcite.

To examine the possibility that closed system calcite dissolution reactions are controlling the variability in groundwater $\delta^{13}C$ values, the $\delta^{13}C$ values of water from springs and wells in the Los Alamos area are plotted as a function of their DIC concentration (Fig. D-3). Also shown in

the figure are two curves that show the expected changes in the $\delta^{13}C$ of the water as DIC is added to the system as a result of calcite dissolution. The upper curve assumes $\delta^{13}C$ of the calcite is 0.0 per mil, which is the value typical of marine carbonates (Fritz and Clark, 1997, Fig. 5-1), whereas the lower curve assumes that the $\delta^{13}C$ of the calcite is equal to the value of -4.6 per mil reported by Newman (1996). Paleozoic carbonate rocks crop out locally south of the Los Alamos area and are believed to underlie the tuffs and Santa Fe Group sediments beneath the Pajarito Plateau (Kelley, 1978), so deep-circulating water could conceivably contact these rocks or sediments derived from these rocks.

Although neither curve is capable of explaining all of the variability in the $\delta^{13}C$ values and DIC concentrations of the Pajarito Plateau and White Rock Canyon samples, the curves together seem to indicate that the increases in $\delta^{13}C$ that accompany increases in DIC are at least partly attributable to the dissolution of isotopically heavy calcite. Silicate-mineral weathering reactions will not result in an increase in either $\delta^{13}C$ or DIC because the conversion of dissolved $CO_{2(g)}$ is the only carbon phase participating in these reactions and its $\delta^{13}C$ is already reflected in $\delta^{13}C_{DIC}$. Some of the groundwater east of the Rio Grande has $\delta^{13}C$ values that fall below the lower curve, suggesting either different conditions in the recharge area or different processes have affected the isotopic composition of these water samples.

The ^{14}C data from Rogers et al. (1995) and $\delta^{13}C$ and HCO_3^- data from Blake et al. (1995) for the same wells are shown in Figures D-4A to D-4C. Note that in Figures A-3b and A-3c, one data point (from well LA-1a) has been omitted from the regression calculations. The increase in $\delta^{13}C$ with increasing DIC concentrations (Fig. D-4B) and the decrease in ^{14}C activities (Fig. D-4A) with increasing $\delta^{13}C$ indicate that the ^{14}C in the groundwater has been diluted to varying degrees by isotopically heavy calcite that is depleted in ^{14}C compared to the groundwater. These trends would not be expected if only silicate weathering reactions were taking place, because these reactions involve only dissolved $CO_{2(g)}$ as a source of carbon and soil $CO_{2(g)}$ is isotopically light compared to the groundwater. Thus, at least some of the decrease in ^{14}C activities that accompany increases in DIC concentrations (Fig. D-4C) are due to contact between the groundwater and carbonate minerals. Qualitatively, these conclusions are not different from those described in Rogers et al. (1995).

In this appendix, the groundwater ^{14}C ages are reinterpreted in light of the above discussions using two correction models. The first correction model uses the estimated $\delta^{13}C$ of

the recharge water, groundwater DIC, soil gas CO_2, and carbonate minerals to determine the ^{14}C dilution the groundwater has undergone up to the time of sampling to estimate a dilution factor:

$$q_{\_13C} = (\_^{13}C_{DIC} - \_^{13}C_{carb})/(\_^{13}C_{rech} - \_^{13}C_{carb}) \qquad \text{(D-2)}$$

where $q_{\_13C}$ is the factor reflecting the dilution that the ^{14}C in the recharge water is estimated to have undergone as a result of carbonate mineral dissolution. The value of $\_^{13}C_{rech}$ is estimated from

$$\_^{13}C_{rech} = \_^{13}C_{CO2(g)} + \varepsilon_{DIC\text{-}CO2(g)} \qquad \text{(D-3)}$$

The difficulty in applying this method is in estimating the pH-dependent value of $\varepsilon_{DIC\text{-}CO2(g)}$. An estimated value for $\_^{13}C_{rech}$ of –8.5 per mil can be calculated using a value of –16.4 per mil for $\_^{13}C_{CO2(g)}$ and a value of –7.9 per mil for $\varepsilon_{DIC\text{-}CO2(g)}$. However, this value for $\_^{13}C_{rech}$ cannot be generally applicable because most of the spring and groundwater samples in the Los Alamos area have $\_^{13}C$ values less than -8.5 per mil (Fig. D-4A). Given that the value for $\_^{13}C_{CO2(g)}$ of –16.4 per mil is correct, only a value for $\__{DIC\text{-}CO2(g)}$ near zero will permit the correction of all the spring and groundwater samples for calcite dissolution using Equation D-2. Consequently, the dilution factor $q_{\_13C}$ was calculated using values of –16.4 per mil for $\_^{13}C_{CO2(g)}$, 0 permil for $\varepsilon_{DIC\text{-}CO2(g)}$, and two different values for $\_^{13}C_{carb}$. In case 1, $\_^{13}C_{carb}$ is assumed to be –4.6 per mil, the value of the pedogenic fracture calcite (Newman, 1996) and approximately the $\_^{13}C$ value of the end-member carbon source indicated by the intercept of the regression line in Figure D-4A. In case 2, $\_^{13}C_{carb}$ is assumed to be 0 per mil, the average value of marine carbonate. In turn, $^{14}A_o = q_{\_13C}\ ^{14}A_{atm}$ was used in the radioactive decay equation (Equation 6-5) to calculate the corrected ^{14}C age of the groundwater. These ages are listed in Table D-1 as "$\_^{13}C$-corrected ages". The fact that the dilution factor $q_{\_13C}$ is substantially less than 0.5 may indicate that isotope exchange is an important process influencing carbon isotopes in groundwater near Los Alamos, because simple carbonate dissolution under closed-system conditions (Equation D-1) would not dilute the ^{14}C activity by more than half.

A second method for correcting groundwater ^{14}C ages for the effects of carbonate mineral dissolution involves calculating the ratio of the DIC gained from dissolving soil gas CO_2 to the

DIC measured in the groundwater sample. In this case, the dilution of the ^{14}C in the groundwater by carbonate mineral dissolution is calculated from

$$q_{DIC} = mDIC_{rech}/mDIC_{sample} \qquad (D\text{-}4)$$

where $mDIC_{rech}$ and $mDIC_{sample}$ are the concentrations of DIC in the recharge water and groundwater sample, respectively. The basis for this method is that, under closed-system conditions, the DIC of the groundwater is constant (although the relative proportions of the dissolved carbon species may change) unless additional sources of carbon in the form of carbonate minerals are encountered along the flow path. Any increase in groundwater DIC downgradient from the recharge area thus reflects interaction with carbonate minerals. This method implicitly assumes that the ^{14}C of the recharge water is 100 pmc, a condition likely to be true only if no carbonate dissolution occurred in the unsaturated zone or if open system exchange between $CO_{2(g)}$ and the unsaturated zone water re-established the ^{14}C of the water at 100 pmc after calcite dissolution had occurred.

Geochemical modeling of groundwater silicate weathering and calcite dissolution reactions done in support of this work using PHREEQC (Parkhurst, 1994) but not discussed in this report indicate that, although the calculated P_{CO2} values of some spring samples are somewhat higher, an assumed soil gas P_{CO2} of $10^{-1.5}$ atm best explains the pH and alkalinity of the groundwater data. Assuming a recharge temperature of 15 degrees celsius and that, in dilute waters, activities are approximately equal to molalities, the total DIC of the recharge water is estimated to be 89.6 mg/L as HCO_3^-, with about 98.5 percent of the DIC actually present as $CO_{2(aq)}$. This value of $mDIC_{rech}$ was compared to the measured alkalinities (which approximate $mDIC_{sample}$ at neutral pH) to compute values for q_{DIC}.

The computed values of q_{DIC} are listed in Table D-1, along with the DIC-corrected ^{14}C ages. Several values of q_{DIC} are above 1.0, which indicates the DIC age-correction method is invalid for these samples. However, for the groundwater samples for which meaningful values of q_{DIC} were calculated, the corrected ages are in good agreement with the corrected ages calculated for case 1 using $\_^{13}C$. Based on the agreement between these estimates of corrected ages, the $\_^{13}C$-corrected ^{14}C ages for case 1 are considered to be the best approximation to the true age of the water. These ages are shown in Figure 6-10 in the main body of the report.

Table D-1. Table showing the results of groundwater carbon-14 age corrections

Well	^{14}C activity (pmc)	Uncorrected Age (years)	$\delta^{13}C$ (in permil)	DIC, (as mg/L HCO_3^-)	$Q_{\delta 13C}$ (case 1)[a]	$\delta^{13}C$ Corrected Age –case 1[a] (years)	$Q_{\delta 13C}$ (case 2)[b]	$\delta^{13}C$ Corrected Age – case 2[b] (years)	Q_{DIC}	DIC-corrected age (years)
PM-5	53.7	5,140	-13.9	79.9	0.85	3,773	0.79	3,172	1.12	---
DT-5A	57.6	4,560	-14.2	68.5	0.87	3,370	0.81	2,855	1.31	---
O-4	25	11,460	-9.05	152.9	0.55	6,546	0.38	3,399	0.59	7,042
PM-3	23.9	11,832	-8.95	177.8	0.55	6,826	0.37	3,583	0.50	6,167
PM-1	18.5	13,949	-9.15	133	0.56	9,126	0.39	6,072	0.67	10,684
G-5	26.8	10,885	-13.0	94.4	0.79	8,965	0.71	8,076	0.95	10,454
LA-1A	13.9	16,312	-7.1	82.1	0.43	9,392	0.21	3,484	1.09	---
Eastside Artesian	3.8	27,033	-9.38	178.3	0.57	22,416	0.41	19,564	0.50	21,345
LA-1B	0.9	38,940	-5.8	411.7	0.35	30,349	0.10	20,045	0.22	26,334
Westside Artesian	0.05	62,834	-6.25	398.3	0.38	54,861	0.14	46,573	0.22	50,501

[a]In case 1 it was assumed that calcite had a $\delta^{13}C$ of 0.0 per mil

[b]In case 2 it was assumed that calcite had a $\delta^{13}C$ of –4.6 per mil

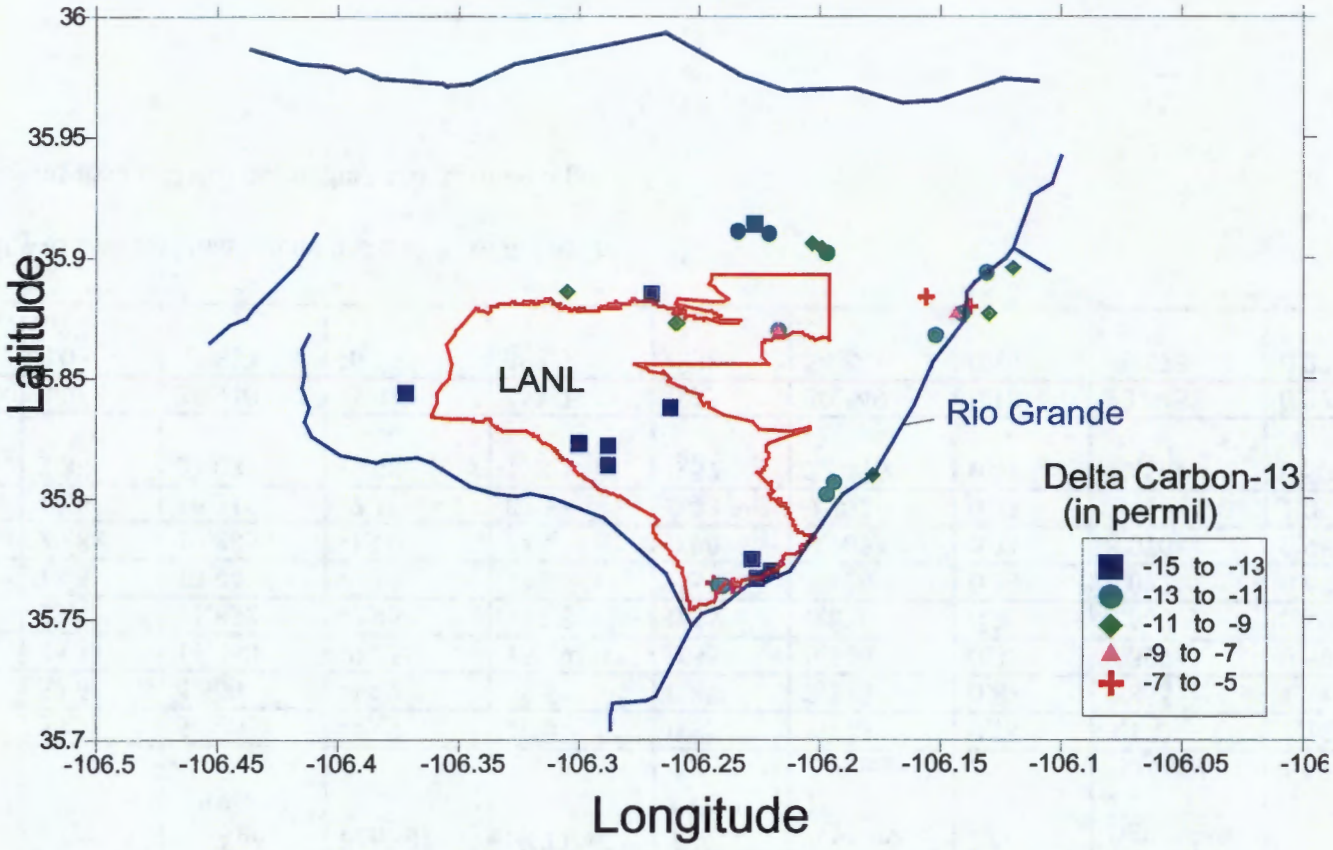

Figure D-1. Map showing the distribution of delta carbon-13 ($\delta^{13}C$) of water from springs and wells in the Los Alamos area.

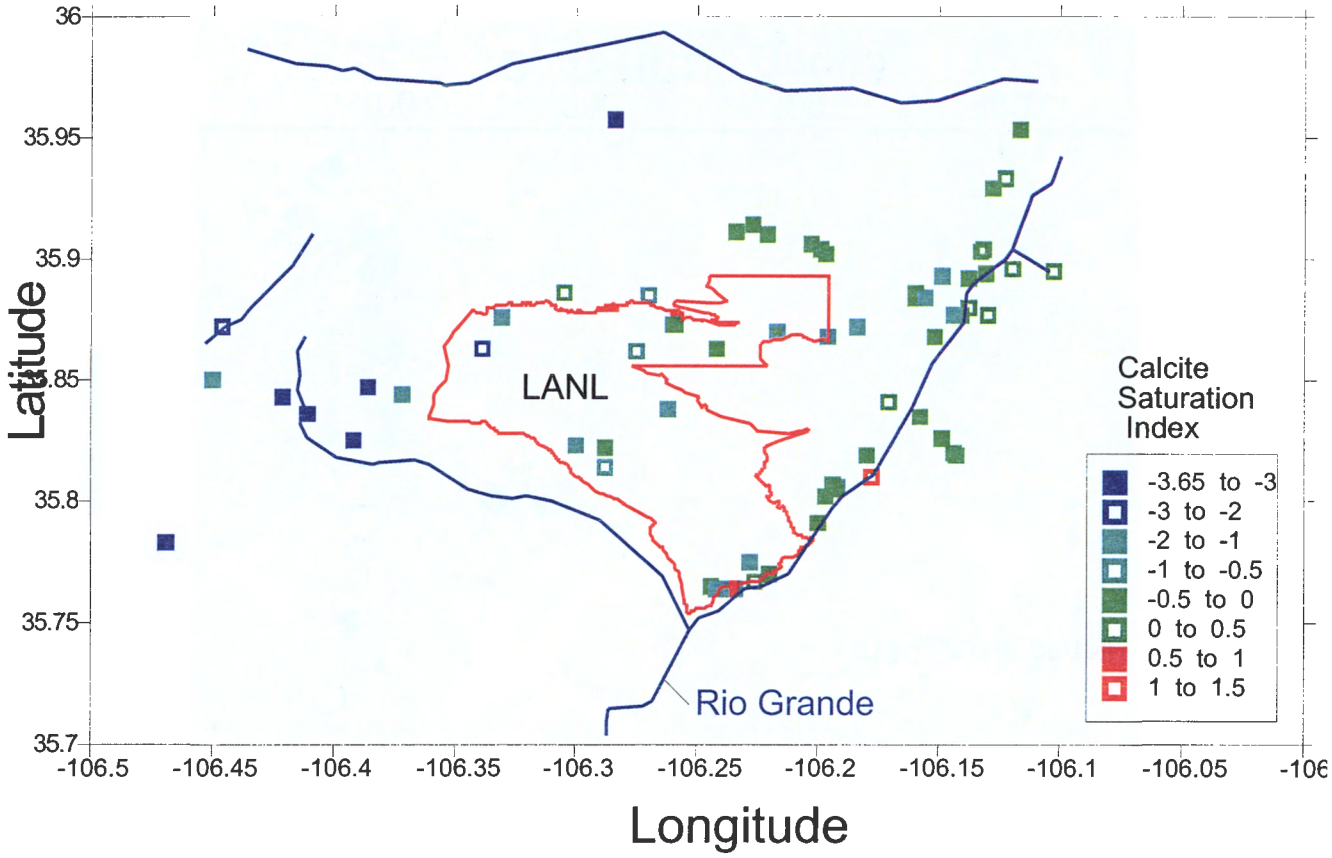

Figure D-2. Map showing the distribution of calculated calcite saturation indices (SI_{cal}) of water from springs and wells in the Los Alamos area

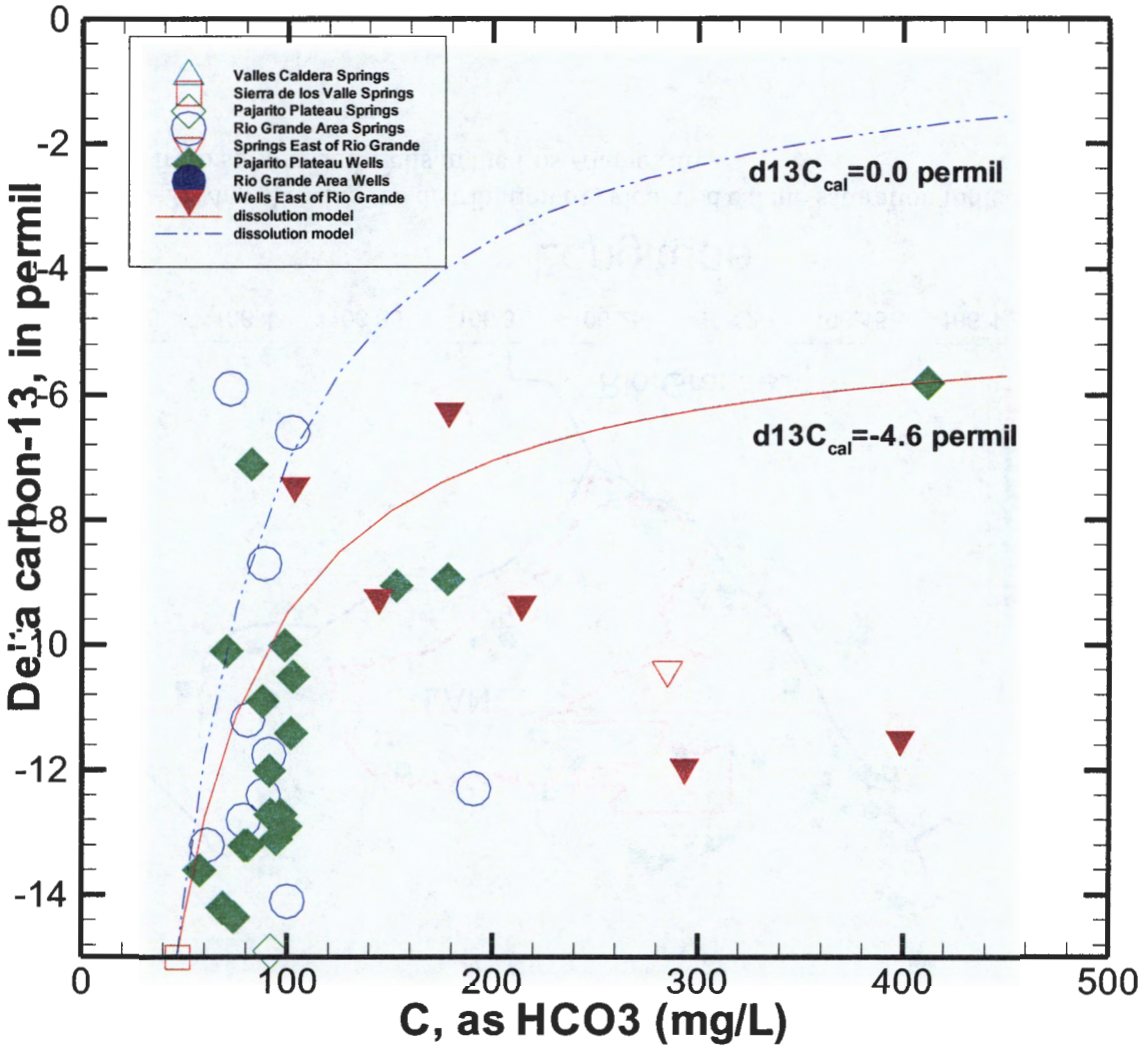

Figure D-3. Relation of delta carbon-13 ($\delta^{13}C$) to DIC concentration of water from springs and wells in the Los Alamos area.

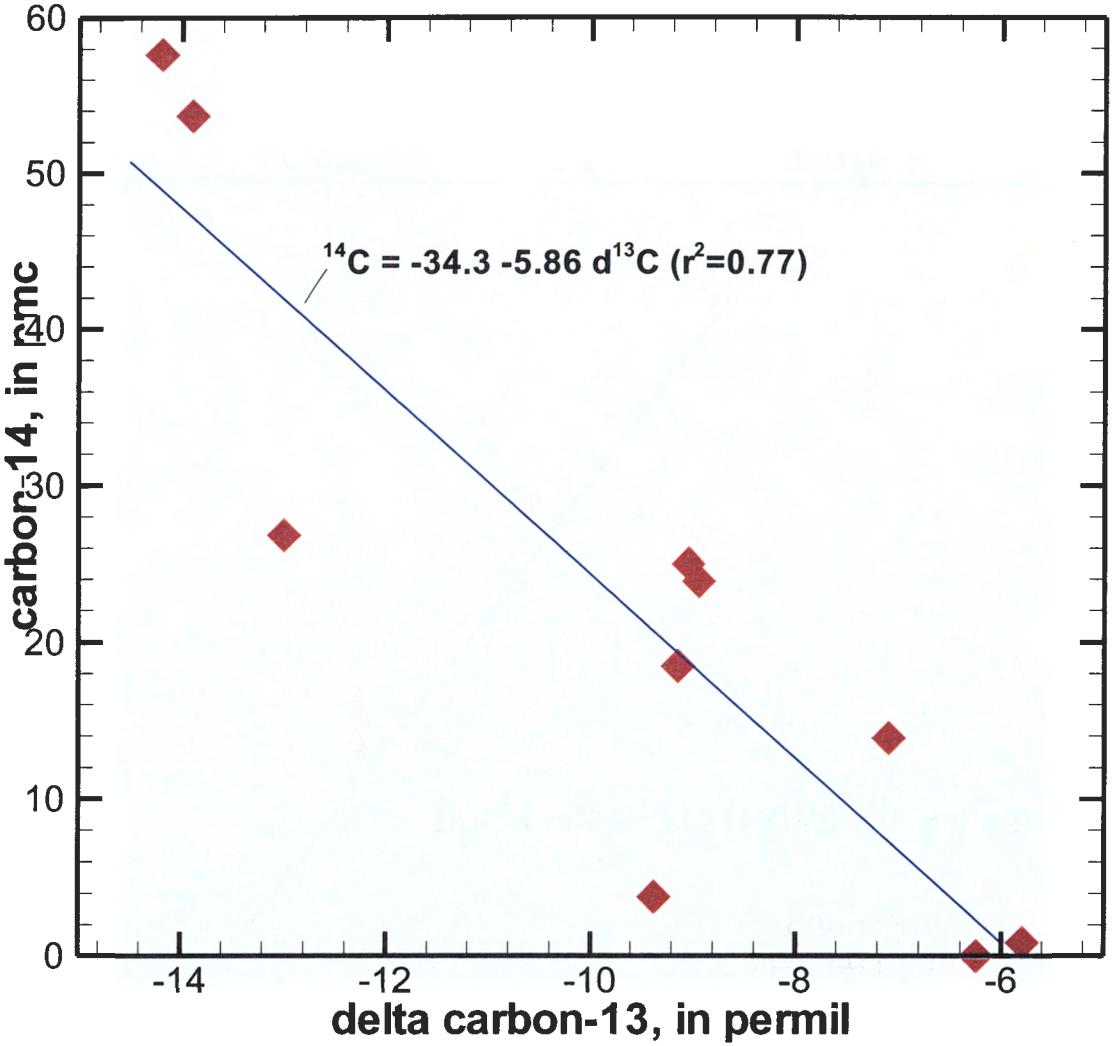

Figure D-4(A). Relation of (a) carbon-14 (^{14}C) activity to delta carbon-13 ($\delta^{13}C$) values.

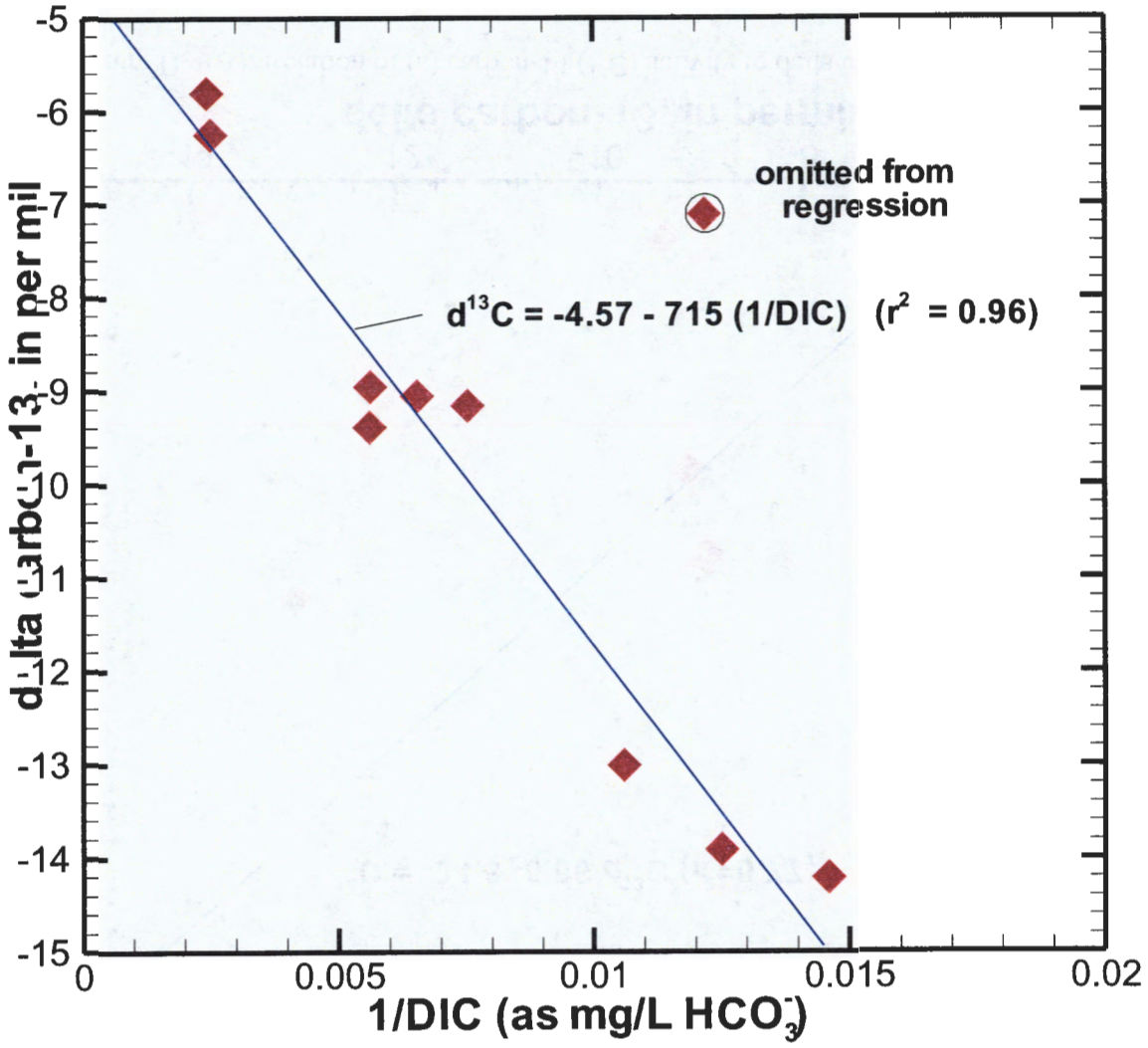

Figure D-4(B). Relation of $\delta^{13}C$ to the reciprocal of DIC concentration ($1/m_{DIC}$).

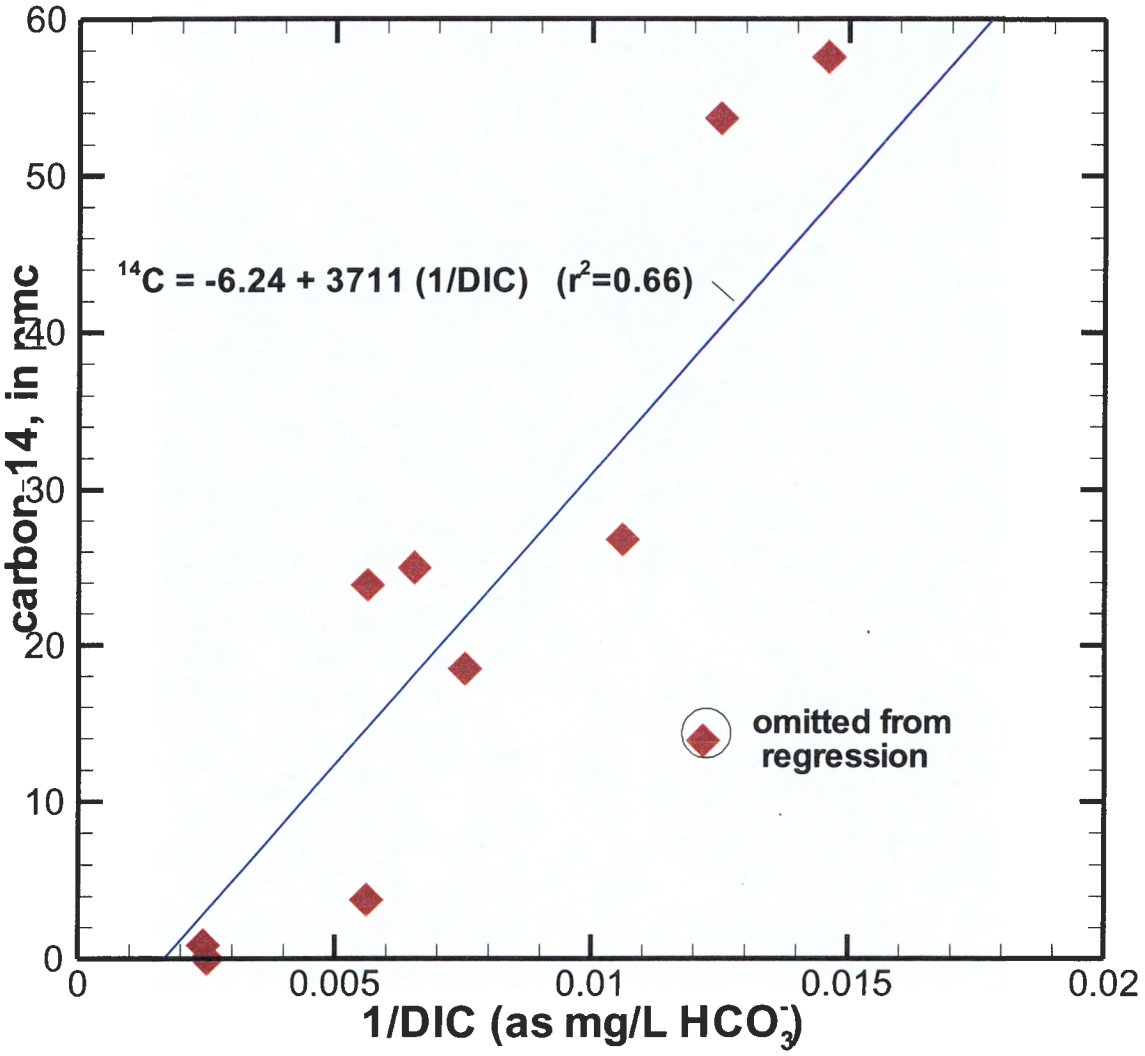

Figure D-4(C). Relation of ^{14}C to $1/m_{DIC}$ for groundwater samples with measured ^{14}C activities.